

**THE UNIVERSITY OF MANCHESTER - APPROVED ELECTRONICALLY
GENERATED THESIS/DISSERTATION COVER-PAGE**

Electronic identifier: 34159

Date of electronic submission: 22/09/2021

Thesis format: Traditional

The University of Manchester makes unrestricted examined electronic theses and dissertations freely available for download and reading online via Manchester eScholar at <http://www.manchester.ac.uk/escholar>.

This print version of my thesis/dissertation is a TRUE and ACCURATE REPRESENTATION of the electronic version submitted to the University of Manchester's institutional repository, Manchester eScholar.

MANCHESTER
1824

The University of Manchester

QCD Evolution At Amplitude Level

Author:

Matthew V. De Angelis

Supervisor:

Professor Jeff Forshaw

A thesis submitted to the University of Manchester for the degree of
Doctor of Philosophy in the Faculty of Science and Engineering

Particle Physics Group
School of Physics and Astronomy

2021

Contents

List of Figures	7
List of Tables	15
Abstract	21
Acknowledgements	29
Introduction	31
1 QCD Preliminaries	35
1.1 A Brief History	36
1.2 Quantum Chromodynamics	37
1.2.1 $SU(N_c)$ Group	37
1.2.2 Gauge Invariance	42
1.2.3 QCD Lagrangian	46
1.3 Feynman Rules	50
1.4 Basic features of QCD radiation	53
1.4.1 Born Amplitude	53
1.4.2 Eikonal approximation	56
1.4.3 Emission contribution	58
1.4.4 Virtual Contribution	60
1.4.5 Resummation	64
1.5 Colour Flow Representation	67
2 Amplitude Evolution	73
2.1 The General Algorithm	75
2.1.1 Non-global Contribution To The Hemisphere Jet-Mass	81
2.2 Colour Mechanics	87
2.2.1 Colour Flow Basis	88
2.2.2 Working In A Non-Orthogonal Colour Basis	91
2.3 Amplitudes And Matrix Elements	92

2.3.1	Leading-Colour Contributions	98
2.3.2	BMS Equation	102
2.3.3	Subleading-Colour Contributions	106
3	Monte Carlo Methods	113
3.1	Integration and Variance	114
3.1.1	Hit-or-Miss Monte Carlo	118
3.1.2	Crude Monte Carlo	120
3.2	Sampling	121
3.2.1	Sampling by Inversion	121
3.2.2	Rejection Sampling	123
3.2.3	Sampling Discrete Distributions	125
3.3	Importance Sampling	126
3.4	Random Number Generators	128
3.5	Parton Showers	129
3.5.1	Angular Ordering	129
3.5.2	Veto Algorithm	133
3.5.3	Competition Algorithm	136
4	CVolver	139
4.1	Algorithmic Overview	142
4.2	CVolver Structure	147
4.2.1	CVolver Overview	147
4.2.2	Colour Flow Mapping And Arithmetic	151
4.2.3	Operator Classes	155
4.2.4	Shower Evolution	157
4.3	Computation of Matrix Elements	164
4.3.1	Sudakov Matrix Elements	165
4.3.2	Sudakov Operators	173
4.3.3	Numerical Exponentiation	174
4.3.4	Emission Matrix Elements	176
4.4	Colour Flow Sampling	180
4.5	The Implementation	186
4.5.1	Hard Process Matrix Elements	188
4.5.2	Observable Cross Section	189
4.5.3	Variant A	193
4.5.4	Variant B	200
5	Results	217

5.1	Variant A	219
5.1.1	Fixed Order Calculation	220
5.1.2	Cutoff independence	225
5.1.3	Testing Real Emissions	227
5.1.4	Numerical Exponentiation	229
5.1.5	Fixed Order Validation	231
5.1.6	Emission Spectra	233
5.2	Variant B	237
5.2.1	Emission Colour Factors	238
5.2.2	Angular Correlations	241
5.2.3	N_c Dependence	245
5.2.4	Fixed Order Validation	252
5.2.5	N_c -breakdown	258
5.2.6	Emission Spectra	260
	Conclusions and Outlook	271
	A CVolver UML	275
	Bibliography	281

List of Figures

1.1	A graphical representation of the Fierz identity, relating the colour structure of a one-gluon exchange between a quark and anti-quark pair to quark and anti-quark colour lines.	41
1.2	Feynman diagram of the Born amplitude for the $\gamma^* \rightarrow q\bar{q}$ process.	55
1.3	Feynman diagrams for the $\mathcal{O}(\alpha_s)$ real emission corrections to the total hadronic cross section in $\gamma^* \rightarrow q\bar{q}$	59
1.4	Feynman diagrams for the $\mathcal{O}(\alpha_s)$ one-loop corrections to the Born cross section for $\gamma^* \rightarrow q\bar{q}$	61
1.5	Two diagrams which contribute at $\mathcal{O}(\alpha^n)$ with n soft photon exchanges. The left-hand diagram is the completely uncrossed graph, whilst the right-hand diagram is an example of a graph with a single crossing.	65
1.6	An illustration of the calculation of colour structures using the Feynman rules in the colour flow representation for the $q\bar{q} \rightarrow q\bar{q}$ process.	70
2.1	Depiction of the gaps-between-jets observable. The dark circles represent the two primary jets and any subsequent emission in the in-gap region is constrained to have a transverse momentum smaller than Q_0	74

2.2	Diagrammatic representation of the colour flow basis tensors and their inner products. The top half of the figure presents a four-parton amplitude with $qg\bar{q}$ leg content and three out of the six possible basis tensors which describe potential colour arrangements. Grey arrows indicate how the external leg indices, $i = 1, \dots, 4$ are mapped onto colour and anti colour indices. The lower pane of this figure pictorially represents the contraction of the Kronecker deltas in the calculation of inner products between basis tensors. These are elements of the scalar product matrix described later and are equal to N_c to the power of the number of colour flows, n , minus the number of loops formed after contraction. Figure modified from [99].	90
2.3	Pictorial representation of the \mathbf{t}_{c_i} and $\bar{\mathbf{t}}_{c_i}$ operators in (A) and the \mathbf{s} operator in (B). Figure from [111].	94
2.4	Pictorial representation of the $\mathbf{t}_\alpha \cdot \mathbf{t}_\beta$ colour reconstructor in (A), the $\mathbf{t}_\alpha \cdot \bar{\mathbf{t}}_\beta$ colour reconstructor in the case that α and β are colour connected (B), the $\mathbf{s} \cdot \mathbf{s}$ colour reconstructor in (C) and $\mathbf{t}_\alpha \cdot \mathbf{s}$ colour reconstructor in (D). Figure from [111].	96
2.5	An illustration of one contribution to the leading-colour calculation for the $qq \rightarrow qq$ scattering process. We consider the case of one real emission and one virtual correction to the hard process $[\sigma \setminus n] \mathbf{H} [\sigma \setminus n]$. The dashed lines indicate the basis tensors at each stage of the evolution. Figure from [99].	101
2.6	The pictorial representation of the out-of-gap expansion (see Eq. 2.24) in the leading- N_c limit. This corresponds to Eq. 2.87. Figure modified from [99].	104
2.7	Depiction of the general structure of a calculation which can involve subleading-colour contributions. Figure 2.5 is a specific example involving leading-colour contributions. Figure from [99].	108
2.8	The next-to-leading colour contributions at varying powers of N_c and α_s . Each box in (A) corresponds to a contribution from the virtual evolution operator with increasing powers of α_s from left to right and decreasing powers of N_c from top to bottom, with N_c^0 in the middle. The effect of r real emissions and the $1/N_c^k$ suppression resulting from the scalar product matrix (indicated by the number of flips) is presented in the reals column of the table in (B). Figure modified from [99].	109

4.1	One contribution to the A_1 operator, starting from the $ 12\rangle [12 \mathbf{H} 21] \langle 21 $ term in the $q\bar{q} \rightarrow q\bar{q}$ hard scattering. It corresponds to a single gluon emission and a single virtual gluon exchange in both the amplitude and conjugate-amplitude. The vertical dotted lines identify the intermediate colour states. The algorithm works iteratively outwards, starting from the hard process in the middle and multiplying emission and Sudakov matrix elements as it goes. Figure used in [155].	144
4.2	An overview of the CVolver code.	149
4.3	An example of the $q\bar{q} \rightarrow q\bar{q}$ process amplitude decomposed in the colour flow basis. Outgoing particles are represented by arrows to the left of the blob with positive momenta. Incoming particles are treated as if they were outgoing particles with negative momenta. Figure used in [155].	151
4.4	Illustration of the colour charge products in the colour flow basis which contribute to a single-gluon exchange between a quark (represented by a colour line α) and a gluon (represented by a colour line β and an anti colour line $\bar{\beta}$).	167
4.5	A pictorial representation of the algorithm determining all basis tensors which are exactly two swaps away from σ . In this example, $ \sigma\rangle = 12345\rangle$, a tensor with five colour flows. Figure used in [161].	181
4.6	Diagrammatic representation of the action of a \mathbf{t} ($\bar{\mathbf{t}}$) operator, acting on the same colour (anti colour) line (highlighted by a black dot) in the amplitude and conjugate amplitude. Figure (A) presents the case in which the same anti colour line is connected to the emitting colour line in both the amplitude and conjugate, whilst in Figure (B) the connecting anti colour lines differ. Newly emitted colour and anti colour lines are red. The N_c factor contributed to the scalar product matrix element in contracting the emitting flows is written below each diagram. . . .	207
4.7	Diagrammatic representation of the action of \mathbf{t} ($\bar{\mathbf{t}}$) and \mathbf{s} operators. Newly emitted colour and anti colour lines are coloured red. The black dots denote the colour line on which \mathbf{t} or \mathbf{s} acts and the N_c factor contributed to the scalar product matrix element in contracting the emitting flows is written below each diagram.	208

- 4.8 Diagrammatic representation of the action of a \mathbf{t} ($\bar{\mathbf{t}}$) operator, acting in both the amplitude and conjugate amplitude. In the top two illustrations, the colour flows on which \mathbf{t} ($\bar{\mathbf{t}}$) act share no colour or anti colour indices in common. Newly emitted colour and anti colour lines are coloured red and the black dots denote an example colour line on which \mathbf{t} acts in the amplitude and an anti colour line on which $\bar{\mathbf{t}}$ acts in the conjugate. The lower two diagrams present the scalar product matrix elements before and after the emission has occurred. \bar{n} and m denote the emitting anti colour line in the conjugate and its connecting colour line, whilst l and \bar{k} are the emitting colour line and connecting anti colour line in the amplitude. 210
- 5.1 The jet veto emission cross section as a function of the veto scale ρ , for $V \rightarrow q\bar{q}$. Figure (A) presents the cross section for a gluon multiplicity of one and Figure (B) for two. The solid curves pertain to those generated with **CVolver** for two values of the collinear cutoff, $\lambda = 10^{-2}$ and $\lambda = 10^{-3}$. The light-blue shading indicates the error band for these results, whilst the broken lines labelled ‘analytic’ correspond to the independent **FixedOrderA** results (see text for details). 228
- 5.2 The jet veto cross section dependence on ρ for the $V \rightarrow q\bar{q}$ process. Gluon multiplicities are presented for upto two emissions ($n = 1, 2$). The solid curves denote the results of the **evolve()** method and the dashed curves to **evolveFull()**. 230
- 5.3 The jet veto cross section dependence on ρ for the $V \rightarrow q\bar{q}$ process. Gluon multiplicities are presented for upto two emissions ($n = 0, 1, 2$). The solid curves denote the results of the **CVolver** Variant A, where the shaded region on the green and blue lines demarcates the corresponding errors. The dashed curves present the results of **FixedOrderA**. 232
- 5.4 The jet veto total cross section (for $n \leq 10$) for the $V \rightarrow q\bar{q}$ process, using Variant A of **CVolver**. Results are shown for $d' = 0, 2$. The contributions from $n = 0$ up to 3 emissions are also presented in (a) and (b), and summed over in (c) and (d). The total cross section result is a summation over all emissions. 234
- 5.5 The jet veto total cross section presented for linearly scaled values of the veto energy and the $n \leq 3, 4$ total cross section weight distributions for $\lambda = 10^{-3}$ 235

- 5.6 The inclusive emission cross section for the processes $V \rightarrow q\bar{q}$ and $H \rightarrow gg$. Gluon multiplicities are presented upto three emissions ($n = 1, 2, 3$). The stepped results pertain to those, generated using **CVolver**, with all Ω_{ij} set to $\alpha_s / (2\pi)$ and adopting a uniform direction-sampling over the full angular phase-space. The broken curves correspond to the analytic result described in the text. 239
- 5.7 The inclusive emission cross section as a function of the angular correlation between particles i and j , $\xi = 1 - n_i \cdot n_j$, for $V \rightarrow q\bar{q}$ and $H \rightarrow gg$. This cross section corresponds to a gluon multiplicity of two. The stepped results pertain to those generated with **CVolver**, whilst the broken lines to the independent test code **AngularCorrelations**. The legend specifies which $\xi = 1 - n_i \cdot n_j$ each coloured curve corresponds to. 242
- 5.8 The ratio of inclusive cross sections between **CVolver** and **AngularCorrelations** as a function of the angular correlation between particles i and j , for $V \rightarrow q\bar{q}$ in (A) and $H \rightarrow gg$ in (B). This ratio corresponds to gluon multiplicities $n = 1, 2$. The black dashed line is for reference and takes a value of unity. . . 243
- 5.9 The inclusive emission cross section as a function of the angular correlation between two gluon emissions, for the processes $V \rightarrow q\bar{q}$ and $H \rightarrow gg$. Also shown are the individual contributions at each order of N_c^k . A check on these contributions is illustrated, as described in the text. 245
- 5.10 The inclusive cross section for the process $V \rightarrow q\bar{q}$ as a function of the veto scale, ρ , colour order, d and the number of QCD colours, N_c . Gluon multiplicities are presented upto three emissions ($n = 0, 1, 2, 3$). The coefficients of the colour operators (see the text for more detail) in both the Sudakov and emission operators have been fixed to numerical values at the same order of magnitude. The plot marks denote the result generated using **CVolver** whilst the unbroken curves correspond to the analytic result. 247

- 5.11 The inclusive cross section for the process $H \rightarrow gg$ as a function of the veto scale, ρ , colour order, d and the number of QCD colours, N_c . Gluon multiplicities are presented upto three emissions ($n = 0, 1, 2, 3$). The kinematic coefficients of the colour operators in both the Sudakov and emission operators have fixed numerical values at the same order of magnitude. The plot marks denote the result generated using **CVolver** whilst the unbroken curves correspond to the analytic result. Note that the overlap between the $d' = 0$ and $d' = 1$ results, for multiplicities $n \geq 1$, is a coincidence of the chosen kinematic coefficients. 250
- 5.12 The jet veto cross section for the processes $V \rightarrow q\bar{q}$ and $H \rightarrow gg$. Gluon multiplicities are presented upto two emissions ($n = 0, 1, 2$). The stepped results pertain to those generated using **CVolver**, whilst the broken curves correspond to a numerical integration of the calculation in Section. 5.1.1 255
- 5.13 The jet veto cross section in $V \rightarrow q\bar{q}$ for different gluon multiplicities ($n = 0, 1, 2$ and 3). Also shown are the individual contributions at each order of N_c^k for $d = 0$ and $d' = 0, 2$. Solid curves (except that labelled LC_{R+V}) always correspond to $d' = 2$, dashed-dotted curves to $d' = 0$ and the dotted curve to $d = 0$. Figures modified from [155]. 259
- 5.14 The jet veto cross section in $H \rightarrow gg$ for different gluon multiplicities ($n = 0, 1, 2$ and 3). Also shown are the individual contributions at each order of N_c^k for $d = 0$ and $d = 2$. Solid curves (except that labelled LC_{R+V}) always correspond to $d = 2$ and the broken curves always correspond to $d = 0$. Figures modified from [155]. 261
- 5.15 The jet veto cross section in (a) for the $V \rightarrow q\bar{q}$ process and (b) for the $H \rightarrow gg$ process, for different gluon multiplicities ($n = 0, 1, 2, 3, \leq 20$). Results are shown for $d' = 0, 2$ and $d = 0, 2$ respectively using a **weightCut** value of $w_c = 12800$ and $w_c = 51200$. The contributions from $n = 0$ up to 3 emissions are also presented, however the total cross section result is a summation over all emissions. The total cross section here has been produced by **CVolver**, limited to $n \leq 20$ emissions. Figures modified from [155]. (c) and (d) compare the total cross section (with $n \leq 20$) for different values of the w_c 263

- 5.16 The jet veto cross section in (a) and (b) for the $V \rightarrow q\bar{q}$ process and (c) and (d) for the $H \rightarrow q\bar{q}$ process, for summations over different gluon multiplicities ($n \leq 0, 1, 2, 3, 4, 5, 6$ and 20). Results are shown for $d' = 2$ for the $q\bar{q}$ final state and $d = 2$ for the gg final state. The blue shaded region corresponds to the $n \leq 20$ cross section (one standard deviation) error. Solid curves correspond to a collinear cutoff of 1×10^{-2} , whereas the broken curves correspond to a cutoff of 1×10^{-3} . In Figures (B) and (D), we are comparing the similarity between the total cross section results produced using two cutoff values at large ρ . For clarity: the $n \leq 5, 6$ cross section results in both figures, whilst plotted, reside under the $n \leq 20$ result for both cutoff values, and so are not visible. The $\lambda = 10^{-2}$ and $\lambda = 10^{-3}$ $n \leq 20$ curves are indistinguishable for large ρ values, down to $\rho = 0.1$ in (B) and $\rho = 0.2$ in (D), where their difference becomes apparent. 265
- 5.17 The event-weight distributions corresponding to the $n \leq 3, 4, 5$ total cross section for $\lambda = 10^{-3}$, produced using Variant B. Both the positive and negative event-weights have been plotted separately; for each n , the negative event-weights have been plotted in a lighter version of the same colour as the corresponding positive event-weights. 267
- 5.18 The multiplicity distributions corresponding to the total 20-emission cross section results in Figure 5.15. (a) presents the distributions for the $V \rightarrow q\bar{q}$ process at NNLC'_V and (b) for the $H \rightarrow gg$ process at NNLC_V for a **weightCut** of $w_c = 12800$ and $w_c = 51200$. Both (a) and (b) show the multiplicity distributions using total cross section-weighted events (solid curves) and unit-weighted events (dashed-dotted curves), for two values of the collinear cutoff: $\lambda = 10^{-2}$ and $\lambda = 10^{-3}$. The same distributions using a larger **weightCut** value, $2w_c$, are included. 268

List of Tables

1.1	Feynman rules for external particles in QCD, namely quark and anti-quark spinors and the gluon polarisation vectors. Quarks are represented as solid lines and gluons as coiled lines. The i index labels the spinor components, μ a Lorentz index and a is a colour label. The arrows on the fermion lines denote charge flow, whilst the momenta of the fermion is illustrated below.	52
1.2	Feynman rules for propagators in QCD in a covariant gauge. Quarks are represented as solid lines, gluons as coiled lines and ghosts as dashed lines. The μ, ν indices label Lorentz indices, whilst i, j are colour indices in the SU(3) fundamental representation and a, b are colour indices in the adjoint representation.	53
1.3	Feynman rules for QCD vertices. Quarks are represented as solid lines, gluons as coiled lines and ghosts as dashed lines. The indices i, j label colour indices in the SU(3) fundamental representation, a, b, c, d in the adjoint representation, whilst μ, ν, σ, ρ are Lorentz indices. Note the momenta in the three-gluon vertex are defined as incoming, i.e. $k_1 + k_2 + k_3 = 0$	54
1.4	Correspondence between the Feynman rules for propagators in QCD and those Feynman rules in the colour-flow formalism. Arrows directed to the right represent colour lines, whilst those to the directed to the left represent anti-colour lines. The Kronecker delta functions constraining the colour in both the standard QCD Feynman rules and in the colour flow representation are presented, whilst the Lorentz and momentum factors are omitted as they retain their original form.	71
1.5	Correspondence between the Feynman rules for vertices in QCD and those Feynman rules in the colour-flow formalism.	72

2.1	The specifications of the correspondence between the external leg indices, i , and their colour (c_i) or anti colour (\bar{c}_i) lines for the four-parton amplitude containing the partons $qg\bar{g}\bar{q}$, depicted in Figure 2.2.	89
4.1	Illustration of the tables contained within the ColourFlowCrossing class. They have been populated for the example process $q\bar{q} \rightarrow q\bar{q}$ presented in Figure 4.3. The label i denotes an external leg index, whilst c_i and \bar{c}_i specify the colour and anti colour indices to which i maps. s_i and \bar{s}_i denote the crossing sign attributed to a colour or anti colour index.	152
4.2	The public methods of the ColourFlowCrossing class, used by external classes to access the colour maps.	153
4.3	The protected methods of the ColourFlowCrossing class, used by external classes to manipulate the colour maps.	153
4.4	The public methods of the ColourFlow class, used by external classes to manipulate colour flows and carry out colour flow arithmetic.	154
4.5	The methods of the Core::AnomalousDimensionMatrix class.	156
4.6	The methods of the Core::EmissionMatrix class.	157
4.7	The methods of the Core::Evolver class.	159
4.8	The methods of the EvolutionMatrix class.	175
4.9	A walk-through of the basis tensors which are generated at each layer along the left-most branch in Figure 4.5. Three tensors result in the first layer, and from each those, a further four tensors in the second layer.	183
4.10	List of all possible colour-line operator combinations in Eq. 4.103. Each of these is a contribution to a single term in the sum of Eq. 4.94. The relevant colour-line operator matrix element in the amplitude and conjugate-amplitude are presented with unspecified external leg indices. Conditions on the colour arrangement in τ and $\bar{\tau}$ for each contribution are also listed. The contribution itself is presented in the last column.	209

- 5.1 An event with a large weight, of $> 10^6$, which contributes towards the $n = 4$ cross section. The object values column uses the ‘reference functions’ detailed in Algorithm 4, to indicate which part of the shower contributes the corresponding weight at the n th multiplicity. The total weight, 1.41074×10^6 , can be obtained by multiplying together all of the sampling weights W_{E_n} , $W_{\alpha_n} \times W_{\alpha_n^\dagger}$ and $W_{\alpha_{n+1}} \times W_{\alpha_{n+1}^\dagger}$, the matrix elements $[\alpha_n | \mathbf{V}_{E,E'} | \alpha_{n-1}]$, $\langle \alpha_{n-1}^\dagger | \mathbf{V}_{E,E'} | \alpha_n^\dagger \rangle$ and $[\alpha_{n+1} | \mathbf{D}_E | \alpha_n] \times \langle \alpha_n^\dagger | \mathbf{D}_E^\dagger | \alpha_{n+1}^\dagger \rangle$, the final scalar product matrix element, $\langle 25134 | 34215 \rangle = N_c^2$, and the direction sampling weights from all emissions, $W_{\Phi_{n+1}} \leftarrow 2^4 \times (1 - c_0)^4$ 236
- 5.2 The fixed values of the kinematic and physical-constant coefficients (see the text for details). The variables i and j denote particle numbers, whilst k specifies the multiplicity at which the coefficients are used. Labels a and b denote the primary partons in the processes $V \rightarrow q\bar{q}$ and $H \rightarrow gg$ 248

List of Algorithms

1	Rejection Sampling Algorithm	123
2	Veto Algorithm	134
3	Competition Algorithm	137
4	Overview of the <code>evolve()</code> algorithm in the <code>EvoLver</code> class.	160
5	Overview of the <code>evolveFull()</code> algorithm in the <code>EvoLver</code> class.	163
6	The level-swap algorithm, determining all basis tensors, d' swaps away from σ (as depicted in Figure 4.5).	182
7	The modified Sudakov veto algorithm for Variant A, accounting for the presence of a lower cutoff, ρ , and a potential constraint on the maximum multiplicity, n_{max} . It outlines the emission scale sampling, represented by E_n . This, the hard scale, E' , and the scale sampling weight, W_{E_n} are introduced in Algorithm 4.	195
8	The modified Sudakov veto algorithm with competition Variant B, accounting for the presence of a lower cutoff, ρ , and a potential constraint on the maximum multiplicity, n_{max} . It outlines the emission scale sampling, represented by E_n . This, the hard scale, E' , and the scale sampling weight, W_{E_n} are introduced in Algorithm 4.	203

THE UNIVERSITY OF MANCHESTER

Abstract

A thesis submitted for the degree of Doctor of Philosophy

QCD Evolution At Amplitude Level

by Matthew V. De Angelis

In this thesis, we consider soft-gluon evolution at the amplitude level. We present a general evolution algorithm, which was used originally in the derivation of super-leading logarithms. It includes Coulomb exchanges and applies to generic hard-scattering processes involving any number of coloured partons, resumming soft gluon effects to all orders. To exemplify this algorithm, we perform a calculation of the hemisphere jet mass non-global logarithmic contributions, and show how the algorithm reproduces the well-known Banfi-Marchesini-Smye (BMS) equation. In addition, we explore the colour structures encountered when solving the evolution equations, using the colour flow basis; in preparation of a Monte Carlo implementation. Handling large colour matrices presents a significant challenge to numerical implementations, and we present a means to expand systematically about the leading colour approximation. We subsequently discuss the formulation of our amplitude evolution as a parton branching algorithm, and its implementation into a Monte Carlo code, `CVolver`. The general-purpose colour machinery underpinning the `CVolver` framework is reviewed, and we discuss colour-space sampling strategies. We build on this framework to simulate high-energy particle collisions, based upon simulated two-jet events, with a restriction on the amount of radiation lying in some region outside of the jets. We present the corresponding cross section results broken down by their colour suppressed terms, alongside independent cross-checks, which validate our implementation. We find that colour suppressed terms can significantly contribute to this cross-section, and find agreement with the results of other authors.

Declaration of Authorship

I declare that no portion of the work referred to in the thesis has been submitted in support of an application for another degree or qualification of this or any other university or other institute of learning.

Copyright Statement

The author of this thesis (including any appendices and/or schedules to this thesis) owns certain copyright or related rights in it (the “Copyright”) and he has given The University of Manchester certain rights to use such Copyright, including for administrative purposes.

Copies of this thesis, either in full or in extracts and whether in hard or electronic copy, may be made only in accordance with the Copyright, Designs and Patents Act 1988 (as amended) and regulations issued under it or, where appropriate, in accordance with licensing agreements which the University has from time to time. This page must form part of any such copies made.

The ownership of certain Copyright, patents, designs, trademarks and other intellectual property (the “Intellectual Property”) and any reproductions of copyright works in the thesis, for example graphs and tables (“Reproductions”), which may be described in this thesis, may not be owned by the author and may be owned by third parties. Such Intellectual Property and Reproductions cannot and must not be made available for use without the prior written permission of the owner(s) of the relevant Intellectual Property and/or Reproductions.

Further information on the conditions under which disclosure, publication and commercialisation of this thesis, the Copyright and any Intellectual Property and/or Reproductions described in it may take place is available in the University IP Policy (see <https://documents.manchester.ac.uk/DocuInfo.aspx?DocID=24420>), in any relevant Thesis restriction declarations deposited in the University Library, The University Library’s regulations (see <http://www.library.manchester.ac.uk/about/regulations/>) and in The University’s policy on Presentation of Theses.

*This thesis is dedicated to and in loving memory of,
Myrtle Mound (Nan) and Mercedes De Angelis (Nonna).*

*It has only been with your unabated love,
that I find myself here, today.*

Acknowledgements

There are quite a number of people I would like to thank for their advice and assistance over the past few years, in particular, my supervisor Jeff Forshaw and collaborator Simon Plätzer for their ideas and continual encouragement.

I am lucky enough to have travelled throughout my PhD. I would like to express my gratitude to Ann Durie, Michael Seymour and the MCnet network for the opportunities they gave me to attend both the MCnet school in Lund, and a short-term studentship at KIT. I wish to thank Stefan Gieseke and Renate Weiß for the help they offered, and the enjoyable time I had in Karlsruhe. Thanks also to the secretaries at Vienna for making my many stays there pleasant.

I owe a special thanks to Colin Timperley, for your unwavering assistance, despite the many administrative headaches my PhD brought.

To the dwellers of the HEP theory office, both past and present, thank you for the very many fun, intriguing and enlightening discussions. These include Alex, Dan, Bobby, Pablo, Mulham, Kieran, Sotirios, Kiran, Jack², Baptiste, Graeme and René. To the latter - I'll always remember the warm welcome you showed me as a newcomer. I'd also like to extend my gratitude to the wider Manchester Particle Physics group, for making the department a lively and entertaining place. I am very thankful to Simon Plätzer for his close collaboration over the past few years, and for the opportunities he afforded to me. I look back on my trips to Vienna very fondly, and without his valuable insights, this project wouldn't be what it is.

And to Dr Leon Au, I was fortunate enough, in an incredibly dire situation, to have landed in your safe hands. I distinctly remember my first (of many, many) visits to your office, you sitting across the slit-lamp from a pretty terrified 22-year-old. I will always appreciate the care you showed me, the extra mile you went to try and make things a little bit better - even just the light pat on the shoulder and solemn, 'good man' - and ultimately, to save me from an imminently blinding fate. Manchester is lucky to have you.

Of course, I'd like to thank my family back home in London. You have been integral in shaping me as a person - a history without which, this work wouldn't exist. I would particularly like to thank my brother, Daniel, and friends, Jake, Jamie, Graeme and Baptiste. You've been a great solace these past few years,

and have kept life outside of physics interesting and exciting - with our many late-night conversations and gaming bloodlust to keep me powering on.

I reserve a special gratitude for my supervisor, Jeff Forshaw. Throughout my PhD you've gone above and beyond the role of a supervisor, helping a student struggling with life's difficulties. Whenever I inched close to throwing in the towel, it was your compassion, and devotion to physics, which reignited the spark. I consider you more than a mere supervisor, and it is for this reason, more than any other, that I'm sad this chapter of my life is coming to an end.

Finally, I would like to thank Farah. For whatever fruits my efforts bare, they pale in comparison to finding you. It's interesting - life's twists and turns. And during them all, you have offered me more than a lifetime's fair share of support, reassurance, care and love. I reminisce the past 11 years with you, and look forward to what the future has in store for us. I hope that, in time, I can reciprocate the favour - *that sanguine expectation of happiness which is happiness itself*¹.

¹Jane Austen, Sense and Sensibility

Introduction

*'We are at the very beginning of time for the human race. It is not unreasonable that we grapple with problems. But there are tens of thousands of years in the future. Our responsibility is to do what we can, learn what we can, improve the solutions, and pass them on.'*²

It is in this vein, that particle physics and its participants, attempt to understand the universe in terms of its most fundamental constituents. Our understanding to-date is encompassed in the Standard Model (SM) of particle physics; the theory describing three of the four known fundamental forces in the Universe: the electromagnetic, weak and strong forces. Its current formulation was conceived around the same time as the experimental validation of quarks. Since then, it has been given further credence by the discovery of the W and Z bosons [1, 2], the top quark [3, 4], the tau neutrino [5], and most recently, the Higgs boson [6, 7] at the Large Hadron Collider (LHC) at CERN in Switzerland.

Despite these successes, it is known that the SM leaves some phenomena unexplained, falling short of being a complete theory of fundamental interactions. One major deficit is in its inability to incorporate the theory of gravitation, as described by general relativity. Moreover, cosmological findings indicate an accelerating expansion of the Universe, propelled by dark energy and slowed by dark matter, and a baryon asymmetry; explanations for which the SM does not provide. Furthermore, neutrinos are regarded as massless in the SM, which is in contradiction to the experimental observation of neutrino oscillations [8, 9]. New theoretical models are continuously developed, in an attempt to explain such phenomena Beyond the Standard Model (BSM). And on the other side of the seesaw, experiments such as the LHC, increasingly probe higher energy particle interactions to validate or disprove such models.

Any mathematical model needs to first be converted into numerical data, to

²Richard P. Feynman, What Do You Care What Other People Think?

be compared with measured experimental results. It is the realm of general-purpose event generators (GPEGs), such as **Herwig** [10–12], **Pythia** [13–15] and **Sherpa** [16], which provides the keystone to this phenomenological bridge between theoretical prediction, and experimental validation. GPEGs employ Monte-Carlo techniques to model particle collisions based on the SM and BSM models; tools which have decades of progress in the areas of perturbative calculation and phenomenological models behind them.

In any particle collision at the LHC, typically hundreds of particles are produced, with a wide range of momentum scales. There are relatively few particles at the highest scales, with the evolution from high to low scales mediated by perturbative Quantum Chromodynamics (QCD). In order to compare experimental data with theoretical models, a GPEG must be able to faithfully describe the flurry of final-state particles produced in a collider. To achieve this, one would generally rely on perturbative calculations, such as matrix element calculations. However, these calculations become increasingly difficult, the more particles we wish to describe. Due to the high-multiplicity of particles that are produced in collider interactions, an approximation to the usual matrix-element calculations is required. Correspondingly, GPEGs employ parton shower algorithms which allow us to approximately account for the most dominant contributions to these matrix-element calculations. Being an approximation, there has been a continual effort to improve the accuracy of parton showers since their inception [11, 13, 15, 17]. As an example of where improvements can be made, current parton showers do not include all sub-leading colour contributions. It has been shown that such contributions are relevant in order to accurately describe certain observables, and with recent analyses at the LHC frequently limited by theoretical uncertainties, the inclusion of subleading colour corrections is becoming increasingly important.

One such observable that requires subleading colour corrections, is the ‘gaps between jets’ observable. The series of works [18, 19] explored the ‘gaps between jets’ cross section and were based on a colour-evolution algorithm. Corroborated and extended by [20, 21], this algorithm constitutes a general framework that can be used as a basis for the full-colour calculation of soft-gluon corrections to all orders. This thesis focuses on the development of this framework, such that it can be implemented in a Monte-Carlo parton shower, and addresses the challenges faced in this implementation.

The thesis is divided into five chapters: the first provides a review of the theo-

retical underpinnings of QCD. Subsequently in Chapter 2, we write down the aforementioned evolution algorithm, in a form that is suited to the calculation of multiple soft-gluon contributions in a fully-differential way. We also focus on the colour structures encountered when solving the evolution equations. Chapter 3 explores some of the Monte Carlo methods used in GPEGs. The results of Chapter 2 and 3 have been implemented into a Monte Carlo code, **CVolver**, which was introduced in [22], and which we present in Chapter 4 for two implementation variants. The results of both variants are presented in Chapter 5, alongside a number of validating cross-checks.

Chapter 1

QCD Preliminaries

1.1 A Brief History

A slew of hadrons (further classified as mesons and baryons) were discovered in the early particle scattering experiments at Brookhaven (BH) National Laboratory [23] and the Bevatron [24], with a significant effort made to understand and classify them. Into the 1960's, the Gell-Mann-Nishijima formula led to the Eightfold Way organisation of these hadrons into multiplets, octets and decuplets [25, 26], famously predicting the existence of the spin- $\frac{3}{2}$ Ω^- baryon (discovered at BH).

The picture of strong interactions at the time focused on general principles of scattering amplitudes, which could be developed without an understanding of any fundamental constituents. This paved-way for the development of many areas of study, such as Regge theory [27, 28].

Concurrently, the Eightfold Way was developed into the quark model [29, 30], which strongly suggested that hadrons were made up of more-fundamental constituents (dubbed 'quarks' by Murray Gell-Mann, and 'aces' by George Zweig), adding weight to hadron spectroscopy. It was with the advent of accelerators that could reach the ~ 10 GeV energy range, such as at SLAC, that the point-like substructure of hadrons was first shown [31].

However, with the discovery of hadrons such as the spin- $\frac{3}{2}$ Δ^{++} baryon, the quark model was unable to explain its apparent violation of Fermi-Dirac statistics. As a remedy to this, Moo-Young Han and Yoichiro Nambu suggested the existence of three triplets of quarks [32, 33] - the quarks were given a new quantum number, named colour.

Extending the global colour model [34, 35], to a gauge theory (which had already been done successfully for Quantum Electrodynamics (QED)), was heavily encouraged after it was shown that one could quantise gauge theories in a unitary and renormalisable way in studies of Yang-Mills theory [36–39]. This gauge theory was named Quantum ChromoDynamics (QCD). It was shown that QCD could also satisfy the requirement of asymptotic freedom [40–42], necessary to reconcile the observed confined nature of strong interactions at low-energy, and the almost-free, point-like behaviour of hadron constituents (quarks) at high energies. This latter point is what makes it possible to give a perturbative description of QCD processes (referred to as pQCD). The former notion of confinement is tied to the breakdown of pQCD and is consistent with the fact that we do not observe free quarks, but only their colourless bound

states.

In this chapter we review the theory of QCD. The structure shall be as follows: in Section 1.2 we recall the properties of the SU(3) gauge group, gauge invariance and their implications for the free quark Lagrangian. Subsequently, we present the Feynman rules for QCD and their diagrammatic representations in Section 1.3. These rules are the building blocks for calculating the invariant squared matrix elements at each order of perturbation theory. In Section 1.4 we shall utilise them to showcase the $e^+e^- \rightarrow q\bar{q}g$ calculation, in-part to highlight the intrinsic infrared divergences present. Finally in Section 1.5, we discuss one representation of the QCD colour sector, which is particularly useful for Monte Carlo calculations of QCD processes.

1.2 Quantum Chromodynamics

Yang-Mills theories are a generalisation of QED, with multiple spin-1 massless gauge bosons (the single one in QED being the photon) that can interact among themselves. Akin to QED, the Yang-Mills Lagrangian is heavily constrained by the necessity of gauge invariance, so-called non-Abelian gauge invariance, which is called non-Abelian due to the group generators not commuting with each other. As such, Yang-Mills theories are often referred to as non-Abelian gauge theories and are based on the special unitary group, SU(N). It is this non-Abelian nature that enables self-interaction among the gauge bosons. QCD is a non-abelian gauge field theory of the SU(N_c) gauge symmetry group, with $N_c = 3$ associated colour charges. This describes the interactions between quarks, mediated by gluons, which are generically referred to as partons.

1.2.1 SU(N_c) Group

Lie groups are fundamental to describing the Standard Model (SM). Examples of Lie groups are the unitary and special unitary groups, which are used to describe different sectors of the SM. The SM is a gauge theory with the symmetry group $U(1) \times SU(2) \times SU(3)$. This is composed of the electroweak sector, described by the chiral gauge group $SU(2) \times U(1)$, in which the U(1) symmetries of QED are embedded, and the Quantum Chromodynamics sector described by SU(3).

The group SU(N_c) consists of $N_c \times N_c$ complex matrices, satisfying the rela-

tions $U^\dagger = U^{-1}$, i.e. that they are unitary, preserving the complex inner product and $\det(U) = +1$. These constraints reduce the number of degrees of freedom to specify a group element from $2N_c^2$ to $N_c^2 - 1$. In its defining representation, the $SU(N_c)$ group has a basis of $N_c^2 - 1$ generators (and as such we say the dimension of the group, $\dim(G) = N_c^2 - 1$), denoted by \mathbf{T}^a , where $a = \{1, \dots, N_c^2 - 1\}$. This is such that any group element can be written as

$$U = \exp(i\theta^a \mathbf{T}^a) \mathbf{1} \simeq \mathbf{1} + i\theta^a \mathbf{T}^a, \quad (1.1)$$

where θ^a are real numbers. One can show that \mathbf{T}^a are both Hermitian and traceless matrices. The generators of the Lie group form an algebra, called its Lie algebra, defined through its Lie bracket

$$[\mathbf{T}^a, \mathbf{T}^b] = if^{abc} \mathbf{T}^c, \quad (1.2)$$

where f^{abc} are the structure constants for the algebra. It is totally anti-symmetric under the exchange of any two indices (analogous to the Levi-Civita tensor in the case of $SU(2)$). The defining characteristic of a non-Abelian Lie group is a non-zero structure constant (f^{abc} being equal to 0 if the group is Abelian). When the generators and structure constant are specified in a matrix representation, Eq. 1.2 becomes a commutation relation, fixing the Lie algebra. It automatically follows that

$$[\mathbf{T}^a, [\mathbf{T}^b, \mathbf{T}^c]] + [\mathbf{T}^b, [\mathbf{T}^c, \mathbf{T}^a]] + [\mathbf{T}^c, [\mathbf{T}^a, \mathbf{T}^b]] = 0 \quad (1.3)$$

which is the Jacobi identity. This identity has also been written in terms of the structure constants:

$$f^{abe} f^{ecd} + f^{ace} f^{edb} + f^{ade} f^{ebc} = 0. \quad (1.4)$$

The representation of a Lie algebra can be constructed by attributing matrices to each generator. Two of the most important representations are the fundamental and adjoint representations. The fundamental representation is the smallest non-trivial representation of the algebra; the aforementioned set of $N_c \times N_c$ Hermitian matrices. In the case of $SU(3)$, one such representation is

given by the Gell-Mann matrices,

$$\begin{aligned}
\lambda_1 &= \begin{pmatrix} 0 & 1 & 0 \\ 1 & 0 & 0 \\ 0 & 0 & 0 \end{pmatrix}, & \lambda_2 &= \begin{pmatrix} 0 & -i & 0 \\ i & 0 & 0 \\ 0 & 0 & 0 \end{pmatrix}, & \lambda_3 &= \begin{pmatrix} 1 & 0 & 0 \\ 0 & -1 & 0 \\ 0 & 0 & 0 \end{pmatrix} \\
\lambda_4 &= \begin{pmatrix} 0 & 0 & 1 \\ 0 & 0 & 0 \\ 1 & 0 & 0 \end{pmatrix}, & \lambda_5 &= \begin{pmatrix} 0 & 0 & -i \\ 0 & 0 & 0 \\ i & 0 & 0 \end{pmatrix}, & \lambda_6 &= \begin{pmatrix} 0 & 0 & 0 \\ 0 & 0 & 1 \\ 0 & 1 & 0 \end{pmatrix} \\
\lambda_7 &= \begin{pmatrix} 0 & 0 & 0 \\ 0 & 0 & -i \\ 0 & i & 0 \end{pmatrix}, & \lambda_8 &= \frac{1}{\sqrt{3}} \begin{pmatrix} 1 & 0 & 0 \\ 0 & 1 & 0 \\ 0 & 0 & -2 \end{pmatrix},
\end{aligned} \tag{1.5}$$

which are written in a standard basis $\mathbf{T}^a = \frac{1}{2}\lambda^a$. It will occasionally be useful to write the row and column indices of the generators in this work. When this is necessary, they will be denoted by Latin letters, e.g. \mathbf{T}_{ij}^a . The normalisation of the generators is a choice: a common convention in particle physics is to normalise the structure constants such that

$$\sum_{c,d} f^{acd} f^{bcd} = T_A \delta^{ab}, \tag{1.6}$$

where $T_A = N_c = 3$. This implies (through Eq. 1.2) that the generators of the $SU(N_c)$ group in the fundamental representation are normalised such that

$$\text{Tr} \left(\mathbf{T}^a \mathbf{T}^b \right) = T_F \delta_{ab}, \tag{1.7}$$

where $T_F = \frac{1}{2}$, as per the Gell-Mann matrices in Eq. 1.5. The structure constants themselves satisfy the Lie bracket and provide a representation of the group. This is called the adjoint representation, in which the matrices are instead $(N_c^2 - 1) \times (N_c^2 - 1)$. The generators of the adjoint representation are given by

$$\left(\mathbf{T}_{\text{adjoint}}^a \right)_{bc} = -i f^{abc}, \tag{1.8}$$

and are the representation in which the gauge fields transform. Within the $SU(N_c)$ Lie group there are Casimir operators, which characterise the representations. These operators commute with the generators, and the quadratic Casimirs are defined such that

$$\sum_a \mathbf{T}_R^a \mathbf{T}_R^a = C_R \mathbf{1}, \tag{1.9}$$

where R labels the representation. That this operator is always proportional to the identity of the representation is a consequence of Schur's lemma [43]. This can be seen explicitly by writing

$$\begin{aligned} [(\mathbf{T}^a \mathbf{T}^a), \mathbf{T}^b] &= \mathbf{T}^a [\mathbf{T}^a, \mathbf{T}^b] + [\mathbf{T}^a, \mathbf{T}^b] \mathbf{T}^a \\ &= (if^{abc} \mathbf{T}^c) \mathbf{T}^a + \mathbf{T}^a (if^{abc} \mathbf{T}^c) = 0, \end{aligned} \quad (1.10)$$

where the last equality is obtained by exploiting the anti-symmetric nature of the structure constants. In order to determine the Casimir invariant, we also write the inner product for the generators in a general representation as

$$\text{Tr}(\mathbf{T}_R^a \mathbf{T}_R^b) = T_R \delta^{ab}, \quad (1.11)$$

where from Eq. 1.7 and 1.6, $T_F = 1/2$ and $T_A = N_c$ respectively. QCD calculations often require manipulation of the fundamental and adjoint representation generators. As such it is useful to write

$$\text{Tr}([\mathbf{T}_R^a, \mathbf{T}_R^b], \mathbf{T}_R^c) = if^{abd} \text{Tr}(\mathbf{T}_R^d \mathbf{T}_R^c) = if^{abc} T_R, \quad (1.12)$$

to relate the generators of the adjoint representation to those of the fundamental one:

$$f^{abc} \equiv -\frac{i}{T_F} \text{Tr}([\mathbf{T}_F^a, \mathbf{T}_F^b] \mathbf{T}_F^c). \quad (1.13)$$

The trace of $\mathbf{T}_R^a \mathbf{T}_R^a$ then results in an equation which relates the Casimir to the normalisation of the representation, T_R , dimension of representation, $\dim(R)$ and dimension of the group, $\dim(G)$:

$$C_R = \frac{T_R \dim(G)}{\dim(R)}. \quad (1.14)$$

The dimension of the representations are $\dim(F) = N_c$ and $\dim(A) = N_c^2 - 1$, whilst the dimension of the group is fixed and equal to the number of generators, $\dim(G) = N_c^2 - 1$. Thus the Casimirs for the fundamental and adjoint representations are

$$C_F = \frac{N_c^2 - 1}{2N_c} = \frac{1}{2}N_c - \frac{1}{2N_c}, \quad C_A = N_c. \quad (1.15)$$

Calculations in QCD will contain factors of C_F and C_A and it is worth noting that the Casimir of the adjoint representation is exactly twice that of the fundamental Casimir in the large- N_c limit. The values of these Casimirs have

been experimentally validated at the Large Electron-Positron Collider (LEP), by for example measuring the ratio of production between hadrons and muon-antimuon pairs [44].

An arbitrary $N_c \times N_c$ hermitian matrix, \mathbf{M} , can be written as a linear combination of the $SU(N_c)$ generators (and the identity element). In the fundamental representation this is

$$\mathbf{M} = m_0 \mathbf{1} + \sum_a m_a \mathbf{T}^a, \quad (1.16)$$

where m_0 and m_a are real coefficients. Using Eq. 1.2 and the traceless property of the generators, one can determine these coefficients: $m_0 = 1/N_c \text{Tr} \mathbf{M}$ and $m_a = 2 \text{Tr} (\mathbf{M} \mathbf{T}^a)$. If \mathbf{M} represents the commutator of the generators in the fundamental representation, then we reproduce Eq. 1.13. However, if one chooses \mathbf{M} to have one non-zero component such that $\mathbf{M}_i^k = \delta_i^j \delta_j^k$, where i and j are fixed indices, one yields the relation

$$(\mathbf{T}^a)_k^l (\mathbf{T}^a)_i^j = \frac{1}{2} \left(\delta_i^k \delta_l^j - \frac{1}{N_c} \delta_i^i \delta_l^j \right), \quad (1.17)$$

which is the Fierz identity for $SU(N_c)$; a very useful tool in QCD calculations. Considering k as the colour index of a quark and l as the colour index of an antiquark we can see that the physical interpretation is of a decomposition of N_c^2 colour states of a $q\bar{q}$ system into the colour octet and colour singlet parts. Alternatively, it can be represented pictorially in Figure 1.1. Figure 1.1 represents a

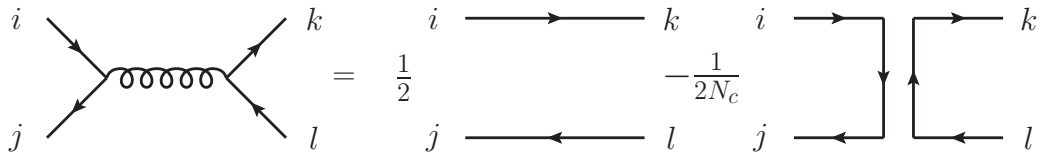


FIGURE 1.1: A graphical representation of the Fierz identity, relating the colour structure of a one-gluon exchange between a quark and anti-quark pair to quark and anti-quark colour lines.

one-gluon exchange between two quarks, or a quark and antiquark, expressed as quark lines (we shall discuss these particles in more detail in the next section). In group theory parlance, one can combine a fundamental colour with a fundamental anticolour to produce an adjoint colour and a colour singlet. In the limit that N_c becomes infinitely large and $\alpha_s N_c$ is fixed, Figure 1.1 suggests that the colour structure of a gluon becomes that of a quark and antiquark (modulo a factor of 2, as per Eq. 1.15) if we neglect the singlet component. This is more widely known as the large- N_c limit. This approximation was first in-

roduced by 't Hooft in [45] and limits the number of Feynman diagrams which contribute to a specific process. Each diagram is decomposed, using Eq. 1.17, into a set of delta functions between fundamental colours; the so-called colour flow of a diagram. 't Hooft found that only topologically planar diagrams, i.e. those for which the fundamental colours can be drawn in a single plane without crossing, contribute to leading order in N_c , whilst the contributions from non-planar diagrams are suppressed by $1/N_c^2$ for each colour-connection that comes out of the plane. This approximation is used in several different aspects of event modelling: for instance, the generation of the hard scattering process [46–48], parton showers [49, 50] (e.g. the dipole shower [51–53] in Herwig [10]) and hadronisation models [54].

1.2.2 Gauge Invariance

Having discussed Lie groups in Section 1.2.1, we now move onto the concepts of gauge symmetry and gauge invariance, in which they are involved. We shall use QED as our exemplary focus for simplicity.

A natural starting point is to discuss the equations governing the behaviour of quarks, or more generally, fermions. Fermions have two spin states, $\pm\frac{1}{2}$. The equation of motion governing the field of a free fermion (or anti-fermion) of mass m , $\psi \equiv \psi(x^\mu)$, is the Dirac equation [55]:

$$(i\gamma^\mu\partial_\mu - m)\psi = (i\not{\partial} - m)\psi = 0. \quad (1.18)$$

Here we have used four-vector notation, where a point in space-time is described by a contravariant vector $x^\mu = (x^0, x^1, x^2, x^3)$; the x^0 term describes the temporal component, whilst x^1, x^2 and x^3 describe the spatial components. The 'distance' measure of space-time is known as the space-time interval, and is encoded into the metric tensor. For the purposes of particle physics, the geometric structure of space-time is assumed to be flat, which we denote as $\eta_{\mu\nu} = \text{diag}(1, -1, -1, -1)$; the so-called Minkowski metric. It is this that relates contravariant four-vectors to their covariant counterparts: $x_\mu = \eta_{\mu\nu}x^\nu$. The repeated Lorentz-indices have an implicit sum over their values, as per the Einstein summation convention and we have used the common Feynman slash notation, $\not{x} = \gamma^\mu x_\mu$. The inverse metric, $\eta^{\mu\nu}$, has the same form as $\eta_{\mu\nu}$, such that they obey the relation $\eta^{\mu\rho}\eta_{\rho\nu} = \delta_\nu^\mu$. In Eq. 1.18 we have also adopted natural units, where the speed of light in a vacuum and the reduced Planck constant are equal to unity.

There is a strong connection between Lorentz invariance and spin: it turns out that Pauli matrices naturally come out of the representations of the Lorentz group (which can be constructed from representations of $SU(2)$), describing spin- $\frac{1}{2}$ particles which transform in spinor representations. This informs the structure of the 4×4 γ -matrices (the Dirac matrices) in Eq. 1.18:

$$\gamma^\mu = \begin{pmatrix} 0 & \sigma^\mu \\ \bar{\sigma}^\mu & 0 \end{pmatrix}, \quad (1.19)$$

where $\sigma^\mu = (\mathbf{1}, \vec{\sigma})$, $\bar{\sigma}^\mu = (\mathbf{1}, -\vec{\sigma})$, $\mathbf{1} = \text{diag}(1, 1)$, and $\vec{\sigma}$ are the Pauli matrices:

$$\sigma^1 = \begin{pmatrix} 0 & 1 \\ 1 & 0 \end{pmatrix}, \quad \sigma^2 = \begin{pmatrix} 0 & -i \\ i & 0 \end{pmatrix}, \quad \sigma^3 = \begin{pmatrix} 1 & 0 \\ 0 & -1 \end{pmatrix}. \quad (1.20)$$

The Dirac matrices satisfy the definition of a Clifford algebra, expressed in the anti-commutation relation

$$\{\gamma^\mu, \gamma^\nu\} = 2\eta^{\mu\nu}, \quad (1.21)$$

and the representation of the γ -matrices in Eq. 1.19 are the simplest which fulfill this condition. This particular representation of the Dirac matrices is known as the Weyl representation, where γ^μ are traceless, and obey hermiticity conditions: γ^0 is Hermitian, whilst γ^i are anti-Hermitian.

Since the γ -matrices are represented as 4×4 matrices, the quark fields are accordingly four-dimensional complex vectors, commonly referred to as Dirac spinors. These four degrees of freedom correspond to the up and down spin of the quark and anti-quark, which solve the Dirac equation. It is also worth noting that if we act on the Dirac equation with $(i\partial + m)$, we find that ψ satisfies the Klein-Gordon equation, implying on-shell spinor momenta obey the energy-momentum relation $p^2 = m^2$.

Free fermions can be included in the description of the SM through the Dirac Lagrangian ¹,

$$\mathcal{L}_{\text{Dirac}} = \bar{\psi} (i\partial - m) \psi, \quad (1.22)$$

describing a free fermion (ψ) and anti-fermion ($\bar{\psi}$) with an associated mass m . The Dirac adjoint, $\bar{\psi} = \psi^\dagger \gamma^0$ ², ensures that our Lagrangian obeys Lorentz

¹This is actually a Lagrangian density, but we use the two terms interchangeably through this work, where the Lagrangian is just the integral of the density over a space-measure.

²Here and throughout this work, the dagger notation, \dagger , is used to denote the complex-conjugate transpose.

invariance. Each fermionic species can be described by including their own equivalent term in the Dirac Lagrangian.

The Dirac Lagrangian has a global symmetry under the transformation

$$\psi(x) \rightarrow \psi'(x) = U\psi(x), \quad \bar{\psi}(x) \rightarrow \bar{\psi}'(x) = \bar{\psi}(x)U^{-1} \quad (1.23)$$

where U is a unitary object, which forms part of a group of transformations. In order to construct a locally invariant theory, we require that the Lagrangian also be invariant under local transformations (such as those in Section 1.2.1), where U becomes a function of some space-time point x^μ , $U = U(x)$. The transformation now has the form

$$\psi(x) \rightarrow \psi'(x) = U(x)\psi(x), \quad \bar{\psi}(x) \rightarrow \bar{\psi}'(x) = \bar{\psi}(x)U^{-1}(x), \quad (1.24)$$

which no longer leaves the Dirac Lagrangian invariant, due to the action of the derivative, ∂_μ , which introduces additional terms. In order to compensate for these terms, we can define a new covariant derivative operator, D_μ , which transforms as

$$D_\mu \rightarrow D'_\mu = U(x)D_\mu U^{-1}(x). \quad (1.25)$$

To determine the form of D_μ , we first review QED and the photon.

The free photon is a quantum of the electromagnetic field in a vacuum, and is the force carrier of the electromagnetic force. It is a massless spin-1 gauge boson with two degrees of freedom and can be mathematically represented by a vector field, A_μ , which has four. This discrepancy in degrees of freedom is surprising at first, however it is reconciled by the fact that massless spin-1 fields exhibit gauge invariance. That is, they are invariant under local gauge transformations, e.g.

$$A_\mu(x) \rightarrow A'_\mu(x) = A_\mu(x) - \partial_\mu\alpha(x), \quad (1.26)$$

where $\alpha(x)$ is a real-valued function of space-time and e is a constant. Both $A_\mu(x)$ and $A'_\mu(x)$ give equivalent descriptions of the photon and the field is said to be gauge invariant. The extra degrees of freedom in A_μ are removed by this gauge invariance through a procedure known as gauge-fixing and the kinetic Lagrangian,

$$\mathcal{L}_{\text{kin}} = -\frac{1}{4}F_{\mu\nu}F^{\mu\nu} \equiv -\frac{1}{4}(F_{\mu\nu})^2, \quad \text{where } F_{\mu\nu} = \partial_\mu A_\nu - \partial_\nu A_\mu, \quad (1.27)$$

is invariant under this gauge transformation. The object $F_{\mu\nu}$ is the electromagnetic field-strength tensor encountered in classical electromagnetism, and is written in terms of our vector field A^μ .

Going back to the form of the covariant derivative, we know that the quark is electrically charged and so couples to the photon. In order for the A_μ field to interact with matter, the interactions have to also preserve the gauge symmetry. This can be achieved by defining the form of D_μ to be

$$D_\mu = \partial_\mu + ie_q e A_\mu(x), \quad (1.28)$$

and identifying $U(x)$ in Eq. 1.24 as a group element of the local Abelian $U(1)$ symmetry group,

$$U(x) = \exp(i e_q e \alpha(x)), \quad (1.29)$$

so that the Dirac Lagrangian is invariant under the simultaneous transformations of $\psi(x)$, $A_\mu(x)$ and D_μ . It is worth pointing out that the photon-quark interaction is included in the covariant derivative. Crucially, it is the requirement that our Lagrangian remain invariant under a local transformation that leads to the presence of such interactions. This enables us to identify the e constant as the strength of the electric charge, or the interaction strength; e_q is the flavour-dependent electric charge of the quark.

The field tensor can be written in terms of the covariant derivative: as $D_\mu \psi(x)$ transforms in a locally gauge-invariant way, then so will $D_\mu D_\nu \psi(x)$. It is then possible to construct the Lorentz structure

$$[D_\mu, D_\nu] = -ie_q e (\partial_\mu A_\nu - \partial_\nu A_\mu - ie_q e [A_\mu, A_\nu]) = -ie_q e F_{\mu\nu}. \quad (1.30)$$

For an Abelian theory the group elements (and therefore the gauge field A^μ) commute. Then, the third term in Eq. 1.30 vanishes and we recover the QED field strength tensor definition in Eq. 1.27. Whilst this relation between the field strength tensor and covariant derivative commutator still holds for a non-Abelian theory, the gauge fields no longer commute. We shall see later that this leads to self-interaction of the gauge field, characterising the crucial difference between QED and QCD. Eq. 1.30 also shows that the field strength tensor, $F_{\mu\nu}$, transforms in the same way as the covariant derivative:

$$F_{\mu\nu} \rightarrow F'_{\mu\nu} = U(x) F_{\mu\nu} U^{-1}(x). \quad (1.31)$$

Taking all of this together, the QED Lagrangian reads

$$\mathcal{L}_{\text{QED}} = \bar{\psi} (i\mathcal{D} - m) \psi - \frac{1}{4} (F_{\mu\nu})^2, \quad (1.32)$$

where the first term encapsulates the kinetic term associated with the quark and its interaction with the photon, the second term gives the mass of the quark and the last term describes the kinetics of the photon. There is no equivalent mass term for the photon as such a contribution would violate gauge invariance.

1.2.3 QCD Lagrangian

Section 1.2.1 reviewed the group which governs the description of QCD, this being $SU(N_c) = SU(3)$ [35, 56]. As is the case with QED, we would like to study the impact on the Dirac Lagrangian of a local transformation, but this time under the $SU(3)$ group. We have seen in Section 1.2.1, that the elements of $SU(3)$ are represented by 3×3 matrices. And so, the quark fields are represented by a triplet,

$$q_i = \begin{pmatrix} q_r \\ q_b \\ q_g \end{pmatrix} \quad (1.33)$$

where each of the three new degrees of freedom are referred to as ‘colours’ (which play the same role as the electric charge in QED). Each colour contains a fermionic field, and are mnemonically referred to as red (r), blue (b) and green (g). These colours represent indices of the degree of the group, i.e. $i = \{1, 2, 3\} = \{\text{red, blue, green}\}$. From the group perspective, the quark spinor is associated with the fundamental representation of $SU(3)$, whilst the anti-quark spinor is associated with the anti-fundamental representation (denoted \bar{r} , \bar{b} and \bar{g}). The local transformations for the components of the quark field can be expressed as [57]

$$\psi_i(x) \rightarrow \psi'_i(x) = U_{ij}(x) \psi_j(x), \quad (1.34)$$

where

$$U(x) = \exp(i g_s \theta^a(x) \mathbf{T}^a) \quad (1.35)$$

is the group element for the transformation at the space-time point x^μ , and \mathbf{T}^a are the generators of the $SU(N_c)$ group written in Eq. 1.1. In a non-Abelian group, it is convenient to represent the gauge field as a Lie-algebra-valued field

by writing,

$$A_\mu(x) = A_\mu^a(x)\mathbf{T}^a. \quad (1.36)$$

There is an implicit sum over $a = 1, \dots, 8$, where each index corresponds to a gluon colour. Each component of the gauge field transforms as

$$A_\mu^a(x) \rightarrow A_\mu^{a'}(x) = A_\mu^a(x) - g_s f^{abc} \theta^b(x) A_\mu^c(x) - \partial_\mu \theta^a(x). \quad (1.37)$$

It is worth noting that this relation contains only the structure constant generators. As such, gluons are said to transform under the adjoint representation. The g_s constant is the coupling constant in QCD that determines the strength of interactions in the coloured sector of the SM and the covariant derivative in Eq. 1.28 can then be written,

$$(D_\mu)_{ij} = \delta_{ij} \partial_\mu + i g_s A_\mu^a \mathbf{T}_{ij}^a. \quad (1.38)$$

Expanding the gauge field in the definition of the field strength tensor in Eq. 1.30, we find

$$F_{\mu\nu}^a = \partial_\mu A_\nu^a - \partial_\nu A_\mu^a - g_s f^{abc} A_\mu^b A_\nu^c, \quad (1.39)$$

where the field strength tensor $F_{\mu\nu} = F_{\mu\nu}^a \mathbf{T}^a$. In the Abelian case $f^{abc} = 0$ and $F_{\mu\nu}^a$ reduces to the electromagnetic field strength. This term being non-zero for QCD (due to its non-Abelian nature) corresponds to self-interactions between the corresponding gauge bosons. This can be seen if one fully expands the kinetic term associated with the gluon:

$$\begin{aligned} -\frac{1}{4} (F_{\mu\nu}^a)^2 &= -\frac{1}{4} (\partial_\mu A_\nu^a - \partial_\nu A_\mu^a) (\partial_\mu A_\nu^a - \partial_\nu A_\mu^a) \\ &\quad + g_s f^{abc} (\partial_\mu A_\nu^a) A^{\mu,b} A^{\nu,c} - \frac{g_s^2}{4} f^{abc} f^{ade} A^{\mu,b} A^{\nu,c} A_\mu^d A_\nu^e. \end{aligned} \quad (1.40)$$

We can see that the gluon kinetic term is composed of a 'pure' kinetic term plus two interaction terms. The first of these interaction terms represents a three-gluon interaction, whilst the second represents a four-gluon interaction. Each component of the gluon field strength tensor transforms as

$$F_{\mu\nu}^a \rightarrow F_{\mu\nu}^{a'} = F_{\mu\nu}^a - f^{abc} \theta^b(x) F_{\mu\nu}^c \quad (1.41)$$

under a gauge transformation. It is worth noting once again that this equation only contains structure constants and as such, whilst the component decomposition of the gluon field strength tensor was originally written in terms of generators in the fundamental representation, the gluon kinetic term naturally

transforms in the adjoint representation.

Combining all of the aforementioned results, we are able to write down the classical QCD Lagrangian:

$$\mathcal{L}_{\text{QCD}} = -\frac{1}{4} \left(F_{\mu\nu}^a \right)^2 + \sum_f \sum_{i,j=1}^{N_c} \bar{\psi}_i \left(\delta_{ij} i \not{D} - g_s A^a T_{ij}^a - m_f \delta_{ij} \right) \psi_j, \quad (1.42)$$

where f is the sum over different quark flavours and we have left the covariant derivative, \not{D}_{ij} , in its expanded form for use in Section 1.5. Additionally, m_f is the mass of the fermion species f . We shall work in the massless limit when performing QCD calculations and shall henceforth set $m_f = 0$.

We have so far been talking of our QCD Lagrangian essentially in the purview of a classical field theory. Quantum field theories such as QCD, extend classic field theories: the fields are promoted to operators (which act on states in Fock space), i.e. they are canonically quantised (in a similar manner to how position or momentum are thought of as operators in first quantisation) [58]. The fields can be written as a continuous function of momentum, p . For each (infinite number of) p , the fields describe a quantum mechanical system, where the n th excitation of the system is interpreted as having n particles [59]. The Lagrangian, being a function of fields, also becomes an operator. Briefly put, the Lagrangian operator can be split into a free part (containing terms bilinear in the fields), describing the free propagation of particles, and an interacting part, which can be calculated using perturbation theory [60] - something we shall discuss further in the next section.

In order to carry out calculations in QCD, there must exist a propagator for each particle - for instance, the gluon propagator. This is achieved by examining the bilinear terms of the gauge boson field in momentum space and inverting the kinetic term. For the Lagrangian as is written in Eq. 1.42, this is not possible, which is a manifestation of gauge invariance, meaning the field A_μ^a is degenerate. To remedy this, we add a new non-propagating field that behaves like a Lagrange multiplier, which when extremised resolves to the gauge constraint $\partial_\mu A^\mu = 0$, the Lorenz gauge:

$$\mathcal{L}_{\text{gauge-fix}} = -\frac{1}{2\xi} \left(\partial^\mu A_\mu^a \right) \left(\partial^\nu A_\nu^a \right). \quad (1.43)$$

This means the kinetic terms of the gluon field can be inverted to find,

$$\Delta^{\mu\nu,ab}(p) = \frac{i\delta^{ab}}{p^2 + i\epsilon} \left(-\eta^{\mu\nu} + (1 - \xi) \frac{p^\mu p^\nu}{p^2 + i\epsilon} \right), \quad (1.44)$$

which is the gluon propagator in covariant or R_ξ -gauges. In these gauges, each choice of ξ is a different Lorentz-invariant gauge: $\xi = 1$ is the Feynman gauge, whilst $\xi = 0$ is the Landau or Lorenz gauge. The Lorentz indices, μ, ν correspond to the polarisation of the gluons whilst a, b are colour indices (in the adjoint representation). Unlike in QED, the gluon fields by their (non-Abelian) nature can self-interact which means any covariant gauge-fixing must be accompanied by unphysical ghost particles [37, 61] that cancel unphysical propagating modes in a gauge invariant way. These ghosts are described by the Lagrangian

$$\mathcal{L}_{\text{ghost}} = (\partial_\mu \bar{c}^a) \left(\delta^{ac} \partial_\mu + g_s f^{abc} A_\mu^b \right) c^c, \quad (1.45)$$

where c^a and \bar{c}^a are anticommuting Lorentz scalars, the Faddeev-Popov ghosts and anti-ghosts. There is one of these for each gauge field. Their inclusion is related to the global symmetry called BRST invariance [62] and ensures the renormalisability of QCD. An alternative to using covariant gauges (and as a consequence, including ghosts), are non-covariant gauges such as the axial gauges. One can instead use a gauge-fixing term

$$\mathcal{L}_{\text{gauge-fix}} = -\frac{1}{2\xi} \left(n^\mu A_\mu^a \right) \left(n^\nu A_\nu^a \right), \quad (1.46)$$

where n^μ is an arbitrary four-vector, satisfying the constraint $n_\mu A^\mu = 0$. The gluon propagator following this modification reads

$$\Delta^{\mu\nu,ab}(p) = \frac{i\delta^{ab}}{p^2 + i\epsilon} \left(-\eta^{\mu\nu} + \frac{p^\mu n^\nu + n^\mu p^\nu}{p \cdot n} - \left(n^2 + \xi p^2 \right) \frac{p^\mu p^\nu}{(p \cdot n)^2} \right). \quad (1.47)$$

If n^μ is a light-like vector and $\xi = 0$, then Eq. 1.47 reduces to a special case called the lightcone gauge. Whilst such gauges have the advantage of not requiring ghost particles, in practice, unless there is a context with a preferred direction for n^μ , the additional terms in the gluon propagator lengthen a calculation considerably. In particular, when conducting numerical calculations, it is difficult to ensure that the singularities (as $p \cdot n$ become infinitely small) cancel as they would analytically. Following the form of the QCD Lagrangian in Eq. 1.42, the corresponding Feynman rules and connection to observable quantities is outlined in Section 1.3.

1.3 Feynman Rules

In order to make predictions, we must calculate the scattering amplitudes that describe the evolution from an initial state $|i\rangle$ to a final state $|f\rangle$, using the Hamiltonian (or equivalently, the Lagrangian). This evolution occurs from a time t_i in the past to a time t_f in the future.

Having discussed the QCD Lagrangian density in Section 1.2.2, we can decompose it schematically as

$$\mathcal{L} = \mathcal{L}_0 + \mathcal{L}_{\text{int}}, \quad (1.48)$$

where \mathcal{L}_0 is the free part of the Lagrangian density, usually containing all terms which are bilinear in fields, i.e. kinetic terms, and \mathcal{L}_{int} is the interaction part of the Lagrangian density, including all remaining terms of the full Lagrangian [55].

The interaction picture is the default picture for quantum field theories in which responsibility for time dependence is placed on both the particle states and an evolution operator. This time evolution operator is built from the interaction Lagrangian [62]:

$$U(t_f, t_i) = T \left\{ \exp \left[i \int_{t_i}^{t_f} d^4x \mathcal{L}_{\text{int}}(x) \right] \right\}, \quad (1.49)$$

where $T\{\dots\}$ indicates a time-ordered product of the fields contained in the exponent, i.e. the fields are arranged so that they act in chronological order.

In the limit that we evolve the initial and final momentum eigenstates from a long time in the past, $t_i = -\infty$, to a long time in the future, $t_f = +\infty$, this evolution operator is called the scattering or S-matrix:

$$S \equiv \lim_{t_f/t_i \rightarrow \pm\infty} U(t_f, t_i), \quad (1.50)$$

where the states $|i\rangle$ and $|f\rangle$ are said to be asymptotic states (and assumed free of interactions) at asymptotic times. It is not currently known how to calculate the exponentiated form of the S-matrix. Instead, calculations are performed as a perturbative expansion:

$$S_{fi} = \delta_{fi} + i \int d^4x_1 \langle f | \mathcal{L}_{\text{int}}(x_1) | i \rangle + i^2 \int d^4x_1 \int d^4x_2 \langle f | T \{ \mathcal{L}_{\text{int}}(x_1) \mathcal{L}_{\text{int}}(x_2) \} | i \rangle + \dots, \quad (1.51)$$

where $S_{fi} = \langle f | S | i \rangle$ is a matrix element of the S-matrix and the Kronecker delta δ_{fi} , one of the identity matrix. Perturbation theory is built on the basis that the interacting part of the Lagrangian density, \mathcal{L}_{int} , can be treated as small perturbations and successive corrections to the free theory. The perturbative expansion is then written as a power series in terms of the coefficients of these interacting terms - the coupling constants.

The S-matrix elements are related to the transfer matrix elements, \mathcal{T}_{fi} , through

$$S_{fi} = \langle f | \mathbf{1} + i\mathcal{T} | i \rangle = \langle f | \mathbf{1} | i \rangle + i\mathcal{T}_{fi}, \quad (1.52)$$

to remove the trivial non-interaction term, so that we only describe deviations from the free theory. The transfer matrix element is related to the invariant matrix element as

$$i\mathcal{T}_{fi} = (2\pi)^4 \delta^{(4)} \left(\sum_i p_i - \sum_f p_f \right) i\mathcal{M}_{fi} \quad (1.53)$$

where \mathcal{M}_{fi} is an invariant matrix element for a given transition $|i\rangle \rightarrow |f\rangle$. Since the S-matrix should vanish unless the initial and final states have the same total four-momentum, a momentum-conserving delta function has been factored. The momenta p_i and p_f are the four-momenta of incoming or outgoing particles and the summations in the four-dimensional delta function are over all particles in the initial (i) and final (f) state.

In general, the experimentally measurable quantities that are predicted by quantum field theories are differential probabilities, known as cross sections. The differential cross section is given by [58]

$$d\sigma = \frac{1}{\mathcal{F}} |\mathcal{M}_{fi}|^2 d\Pi_{\text{LIPS}}, \quad (1.54)$$

where

$$d\Pi_{\text{LIPS}} = \prod_{p_j \in p_f} \frac{d^3 p_j}{(2\pi)^3} \frac{1}{2E_{p_j}} \delta^{(4)} \left(\sum p_i - \sum p_f \right), \quad (1.55)$$

is the differential Lorentz-invariant phase space (LIPS). The product is over all particles p_j in the final state, and by integrating over this factor we sum over all possible outgoing momenta. The factor \mathcal{F} is a flux factor describing the initial-state particles, whilst the object $|\mathcal{M}_{fi}|^2$ is the invariant matrix element squared which has been averaged over initial state and summed over final state spin, colour and polarisation.

The invariant matrix element, \mathcal{M}_{fi} , is calculated at each order in perturbation theory using a set of Feynman rules. Each rule corresponds to a segmented part of the scattering process: the external particles, vertices and internal propagators, which are diagrammatically represented as Feynman diagrams. There may be a number of possible arrangements for the rules representing the scattering process, each with its own Feynman diagram.

The Feynman rules for QCD [58, 63] are presented in Tables 1.1, 1.2 and 1.3. Table 1.1 summarises the rules for external particles, in particular for spinors and polarisation vectors. The interaction vertex Feynman rules are presented in Table 1.3 and the rules for the propagators in a covariant gauge in Table 1.2.

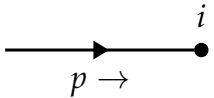
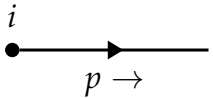
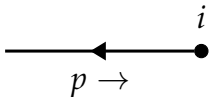
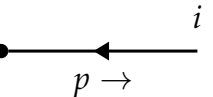
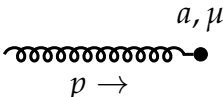
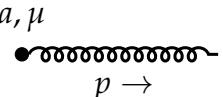
Incoming		Outgoing	
Diagram	Feynman Rule	Diagram	Feynman Rule
	$u_i(p, s)$		$\bar{u}_i(p, s)$
	$\bar{v}_i(p, s)$		$v_i(p, s)$
	$\epsilon^\mu(p)$		$\epsilon^{\mu,*}(p)$

TABLE 1.1: Feynman rules for external particles in QCD, namely quark and anti-quark spinors and the gluon polarisation vectors. Quarks are represented as solid lines and gluons as coiled lines. The i index labels the spinor components, μ a Lorentz index and a is a colour label. The arrows on the fermion lines denote charge flow, whilst the momenta of the fermion is illustrated below.

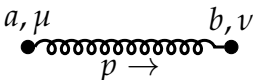
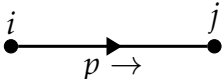
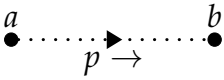
Diagram	Feynman Rule
	$\Delta^{\mu\nu,ab}(p) = \frac{i\delta^{ab}}{p^2+i\epsilon} \left(-\eta^{\mu\nu} + (1-\xi)\frac{p^\alpha p^\beta}{p^2+i\epsilon} \right)$
	$\Delta^{ij}(p) = \frac{i\delta^{ij}(p+m)}{p^2-m^2+i\epsilon}$
	$\Delta^{ab}(p) = \frac{i\delta^{ab}}{p^2+i\epsilon}$

TABLE 1.2: Feynman rules for propagators in QCD in a covariant gauge. Quarks are represented as solid lines, gluons as coiled lines and ghosts as dashed lines. The μ, ν indices label Lorentz indices, whilst i, j are colour indices in the SU(3) fundamental representation and a, b are colour indices in the adjoint representation.

1.4 Basic features of QCD radiation

Now that we have reviewed the QCD Lagrangian and written down the rules for calculating Feynman graphs, we shall put them to good use to show some of the most basic elements of calculations in perturbative QCD and to introduce the eikonal approximation. Perturbative calculations of QCD observables contain divergences in both the Ultraviolet (UV) and Infrared (IR) limit in general [64]. The UV divergences are removed by a process known as renormalisation. Whilst this won't be used (and will not be covered) in this work, suffice it to say that QCD is a renormalisable theory [36, 65, 66]. This means that all UV divergences can be reabsorbed into a finite number of redefinitions of parameters in the Lagrangian density: the coupling, the masses and the fields [64, 67, 68]. We now wish to examine the perturbative structure of QCD emissions from outgoing partons which contain IR divergences in the soft and / or collinear limits. To this end, we consider the calculation of the $\gamma^* \rightarrow q\bar{q}$ cross section to explore these divergences.

1.4.1 Born Amplitude

We shall begin our discussion by calculating the matrix element and subsequently the cross section for the $e^+e^- \rightarrow q\bar{q}$ process. Since we are interested in the high-energy limit, we will consider all fermions to be massless. Using the Feynman rules in Section 1.3, we can write down the matrix element cor-

Diagram	Feynman Rule
	$-ig_s \mathbf{T}^a \gamma^\mu$
	$g_s f^{abc} p^\mu$
	$-g_s f^{abc} \left[(k_1 - k_2)^\sigma \eta^{\mu\nu} + (k_2 - k_3)^\mu \eta^{\nu\sigma} + (k_3 - k_1)^\nu \eta^{\sigma\mu} \right]$
	$-ig_s^2 \left[f^{abe} f^{cde} (\eta^{\mu\sigma} \eta^{\nu\rho} - \eta^{\mu\rho} \eta^{\nu\sigma}) + f^{ace} f^{bde} (\eta^{\mu\nu} \eta^{\sigma\rho} - \eta^{\mu\rho} \eta^{\nu\sigma}) + f^{ade} f^{bce} (\eta^{\mu\nu} \eta^{\sigma\rho} - \eta^{\mu\sigma} \eta^{\nu\rho}) \right]$

TABLE 1.3: Feynman rules for QCD vertices. Quarks are represented as solid lines, gluons as coiled lines and ghosts as dashed lines. The indices i, j label colour indices in the SU(3) fundamental representation, a, b, c, d in the adjoint representation, whilst μ, ν, σ, ρ are Lorentz indices. Note the momenta in the three-gluon vertex are defined as incoming, i.e. $k_1 + k_2 + k_3 = 0$.

responding to Figure 1.2 as

$$\mathcal{M}_0^{(0)} = \bar{u}_i(p_1, s_1) \gamma^\mu H_\mu v_j(p_2, s_2) \delta_{ij}, \quad (1.56)$$

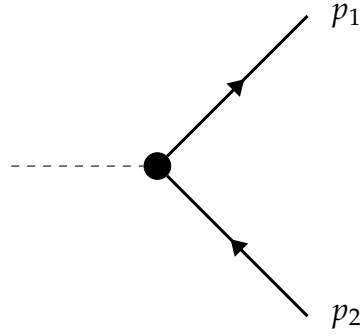


FIGURE 1.2: Feynman diagram of the Born amplitude for the $\gamma^* \rightarrow q\bar{q}$ process.

where $u_i(p_1, s_1)$ and $v_j(p_2, s_2)$ are the Dirac spinors corresponding to a quark of momentum p_1 and spin s_1 , and anti-quark of momentum and spin of p_2 and s_2 . The object H_μ contains all the information about the colour neutral vertex represented by the dashed line in Figure 1.2, and the process which created the final-state quark-antiquark pair. Also note the colour-conserving δ_{ij} which is include to ensure that the $q\bar{q}$ is a colour singlet (as the photon is colour blind). In the case that the initial colour singlet arises from electron-positron annihilation with a subsequent photon exchange,

$$H_\mu = -ie_q \bar{v}(p_b, s_b) (-ie\gamma^\nu) u(p_a, s_a) \frac{-i\eta_{\nu\mu}}{(p_a + p_b)^2}. \quad (1.57)$$

The Born-level matrix element squared is then

$$\begin{aligned} \sum |\mathcal{M}_0^{(0)}|^2 &= N_c e_q^2 \frac{(4\pi\alpha_{em})^2}{s} \text{Tr}(\not{p}_b \gamma_\mu \not{p}_a \gamma_\nu) \text{Tr}(\not{p}_1 \gamma^\mu \not{p}_2 \gamma^\nu) \\ &= N_c e_q^2 \frac{32(4\pi\alpha_{em})^2}{s^2} ((p_a \cdot p_1)(p_b \cdot p_2) + (p_a \cdot p_2)(p_b \cdot p_1)), \end{aligned} \quad (1.58)$$

where the sum in front signifies a sum over final-state colour and spin, with an averaging over initial-state spin and $\sqrt{s} = \sqrt{(p_a + p_b)^2}$ is the centre-of-mass energy of the e^+e^- system. The cross section then reads

$$\sigma_0 = \frac{1}{8s} \int \sum |\mathcal{M}_0^{(0)}|^2 \frac{d^3 p_1}{2E_1 (2\pi)^3} \frac{d^3 p_2}{2E_2 (2\pi)^3} (2\pi)^4 \delta^4(p_a + p_b - p_1 - p_2), \quad (1.59)$$

which produces the result

$$\sigma_0 = N_c e_q^2 \frac{4\pi\alpha_{em}^2}{3s}, \quad (1.60)$$

where e_q is the electric charge of the quark and α_{em} is the electroweak coupling, $\alpha_{em} = e^2/4\pi$. The Born cross section, σ_0 , does not exhibit any IR divergences - these begin to appear in the cross sections involving one or more real-emissions (at order α_s). We shall compute these contributions in Section 1.4.3. Firstly however, we shall review the eikonal approximation.

1.4.2 Eikonal approximation

As we shall see, one source of IR divergences is when emitted gluons have vanishing energy, known as the soft limit. These singularities show up after integrating over an emitted gluon momentum, k , as contributions that are singular as the gluon momentum becomes infinitely small. In particular, that all components of the gluon momentum are much smaller than the largest component of the momentum of the parton from which it is emitted. This limit can be parametrised by rescaling the gluon momentum by a scalar, λ , such that

$$k^\mu \rightarrow \lambda k^\mu. \quad (1.61)$$

The leading behaviour of an amplitude containing soft gluons can be captured by taking the limit $\lambda \rightarrow 0$, whilst only retaining terms leading in λ . This is the eikonal approximation [51, 69].

In order to exhibit the property of soft factorisation and determine an effective Feynman rule for soft gluons, we begin by considering an arbitrary amplitude, $\mathcal{M}_n(\{p_n\})$. This amplitude consists of n external hard partons whose set of momenta are signified by $\{p_n\}$. If we denote \mathcal{M}_{n+g}^f as the amplitude for the same hard process with an additional gluon emission (with momentum k) off

an outgoing quark (with momentum p), one obtains the following amplitude

$$\begin{aligned}
\mathcal{M}_{n+g}^f &= \bar{u}_i(p) \left[\left(-ig_s \mathbf{T}_{ij}^a \gamma^\mu \epsilon_\mu^{*a}(k) \right) \frac{i(\not{p} + \not{k} + m)}{(p+k)^2 - m^2 + i\epsilon} \right] \\
&\quad \times \mathcal{M}_{n,j}(\{p_1, \dots, p+k, \dots, p_n\}) \\
&= \bar{u}_i(p) \left[\left(-ig_s \mathbf{T}_{ij}^a \epsilon_\mu^{*a}(k) \right) \frac{i(2p^\mu + 2k^\mu - \not{k} \gamma^\mu)}{(p+k)^2 - m^2 + i\epsilon} \right] \\
&\quad \times \mathcal{M}_{n,j}(\{p_1, \dots, p+k, \dots, p_n\}). \quad (1.62)
\end{aligned}$$

The spinor associated with the quark has been explicitly extracted from the amplitude, $\mathcal{M}_{n,j}(\{p_1, \dots, p+k, \dots, p_n\})$. Additionally, here and throughout this work the high energy limit is assumed, whereby the momenta of quarks are much greater than their masses. As such, we make the approximation $m_i \simeq 0$, although the results of this section still hold true for the case of on-shell massive quarks. The second line of Eq. 1.62 utilises the standard Dirac matrix Clifford algebra in Eq. 1.21, and exploits the Dirac equation, $\bar{u}_i(p) \not{p} = \not{p} v_i(p) = 0$. Implementing Eq. 1.61 and taking the $\lambda \rightarrow 0$ limit, one arrives at

$$\begin{aligned}
\mathcal{M}_{n+g}^f &= \frac{\bar{u}_i(p)}{\lambda} \epsilon_\mu^{*a}(k) \left[\frac{g_s \mathbf{T}_{ij}^a p^\mu}{p \cdot k + i\epsilon} \right] \mathcal{M}_{n,j}(p_1, \dots, p, \dots, p_n) \\
&\quad + \mathcal{O}(\lambda^0). \quad (1.63)
\end{aligned}$$

We see that the soft gluon emission factorises. It is also worth pointing out that we have not specified a gauge in doing this. The term in square brackets can be thought of as an effective Feynman rule composed of a scalar propagator between the leading order amplitude and an effective vector vertex with the rule, $-2ig_s p^\mu \mathbf{T}_{ij}^a$. This is known as the eikonal Feynman rule, with

$$\frac{p^\mu}{p \cdot k'} \quad (1.64)$$

the so-called eikonal factor. The gluon has dissociated from the emitter becoming insensitive to spin, and is now associated with the entire hard process. The reason being, that such a gluon has an infinite wavelength and can therefore no longer resolve details of the hard interaction. Whilst we have considered a soft gluon emission from an outgoing fermion line, the same factor results modulo a sign difference, for an outgoing anti-fermion line. Indeed, the same effective Feynman rule would result had we considered emission from a scalar or vector particle.

Considering a soft gluon emission from an outgoing vector boson external leg, ϵ_β^* (with momentum p), connected to an arbitrary leading order amplitude $\mathcal{M}_n^{\mu,c}$. The gluon propagator in the axial gauge is

$$\Delta^{\mu\nu,ab}(p+k) = \frac{i\delta^{ab}}{(p+k)^2 + i\epsilon} \left(-\eta_{\mu\nu} + \frac{n_\mu(p+k)_\nu + (p+k)_\nu n_\mu}{(p+k) \cdot n} \right). \quad (1.65)$$

This is simply Eq. 1.47 with the choice $\xi \rightarrow 0$ and $n^2 = 0$, i.e. the lightcone gauge [70]. The resulting amplitude reads

$$\begin{aligned} \mathcal{M}_{n+g}^g &= \epsilon_b^{*,\beta}(p) \epsilon_a^{*,\alpha}(k) \\ &\times \left(-g_s f^{abc} \left((2p+k)_\alpha \eta_{\beta\gamma} + (-p-2k)_\beta \eta_{\alpha\gamma} + (k-p)_\gamma \eta_{\alpha\beta} \right) \right) \\ &\times \frac{i \left(-\eta_{\mu\gamma} + \frac{n_\mu(p+k)_\gamma + n_\gamma(p+k)_\mu}{n \cdot (p+k)} \right)}{(p+k)^2 + i\epsilon} \mathcal{M}_n^{\mu,c}(p_1, \dots, p+k, \dots, p_n), \\ &= \epsilon_b^{*,\beta}(p) \epsilon_a^{*,\alpha}(k) \left(-g_s f^{abc} 2p_\alpha \eta_{\beta\gamma} \right) \\ &\times \frac{i \left(-\eta_{\mu\gamma} + \frac{n_\mu p_\gamma}{n \cdot p} \right)}{2\lambda p \cdot k + i\epsilon} \mathcal{M}_n^{\mu,c}(p_1, \dots, p, \dots, p_n) + \mathcal{O}(\lambda^0). \end{aligned} \quad (1.66)$$

We have exploited both gauge invariance, represented by the relation $\mathcal{M}^\mu(p+k, \dots, p_n)(p+k)_\mu = 0$, the property of the axial gauge, $p_i^\beta \epsilon_\beta^{*b} = 0$, and taken the soft limit to arrive at the last line of Eq. 1.66. This reduces to

$$\mathcal{M}_{n+g}^g = \frac{\epsilon_b^{*,\gamma}(p) \epsilon_a^{*,\alpha}(k)}{\lambda} \left[\frac{g_s i f^{abc} p^\alpha}{p \cdot k + i\epsilon} \right] \mathcal{M}_n^{\gamma,c}(p_1, \dots, p, \dots, p_n) + \mathcal{O}(\lambda), \quad (1.67)$$

where once again, the term in the square brackets can be thought of as an effective Feynman rule. Replacing the structure constant with a generator using Eq. 1.8, highlights the shared eikonal factor for both fermion and vector emitters. The important part is that these eikonal factors appear for any number of soft gluons and the factorisation they exhibit does not depend on the internal structure of the amplitude. We shall use these rules in the following sections to calculate the $\mathcal{O}(\alpha_s)$ corrections to the cross section for the $\gamma^* \rightarrow q\bar{q}$ process including soft corrections, i.e. emission and one-loop corrections.

1.4.3 Emission contribution

We begin our discussion of the $\mathcal{O}(\alpha_s)$ soft corrections to the $\gamma^* \rightarrow q\bar{q}$ cross section by considering the emission of a real gluon with momentum k , colour

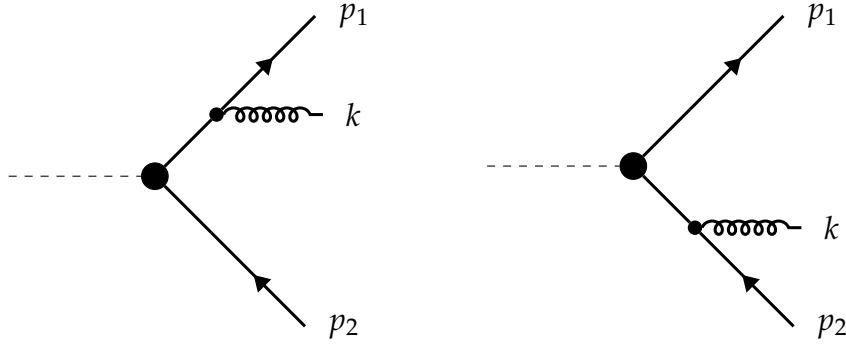


FIGURE 1.3: Feynman diagrams for the $\mathcal{O}(\alpha_s)$ real emission corrections to the total hadronic cross section in $\gamma^* \rightarrow q\bar{q}$.

index c and polarisation λ_k from either leg of the $q\bar{q}$ pair, as depicted in Figure 1.3. The amplitude for a soft-gluon emission from the quark can be written as

$$\mathcal{M}_1^{(0),1} = g_s \mathbf{T}_{ij}^a \gamma^\alpha \epsilon_\alpha^{*,a}(k, \lambda_k) \frac{p_1^\alpha}{p_1 \cdot k} \bar{u}_i(p_1, s_1) \gamma^\mu H_\mu v_j(p_2, s_2). \quad (1.68)$$

An equivalent amplitude, $\mathcal{M}_1^{(0),2}$, holds for a soft-gluon emission off the antiquark, with the only difference being an additional minus sign as noted in Section 1.4.2. Summing the two contributions gives

$$\begin{aligned} \mathcal{M}_1^{(0)} &= \mathcal{M}_1^{(0),1} + \mathcal{M}_1^{(0),2} \\ &\simeq g_s \mathbf{T}_{ij}^a \gamma^\alpha \epsilon_\alpha^{*,a}(k, \lambda_k) \left[\frac{p_1^\alpha}{p_1 \cdot k} - \frac{p_2^\alpha}{p_2 \cdot k} \right] \bar{u}_i(p_1, s_1) \gamma^\mu H_\mu v_j(p_2, s_2) \\ &= \epsilon_\alpha^{*,a}(k, \lambda_k) A^{\alpha,a} \mathcal{M}_0. \end{aligned} \quad (1.69)$$

The object $A^{\alpha,a}$ is the eikonal current. It's interesting to note that if we substitute $\epsilon_\alpha^{*,a}(k, \lambda_k)$ with k_α and contract with $A^{\alpha,a}$, we get a null result, which is a result of gauge invariance. This is a consequence of colour conservation and can be generalised to an arbitrary number of coloured final-state external legs [71, 72]. Squaring $\mathcal{M}_1^{(0)}$ and summing over final-state spins, colours and polarisations we have

$$\sum_{\lambda_k} \left| \mathcal{M}_1^{(0)} \right|^2 = \sum_{\lambda_k} \epsilon_\alpha^{*,c}(k, \lambda_k) \epsilon_\beta^d(k, \lambda_k) A^{\alpha,c} A^{+\beta,d} |\mathcal{M}_0|^2, \quad (1.70)$$

where the sum and trace over the $SU(N_c)$ generators in the fundamental representation, are

$$\sum_{i,j,a} \mathbf{T}_{ij}^a \left(\mathbf{T}_{ij}^a \right)^* = C_F \text{Tr}(\mathbf{1}) = C_F N_c. \quad (1.71)$$

Taking all of these results together, we can write the cross section for $q\bar{q}$ pair production, with the emission of a soft-gluon as

$$\sigma_1^{(0)} = \frac{2\alpha_s}{\pi} C_F \int \frac{dE_k}{E_k} \frac{d\Omega}{4\pi} E_k^2 \frac{p_1 \cdot p_2}{(p_1 \cdot k)(p_2 \cdot k)} d\sigma_0, \quad (1.72)$$

where $d\sigma_0$ is the differential Born cross section for creating the quark-antiquark pair. From Eq. 1.72, we can glean that the cross section for emitting a gluon is divergent in three regions: when the gluon is collinear to the quark, i.e. $p_1 \cdot k \rightarrow 0$, when the gluon is collinear to the anti-quark, $p_2 \cdot k \rightarrow 0$ and when the gluon momentum approaches zero, $k \rightarrow 0$. We can specify the back-to-back kinematics for the quark-antiquark pair, for a centre-of-mass energy, Q , (and generally pick the azimuth of the emitted gluon to be 0) as:

$$\begin{aligned} p_1 &= \frac{Q}{2} (1, 0, 0, 1) \\ p_2 &= \frac{Q}{2} (1, 0, 0, -1) \\ k &= E_k (1, \sin\theta, 0, \cos\theta), \end{aligned} \quad (1.73)$$

where θ is the polar angle between the emitted gluon and the quark. We can then see that the aforementioned divergent limits correspond to the collinear (with the quark) limit $\theta \rightarrow 0$ ($p_1 \cdot k \rightarrow 0$), the anti-collinear limit $\theta \rightarrow \pi$ ($p_2 \cdot k \rightarrow 0$) and soft limit, $E_k \rightarrow 0$. The first two divergences are called collinear divergences, whilst the last is called a soft divergence. These are collectively termed infrared divergences. Physically, the $\gamma^* \rightarrow q\bar{q}$ process with a gluon that is either soft, or collinear with the quark or anti-quark, is indistinguishable from the process in which no gluon was emitted.

Alone, these real emission contributions would lead to an infinite, and unphysical cross section. There are further diagrams that contribute to the $\gamma^* \rightarrow q\bar{q}$ cross section at this order however. They are the one-loop virtual corrections to the Born amplitude and shall be discussed in the next section, where we will see that with their inclusion, the infrared divergences cancel.

1.4.4 Virtual Contribution

Physically, the infrared divergences in Eq. 1.72 would indicate that the cross-section is sensitive to long-distance effects. However the cross-section containing one emission at $\mathcal{O}(\alpha_s)$ is not the only contribution at this order. The emission of a virtual gluon exchanged between the quark-antiquark final state

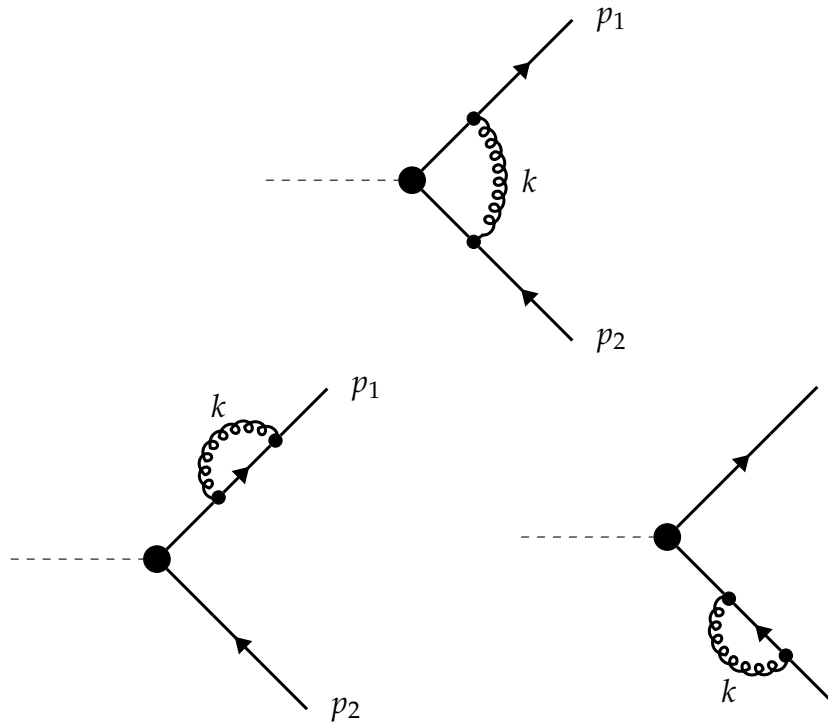


FIGURE 1.4: Feynman diagrams for the $\mathcal{O}(\alpha_s)$ one-loop corrections to the Born cross section for $\gamma^* \rightarrow q\bar{q}$.

particles in the Born amplitude (known as the vertex correction), contributes to \mathcal{M}_0 at $\mathcal{O}(\alpha_s)$. This is depicted in the top diagram of Figure 1.4 and we shall denote this contribution as $\mathcal{M}_0^{(1)}$.

There are two additional diagrams in Figure 1.4, containing self-energy gluon exchanges of the quark and anti-quark. However, it can be shown that these contributions can be consistently set to 0, and so we won't consider them here. One way to see this is with the dimensional regularisation (DR) scheme [65], where both infrared and ultraviolet divergences are regularised, performing calculations in $d = 4 + \epsilon$ dimensions. In the DR scheme the self-energy corrections vanish if we adopt the Landau gauge (where we set $\zeta = 0$ in the gluon propagator). Moreover, using the DR scheme, one can show that we can treat these self-energy corrections as equal to zero, for any value of ζ and ϵ , provided we are dealing with massless fermions [73].

It is therefore sufficient to examine only the vertex correction Feynman diagram in the Feynman gauge. In order to calculate the effects of this contribution to the cross section, we must again calculate $|\mathcal{M}_0|^2$, where it is the inter-

ference terms in

$$|\mathcal{M}_0|^2 = \left| \mathcal{M}_0^{(0)} \right|^2 + \mathcal{M}_0^{(0)} \mathcal{M}_0^{\dagger,(1)} + \mathcal{M}_0^{(1)} \mathcal{M}_0^{\dagger,(0)}, \quad (1.74)$$

which ultimately contribute to the cross section at $\mathcal{O}(\alpha_s)$. The $\mathcal{M}_0^{(1)}$ amplitude for a soft-gluon exchange is given by

$$\mathcal{M}_0^{(1)} = -4iC_F g_s^2 \mathcal{M}_0^{(0)} \int \frac{d^4k}{(2\pi)^4} \frac{(p_1 \cdot p_2)}{(k^2 + i\epsilon) (2(p_1 \cdot k) + i\epsilon) (2(p_2 \cdot k) - i\epsilon)}, \quad (1.75)$$

where we have an explicit integral over the loop four-momentum, k . We have once again explicated the four momenta inner products by specifying the centre-of-mass frame of reference. To make note of an interesting result we can write the exchanged gluon in terms of its transverse and longitudinal momentum components, which exposes poles at $E_k = \pm(k_z - i\epsilon)$ and $E_k = \pm(|\mathbf{k}| - i\epsilon)$:

$$\begin{aligned} \mathcal{M}_0^{(1)} &= -4iC_F g_s^2 \mathcal{M}_0^{(0)} \int \frac{d^4k}{(2\pi)^4} \frac{p_1 \cdot p_2}{(E_k + |\mathbf{k}| - i\epsilon)} \\ &\quad \times \frac{1}{(E_k - |\mathbf{k}| + i\epsilon) (E_k + k_z - i\epsilon) (E_k - k_z + i\epsilon)}. \end{aligned} \quad (1.76)$$

Closing this contour in the lower plane, the relevant poles are $E_k = k_z$ and $E_k = |\mathbf{k}|$, and applying the residue theorem we find,

$$\mathcal{M}_0^{(1)} = C_F g_s^2 \mathcal{M}_0^{(0)} \int \frac{d^3k}{2E_k (2\pi)^3} \left(-\frac{p_1 \cdot p_2}{(p_1 \cdot k) (p_2 \cdot k)} + \frac{E_k}{(k_z - i\epsilon) k_T^2} \right), \quad (1.77)$$

where the second term in this integral results in an imaginary contribution, commonly referred to as the Coulomb gluon contribution. Integrated out, this results in

$$\mathcal{M}_0^{(1)} = C_F g_s^2 \mathcal{M}_0^{(0)} \left(-\int \frac{d^3k}{2E_k (2\pi)^3} \frac{p_1 \cdot p_2}{(p_1 \cdot k) (p_2 \cdot k)} + i\pi \int \frac{dk_T}{(2\pi)^2 k_T} \right). \quad (1.78)$$

This imaginary term always cancels when considering physical cross-sections in Abelian theories to all orders. However for non-abelian gauge theories such as QCD, this is not the case. Indeed, the Coulomb gluon can have measurable effects in the presence of a high enough number of coloured legs [74–76]. And, they have been shown to introduce super-leading logarithms [77, 78].

The interference terms of interest for the cross section are

$$\begin{aligned}
2\Re \left(\mathcal{M}_0^{(0)} \mathcal{M}_0^{(1),*} \right) &= C_F g_s^2 \left| \mathcal{M}_0^{(0)} \right|^2 \\
&\times \left(-2 \int \frac{d^3k}{E_k (2\pi)^3} \frac{p_1 \cdot p_2}{(p_1 \cdot k)(p_2 \cdot k)} + i\pi \int \frac{dk_T}{(2\pi)^2 k_T} - i\pi \int \frac{dk_T}{(2\pi)^2 k_T} \right) \\
&= -2C_F g_s^2 \left| \mathcal{M}_0^{(0)} \right|^2 \int \frac{d^3k}{E_k (2\pi)^3} \frac{p_1 \cdot p_2}{(p_1 \cdot k)(p_2 \cdot k)}. \tag{1.79}
\end{aligned}$$

It is clear that the first contribution to this squared amplitude has an identically divergent structure to that of Eq. 1.69 - the squared amplitude corresponding to real gluon emission - with opposite sign, and that in this particular instance, the Coulomb contributions cancel. Constructing the cross section from Eq. 1.79, we find that at $\mathcal{O}(\alpha_s)$

$$\sigma_1^{(0)} + \sigma_0^{(1)} = 0, \tag{1.80}$$

i.e. there are no corrections to the Born cross section from eikonal emission. Had we performed the full $\mathcal{O}(\alpha_s)$ calculation without taking the eikonal approximation, we would have found [79]

$$\sigma(e^+e^- \rightarrow q\bar{q}) = \sigma_0 \left(1 + \frac{\alpha_s}{\pi} \right), \tag{1.81}$$

resulting in an additional finite term.

The crucial point for both the eikonal and full calculation being, in combining all virtual and real-emission contributions at $\mathcal{O}(\alpha_s)$, the soft and collinear divergences exactly cancel. Infact, this pattern of divergence cancellation carries to all orders in α_s : we have witnessed the lowest-order manifestation of the Bloch-Nordsieck (BN) theorem (proven for QED) [80], which was generalised to non-Abelian theories by the Kinoshita-Lee-Nauenberg (KLN) theorem [81, 82]. This states that in a theory consisting of massless fields, the transition rate is free of infrared divergences at each order of perturbation theory provided the summation over all initial and final degenerate states is carried out. The degenerate state in this context being a final state consisting of a massless quark-antiquark pair, which is indistinguishable from the same state with an arbitrary number of collinear and/or soft gluons.

Whilst we have noted that the fully inclusive cross section corrections in the soft limit cancel entirely, what happens if we place restrictions on the emission phase-space? We still want our observables to remain unaffected by infrared

and collinear divergences, i.e. to not spoil the BN or KLN theorems. An observable that respects this condition is called InfraRed and Collinear (IRC) safe.

Remembering the exhibited factorisation of the real and virtual contributions in the soft limit, we can schematically write the NLO distribution of an exclusive observable ρ by introducing an observable (or measurement) function $u_n(\{k\}_n)$. This can be written

$$\sigma(\rho) = g_s^2 C_F \int d\sigma_0 \int \frac{d^3k}{E_k (2\pi)^3} \frac{p_1 \cdot p_2}{(p_1 \cdot k)(p_2 \cdot k)} \times [u_3(\{p_1, p_2, k\}) - u_2(\{p_1, p_2\})]. \quad (1.82)$$

From this we can see that for an observable to be infrared and collinear safe, the measurement function must satisfy

$$\begin{aligned} u_{n+1}(\{\dots, k_i, k_j, \dots\}) &\rightarrow u_n(\{\dots, k_i + k_j, \dots\}), & \text{if } k_i \parallel k_j \\ u_{n+1}(\{\dots, k_i, \dots\}) &\rightarrow u_n(\{\dots, k_{i-1}, k_{i+1}, \dots\}), & \text{if } k_i \rightarrow 0. \end{aligned} \quad (1.83)$$

We shall discuss a particular soft measurement function in more detail in Section 2.1.1. In the case $u_n(\{k\}_n) = 1$ this is our fully inclusive observable and the cancellation between real and virtual contributions is complete, as we have already shown. If our observable is exclusive to some degree, the above constraints ensure the IRC singularities cancel. However, the kinematic dependence can cause the cancellation of non-singular terms to be incomplete.

This miscancellation can leave behind a finite, but potentially large logarithmic contribution, making the perturbative expansion unreliable. The logarithms spoil the perturbative expansion in the strong coupling and must be resummed to all orders to regain reliable theoretical predictions. We shall examine this procedure for the simple case in which we set the non-Abelian generators to unity, effectively restricting ourselves to the Abelian gauge theory, QED. We shall show that for the one-loop exchange of a soft photon between the quark-antiquark pair in Figure 1.4, contributions from this graph exponentiate.

1.4.5 Resummation

We have observed the factorisation of soft photon (gluon) physics at the one-loop level. We could schematically write the amplitude of this diagram (where we neglect the integral over the loop momentum k and ignore coupling con-

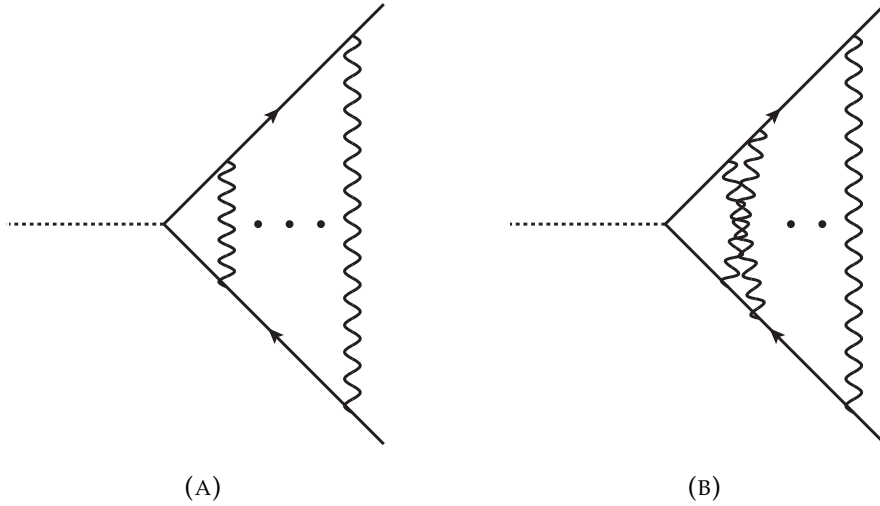


FIGURE 1.5: Two diagrams which contribute at $\mathcal{O}(\alpha^n)$ with n soft photon exchanges. The left-hand diagram is the completely uncrossed graph, whilst the right-hand diagram is an example of a graph with a single crossing.

starts) as

$$\mathcal{M}_0^{(1)} = \mathcal{M}_0^{(0)} \left(-\frac{p_1^\mu}{p_1 \cdot k} \right) \left(\frac{p_2^\nu}{p_2 \cdot k} \right) \Delta_{\mu\nu}(k), \quad (1.84)$$

where $\Delta_{\mu\nu}(k)$ denotes a photon propagator. If we consider an equivalent Feynman graph to the one-loop exchange in Figure 1.4, but with n uncrossed photon exchanges, we would find the contribution to $\mathcal{M}_0^{(n)}$ to be

$$\begin{aligned} \mathcal{M}_{0,\text{uncrossed}}^{(n)} &= \mathcal{M}_0^{(0)} \times \prod_{i=1}^n \Delta_{\mu_i \nu_i}(k_i) \\ &\times \left(\frac{(-1)^n p_1^{\mu_1} \dots p_1^{\mu_n} p_2^{\nu_1} \dots p_2^{\nu_n}}{(p_1 \cdot k_1) \dots (p_1 \cdot (k_1 + \dots + k_n)) (p_2 \cdot k_1) \dots (p_2 \cdot (k_1 + \dots + k_n))} \right), \end{aligned} \quad (1.85)$$

which is pictorially depicted in Figure 1.5a. There are of course other diagrams at this order which contribute. They involve all possible permutations of the ordering of the photon exchanges with regards to the quark and anti-quark line. An example of one such diagram is illustrated in Figure 1.5b. Including

all such diagrams, one can write the full $\mathcal{M}_0^{(n)}$ amplitude as

$$\begin{aligned} \mathcal{M}_0^{(n)} &= \mathcal{M}_0^{(0)} \left(\frac{(-1)^n p_1^{\mu_1} \dots p_1^{\mu_n} p_2^{\nu_1} \dots p_2^{\nu_n}}{(p_2 \cdot k_1) \dots (p_2 \cdot (k_1 + \dots + k_n))} \right) \prod_{i=1}^n \Delta_{\mu_i \nu_i}(k_i) \\ &\times \sum_{\pi} \frac{1}{(p_1 \cdot k_{\pi_1}) \dots (p_1 \cdot (k_{\pi_1} + \dots + k_{\pi_n}))}, \end{aligned} \quad (1.86)$$

where π here labels a permutation of the list $(1, 2, \dots, n)$ such that it maps to $(\pi_1, \pi_2, \dots, \pi_n)$. The second denominator can be related to a much simpler one through the use of the eikonal identity

$$\sum_{\pi} \frac{1}{(p_1 \cdot k_{\pi_1}) \dots (p_1 \cdot (k_{\pi_1} + \dots + k_{\pi_n}))} = \prod_i \frac{1}{p_1 \cdot k_i}. \quad (1.87)$$

The first denominator still has a complicated dependence on the photon momenta, where the photons depend on all other photons lying between itself and the original final-state quark-antiquark pair. Noting that the momenta of the photon loops will inevitably be integrated over, the photon momenta k_i are dummy variables. Then one can replace the particular combination of photon momenta in the first denominator with a sum over all permutations of these momenta (modulo a $1/n!$ symmetry factor). Using Eq. 1.87, one can then rewrite Eq. 1.86 as

$$\mathcal{M}_0^{(n)} = \mathcal{M}_0^{(0)} \frac{1}{n!} \prod_{i=1}^n \frac{d^4 k_i}{(2\pi)^4} \left(-\frac{p_1^{\mu_i}}{p_1 \cdot k_i} \right) \left(\frac{p_2^{\nu_i}}{p_2 \cdot k_i} \right) \Delta_{\mu_i \nu_i}(k_i). \quad (1.88)$$

One may then explicitly compute the sum of all diagrams involving any number of soft photon emissions, to all orders in perturbation theory and find

$$\mathcal{M} = \mathcal{M}_0 \exp \left[\int \frac{d^4 k}{(2\pi)^4} \left(-\frac{p_1^{\mu}}{p_1 \cdot k} \right) \left(\frac{p_2^{\nu}}{p_2 \cdot k} \right) \Delta_{\mu\nu}(k) \right]. \quad (1.89)$$

This is the exponential of the one-loop graph in Eq. 1.84, where we have reinstated the loop integral over the photon momentum. A few comments are in order. The one-loop graph in the exponent contains IR divergences as already outlined. This means that there is a pattern of IR singularities that appear order-by-order as one expands the exponential. We shall see in Chapter 2 that these divergences cancel against those from real emission contributions at each order (as they did for the first order in Sections 1.4.3 and 1.4.4). Eq. 1.89 was

derived, only assuming soft photons with no restriction on the ordering with which they attach to the hard external legs. However, had we assumed energy ordering, $Q \ll k_1^0 \ll k_2^0 \ll \dots \ll k_n^0$ where Q is the energy of the hard process, we would have found the same result. Resummation in QCD is more complicated as each Feynman graph can carry the colour matrices, T^a , which weight the graph and do not commute. Despite this, using approximations like the soft limit and energy-ordering, the process of resumming logarithmically-enhanced terms at all orders to restore the predictive power of perturbative QCD is a well-known technique [83–90], to the point that it has been automated for a number of observables [88, 91–95].

Consider a global IRC safe observable,

$$\Sigma(\rho) = \int_0^\rho \frac{1}{\sigma} \frac{d\sigma}{d\rho'} d\rho'. \quad (1.90)$$

This is the integrated distribution, i.e. the probability for the observable to take on a value smaller than ρ . If its logarithmically-enhanced terms exponentiate, $\Sigma(\rho)$ can be written in the resummed form [83],

$$\Sigma(\rho) \propto \left(1 + \sum_n C_n \left(\frac{\alpha_s}{2\pi} \right)^n \right) \exp(Lg_1(\alpha_s L) + g_2(\alpha_s L) + \dots), \quad (1.91)$$

valid for small ρ . In the above equation $L = \ln(1/\rho)$ is a logarithm involving ρ and the terms resummed by $Lg_1(\alpha_s L)$ are referred to as leading (or ‘double’) logarithms (sourced from both collinear and soft divergences). Next-to-leading (or ‘single’) logarithms are resummed by $g_2(\alpha_s L)$, and so forth. Whilst Eq. 1.91 looks straightforward, there are a number of ‘catches’. One being: for observables with emissions that are only sensitive to a limited ‘patch’ of phase-space, it was shown [96] that there are additional classes of next-to-leading logarithmic terms that do not exponentiate. These so-called non-global logarithms shall be our focus in Chapter 2.

1.5 Colour Flow Representation

We saw in Section 1.2 that quarks and antiquarks come in three colours, whilst gluons come in eight. There are then many amplitudes with different colour arrangements that must be computed and summed in order to determine the invariant matrix element, \mathcal{M}_{fi} , in Eq. 1.53. Each Feynman graph contributing to this calculation can be factorised into a kinematical and colour amplitude.

With a view to introducing a general evolution algorithm (in Chapter 2) and discussing its implementation into a Monte-Carlo code (in Chapter 4), we need an efficient and automated way to calculate colour-dependence.

In typical calculations, the colour amplitude consists of a string of \mathbf{T}^a and f^{abc} tensors, contracted over all internal indices. The ‘outermost’ tensors carry external colour indices which are summed over when calculating the squared invariant matrix element. Commonly, the structure constants in the adjoint representation are rewritten into the fundamental representation (using for example Eq. 1.13).

The colour-flow representation is one in which the basis of the fundamental representation, \mathbf{T}^a , is eliminated. It is conventional to decompose the gluon field using the fundamental-representation matrices as

$$(A_\mu)_j^i = A_\mu^a (\mathbf{T}^a)_j^i. \quad (1.92)$$

Instead, the QCD Lagrangian and corresponding Feynman rules can be written in terms of individual matrix elements of the $N_c \times N_c$ gauge matrix fields, $(A_\mu)_j^i$. Expressing calculations in this way is beneficial for both automated colour computation and interfacing to the components of existing event generators: parton showers, matrix element generators and hadronisation models. Resulting amplitudes describe colour connections, or colour flows, through a weighted-sum of products of Kronecker-deltas.

One can then rewrite the QCD Lagrangian to account for this change, as

$$\begin{aligned} \mathcal{L}_{\text{QCD}} = & -\frac{1}{4} (F_{\mu\nu})_j^i (F^{\mu\nu})_i^j + \bar{\psi}_i \gamma^\mu \left(i\partial_\mu \delta_j^i + \frac{g_s}{\sqrt{2}} (A_\mu)_j^i \right) \psi^j \\ & + \mathcal{L}_{\text{gauge-fix}} + \mathcal{L}_{\text{ghost}}, \end{aligned} \quad (1.93)$$

where

$$(F_{\mu\nu})_j^i = \partial_\mu (A_\nu)_j^i - \partial_\nu (A_\mu)_j^i - ig_s (A_\mu)_k^i (A_\nu)_j^k + ig_s (A_\nu)_k^i (A_\mu)_j^k. \quad (1.94)$$

We have expressed the QCD Lagrangian for just one massless fermion species for brevity, although the generalisation to multiple species is the same as in Eq. 1.42. The indices on the gauge field matrix elements follow the conventions of [97, 98], where upper indices transform under the fundamental representation of $\text{SU}(N_c)$ and the lower indices transform in the anti-fundamental

representation. Additionally, the coupling constant has been renormalised, $g_s \rightarrow g_s/\sqrt{2}$, so that the gauge matrix field is canonically normalised.

The tensor product of the fundamental and anti-fundamental representation is isomorphic to the adjoint representation of $U(N_c)$. This is the equivalence employed in 't Hooft's double line notation [45], mentioned in Section 1.2.1. Written in this way, the colour part of the $SU(N_c)$ gluon propagator can be split into a $U(N_c)$ gluon propagator and a $U(1)$ gluon propagator,

$$\Delta^{\mu\nu,ab}(p) \propto \delta_i^a \delta_j^b - \frac{1}{N_c} \delta_j^a \delta_i^b \quad (1.95)$$

such that the usual algebraic constraints of hermiticity and tracelessness are satisfied (just as they are when A_μ is decomposed in the fundamental representation, see Eq. 1.36). The $U(1)$ gluon interacts only with quarks and acts as a 'photon', i.e. it takes no part in the colour flow. It is unphysical and carries a factor of $1/N_c$.

The correspondence between the standard QCD Feynman rules (expressed in the fundamental and adjoint representations) and the Feynman rules in the colour-flow representation, for propagator and vertex factors, are presented in Tables 1.4 and 1.5. An upper index represents a colour line, whilst a lower index represents an anti colour line, where there are N_c different colours corresponding to the values each index can take. An arrow on each line indicates whether it is a colour (directed to the right) or anti colour (to the left) line and the arrows track the flow of colour from lower to upper indices. Gluons are represented by double lines, one for the colour and one for the anti colour, flowing in opposite directions. Similarly, fermion (anti fermion) propagators are represented by a single directed colour (or anti colour) line. The vertex colour factors are a product of Kronecker deltas, which correspond to colour lines continuing through the vertex. As we can see from Eq. 1.93, the basic coupling is $g_s/\sqrt{2}$ in the colour-flow formalism. Aside from this rescaling, all Lorentz and momentum factors in the colour flow Feynman rules retain their original form and so are omitted from Tables 1.4 and 1.5. It is worth noting that since ghosts carry colour, they would also have a corresponding Feynman rule in the colour flow representation. However, they are not used in this work and so will not be discussed here.

As an example of using the colour flow representation, let's look at the exchange of a gluon between fermion lines. Figure 1.6 illustrates a one-gluon

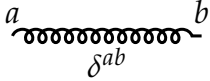
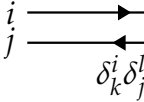
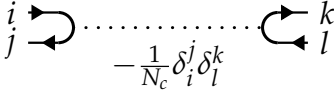
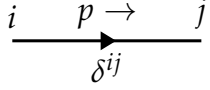
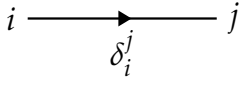
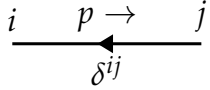
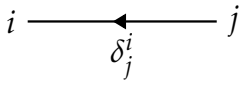
QCD Propagator	Colour-flow representation	
		
		
		

TABLE 1.4: Correspondence between the Feynman rules for propagators in QCD and those Feynman rules in the colour-flow formalism. Arrows directed to the right represent colour lines, whilst those to the left represent anti-colour lines. The Kronecker delta functions constraining the colour in both the standard QCD Feynman rules and in the colour flow representation are presented, whilst the Lorentz and momentum factors are omitted as they retain their original form.

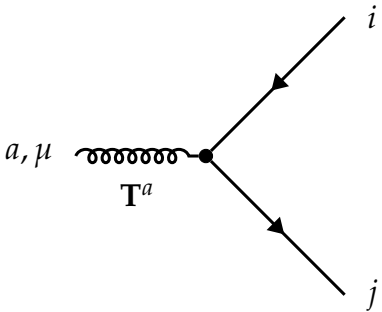
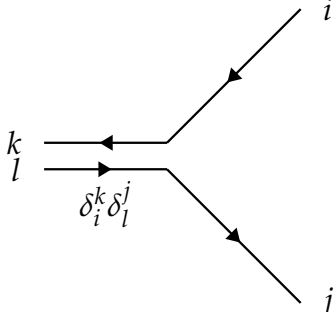
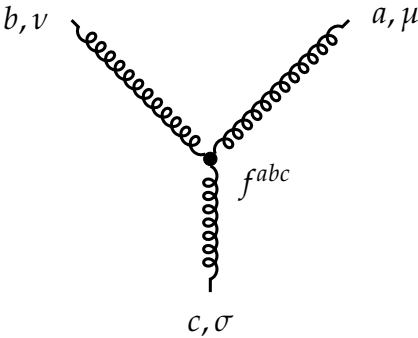
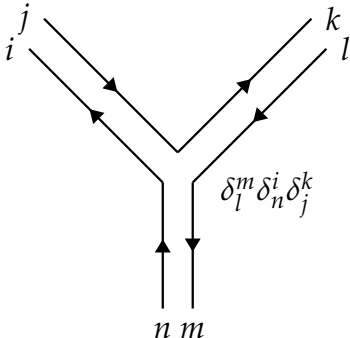
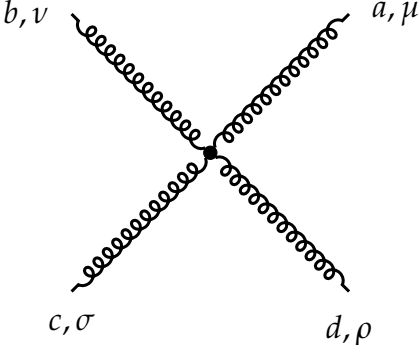
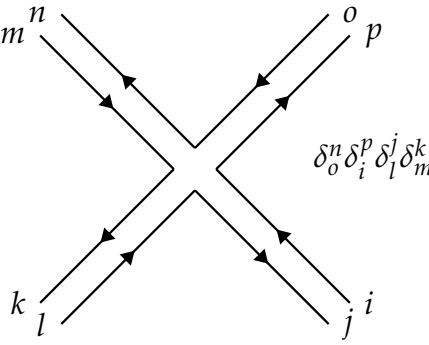
QCD Propagator	Colour-flow representation
	
	
	

TABLE 1.5: Correspondence between the Feynman rules for vertices in QCD and those Feynman rules in the colour-flow formalism.

Chapter 2

Amplitude Evolution

In this chapter, we shall bring together concepts from Chapter 1 and the works [18–21, 78] to present a general framework that can be used as basis for automated resummations. We consider algorithmic, recursive definitions of QCD amplitudes for the radiation of an arbitrary number of soft gluons including virtual corrections to all orders. This chapter is based on work performed in reference [99] which was produced in collaboration with R. Ángeles Martínez, J. R. Forshaw, S. Plätzer and M. H. Seymour.

The works [18, 19, 74, 75] focused on one particular observable, namely the gaps-between-jets cross section. This is the cross section for producing a pair of jets with a restriction on the transverse momentum (such that k_T is less than some veto scale Q_0) of any additional jets in the rapidity region between the two leading jets (of extent Y), the so-called in-gap region. This is depicted in Figure 2.1.

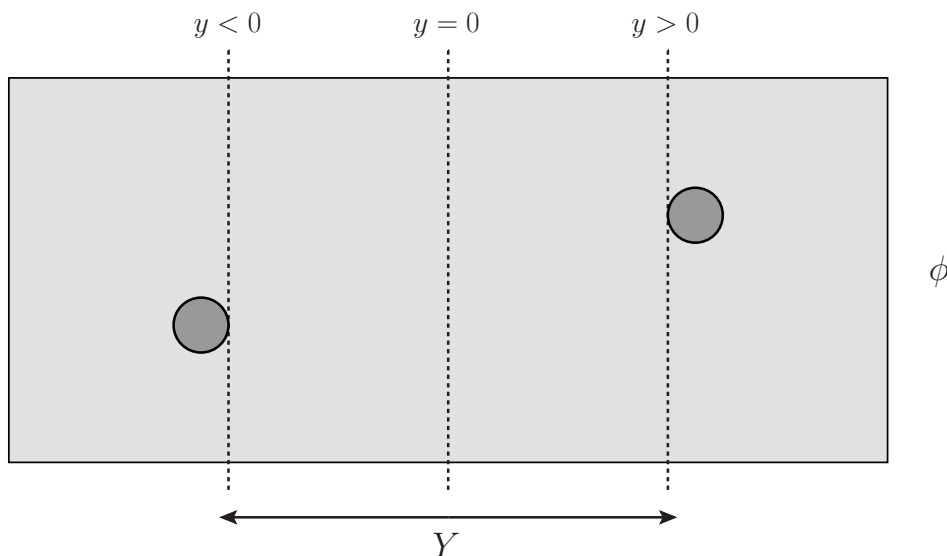


FIGURE 2.1: Depiction of the gaps-between-jets observable. The dark circles represent the two primary jets and any subsequent emission in the in-gap region is constrained to have a transverse momentum smaller than Q_0 .

In the original calculations of the gaps-between-jets cross section [74, 75], a cut Q_0 on the transverse momentum of any particle in the inter-jet region is imposed. All those terms which go as $\sim \alpha_s^n \ln^n(Q/Q_0)$, where Q is the transverse momentum of the primary jets, that can be obtained from dressing the lowest order $2 \rightarrow 2$ scattering in all possible ways with soft virtual gluons, were summed. Furthermore, they argued that one need only consider the subset of virtual corrections with transverse momentum $Q_0 < k_T < Q$, to capture all of the leading logarithms. This followed the rationale: knowing that the contri-

butions arising from real gluon emission cancel with a corresponding virtual correction, as per Eq. 1.82, it seems a consequence of the Bloch-Nordsieck Theorem that the only region in phase-space where real-virtual cancellation would not occur is the region where the real emissions are forbidden, i.e. within the gap and where the transverse momentum is above Q_0 . However, the work [96, 100] discovered additional single-logarithm contributions to observables such as gaps-between-jets, which they termed non-global.

These non-global contributions arise due to the subtlety that whilst the real and virtual contributions cancel exactly at the level of the cross section in the case we dress the primary jets with a single soft-gluon, this cancellation does not survive subsequent dressing. If we consider an emission above Q_0 , it is necessarily out of the gap. The virtual corrections to this five-parton amplitude which occur out-of-gap or in-gap, with $k_T < Q_0$, always have an emission to cancel against. However, due to the phase-space constraint, the out-of-gap real emission is forbidden from radiating back into the gap with $k_T > Q_0$ and those virtual corrections in-gap with $k_T > Q_0$ have nothing to cancel against. We then have total cancellation in both the in- and out-gap regions below Q_0 , but it is necessary to include the emission of any number of soft gluons, be them real or virtual, outside of the gap, dressed with any number of in-gap virtual gluons. The work [18] calculated the non-global contribution coming from one real or virtual gluon being emitted in the out-region dressed with an arbitrary number of in-gap virtual gluons. Their approach was generalised to use the colour basis-independent notation [51, 101, 102] in [19], keeping the full colour structure and setting out the basis of a framework to systematically calculate non-global contributions. The authors also retained the imaginary part of the virtual loop integrals, the so-called Coulomb gluon contributions. It turned out that these terms give rise to an additional source of real-virtual miscancellation, leading to towers of super-leading logarithms. It is this framework that forms the basis for the general algorithm outlined in the following section.

2.1 The General Algorithm

In this section we describe the general evolution algorithm in a form that is suited to the calculation of multiple soft-gluon contributions to any observable in a fully-differential way. We then proceed to reformulate this algorithm such that the cancellation of infrared divergences is manifest at each order and use this in an explicit calculation of the non-global contribution to the hemi-

sphere mass in electron-positron collisions to order α_s^3 . We begin by stating the differential cross section for emitting n soft gluons. This is

$$\begin{aligned}
\sigma_0 &= \text{Tr} \left(\mathbf{V}_{\mu,Q} \mathbf{H}(Q) \mathbf{V}_{\mu,Q}^\dagger \right) \equiv \text{Tr} \mathbf{A}_0(\mu) \\
d\sigma_1 &= \text{Tr} \left(\mathbf{V}_{\mu,E_1} \mathbf{D}_1^\mu \mathbf{V}_{E_1,Q} \mathbf{H}(Q) \mathbf{V}_{E_1,Q}^\dagger \mathbf{D}_{1\mu}^\dagger \mathbf{V}_{\mu,E_1}^\dagger \right) d\Pi_1 \\
&\equiv \text{Tr} \mathbf{A}_1(\mu) d\Pi_1 \\
d\sigma_2 &= \text{Tr} \left(\mathbf{V}_{\mu,E_2} \mathbf{D}_2^\nu \mathbf{V}_{E_2,E_1} \mathbf{D}_1^\mu \mathbf{V}_{E_1,Q} \mathbf{H}(Q) \mathbf{V}_{E_1,Q}^\dagger \mathbf{D}_{1\mu}^\dagger \mathbf{V}_{E_2,E_1}^\dagger \mathbf{D}_{2\nu}^\dagger \mathbf{V}_{\mu,E_2}^\dagger \right) d\Pi_1 d\Pi_2 \\
&\equiv \text{Tr} \mathbf{A}_2(\mu) d\Pi_1 d\Pi_2 \\
&\vdots
\end{aligned} \tag{2.1}$$

In Eq. 2.1, $\mathbf{H}(Q)$ is the hard scattering matrix for a process at some hard scale, Q , where $\mathbf{H} = |\mathcal{M}\rangle \langle \mathcal{M}|$. The vector $|\mathcal{M}\rangle$ represents a fixed-order matrix element in colour and spin, although only the colour shall be considered in this work. Eq. 2.1 presents the first three steps in a Markovian process, that builds upon the hard scattering matrix with virtual evolution operators (\mathbf{V}), which preserve the representation of \mathbf{H} in colour space and emission (\mathbf{D}) operators which increase the dimension. For n soft-gluon emissions, there are n emission operators and $n + 1$ virtual evolution operators. The last virtual operator evolves down to an infrared cutoff scale μ . The amplitude operators \mathbf{A}_n satisfy the recurrence relation

$$\mathbf{A}_n(E) = \mathbf{V}_{E,E_n} \mathbf{D}_n^\mu \mathbf{A}_{n-1}(E_n) \mathbf{D}_{n\mu}^\dagger \mathbf{V}_{E,E_n}^\dagger \theta(E \leq E_n), \tag{2.2}$$

where $\theta(E \leq E_n)$ is a Heaviside step function which constrains each subsequent emission to be at a lower or equal energy to the last. At each step in this recursion the emission operators add a new particle, whilst the virtual evolution operators (the so-called Sudakov operators) encode loop corrections to all orders. It is worth noting that we have ordered successive emissions in energy. This is a valid assumption for processes that are insensitive to Coulomb gluon exchanges, such as those used throughout this work, but not otherwise [20, 92, 99]. The amplitude operators, \mathbf{A}_n , contain fixed-order infrared divergences. The cancellation of these between real emission and virtual contributions only occurs in the sum over n after integration over the real emission phase-space. The emission operator for the i th gluon with energy E_i and four-momentum

q_i , \mathbf{D}_i^μ , in the eikonal approximation is

$$\mathbf{D}_i^\mu = \sum_j \mathbf{T}_j E_i \frac{p_j^\mu}{p_j \cdot q_i}, \quad (2.3)$$

where the sum over partons j in Eq. 2.3 is context-specific: the summation runs over all partons in the hard scattering and any prior soft-gluon emissions that have occurred in previous iterations of the process. Likewise, the colour charge operators, \mathbf{T}_j , are in a context-specific representation of $SU(3)_c$. The associated phase-space element, $d\Pi_i$, is defined as

$$d\Pi_i = -\frac{\alpha_s}{\pi} \frac{dE_i}{E_i} \frac{d\Omega_i}{4\pi}, \quad (2.4)$$

where α_s is the QCD coupling constant and $d\Omega_i = \sin\theta_i d\theta_i d\phi_i$. Here, θ_i and ϕ_i are the polar angle and azimuth of the emitted gluon respectively. The soft-gluon anomalous dimension operator describes the dressing of all pairs of partons in the cascade at any given time with a single soft-gluon exchange and forms the basis of the Sudakov operator. The anomalous dimension operator is

$$\Gamma = \frac{\alpha_s}{\pi} \sum_{i<j} (-\mathbf{T}_i \cdot \mathbf{T}_j) \left\{ \int \frac{d\Omega_k}{4\pi} \omega_{ij}(\hat{k}) - i\pi\tilde{\delta}_{ij} \right\}. \quad (2.5)$$

The object $\tilde{\delta}_{ij}$ in Eq. 2.5 is defined such that $\tilde{\delta}_{ij} = 1$ if the partons i and j are both in the initial or both in the final state and equal to zero otherwise. This is the term corresponding to Coulomb exchanges. The carat on the momentum k signifies that the dipole factor (defined below) is dependent only on the direction of the vector k . The sum in the soft-gluon anomalous dimension matrix is also context-specific, running over any prior soft gluon emissions and partons in the hard scattering process. Akin to the colour charge operators, the colour charge products in Eq. 2.5 are in a context-specific representation of $SU(3)_c$. The Sudakov operator, $\mathbf{V}_{a,b}$, is the path-ordered exponential of the soft-gluon anomalous dimension matrix integrated over the ordering variable:

$$\mathbf{V}_{a,b} = \text{P exp} \left[-\frac{\alpha_s}{\pi} \int_a^b \frac{dE_k}{E_k} \sum_{i<j} (-\mathbf{T}_i \cdot \mathbf{T}_j) \times \left\{ \int \frac{d\Omega_k}{4\pi} \omega_{ij}(\hat{k}) - i\pi\tilde{\delta}_{ij} \right\} \right], \quad (2.6)$$

where the dipole factors are defined as

$$\omega_{ij}(\hat{k}) = E_k^2 \frac{(p_i \cdot p_j)}{(p_i \cdot k)(p_j \cdot k)}. \quad (2.7)$$

The path-ordering, P , in the definition of $\mathbf{V}_{a,b}$ is not actually needed in this work, because the expression in curly brackets in Eq. 2.6 is independent of the ordering variable and we shall henceforth drop it. Physically, the Sudakov operator expresses the non-emission at the intermediate scales between two subsequent emissions.

A general observable, Σ , can be computed using

$$\Sigma(\mu) = \int \sum_n d\sigma_n(\mu) u_n(\{k\}_n), \quad (2.8)$$

where the u_n are the measurement functions which define the observable and depend on the set of momenta for all soft-gluons, $\{k\}_n$, at a given multiplicity n . We suppress dependence on the hard partons and integration over their phase-space. In terms of the amplitude operators this is

$$\Sigma(\mu) = \int \sum_n \left(\prod_{i=1}^n d\Pi_i \right) \text{Tr} \mathbf{A}_n(\mu) u_n(\{k\}_n). \quad (2.9)$$

The cutoff scale μ is an infrared regulator and one should take the limit that μ tends to 0. If we are interested in a specific observable we know to be inclusive of real emissions below some scale, ρ , then we instantiate the rationale of Bloch-Nordsieck cancellation to fix $\mu = \rho$. The real emission phase-space should then be integrated over energy values $E > \rho$. This can be shown if we make use of the identities [99]

$$\begin{aligned} \mathbf{V}_{a,b}^\dagger \mathbf{V}_{a,b} - 1 &= -\frac{\alpha_s}{\pi} \int_a^b \frac{dE}{E} \frac{d\Omega_k}{4\pi} \mathbf{V}_{E,b}^\dagger \mathbf{D}^2(\hat{k}) \mathbf{V}_{E,b}, \\ \frac{1}{2} \mathbf{D}^2(\hat{k}) &= \sum_{i < j} (-\mathbf{T}_i \cdot \mathbf{T}_j) \omega_{ij}(\hat{k}), \end{aligned} \quad (2.10)$$

where we have defined $\mathbf{D}^2(\hat{k}) \equiv \mathbf{D}^\mu(k) \mathbf{D}_\mu(k)$. We can write the observable for n real emissions as

$$d\sigma_n = \left(\prod_{m=1}^n d\Pi_m \right) \text{Tr} \left(\mathbf{V}_{E_n,0} \mathbf{A}_n(E_n) \mathbf{V}_{E_n,0}^\dagger \right). \quad (2.11)$$

Making use of the identities in Eq. 2.10, and exploiting the cyclic property of the trace, this can be written as

$$d\sigma_n = \left(\prod_{m=1}^n d\Pi_m \right) \text{Tr} \left(\mathbf{A}_n(E_n) - \int d\Pi_{n+1} \mathbf{A}_{n+1}(E_{n+1}) \right), \quad (2.12)$$

where it should be understood that $E_0 = Q$, such that $\mathbf{A}_0(E_0) = \mathbf{H}$. It follows that

$$\begin{aligned} \sigma = \text{Tr} \mathbf{H} + \sum_{n=0}^{\infty} \int \left(\prod_{m=1}^{n+1} d\Pi_m \right) \text{Tr} (\mathbf{A}_{n+1}(E_{n+1})) \\ \times (u_{n+1}(\{k_1, \dots, k_{n+1}\}) - u_n(\{k_1, \dots, k_n\})). \end{aligned} \quad (2.13)$$

In the case that $u_{n+1}(\{k_1, \dots, k_{n+1}\}) = u_n(\{k_1, \dots, k_n\})$ for $E_{n+1} < \rho$, then the scale ρ can be set as the lower bound on the energy integrals for both real emissions and virtual exchanges.

The algorithm as written in Eq. 2.1 is systematic to all orders in colour and accounts for the leading soft logarithms. Using the emission transverse momentum, k_T , as their ordering variable the authors of [20, 21] analytically verified this algorithm for a general hard process dressed with up to two soft real emissions and one loop. In addition, this framework has since been extended in [103] to account for the leading soft and/or collinear logarithms.

The iterative form of the algorithm is well suited to a Monte Carlo implementation to generate partonic events, which has been carried out and will be detailed in Chapter 4. We shall adopt the use of the colour flow basis to represent the operators in Eq. 2.1 and efficiently calculate multi-parton amplitudes [97].

Firstly however, we discuss a manifestly infrared-finite version of the algorithm, such that the infrared divergences arising in the eikonal approximation cancel at each iteration of the algorithm. This will enable us to calculate the non-global contribution to the hemisphere mass observable for e^+e^- collisions to order α_s^3 , which we can compare with the known results [96, 104, 105]. It is useful to consider a generalised measurement function in the soft gluon limit as follows

$$\begin{aligned} u_n(\{k_1, \dots, k_n\}) = u(k_i, \{k_1, \dots, k_{i-1}, k_{i+1}, \dots, k_n\}) \\ u_{n-1}(\{k_1, \dots, k_{i-1}, k_{i+1}, \dots, k_n\}), \end{aligned} \quad (2.14)$$

where $u(k_i, \{k_1, \dots, k_{i-1}, k_{i+1}, \dots, k_n\})$ goes to 1 as gluon i approaches the limit of having zero energy. Motivated by the work of [18, 19], general observables may be defined by dividing the total angular phase-space into two complementary regions. We refer to these regions as the "in" and "out" regions, where there is total inclusivity of the observable in the latter. The in-region places exclusionary constraints on radiation, e.g. disallowing radiation above some veto scale ρ . We can then write the measurement function as

$$u(k, \{q\}) = \Theta_{\text{out}}(k) + \Theta_{\text{in}}(k) u_{\text{in}}(k, \{q\}), \quad (2.15)$$

where the Heaviside functions $\Theta_{\text{in}}(k)$ and $\Theta_{\text{out}}(k)$ are defined to be unity if the emission k is in the in- or out-region respectively and zero otherwise. The set $\{q\}$ corresponds to all other real emissions. If the out-region is of zero extent, then the observable is referred to as a global observable and so $\Theta_{\text{out}}(k) = 0$ in which case $u(k, \{q\}) = u_{\text{in}}(k, \{q\})$. Otherwise, the observable is known as a non-global observable. In order to make the soft and soft-collinear divergences manifest and expose the infrared cancellation, it is useful to break the virtual loop-integral in the soft-gluon anomalous dimension matrix into two parts: that which is destined to cancel against a corresponding real emission contribution, and the remainder. We define

$$\mathbf{\Gamma} = \mathbf{\Gamma}_u + \bar{\mathbf{\Gamma}}_u, \quad (2.16)$$

where the bar indicates virtual exchanges in the in-region and

$$\begin{aligned} \mathbf{\Gamma}_u &= \frac{\alpha_s}{\pi} \int \frac{d\Omega_k}{4\pi} u(k, \{q\}) \frac{\mathbf{D}_k^2}{2}, \\ \bar{\mathbf{\Gamma}}_u &= \frac{\alpha_s}{\pi} \left(\int \frac{d\Omega_k}{4\pi} (1 - u(k, \{q\})) \frac{\mathbf{D}_k^2}{2} + i\pi \sum_{i < j} \tilde{\delta}_{ij} \mathbf{T}_i \cdot \mathbf{T}_j \right), \\ \bar{\mathbf{V}}_{a,b} &= P \exp \left(-\frac{\alpha_s}{\pi} \int_a^b \frac{dE}{E} \bar{\mathbf{\Gamma}}_u \right). \end{aligned} \quad (2.17)$$

As discussed in the introduction to this chapter, only the in-gap virtual gluons are summed to all orders. One can also see that $\bar{\mathbf{V}}$ does not contain any soft singularities in the real part (as $1 - u(k, \{q\}) \rightarrow 0$ as $E_k \rightarrow 0$). The imaginary Coulomb gluon contribution does, although these divergences cancel at the level of the cross section due to the cyclic property of the trace and they

combine into the identity matrix [101]. After expanding,

$$\begin{aligned} \mathbf{V}_{a,b} &= \bar{\mathbf{V}}_{a,b} - \int d\Pi_1 u(k_1, \{q\}) \bar{\mathbf{V}}_{a,1} \frac{\mathbf{D}_1^2}{2} \bar{\mathbf{V}}_{1,b} \\ &+ (-1)^2 \int d\Pi_1 d\Pi_1 u(k_1, \{q\}) u(k_2, \{q\}) \Theta(E_2 < E_1) \bar{\mathbf{V}}_{a,2} \frac{\mathbf{D}_2^2}{2} \bar{\mathbf{V}}_{2,1} \frac{\mathbf{D}_1^2}{2} \bar{\mathbf{V}}_{1,b} + \dots, \end{aligned} \quad (2.18)$$

the observable, Σ , can be written as

$$\Sigma(\mu) = \int \sum_n \left(\prod_{i=1}^n d\Pi_i \right) \text{Tr} \mathbf{B}_n(\mu) \Phi_n(\{q\}_n). \quad (2.19)$$

The operators \mathbf{B}_n satisfy a recurrence relation analogous to that of Eq. 2.2:

$$\begin{aligned} \mathbf{B}_n(E) &= \bar{\mathbf{V}}_{E,E_n} \left(\mathbf{D}_n^\mu \mathbf{B}_{n-1}(E_n) \mathbf{D}_{n,\mu}^\dagger \delta_n^R \right. \\ &\quad \left. - \left\{ \mathbf{B}_{n-1}(E_n), \frac{\mathbf{D}_n^2}{2} \right\} \delta_n^V u(q_n, \{q\}) \right) \bar{\mathbf{V}}_{E,E_n}^\dagger \Theta(E \leq E_n), \end{aligned} \quad (2.20)$$

with $\mathbf{B}_0(E) = \bar{\mathbf{V}}_{E,Q} \mathbf{H}(Q) \bar{\mathbf{V}}_{E,Q}^\dagger$ and where $\delta_i^R = 1$ if parton i is a real emission and $\delta_i^V = 1$ if i is virtual. The two are related by $\delta_i^R = 1 - \delta_i^V$. Provided that the measurement function is infrared safe, the infrared regulator, μ , can be safely set to 0, leaving Σ_n finite. In Eq. 2.19, $\Phi_n(\{q\}_n)$ contains the measurement on the phase-space of real particles and is defined in [99]. In the case of two real emissions,

$$\Phi_2(q_1, q_2) = \delta_1^V \delta_2^V + u_1(q_1) \delta_1^R \delta_2^V + u_1(q_2) \delta_1^V \delta_2^R + u_2(q_1, q_2) \delta_1^R \delta_2^R. \quad (2.21)$$

Written in this form, each \mathbf{B}_n is explicitly infrared finite. We shall now use this machinery to compute the non-global contribution to the hemisphere mass observable, showing how the cancellation of infrared poles occurs explicitly.

2.1.1 Non-global Contribution To The Hemisphere Jet-Mass

In this work we shall focus on two non-global observables: the Hemisphere Mass, which we shall calculate in this current section and the Gaps-Between-Jets, which shall be used as an exemplary observable in Chapters 4 and 5. The measurement function for these observables vetoes real emissions into some

region of phase-space, with the single-emission measurement function

$$u_1(q) = \Theta_{\text{out}}(q) + \Theta_{\text{in}}(q)\Theta(\rho > E), \quad (2.22)$$

where ρ is the minimum energy scale of any real emission and in the leading logarithm approximation, many (including these) observables can be computed with a factorisable measurement function,

$$u_n(\{k\}_n) = \prod_{i=1}^n u_1(k_i). \quad (2.23)$$

In the case of such observables, their inclusivity for energies less than the veto scale, ρ , leads to a complete cancellation of the real emission and virtual exchange contributions as described in Eq. 2.13. We can therefore set $\mu = \rho$ in Eq. 2.19 in addition to setting $u(k, \{q\})$ to $\Theta_{\text{out}}(k)$ for the integration over the phase-space of real emissions (see Eq. 2.21). In other words, Σ_n is the contribution from n gluons, be them real or virtual, in the out-region. Using Eq. 2.19 and 2.21, we can write

$$\begin{aligned} \Sigma_0 &= \text{Tr} \left(\bar{\mathbf{V}}_{\rho, Q} \mathbf{H} \bar{\mathbf{V}}_{\rho, Q}^\dagger \right), \\ \Sigma_1 &= \int_{\text{out}} d\Pi_1 \text{Tr} \left(\boldsymbol{\Sigma}_1^R + \boldsymbol{\Sigma}_1^V \right), \\ \Sigma_2 &= \int_{\text{out}} d\Pi_1 \int_{\text{out}} d\Pi_2 \text{Tr} \left(\boldsymbol{\Sigma}_2^{VR} + \boldsymbol{\Sigma}_2^{VV} + \boldsymbol{\Sigma}_2^{RR} + \boldsymbol{\Sigma}_2^{RV} \right), \end{aligned} \quad (2.24)$$

where

$$\begin{aligned}
\Sigma_1^R &= \text{Tr} \left(\bar{\mathbf{V}}_{\rho,E_1} \mathbf{D}_1^\mu \bar{\mathbf{V}}_{E_1,Q} \mathbf{H} \bar{\mathbf{V}}_{E_1,Q}^\dagger \mathbf{D}_{1\mu}^\dagger \bar{\mathbf{V}}_{\rho,E_1}^\dagger \right) \\
\Sigma_1^V &= -\text{Tr} \left(\bar{\mathbf{V}}_{\rho,Q} \mathbf{H} \bar{\mathbf{V}}_{E_1,Q}^\dagger \frac{\mathbf{D}_1^2}{2} \bar{\mathbf{V}}_{\rho,E_1}^\dagger + \bar{\mathbf{V}}_{\rho,E_1} \frac{\mathbf{D}_1^2}{2} \bar{\mathbf{V}}_{E_1,Q} \mathbf{H} \bar{\mathbf{V}}_{\rho,Q}^\dagger \right) \\
\Sigma_2^{RR} &= \text{Tr} \left(\bar{\mathbf{V}}_{\rho,E_2} \mathbf{D}_2^\nu \bar{\mathbf{V}}_{E_2,E_1} \mathbf{D}_1^\mu \bar{\mathbf{V}}_{E_1,Q} \mathbf{H} \bar{\mathbf{V}}_{E_1,Q}^\dagger \mathbf{D}_{1\mu}^\dagger \bar{\mathbf{V}}_{E_2,E_1}^\dagger \mathbf{D}_{2\nu}^\dagger \bar{\mathbf{V}}_{\rho,E_2}^\dagger \right) \\
\Sigma_2^{VR} &= -\text{Tr} \left(\bar{\mathbf{V}}_{\rho,E_2} \mathbf{D}_2^\nu \bar{\mathbf{V}}_{E_2,Q} \mathbf{H} \bar{\mathbf{V}}_{E_1,Q}^\dagger \frac{\mathbf{D}_1^2}{2} \bar{\mathbf{V}}_{E_2,E_1}^\dagger \mathbf{D}_{2\nu}^\dagger \bar{\mathbf{V}}_{\rho,E_2}^\dagger \right. \\
&\quad \left. + \bar{\mathbf{V}}_{\rho,E_2} \mathbf{D}_2^\nu \bar{\mathbf{V}}_{E_2,E_1} \frac{\mathbf{D}_1^2}{2} \bar{\mathbf{V}}_{E_1,Q} \mathbf{H} \bar{\mathbf{V}}_{E_2,Q}^\dagger \mathbf{D}_{2\nu}^\dagger \bar{\mathbf{V}}_{\rho,E_2}^\dagger \right) \\
\Sigma_2^{RV} &= -\text{Tr} \left(\bar{\mathbf{V}}_{\rho,E_1} \mathbf{D}_1^\mu \bar{\mathbf{V}}_{E_1,Q} \mathbf{H} \bar{\mathbf{V}}_{E_1,Q}^\dagger \mathbf{D}_{1\mu}^\dagger \bar{\mathbf{V}}_{E_2,E_1}^\dagger \frac{\mathbf{D}_2^2}{2} \bar{\mathbf{V}}_{\rho,E_2}^\dagger \right. \\
&\quad \left. + \bar{\mathbf{V}}_{\rho,E_2} \frac{\mathbf{D}_2^2}{2} \bar{\mathbf{V}}_{E_2,E_1} \mathbf{D}_1^\mu \bar{\mathbf{V}}_{E_1,Q} \mathbf{H} \bar{\mathbf{V}}_{E_1,Q}^\dagger \mathbf{D}_{1\mu}^\dagger \bar{\mathbf{V}}_{\rho,E_1}^\dagger \right) \\
\Sigma_2^{VV} &= \left(\bar{\mathbf{V}}_{\rho,Q} \mathbf{H} \bar{\mathbf{V}}_{E_1,Q}^\dagger \frac{\mathbf{D}_1^2}{2} \bar{\mathbf{V}}_{E_2,E_1}^\dagger + \bar{\mathbf{V}}_{\rho,E_1} \frac{\mathbf{D}_1^2}{2} \bar{\mathbf{V}}_{E_1,Q} \mathbf{H} \bar{\mathbf{V}}_{E_2,Q}^\dagger \right) \frac{\mathbf{D}_2^2}{2} \bar{\mathbf{V}}_{\rho,E_2}^\dagger \\
&\quad + \bar{\mathbf{V}}_{\rho,E_2} \frac{\mathbf{D}_2^2}{2} \left(\bar{\mathbf{V}}_{E_2,Q} \mathbf{H} \bar{\mathbf{V}}_{E_1,Q}^\dagger \frac{\mathbf{D}_1^2}{2} \bar{\mathbf{V}}_{\rho,E_1}^\dagger + \bar{\mathbf{V}}_{E_2,E_1} \frac{\mathbf{D}_1^2}{2} \bar{\mathbf{V}}_{E_1,Q} \mathbf{H} \bar{\mathbf{V}}_{\rho,Q}^\dagger \right). \quad (2.25)
\end{aligned}$$

This is the out-of-gap expansion used in [18, 19] to derive the super-leading logarithmic contribution to the gaps-between-jets observable. We now use this reformulation to show that the Σ_n are indeed separately infrared-finite at each order and to compute the fixed-order expansion of the non-global logarithmic contribution to the hemisphere jet mass observable. This shall be carried out to the non-trivial order of α_s^3 to compare with known-results. As in [96], we compute the lowest order non-global correction to the cumulative event shape where the jet mass is required to be less than ρ . This can be achieved by taking the out-region of our algorithm to be the region of phase-space that does not contribute to the hemisphere jet mass (the left hemisphere in [96]). We shall set $\mathbf{H} = \frac{1}{N_c} \mathbf{1}$ as we are considering a two-jet e^+e^- event shape. The $1/N_c$ factor cancels the lowest-order cross section colour factor. We wish to calculate

$$\begin{aligned}
\Sigma_1(\rho) &= \frac{1}{\sigma} \int_0^\rho \frac{d\sigma}{d\rho} d\rho = \frac{1}{N_c} \int_{\text{out}} d\Pi_1 \left[\text{Tr} \left(\mathbf{v}_{\rho,E_1}^{\text{in}} \mathbf{D}_1^\mu \mathbf{v}_{E_1,Q}^{\text{in}} \mathbf{v}_{E_1,Q}^{\text{in},\dagger} \mathbf{D}_{1\mu}^\dagger \mathbf{v}_{\rho,E_1}^{\text{in},\dagger} \right) \right. \\
&\quad \left. - \text{Tr} \left(\mathbf{v}_{\rho,E_1}^{\text{in}} \frac{\mathbf{D}_1^2}{2} \mathbf{v}_{E_1,Q}^{\text{in}} \mathbf{v}_{\rho,Q}^{\text{in},\dagger} \right) - \text{Tr} \left(\mathbf{v}_{\rho,Q}^{\text{in}} \mathbf{v}_{E_1,Q}^{\text{in}} \frac{\mathbf{D}_1^2}{2} \mathbf{v}_{\rho,E_1}^{\text{in}} \right) \right], \quad (2.26)
\end{aligned}$$

where to the lowest order, we expand the in-gap Sudakov operator as

$$\mathbf{V}_{a,b}^{\text{in}} \equiv \bar{\mathbf{V}}_{a,b} \simeq 1 - \frac{\alpha_s}{\pi} \int_a^b \frac{dE_k}{E_k} \sum_{i<j} (-\mathbf{T}_i \cdot \mathbf{T}_j) \int_{\text{in}} \frac{d\Omega_k}{4\pi} \omega_{ij}. \quad (2.27)$$

Additionally, we shall layout some useful definitions and results before proceeding with the calculation. The particle four-momenta are defined as

$$\begin{aligned} p_a &= \frac{Q}{2} (1, 0, 0, 1) \\ p_b &= \frac{Q}{2} (1, 0, 0, -1) \\ q_1 &= x_1 \frac{Q}{2} (1, 0, \sin \theta_1, \cos \theta_1) \\ q_2 &= x_2 \frac{Q}{2} (1, \sin \theta_2 \sin \phi_2, \sin \theta_2 \cos \phi_2, \cos \theta_2) \\ k &= x_k \frac{Q}{2} (1, \sin \theta_k \sin \phi_k, \sin \theta_k \cos \phi_k, \cos \theta_k) \end{aligned} \quad (2.28)$$

to assist comparison with [96] and the dipole factors are

$$\begin{aligned} \omega_{ab}(q_1) &= \frac{2}{\sin^2 \theta_1} \\ \omega_{ab}(q_2) &= \frac{2}{\sin^2 \theta_2} \\ \omega_{ab}(k) &= \frac{2}{\sin^2 \theta_k} \\ \omega_{aq_1}(k) &= \frac{(1 - \cos \theta_1)}{(1 - \cos \theta_k) (1 - \sin \theta_1 \sin \theta_k \cos \phi_k - \cos \theta_1 \cos \theta_k)} \\ \omega_{bq_1}(k) &= \frac{(1 + \cos \theta_1)}{(1 + \cos \theta_k) (1 - \sin \theta_1 \sin \theta_k \cos \phi_k - \cos \theta_1 \cos \theta_k)} \\ &\vdots \\ &\text{etc.} \end{aligned} \quad (2.29)$$

The relevant traces over colour factors for the Σ_1 calculation are

$$\begin{aligned} \text{Tr} \left(\mathbf{T}_a^0 \cdot \mathbf{T}_b^0 \mathbf{T}_a^0 \cdot \mathbf{T}_b^0 \right) &= N_c C_F^2 \\ \text{Tr} \left(\mathbf{T}_a^1 \cdot \mathbf{T}_b^1 \mathbf{T}_a^0 \cdot \mathbf{T}_b^0 \right) &= -\frac{C_F}{2} \\ \text{Tr} \left(\mathbf{T}_a^1 \cdot \mathbf{T}_q^1 \mathbf{T}_a^0 \cdot \mathbf{T}_b^0 \right) &= \text{Tr} \left(\mathbf{T}_b^1 \cdot \mathbf{T}_q^1 \mathbf{T}_a^0 \cdot \mathbf{T}_b^0 \right) = N_c C_F^2 + \frac{C_F}{2}, \end{aligned} \quad (2.30)$$

where the notation \mathbf{T}_a^i denotes that the colour-charge operator, acts on a $(2+i)$ -parton object. Lastly, we write the result of the integral over the azimuthal angle of the virtual exchange

$$\int_0^{2\pi} \frac{1}{(1 - \sin \theta_1 \sin \theta_2 \cos \phi - \cos \theta_1 \cos \theta_2)} \frac{d\phi}{2\pi} = \frac{1}{|\cos \theta_1 - \cos \theta_2|}. \quad (2.31)$$

Expanding out Eq. 2.26 gives

$$\begin{aligned} \Sigma_1(\rho) = & \frac{1}{N_c} \left(\frac{\alpha_s}{\pi} \right)^2 \int_{\text{in}} \frac{d\Omega_k}{4\pi} \int_{\rho}^Q \frac{dE_1}{E_1} \int_{\text{out}} \frac{d\Omega_1}{4\pi} \left[\right. \\ & - 4\omega_{ab}(q_1) \int_{\rho}^{E_1} \frac{dE_k}{E_k} \text{Tr} \left(\mathbf{T}_a^0 \cdot \mathbf{T}_b^0 \left(\mathbf{T}_a^1 \cdot \mathbf{T}_{q_1}^1 \omega_{aq_1}(k) \right. \right. \\ & \quad \left. \left. + \mathbf{T}_b^1 \cdot \mathbf{T}_{q_1}^1 \omega_{bq_1}(k) + \mathbf{T}_a^1 \cdot \mathbf{T}_b^1 \omega_{aq_1}(k) \right) \right) \\ & - 4\omega_{ab}(q_1) \int_{E_1}^Q \frac{dE_k}{E_k} \omega_{ab}(k) \text{Tr} \left(\mathbf{T}_a^0 \cdot \mathbf{T}_b^0 \mathbf{T}_a^0 \cdot \mathbf{T}_b^0 \right) \\ & + 2\omega_{ab}(q_1) \int_{\rho}^{E_1} \frac{dE_k}{E_k} \omega_{ab}(k) \text{Tr} \left(\mathbf{T}_a^0 \cdot \mathbf{T}_b^0 \mathbf{T}_a^0 \cdot \mathbf{T}_b^0 \right) \\ & + 2\omega_{ab}(q_1) \int_{E_1}^Q \frac{dE_k}{E_k} \omega_{ab}(k) \text{Tr} \left(\mathbf{T}_a^0 \cdot \mathbf{T}_b^0 \mathbf{T}_a^0 \cdot \mathbf{T}_b^0 \right) \\ & \left. + 2\omega_{ab}(q_1) \int_{\rho}^Q \frac{dE_k}{E_k} \omega_{ab}(k) \text{Tr} \left(\mathbf{T}_a^0 \cdot \mathbf{T}_b^0 \mathbf{T}_a^0 \cdot \mathbf{T}_b^0 \right) \right], \quad (2.32) \end{aligned}$$

reducing to

$$\begin{aligned} \Sigma_1(\rho) = & -\frac{4}{N_c} \left(\frac{\alpha_s}{\pi} \right)^2 \int_{\rho}^Q \frac{dE_1}{E_1} \int_{\text{out}} \frac{d\Omega_1}{4\pi} \frac{dE_k}{E_k} \int_{\text{out}} \frac{d\Omega_k}{4\pi} \\ & \times \text{Tr} \left[\omega_{ab}(q_1) \mathbf{T}_a^0 \cdot \mathbf{T}_b^0 \left(\omega_{aq_1}(k) \mathbf{T}_a^1 \cdot \mathbf{T}_{q_1}^1 + \omega_{bq_1}(k) \mathbf{T}_b^1 \cdot \mathbf{T}_{q_1}^1 \right. \right. \\ & \quad \left. \left. + \omega_{ab}(k) \left(\mathbf{T}_a^1 \cdot \mathbf{T}_b^1 - \mathbf{T}_a^0 \cdot \mathbf{T}_b^0 \right) \right) \right]. \quad (2.33) \end{aligned}$$

We employ the colour traces and azimuthal integral to arrive at

$$\begin{aligned}
\Sigma_1(\rho) &= -N_c C_F \left(\frac{\alpha_s}{\pi}\right)^2 \int_\rho^Q \frac{dE_1}{E_1} \int_{-1}^0 \frac{d \cos \theta_1}{\sin^2 \theta_1} \int_\rho^{E_1} \frac{dE_k}{E_k} \int_0^1 \frac{d \cos \theta_k}{\sin^2 \theta_k} \\
&\times \left[\text{Tr} \left(\mathbf{T}_a^1 \cdot \mathbf{T}_{q_1}^1 \mathbf{T}_a^0 \cdot \mathbf{T}_b^0 \right) \frac{(1 - \cos \theta_1)(1 + \cos \theta_k)}{\cos \theta_k - \cos \theta_1} \right. \\
&\quad + \text{Tr} \left(\mathbf{T}_b^1 \cdot \mathbf{T}_{q_1}^1 \mathbf{T}_a^0 \cdot \mathbf{T}_b^0 \right) \frac{(1 - \cos \theta_k)(1 + \cos \theta_1)}{\cos \theta_k - \cos \theta_1} \\
&\quad \left. + 2 \text{Tr} \left(\left(\mathbf{T}_a^1 \cdot \mathbf{T}_b^1 - \mathbf{T}_a^0 \cdot \mathbf{T}_b^0 \right) \mathbf{T}_a^0 \cdot \mathbf{T}_b^0 \right) \right] \quad (2.34)
\end{aligned}$$

$$\begin{aligned}
&= -N_c C_F \left(\frac{\alpha_s}{\pi}\right)^2 \ln^2 \left(\frac{Q}{\rho} \right) \int_{-1}^0 d \cos \theta_1 \int_0^1 d \cos \theta_k \\
&\quad \times \frac{1}{(1 - \cos \theta_1)(1 + \cos \theta_k)(\cos \theta_k - \cos \theta_1)}, \quad (2.35)
\end{aligned}$$

which gives

$$\Sigma_1(\rho) = -\frac{N_c C_F}{2} \left(\frac{\alpha_s}{\pi}\right)^2 \ln^2 \left(\frac{Q}{\rho} \right) \zeta(2), \quad (2.36)$$

where $\zeta(x)$ is the Riemann zeta function,

$$\zeta(x) = \sum_{n=1}^{\infty} n^{-x} \quad (2.37)$$

such that $\zeta(2) = \pi^2/6$ and $\zeta(3) \simeq 1.20205$, the so-called Apéry's constant. The result in Eq. 2.36 is equal to the result presented in [96]. The same methodology can be used to compute both Σ_2 and Σ_1 at order α_s^3 with their summed result

giving the non-global contribution. They are as follows

$$\begin{aligned}
\Sigma_2(\rho) &= \frac{1}{N_c} \int_{\text{out}} \frac{\alpha_s}{\pi} \int_{\rho}^Q \frac{dE_1}{E_1} \frac{d\Omega_1}{4\pi} \int_{\text{out}} \frac{\alpha_s}{\pi} \int_{\rho}^{E_1} \frac{dE_2}{E_2} \frac{d\Omega_2}{4\pi} \frac{\alpha_s}{\pi} \int_{\text{in}} \frac{d\Omega_k}{4\pi} \int_{\rho}^{E_2} \frac{dE_k}{E_k} \left[\right. \\
&\quad - 4C_A^2 C_F^2 (\omega_{ab}(q_1)\omega_{ab}(q_2)\omega_{aq_1}(k) + \omega_{ab}(q_1)\omega_{ab}(q_2)\omega_{bq_1}(k)) \\
&\quad - 2C_A C_F (\omega_{ab}(q_1)\omega_{ab}(q_2)\omega_{aq_2}(k) + \omega_{ab}(q_1)\omega_{ab}(q_2)\omega_{bq_2}(k)) \\
&\quad + 2C_A^3 C_F (\omega_{ab}(q_1)\omega_{ab}(q_2)\omega_{ab}(k) - \omega_{ab}(q_1)\omega_{aq_1}(q_2)\omega_{aq_1}(k) \\
&\quad + \omega_{ab}(q_1)\omega_{aq_1}(q_2)\omega_{aq_2}(k) + \omega_{ab}(q_1)\omega_{aq_1}(q_2)\omega_{q_1q_2}(k) \\
&\quad - \omega_{ab}(q_1)\omega_{bq_1}(q_2)\omega_{bq_1}(k) + \omega_{ab}(q_1)\omega_{bq_1}(q_2)\omega_{bq_2}(k) \\
&\quad \left. + \omega_{ab}(q_1)\omega_{bq_1}(q_2)\omega_{q_1q_2}(k) \right] \\
&= -\frac{N_c^2 C_F}{3!} \left(\frac{\alpha_s}{\pi}\right)^3 \ln^3\left(\frac{Q}{\rho}\right) \zeta(3). \tag{2.38}
\end{aligned}$$

and

$$\begin{aligned}
\Sigma_1^{\alpha_s^3}(\rho) &= \frac{1}{N} \int_{\text{out}} \frac{\alpha_s}{\pi} \int_{\rho}^Q \frac{dE_1}{E_1} \frac{d\Omega_1}{4\pi} \int_{\text{in}} \frac{\alpha_s}{\pi} \int_{\rho}^{E_1} \frac{dE_2}{E_2} \frac{d\Omega_2}{4\pi} \frac{\alpha_s}{\pi} \int_{\text{in}} \frac{d\Omega_k}{4\pi} \int_{\rho}^{E_2} \frac{dE_k}{E_k} \left[\right. \\
&\quad C_A C_F (\omega_{ab}(q_1)\omega_{ab}(q_2)(\omega_{aq_1}(k) + \omega_{bq_1}(k) - \omega_{ab}(k)) \\
&\quad + \omega_{ab}(q_1)\omega_{ab}(k)(\omega_{aq_1}(q_2) + \omega_{bq_1}(q_2) - \omega_{ab}(q_2))) \\
&\quad + C_A^3 C_F \omega_{ab}(q_1)(\omega_{ab}(q_2)\omega_{ab}(k) - \omega_{a1}(q_2)\omega_{aq_1}(k) \\
&\quad - \omega_{bq_1}(q_2)\omega_{bq_1}(k) - \omega_{bq_1}(q_2)\omega_{aq_1}(k) - \omega_{aq_1}(q_2)\omega_{bq_1}(k)) \left. \right] \\
&= \frac{2N_c^2 C_F}{3!} \left(\frac{\alpha_s}{\pi}\right)^3 \ln^3\left(\frac{Q}{\rho}\right) \zeta(3). \tag{2.39}
\end{aligned}$$

This result is in agreement with the work of Delenda & Khelifa-Kerfa [104, 105]. Having outlined our general algorithm in Eq. 2.1 and validated its ability to compute the non-global contributions to the Hemisphere Jet-Mass observable, we shall proceed to explore the groundwork for its implementation into a Monte Carlo code. We begin by discussing the colour flow basis.

2.2 Colour Mechanics

In practical calculations, the colour algebra becomes rapidly intractable for only a handful of real gluon emissions. To automate the calculation of the algo-

rithm in Eq. 2.1, we must first identify a basis which is well-suited to a Monte Carlo implementation. One such basis is the colour flow basis [98]. In addition to being similar to the way in which colour is treated in dipole parton shower algorithms [106–108], it has led to efficient implementations of tree-level amplitudes [97, 109] and constitutes the initial condition to other aspects of event generators such as hadronisation models [54, 110]. The colour flow basis is also well-suited to sampling over colour assignments (where each basis tensor describes a single colour assignment) if the number of external partons is large [97], removing the need for computationally-intensive matrix multiplications.

We shall review the colour flow basis and use it to present a systematic procedure to calculate the colour traces that result from Eq. 2.1. Moreover, we determine the colour structures encountered in calculating this trace. Using these results we identify the leading-colour contributions and re-derive the Banfi-Marchesini-Syme equation [92]. Our formalism is more general than this however and can systematically perform summation of contributions enhanced by the 't Hooft coupling, $\alpha_s N_c \sim 1$ [45], providing successive approximations which are parametrically suppressed by powers of $1/N_c$. We subsequently discuss the first subleading-colour corrections.

2.2.1 Colour Flow Basis

In Section 1.5 we laid out the colour flow representation for QCD, whereby instead of decomposing the gluon field using the fundamental-representation matrices, we work directly with an $N_c \times N_c$ matrix field to describe the gluon. As such, the colour part of the $SU(N_c)$ gluon propagator can be split into a $U(N_c)$ gluon propagator (with an associated colour and anti-colour index) and a $U(1)$ gluon propagator. Quarks have an associated colour index, whilst anti-quarks have an associated anti-colour index.

And so, the colour part of QCD calculations becomes a matter of manipulating the flow of colour between colour and anti-colour indices. To this end, we begin this section by collating some key results regarding the colour flow basis. Firstly we assign a colour or anti colour index, c_i or \bar{c}_i , to each external leg i of an arbitrary scattering amplitude. Whilst outgoing quarks carry colour (with an associated index), incoming quarks carry anti colour and vice versa for anti-quarks. The colour indices are labelled from 1 to n and are assigned to the first n colour-carrying partons. We denote the colour index of a particle, i , which only carries anti colour, as $c_i = 0$. A corresponding labelling holds for

anti colour indices, where $\bar{c}_i = 0$ if i only carries colour. An example of this labelling for a four-parton amplitude containing the partons $qg\bar{g}\bar{q}$ is illustrated in Table. 2.1.

i	c_i	\bar{c}_i	λ_i	$\bar{\lambda}_i$
1	1	0	$\sqrt{T_R}$	0
2	2	1	$\sqrt{T_R}$	$\sqrt{T_R}$
3	3	2	$\sqrt{T_R}$	$\sqrt{T_R}$
4	0	3	0	$\sqrt{T_R}$

TABLE 2.1: The specifications of the correspondence between the external leg indices, i , and their colour (c_i) or anti colour (\bar{c}_i) lines for the four-parton amplitude containing the partons $qg\bar{g}\bar{q}$, depicted in Figure 2.2.

The objects c_i and \bar{c}_i act as mappings between the external leg index i , and the corresponding colour or anti colour index. The inverse of this operator, c_α^{-1} , relates the colour index, α , back to the corresponding leg index. This convention shall be used throughout this work.

We denote the set of all basis tensors in the colour flow basis as $\{|\sigma\rangle\}$. Each basis tensor is labelled by a permutation, σ , of the anti colour indices relative to the colour indices:

$$|\sigma\rangle = \left| \begin{array}{ccc} 1 & \cdots & n \\ \sigma(1) & \cdots & \sigma(n) \end{array} \right\rangle = \delta_{\bar{\alpha}_{\sigma(1)}^{\alpha_1}} \cdots \delta_{\bar{\alpha}_{\sigma(n)}^{\alpha_n}} \quad (2.40)$$

where the $\alpha_{1\dots n}$ and $\bar{\alpha}_{1\dots n}$ are fundamental and anti-fundamental indices assigned to the colour and anti colour legs. They take values in the actual number of colours $1, \dots, N_c$ and there are $n = n_q + n_g = n_{\bar{q}} + n_{\bar{g}}$ possible colour and anti colour lines. Each colour line connects to an anti colour line to form a colour flow, of which there are $n!$ potential colour flow arrangements (corresponding to $n!$ basis tensors). This is a natural way to decompose QCD amplitudes, based on the flow of colour, giving a simple physical interpretation. Our convention is to keep the ordering of colour indices fixed (on the top row of Eq. 2.40). As such, we will often use a more compact notation, e.g.

$$\left| \begin{array}{ccc} 1 & 2 & 3 \\ 2 & 1 & 3 \end{array} \right\rangle \equiv |213\rangle. \quad (2.41)$$

Inner products of basis tensors are given by

$$\langle \sigma | \tau \rangle = \delta_{\bar{\alpha}_{\sigma(1)}^{\alpha_1}} \cdots \delta_{\bar{\alpha}_{\sigma(n)}^{\alpha_n}} \delta_{\alpha_1}^{\bar{\alpha}_{\tau(1)}} \cdots \delta_{\alpha_n}^{\bar{\alpha}_{\tau(n)}} = N_c^{n - \#(\sigma, \tau)}, \quad (2.42)$$

where $\#(\sigma, \tau)$ is used as shorthand to denote the number of transpositions by which the permutations σ and τ differ. Defining a swap to be the exchange of two anti colour indices in σ , the number of transpositions is the minimum number of consecutive swaps that map σ onto τ . This is equivalent to the number of colour flows, n , minus the number of "loops" formed when contracting the Kronecker deltas in Eq. 2.42. This is also diagrammatically illustrated in the lower pane of Figure 2.2.

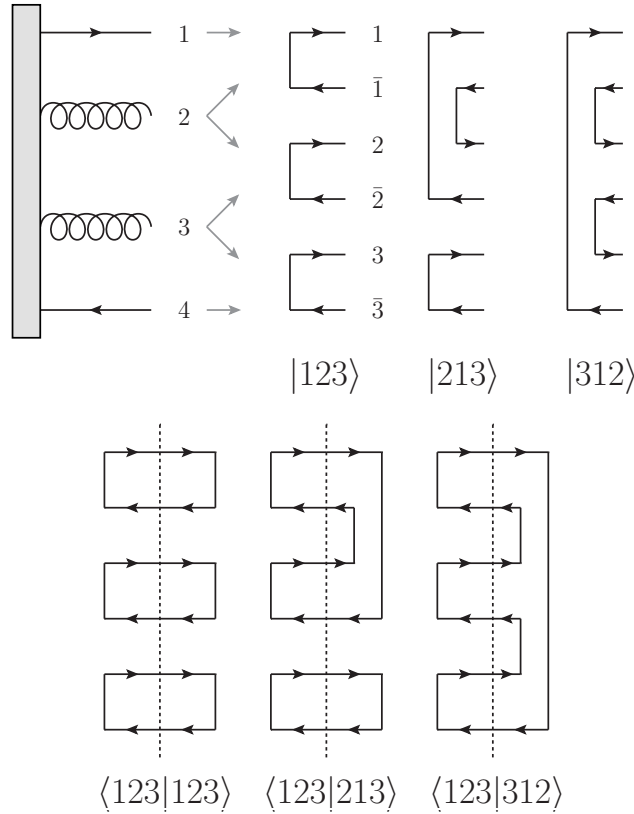


FIGURE 2.2: Diagrammatic representation of the colour flow basis tensors and their inner products. The top half of the figure presents a four-parton amplitude with $qg\bar{g}q$ leg content and three out of the six possible basis tensors which describe potential colour arrangements. Grey arrows indicate how the external leg indices, $i = 1, \dots, 4$ are mapped onto colour and anti colour indices. The lower pane of this figure pictorially represents the contraction of the Kronecker deltas in the calculation of inner products between basis tensors. These are elements of the scalar product matrix described later and are equal to N_c to the power of the number of colour flows, n , minus the number of loops formed after contraction. Figure modified from [99].

As an example, Figure 2.2 presents three of the six possible colour arrangements representing the four-parton state on the left-hand side, involving a quark, anti-quark and two gluons. In anticipation of the results in subsequent sections, we introduce the binary variables λ_i and $\bar{\lambda}_i$. They take the values: $\lambda_i = \sqrt{T_R}$, $\bar{\lambda}_i = 0$ for an outgoing quark; $\lambda_i = 0$, $\bar{\lambda}_i = \sqrt{T_R}$ for an outgoing anti-quark and $\lambda_i = \sqrt{T_R}$, $\bar{\lambda}_i = \sqrt{T_R}$ for a gluon. The value of T_R is equal to 1/2 in the case of QCD. These variables and the correspondence between external leg and colour indices are summarised in Table 2.1.

2.2.2 Working In A Non-Orthogonal Colour Basis

A colour operator, \mathbf{O} , can be written as $\mathbf{O} = \sum_{\tau,\sigma} \mathcal{O}_{\tau\sigma} |\tau\rangle \langle\sigma|$ in any particular basis. In the context of the colour flow basis our basis tensors are non-orthonormal and as such, the coefficients $\mathcal{O}_{\tau\sigma}$, are not the matrix elements of the operator \mathbf{O} .

We wish in general to compute objects of the form outlined in Eq. 2.1:

$$\text{Tr}(\mathbf{O}) = \langle H | \mathbf{R}^\dagger \mathbf{R} | H \rangle \quad (2.43)$$

where $\mathbf{O} = \mathbf{RHR}^\dagger$, $\mathbf{H} = |H\rangle \langle H|$ and \mathbf{R} represents an operator which evolves the colour flow (this could be an emission or Sudakov operator, or a chain of them). $|H\rangle$ represents the hard scattering process.

As we want to represent these objects in the colour flow basis, which is non-orthonormal, we can introduce dual basis tensors, $[\alpha|$, such that

$$\langle\alpha| \beta\rangle = [\alpha| \beta\rangle = \delta_{\alpha\beta}, \quad (2.44)$$

with an identity operator

$$\sum_{\alpha} |\alpha\rangle [\alpha| = \sum_{\alpha} [\alpha| \langle\alpha| = \mathbf{1}. \quad (2.45)$$

Using Eq. 2.45, we can now write our operator, \mathbf{O} , as

$$\sum_{\sigma,\tau} [\sigma| \mathbf{O} |\tau\rangle |\sigma\rangle \langle\tau| \quad (2.46)$$

leading to a form for Eq. 2.43 of

$$\text{Tr}(\mathbf{O}) = \sum_{\sigma,\tau} \text{Tr}([\sigma| \mathbf{O} |\tau\rangle \langle\tau| \sigma\rangle). \quad (2.47)$$

We reiterate that \mathbf{O} can be a chain of successive soft-gluon evolution operators. As such we can evaluate these matrix elements by evolving inwards from the external states towards the hard scattering. Firstly we can make manifest, the outermost evolution operators, by writing \mathbf{O} as

$$\mathbf{O} = \mathbf{R}_1 \mathbf{O}' \mathbf{R}_2. \quad (2.48)$$

Here, \mathbf{R}_i are the constituent colour charge (or colour charge product) operators within any given evolution operator, the so-called colour line operators, which constitute a unique map from one basis tensor to another. In this case, only one term in the sum in Eq. 2.45 contributes, which means

$$\mathbf{R}_2 |\alpha\rangle = C_{R_2}^{\alpha,\beta} |\beta\rangle, \quad (2.49)$$

for example, where the coefficient factor has the form $C_{R_2}^{\alpha,\beta} = [\beta | \mathbf{R}_2 | \alpha]$. A similar relation holds true for \mathbf{R}_1 . The computational objects of interest to us, are the matrix elements $[\sigma | \mathbf{O} | \tau]$ and using Eq. 2.48 we find:

$$\begin{aligned} [\sigma | \mathbf{R}_1 \mathbf{O}' | \tau] &= \sum_{\alpha} [\sigma | \mathbf{R}_1 | \alpha] [\alpha | \mathbf{O}' | \tau], \\ &= \sum_{\alpha} [\sigma | \beta] C_{R_1}^{\alpha,\beta} [\alpha | \mathbf{O}' | \tau], \\ &= \sum_{\alpha} \delta_{\sigma\beta} C_{R_1}^{\alpha,\beta} [\alpha | \mathbf{O}' | \tau], \\ &= C_{R_1}^{\alpha,\sigma} [\alpha | \mathbf{O}' | \tau], \end{aligned} \quad (2.50)$$

where we have suppressed the concomitant contribution from \mathbf{R}_2 for notational brevity, although it follows a similar logic. One can see that it is possible to recursively perform this operation to strip-off evolution operators from \mathbf{O} , leaving coefficients and reduced matrix elements in their place. Anticipating the pattern of this process, one can also act in reverse and build an evolution cascade around the hard scattering, multiplying by operator matrix elements in the amplitude and conjugate and summing over their identifying basis tensors. This is discussed in more detail in Section 4.1.

2.3 Amplitudes And Matrix Elements

In the last section, we discussed how to compute the trace of an arbitrarily long chain of evolution operators. The key result is that by employing a dual basis, one can insert unit operators between each evolution operator leaving behind

a coefficient factor. It is the focus of this section to calculate these coefficient factors for the operators relevant to Eq. 2.1. We express amplitudes as

$$|\mathcal{A}\rangle = \sum_{\sigma} \mathcal{A}_{\sigma} |\sigma\rangle, \quad (2.51)$$

where σ labels a sum over the individual basis tensors in the set $\{\sigma\}$, at a given dimension in colour space. A basis-independent operator can be written as

$$\mathbf{A} = \sum_{\tau, \sigma} \mathcal{A}_{\tau\sigma} |\tau\rangle \langle\sigma|, \quad (2.52)$$

where the coefficients $\mathcal{A}_{\tau\sigma}$ are not matrix elements of the operators \mathbf{A} as the colour flow basis is non-orthonormal. However,

$$\mathcal{A}_{\tau\sigma} \equiv [\tau | \mathbf{A} | \sigma], \quad (2.53)$$

and the evolution and traces in colour space can be performed in terms of complex matrices with elements $\mathcal{A}_{\tau\sigma}$. Eq. 2.47 for the trace of operators represented by \mathbf{A} is then

$$\text{Tr}(\mathbf{A}) = \text{Tr}(\mathcal{A}\mathcal{S}) = \sum_{\tau, \sigma} [\tau | \mathbf{A} | \sigma] \langle\sigma | \tau\rangle, \quad (2.54)$$

where \mathcal{S} is the scalar product matrix with elements $S_{\tau\sigma} = \langle\tau | \sigma\rangle$.

The two important colour operators in Eq. 2.1 are the colour charge operator, \mathbf{T}_i , in the emission operator and the colour charge products, $\mathbf{T}_i \cdot \mathbf{T}_j$, in the soft-gluon anomalous dimension operator. We shall decompose the colour charge operator associated with an external leg i as

$$\mathbf{T}_i = \lambda_i \mathbf{t}_{c_i} + \bar{\lambda}_i \bar{\mathbf{t}}_{c_i} - \frac{1}{N_c} (\lambda_i - \bar{\lambda}_i) \mathbf{s}, \quad (2.55)$$

where the effect of each colour-line operator \mathbf{t} , $\bar{\mathbf{t}}$ and \mathbf{s} on a basis tensor is defined as follows. Starting with \mathbf{t}_{c_i} :

$$\mathbf{t}_{c_i} |\sigma\rangle = \mathbf{t}_{c_i} \left| \begin{array}{cccccc} 1 & \dots & c_i & \dots & n \\ \sigma(1) & \dots & \sigma(c_i) & \dots & \sigma(n) \end{array} \right\rangle \quad (2.56)$$

$$= \left| \begin{array}{cccccc} 1 & \dots & c_i & \dots & n & n+1 \\ \sigma(1) & \dots & n+1 & \dots & \sigma(n) & \sigma(c_i) \end{array} \right\rangle, \quad (2.57)$$

i.e. a new colour and anti colour line, labelled by $n+1$, are added. The anti colour lines $\sigma(c_i)$ and $n+1$ are then swapped. An illustration of this is pre-

sented in Figure 2.3a. Emitting off an anti colour line with operator $\bar{\mathbf{t}}$ is equivalent to emitting off the colour line to which it is connected with an operator \mathbf{t} . Therefore, we can write

$$\bar{\mathbf{t}}_{\bar{c}_i} |\sigma\rangle = \mathbf{t}_{\sigma^{-1}(\bar{c}_i)} |\sigma\rangle, \quad (2.58)$$

where the inverse of the basis tensor σ^{-1} is defined such that $c_i = \sigma^{-1}(\sigma(c_i))$. The colour-line operator \mathbf{s} is the U(1) contribution to the gluon propagator and is unphysical, carrying a $1/N_c$ factor. Its action on a basis tensor is

$$\mathbf{s} |\sigma\rangle = \mathbf{s} \left| \begin{array}{cccc} 1 & \dots & \dots & n \\ \sigma(1) & \dots & \dots & \sigma(n) \end{array} \right\rangle = \left| \begin{array}{cccc} 1 & \dots & \dots & n & n+1 \\ \sigma(1) & \dots & \dots & \sigma(n) & n+1 \end{array} \right\rangle, \quad (2.59)$$

pictorially represented in Figure 2.3b.

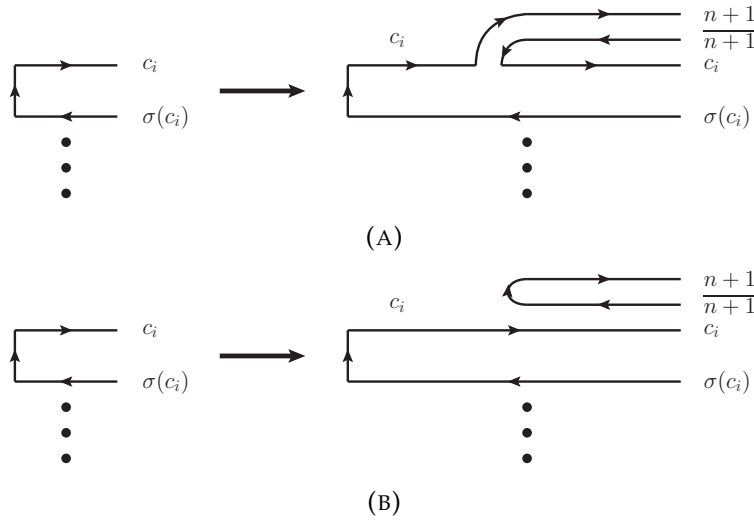


FIGURE 2.3: Pictorial representation of the \mathbf{t}_{c_i} and $\bar{\mathbf{t}}_{\bar{c}_i}$ operators in (A) and the \mathbf{s} operator in (B). Figure from [111].

It is worth noting here, that the \mathbf{t} and $\bar{\mathbf{t}}$ operators can be written as a combination of two operations:

$$\mathbf{t}_\alpha |\sigma\rangle = \mathbf{s}_{\alpha, n+1} \mathbf{s} |\sigma\rangle, \quad (2.60)$$

where $\mathbf{s}_{\alpha\beta}$ exchanges the anti colour indices $\sigma(\alpha)$ and $\sigma(\beta)$ in a basis tensor. Eq. 2.60 represents the creation of a new colour flow, $n+1$, with a subsequent swapping of the new anti colour line with another, $\sigma(\alpha)$. This is instructive as it shows that we cannot map any two distinct basis tensors onto the same basis tensor through the action of any of the colour-line operators.

With a view to categorising emission contributions in both the amplitude and conjugate-amplitude, it is useful to explore the behaviour of combinations of colour-line operators acting on two tensors, $|\sigma\rangle$ and $|\tau\rangle$ which differ by n trans-

positions. If we act on both $|\sigma\rangle$ and $|\tau\rangle$ with an \mathbf{s} operator, the two resultant tensors will still differ by the original n transpositions, but collect a $1/N_c^2$ prefactor. Acting on either $|\sigma\rangle$ or $|\tau\rangle$ with an \mathbf{s} operator and acting on the other with \mathbf{t}_α , the resultant tensors will differ by $n + 1$ transpositions and have a prefactor of $1/N_c$. Lastly the action of $\mathbf{t}_\alpha |\sigma\rangle$ and $\mathbf{t}_\beta |\tau\rangle$, where $\alpha \neq \beta$, will result in tensors which differ by the original n transpositions if $\sigma(\alpha) = \tau(\beta)$. In the case that $\sigma(\alpha) \neq \tau(\beta)$, the new tensors will differ by $n + 2$ transpositions.

The colour charge products in the soft-gluon anomalous dimension operator require the description of colour-line products. These are $\mathbf{s} \cdot \mathbf{t}_\alpha = \mathbf{t}_\alpha \cdot \mathbf{s} = \mathbf{1}$ and $\mathbf{s} \cdot \mathbf{s} = N_c \mathbf{1}$. The same results are true if we replace \mathbf{t} by $\bar{\mathbf{t}}$ due to relation in Eq. 2.58. The product $\mathbf{t}_\alpha \cdot \mathbf{t}_\beta$ is equal to $\mathbf{t}_\beta \cdot \mathbf{t}_\alpha$ and can take two values. If we define $\sigma_{\alpha\beta}$ to denote swapping the elements α and β in the permutation σ , then $\mathbf{t}_\alpha \cdot \mathbf{t}_\beta |\sigma\rangle = |\sigma_{(\alpha\beta)}\rangle$. This result also holds true when we replace \mathbf{t} by $\bar{\mathbf{t}}$. However, there is another subtle case in which $\alpha = \sigma^{-1}(\bar{\beta})$ for colour reconnectors, necessarily of the form $\mathbf{t}_\alpha \cdot \bar{\mathbf{t}}_\beta$. In this scenario $\mathbf{t}_\alpha \cdot \bar{\mathbf{t}}_\beta |\sigma\rangle = N_c |\sigma\rangle$. These results are summarised diagrammatically in Figure 2.4.

We recall the result in Eq. 2.49, that

$$\mathbf{R} |\sigma\rangle = [\tau | \mathbf{R} |\sigma\rangle | \tau\rangle \quad (2.61)$$

and use the defined behaviour of the colour-line operators to write the coefficient factor for the colour charge operator:

$$[\sigma | \mathbf{T}_i | \alpha\rangle = \delta_{\alpha, \sigma \setminus n} \left(\lambda_i \delta_{c_i \sigma^{-1}(\bar{c}_n)} - \bar{\lambda}_i \delta_{\bar{c}_i \sigma^{-1}(c_n)} - \frac{1}{N_c} (\lambda_i - \bar{\lambda}_i) \delta_{c_n \sigma^{-1}(\bar{c}_n)} \right), \quad (2.62)$$

where the colour and anti colour line associated with the emitted particle, n , is labelled by c_n and \bar{c}_n respectively. $\delta_{c_i \sigma^{-1}(\bar{c}_n)}$ constrains the colour line corresponding to particle i to form a colour flow with \bar{c}_n . The object $\sigma \setminus n$ denotes the permutation in which c_n and \bar{c}_n are removed and their colour flows merged, i.e. their connecting anti colour and colour lines now form their own colour flow. More explicitly,

$$\begin{aligned} & \left(\begin{array}{cccccc} 1 & \dots & c_n & \dots & \sigma^{-1}(\bar{c}_n) & \dots & m \\ \sigma(1) & \dots & \sigma(c_n) & \dots & \bar{c}_n & \dots & \sigma(m) \end{array} \right) \setminus n \\ & = \left(\begin{array}{cccccc} 1 & \dots & \sigma^{-1}(\bar{c}_n) & \dots & m \\ \sigma(1) & \dots & \sigma(c_n) & \dots & \sigma(m) \end{array} \right). \quad (2.63) \end{aligned}$$

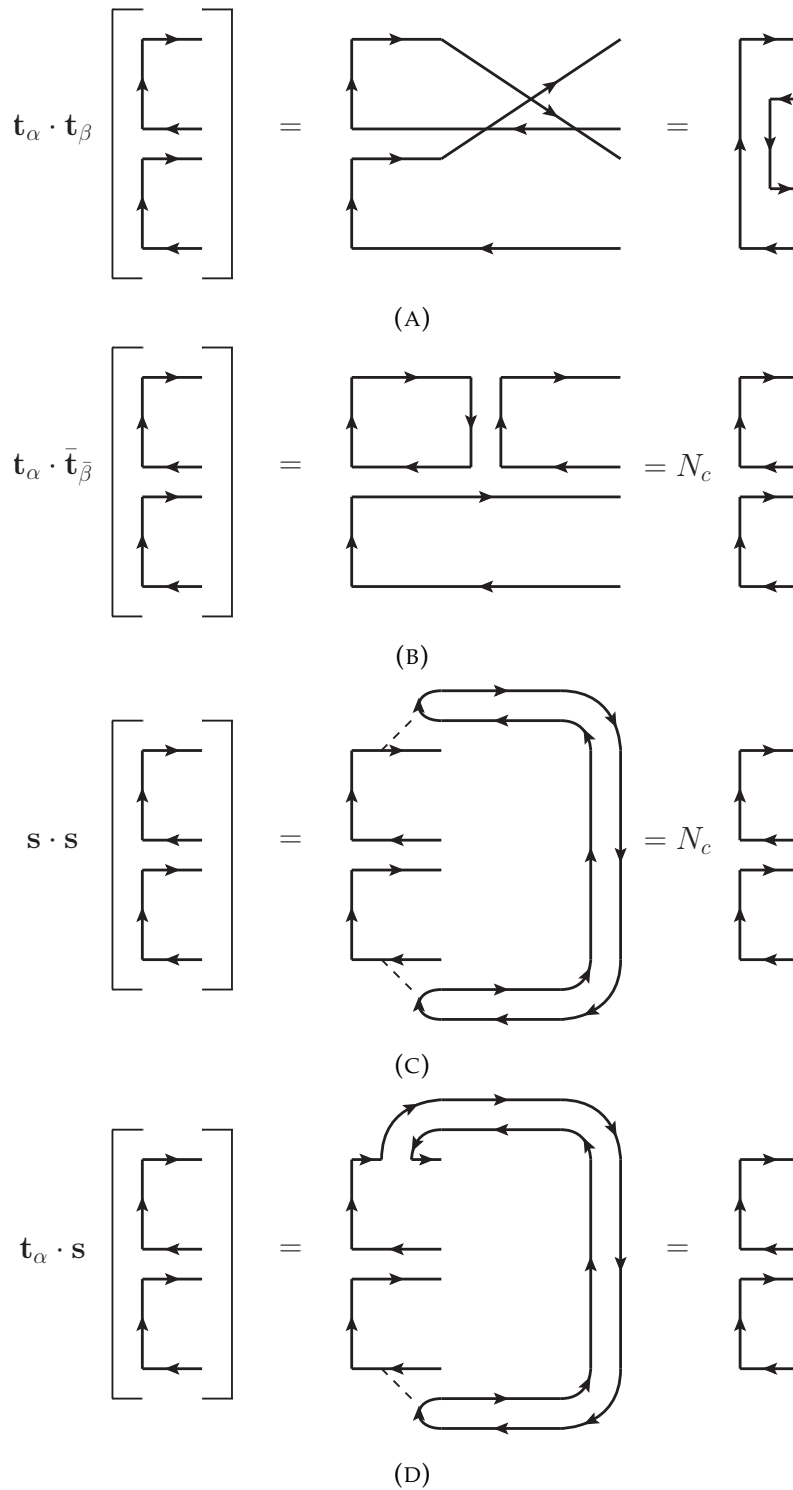


FIGURE 2.4: Pictorial representation of the $\mathbf{t}_\alpha \cdot \mathbf{t}_\beta$ colour reconnector in (A), the $\mathbf{t}_\alpha \cdot \bar{\mathbf{t}}_\beta$ colour reconnector in the case that α and β are colour connected (B), the $\mathbf{s} \cdot \mathbf{s}$ colour reconnector in (C) and $\mathbf{t}_\alpha \cdot \mathbf{s}$ colour reconnector in (D). Figure from [111].

Considering the colour evolution of an emission operator and its conjugate on

an amplitude \mathbf{A} , and using Eq. 2.50, we must evaluate terms of the form

$$[\sigma | \mathbf{T}_i \mathbf{A} \mathbf{T}_j | \tau] = \sum_{\alpha, \beta} [\sigma | \mathbf{T}_i | \alpha] \langle \beta | \mathbf{T}_j | \tau \rangle [\alpha | \mathbf{A} | \beta]. \quad (2.64)$$

Using Eq. 2.62, we find

$$\begin{aligned} [\sigma | \mathbf{T}_i \mathbf{A} \mathbf{T}_j | \tau] = & \left\{ \left(-\lambda_i \bar{\lambda}_j \delta_{c_i \sigma^{-1}(\bar{c}_n)} \delta_{\bar{c}_j \tau(c_n)} - (i, \sigma \leftrightarrow j, \tau) \right) \right. \\ & + \lambda_i \lambda_j \delta_{c_i \sigma^{-1}(\bar{c}_n)} \delta_{c_j \tau^{-1}(\bar{c}_n)} + \bar{\lambda}_i \bar{\lambda}_j \delta_{\bar{c}_i \sigma(c_n)} \delta_{\bar{c}_j \tau(c_n)} \\ & - \frac{1}{N_c} \left(\lambda_i \delta_{c_i \sigma^{-1}(\bar{c}_n)} - \bar{\lambda}_i \delta_{\bar{c}_i \sigma(c_n)} \right) (\lambda_j - \bar{\lambda}_j) \delta_{c_n \tau^{-1}(\bar{c}_n)} \\ & - (i, \sigma \leftrightarrow j, \tau) \\ & \left. + \frac{1}{N_c^2} (\lambda_i - \bar{\lambda}_i) (\lambda_j - \bar{\lambda}_j) \delta_{c_n \sigma^{-1}(\bar{c}_n)} \delta_{c_n \tau^{-1}(\bar{c}_n)} \right\} \\ & \times [\tau \setminus n | \mathbf{A} | \sigma \setminus n]. \end{aligned} \quad (2.65)$$

The matrix element of the colour charge product, $\mathbf{T}_i \cdot \mathbf{T}_j$, for $i \neq j$ is

$$\begin{aligned} [\tau | \mathbf{T}_i \cdot \mathbf{T}_j | \sigma] = & -N_c \delta_{\tau \sigma} \left(\lambda_i \bar{\lambda}_j \delta_{c_i, \sigma^{-1}(\bar{c}_j)} + \lambda_j \bar{\lambda}_i \delta_{c_j, \sigma^{-1}(\bar{c}_i)} \right) \\ & - \frac{N_c \delta_{\tau \sigma}}{N_c^2} (\lambda_i - \bar{\lambda}_i) (\lambda_j - \bar{\lambda}_j) \\ & + \sum_{(ab)} \delta_{\tau(ab), \sigma} \left(\lambda_i \lambda_j \delta_{(ab), (c_i c_j)} + \bar{\lambda}_i \bar{\lambda}_j \delta_{(ab), (\sigma^{-1}(\bar{c}_i) \sigma^{-1}(\bar{c}_j))} \right. \\ & \left. - \lambda_i \bar{\lambda}_j \delta_{(ab), (c_i, \sigma^{-1}(\bar{c}_j))} - \lambda_j \bar{\lambda}_i \delta_{(ab), (c_j, \sigma^{-1}(\bar{c}_i))} \right). \end{aligned} \quad (2.66)$$

The notation of Eq. 2.66 requires some explanation: (ab) denotes an ordered pair of indices, i.e. (ab) becomes ba if $a > b$. Each of the four terms within the summation over ordered pairs, (ab) , can be written without summation after implementing the Kronecker deltas which constrain their colour flows. In this sense, the summation is cumbersome, but it ensures that none of the summed terms contribute in the case that the particles i and j are colour-connected in the tensor σ . By colour-connected we mean that the colour or anti colour line corresponding to particle i forms a colour flow with the anti colour or colour line corresponding to j . More precisely, $c_i = \sigma^{-1}(\bar{c}_j)$ or $c_j = \sigma^{-1}(\bar{c}_i)$. It is an important point that the off-diagonal elements in Eq. 2.66 are non-vanishing only if the permutations τ and σ differ by at-most one transposition.

2.3.1 Leading-Colour Contributions

Having stated the effects of colour line operators on a basis state, we have so far explored their products, and determined the matrix elements for the colour charge and colour charge product operators in Eq. 2.65 and 2.66. These are the key operators which determine the colour evolution of the emission and soft-gluon anomalous dimension matrix operators. In this section we shall turn our attention to organising the cross section as a series of leading powers in N_c , so that we can extract the strict-leading colour contributions and corrections to them. Firstly, we define an operation

$$\text{Leading}_{\tau\sigma}^{(l)}[\mathbf{A}] = \sum_{k=0}^l \mathcal{A}_{\tau\sigma} |_{1/N_c^k} \delta_{\#(\tau,\sigma),l-k}, \quad (2.67)$$

where

$$\mathcal{A}_{\tau\sigma} |_{1/N_c^k} \quad (2.68)$$

denotes those terms in the element $\mathcal{A}_{\tau\sigma}$ that are suppressed by a factor of N_c^k relative to the leading power present in $\mathcal{A}_{\tau\sigma}$. To be more explicit, for any given amplitude described by the operator \mathbf{A} , which can exist at any given point in an emission cascade, this operation recursively searches the chain of operators contained in \mathbf{A} to find the overall explicit $1/N_c^k$ contribution. Upon taking the trace of \mathbf{A} , there will be an additional $1/N_c^{l-k}$ suppression from the scalar product matrix due to σ and τ differing by $l-k$ transpositions. The latter is what is represented by the $\delta_{\#(\tau,\sigma),l-k}$ term. In other words, if \mathbf{A} is an operator in the colour space of n colour lines, then

$$\text{Tr} \left[\text{Leading}^{(l)}[\mathbf{A}] \right] \propto N_c^{n-l}. \quad (2.69)$$

The traces originating from the soft-gluon evolution in Eq. 2.19 can be broken down into two types:

$$\begin{aligned} & \text{Tr} \left[\mathbf{V}_n \mathbf{A}_n \mathbf{V}_n^\dagger \right], \\ & \text{Tr} \left[\mathbf{D}_n \mathbf{A}_{n-1} \mathbf{D}_n^\dagger \right], \end{aligned} \quad (2.70)$$

where we have subscripted the Sudakov and emission operator by the contextual multiplicity in which they act. As our focus is on the colour evolution, we subsume all physical constants and kinematic dependence in Eq. 2.3 and 2.6

into coefficients, so that

$$\begin{aligned} \mathbf{V}_n &= \exp \left(\sum_{i,j} \Omega_{ij}^{(n)} \mathbf{T}_i \cdot \mathbf{T}_j \right) \quad \text{where} \quad \Omega_{ij}^{(n)} = \frac{\alpha_s}{2\pi} \int_a^b \frac{dE_k}{E_k} \int \frac{d\Omega_k}{4\pi} \omega_{ij}(k), \\ \mathbf{D}_n &= \sum_i \omega_i^{(n)} \mathbf{T}_i \quad \text{where} \quad \omega_i^{(n)} = E_i \frac{p_i^\mu}{p_i \cdot q_n}. \end{aligned} \quad (2.71)$$

The leading-colour contributions of the virtual evolution operators are

$$\text{Leading}_{\tau\sigma}^{(0)} \delta_{\tau\sigma} \left[\mathbf{V}_n \mathbf{A}_n \mathbf{V}_n^\dagger \right] = \delta_{\tau\sigma} \left| V_\sigma^{(n)} \right|^2 \text{Leading}_{\tau\sigma}^{(0)} \left[\mathbf{A}_n \right], \quad (2.72)$$

where

$$V_\sigma^{(n)} = \exp \left(-N_c \sum_{i,j \text{ cc in } \sigma} \lambda_i \bar{\lambda}_j \left(\Omega_{ij}^{(n)} + \Omega_{ji}^{(n)} \right) \right). \quad (2.73)$$

The phrase cc in the summation over external legs i and j in Eq. 2.73 means ‘colour-connected’. Precisely, we only sum over external leg indices for which $c_i = \sigma^{-1}(\bar{c}_j)$ or $c_j = \sigma^{-1}(\bar{c}_i)$. Eq. 2.72 arises by considering only the leading diagonal terms in Eq. 2.66 and ignoring those terms which carry an explicit $1/N_c$ suppression. These are the $[\sigma | \mathbf{t}_\alpha \cdot \bar{\mathbf{t}}_\beta | \sigma \rangle$ contributions to the soft anomalous dimension matrix depicted in Figure 2.4b, where $\alpha = \sigma^{-1}(\bar{\beta})$. The two terms $\Omega_{ij}^{(n)}$ and $\Omega_{ji}^{(n)}$ account for the fact that the contribution results from both $\mathbf{T}_i \cdot \mathbf{T}_j$ and $\mathbf{T}_j \cdot \mathbf{T}_i$ in the unordered sum of Eq. 2.71.

Likewise, the leading-colour contribution to an emission operator acting in the amplitude and conjugate is

$$\begin{aligned} \text{Leading}_{\tau\sigma}^{(0)} \left[\mathbf{D}_n \mathbf{A}_{n-1} \mathbf{D}_n^\dagger \right] &= -\delta_{\tau\sigma} \times \\ &\sum_{i,j \text{ cc in } \sigma \setminus n} \lambda_i \bar{\lambda}_j 2\text{Re} \left(\omega_i^{(n)} \left(\omega_j^{(n)} \right)^* \right) \text{Leading}_{\tau \setminus n, \sigma \setminus n}^{(0)} \left[\mathbf{A}_{n-1} \right]. \end{aligned} \quad (2.74)$$

The leading-colour emission contributions arise from colour-line operators acting in the amplitude and conjugate of the form

$$\delta_{c_i, \sigma^{-1}(\bar{c}_j)} \mathbf{t}_{c_i} | \sigma \rangle \langle \sigma | \bar{\mathbf{t}}_{\bar{c}_j}, \quad (2.75)$$

where the colour index corresponding to parton i and the anti colour index corresponding to j are colour-connected in σ . The additional contribution with a $\bar{\mathbf{t}}$ operator in the amplitude and \mathbf{t} in the conjugate is equivalent and accounts

for the factor

$$\omega_i^{(n)} \left(\omega_j^{(n)} \right)^* + \omega_j^{(n)} \left(\omega_i^{(n)} \right)^* = 2\text{Re} \left(\omega_i^{(n)} \left(\omega_j^{(n)} \right)^* \right), \quad (2.76)$$

in Eq. 2.74. These matrix elements correspond to terms in the first line of Eq. 2.65. Matrix elements of the form $\mathbf{t}_{c_i} |\sigma\rangle \langle \sigma| \mathbf{t}_{c_j}$ (and the $\bar{\mathbf{t}}$ equivalent) do not contribute to Eq. 2.74 as they will always act to introduce a transposition between the tensor in the amplitude and conjugate, inducing a $1/N_c$ suppression from the scalar product matrix. Note that the sum over gluon polarisations yields an additional minus sign, which is accounted for in the definition of the phase-space element in Eq. 2.4.

In the case of a single-gluon exchange (used in the out-of-gap gluon expansion discussed in Section 2.1), we are interested in traces of the form

$$\text{Tr} \left[\gamma_n \mathbf{A}_n + \mathbf{A}_n \gamma_n^\dagger \right], \quad (2.77)$$

where

$$\gamma_n = \sum_{i,j} \gamma_{ij}^{(n)} \mathbf{T}_i \cdot \mathbf{T}_j \quad \text{and} \quad \gamma_{ij}^{(n)} = \frac{\alpha_s}{2\pi} \int \frac{d\Omega_k}{4\pi} \omega_{ij}(k). \quad (2.78)$$

The leading colour contribution for single-gluon exchange is then

$$\begin{aligned} \text{Leading}_{\tau\sigma}^{(0)} \left[\gamma_n \mathbf{A}_n + \mathbf{A}_n \gamma_n^\dagger \right] &= -N_c \delta_{\sigma\tau} \times \\ &\sum_{i,j \text{ cc in } \sigma} \lambda_i \bar{\lambda}_j 2\text{Re} \left(\gamma_{ij}^{(n)} + \gamma_{ji}^{(n)} \right) \text{Leading}_{\tau\sigma}^{(0)} \left[\mathbf{A}_n \right]. \end{aligned} \quad (2.79)$$

We now have all of the ingredients necessary to compute traces in the large- N_c limit. Firstly, we note that in the large- N_c limit the basis tensors denoting the operator matrix elements in the amplitude and conjugate-amplitude are kept the same. Therefore we should set $\sigma = \tau$ in Eq. 2.54. This instructs us that we must sum over diagonal basis tensor contributions, $\mathcal{A}_{\sigma\sigma}$, and for each, multiply by N_c raised to the power of the number of colour lines present in σ , i.e. the scalar product matrix element $\langle \sigma | \sigma \rangle$. This power is equal to the number of colour flows in the hard process plus the number of real emissions. Each of the contributions $\mathcal{A}_{\sigma\sigma}$ can be calculated by recursively generating the leading contributions in Eq. 2.72, 2.74 and 2.79, working inwards from the outer-most matrices (multiplied from the left and right) towards the hard process matrix at the heart of the chain of operators (see Eq. 2.1). One must account for the hard process contribution by multiplying by the square of the corresponding ampli-

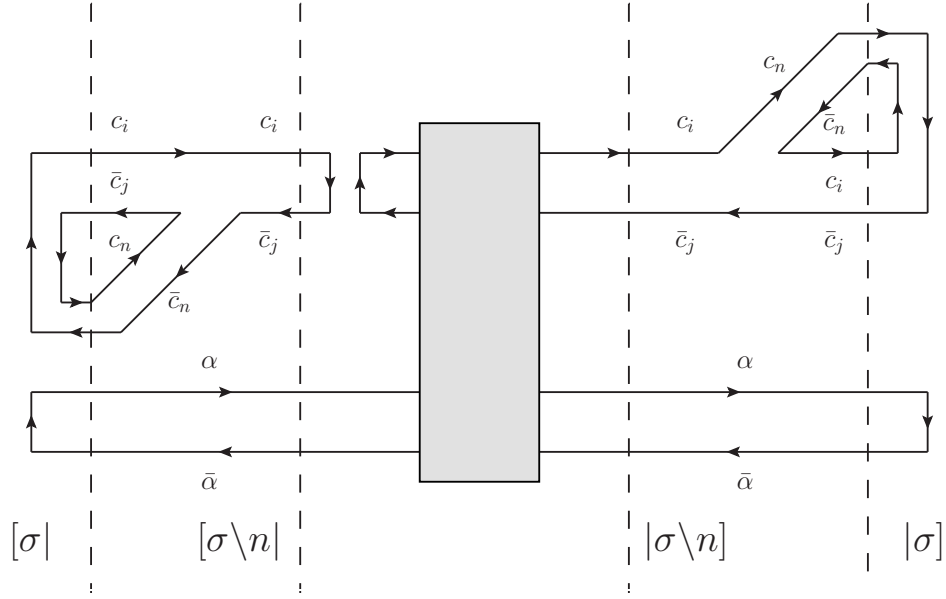


FIGURE 2.5: An illustration of one contribution to the leading-colour calculation for the $qq \rightarrow qq$ scattering process. We consider the case of one real emission and one virtual correction to the hard process $[\sigma \setminus n] \mathbf{H} [\sigma \setminus n]$. The dashed lines indicate the basis tensors at each stage of the evolution. Figure from [99].

tude, $|\mathcal{M}_\sigma|^2$. In summary, starting from the outermost operators, this recursive generation goes as follows: for each pair of evolution operators $\mathbf{V}_n \mathbf{A}_n \mathbf{V}_n^\dagger$ multiply by

$$\exp \left(-2N_c \text{Re} \left(\Omega_{ij}^{(n)} + \Omega_{ji}^{(n)} \right) \lambda_i \bar{\lambda}_j \right), \quad (2.80)$$

for each colour connected dipole (i, j) in σ . For a virtual gluon insertion $\gamma_n \mathbf{A}_n + \mathbf{A}_n \gamma_n^\dagger$ multiply by

$$-2N_c \lambda_i \bar{\lambda}_j \text{Re} \left(\gamma_{ij}^{(n)} + \gamma_{ji}^{(n)} \right), \quad (2.81)$$

and sum over colour connected dipoles (i, j) in σ . Finally for a pair of emission operators $\mathbf{D}_n \mathbf{A}_{n-1} \mathbf{D}_n^\dagger$, combine the dipoles (i, n) and (n, j) in the basis tensor σ , leaving behind a dipole (i, j) in the tensor $\sigma \setminus n$ and multiply by the factor

$$-\lambda_i \bar{\lambda}_j 2 \text{Re} \left(\omega_i^{(n)} \left(\omega_j^{(n)} \right)^* \right). \quad (2.82)$$

This procedure has been illustrated in Figure 2.5 for one contribution to the leading-colour result in the case of soft-gluon evolution of the $qq \rightarrow qq$ hard scattering.

2.3.2 BMS Equation

The work [112] considered a pair of jets produced by e^+e^- annihilation with an exclusion region \mathcal{C}_{out} , separated from the jet axis by large angles. They considered the interjet distribution where the total energy of radiation emitted into \mathcal{C}_{out} is smaller than E_0 , where E_0 is much less than the hard scale of the process Q . As such, this calculation renders large logarithmically-enhanced terms associated with the successive ordered emission of soft-gluons (ordered in energy) that must be resummed. This radiation occurs at larger and larger angles with respect to the thrust axis within the allowed (complementary region), \mathcal{C}_{in} . They derived an evolution equation which resums all single logarithmic contributions for this interjet distribution, the Banfi-Marchesini-Smye (BMS) equation:

$$\begin{aligned} \frac{\partial G_{ab}(t)}{\partial t} = & - \int_{\mathcal{C}_{\text{out}}} \frac{d\Omega_k}{4\pi} \omega_{ab}(k) G_{ab}(t) \\ & + \int_{\mathcal{C}_{\text{in}}} \frac{d\Omega_k}{4\pi} \omega_{ab}(k) [G_{ak}(t)G_{kb}(t) - G_{ab}(t)], \end{aligned} \quad (2.83)$$

where $G_{ab}(t)$ denotes the probability to deposit a total energy lower than E_0 into \mathcal{C}_{out} and $t = (N_c\alpha/\pi) \ln(E/E_0)$. Eq. 2.83 is formulated in the limit of large- N_c . Labelling the two partons of the primary process as a and b , the emission of a soft gluon, k , can be viewed as a splitting of the colour dipole (ab) into two new dipoles (ak) and (kb) as indicated by the $G_{ak}(t)G_{kb}(t)$ term of the second equation on the RHS of Eq. 2.83 whilst the $-G_{ab}(t)$ term describes virtual emission. These splittings can subsequently develop their own evolution, underpinning the iterative nature of this equation. One can also see that soft-collinear singularities cancel in the second term on the RHS of Eq. 2.83. For instance, if k becomes collinear with a , $G_{ak}(t) \rightarrow 1$ and $G_{kb}(t) \rightarrow G_{ab}(t)$ so that the sum of all terms vanishes. It is also important to note that $\omega_{ab}(k)$ in Eq. 2.83 only depends on the directions of the three partons and not their energies and following our labelling of partons, the hard partons have momenta p_a and p_b . Whilst it was derived for a particular interjet distribution, the BMS equation can also be used to determine any distribution in e^+e^- , where the observable is defined by a product of theta functions which restrict each individual emission, i.e. of the form $\prod_k \Theta(E_k - Q_0)$. In Section 2.3.1 we established a set of simple, dipole-type rules for calculating the leading-colour contribution to the colour evolution of a hard scattering. We shall now show how the rules of the preceding section give rise to the BMS equation.

We start by considering e^+e^- scattering in Eq. 2.24, so we can take $\mathbf{H} = 1/N_c \mathbf{1}$. The correspondence between the phase-space regions in Eq. 2.83 and our own work is as follows: \mathcal{C}_{out} is what we coin the in-gap region whilst \mathcal{C}_{in} is our out-gap region. We shall use the in-gap and out-gap conventions henceforth. The coefficient factors in the leading-colour rules of the previous section take the form

$$\begin{aligned}\Omega_{ij}^{(n)} = \Omega_{ji}^{(n)} &= -\frac{1}{2} \int_{\text{in}} d\Pi_k \Theta(E_{n+1} < E < E_n) \omega_{ij}(\hat{k}) \\ \gamma_{ij}^{(n)} = \gamma_{ji}^{(n)} &= -\frac{1}{2} \Theta_{\text{out}} \Theta(E_n < E_{n-1}) \omega_{ij}(\hat{q}_n)\end{aligned}\quad (2.84)$$

$$\omega_i^{(n)} \left(\omega_j^{(n)} \right)^* = \Theta_{\text{out}} \Theta(E_n < E_{n-1}) \omega_{ij}(\hat{q}_n)\quad (2.85)$$

and the evolution with the in-region anomalous dimension contributes a factor

$$V_{ij}^{E_{n+1}, E_n} = \exp \left(-\frac{N_c \alpha_s}{\pi} \int_{E_{n+1}}^{E_n} \frac{dE}{E} \int_{\text{in}} \frac{d\Omega_k}{4\pi} \omega_{ij}(\hat{k}) \right)\quad (2.86)$$

per colour flow. These expressions have a simple diagrammatic interpretation that is illustrated in Figure 2.6. Each double line in the figure corresponds to a Sudakov factor of the form in Eq. 2.86, $V_{ij}^{E_{n+1}, E_n}$, where i and j label the directions associated with the corresponding colour and anti colour lines. The shaded circles correspond to a factor $\omega_{ij}(\hat{k})$, and the vertical dashed line indicates the associated energy. The arguments, E_n and E_{n+1} of the Sudakov are determined by these vertical dashed lines. We can see how the algorithm maps onto a classical dipole shower at leading-colour. The evolution of dipoles is universal, i.e. the process dependence solely enters in through the selection of an initial colour flow weighted by the modulus squared of the corresponding amplitude $|\mathcal{M}_\sigma|^2$.

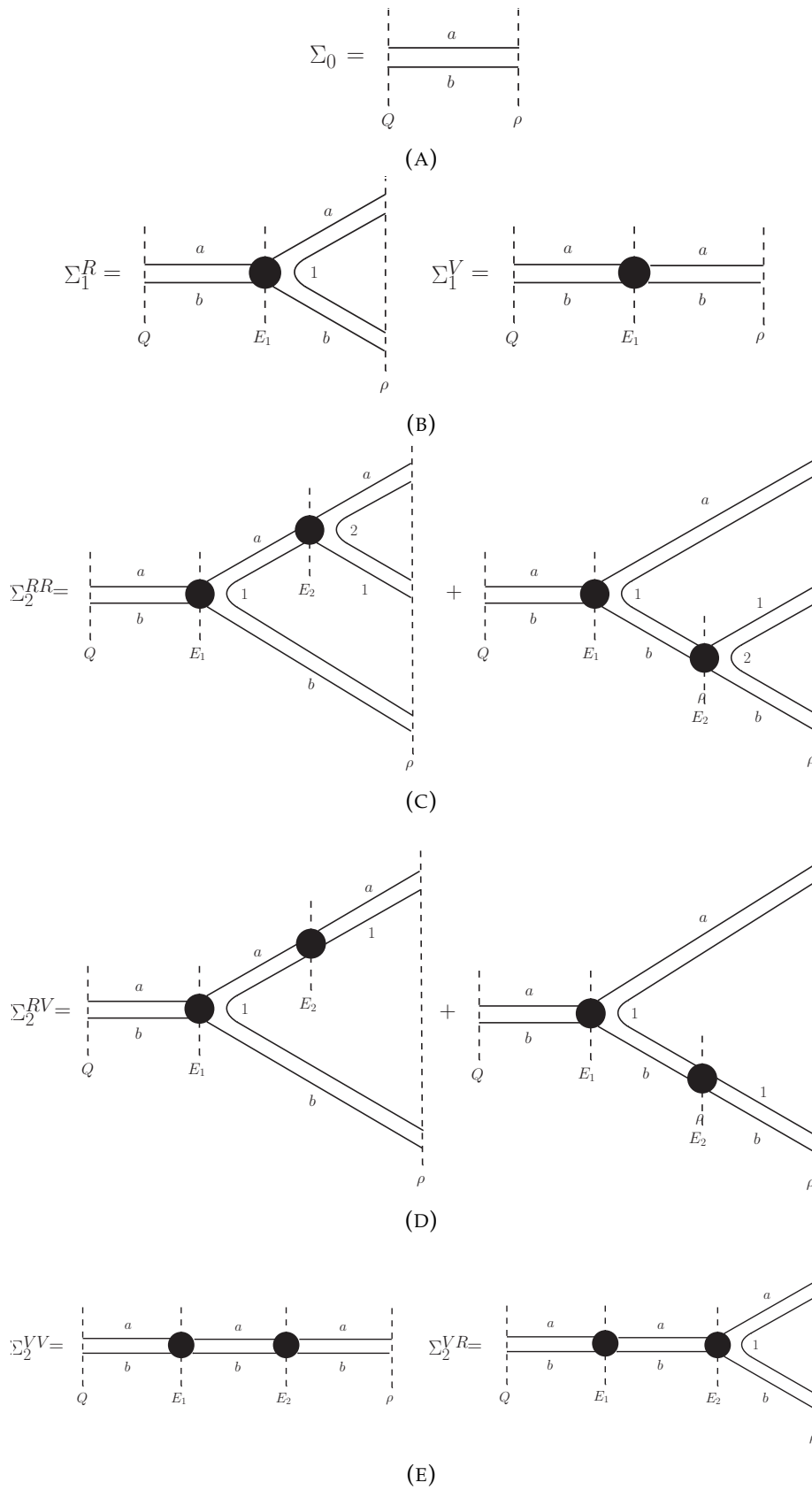


FIGURE 2.6: The pictorial representation of the out-of-gap expansion (see Eq. 2.24) in the leading- N_c limit. This corresponds to Eq. 2.87. Figure modified from [99].

The leading-colour contribution to the non-global logarithms (from Eq. 2.24) is then

$$\begin{aligned}
\Sigma_0 &= V_{ab}^{\rho,Q} \\
\Sigma_1 &= \int_{\text{out}} V_{ab}^{E_1,Q} \omega_{ab}(\hat{q}_1) \left[V_{a_1}^{\rho,E_1} V_{b_1}^{\rho,E_1} - V_{ab}^{\rho,E_1} \right] \frac{d\Omega_1}{4\pi} dt_1 \\
\Sigma_2^{RR} &= \int_{\text{out}} V_{ab}^{E_1,Q} \omega_{ab}(\hat{q}_1) \left[V_{a_1}^{E_2,E_1} V_{b_1}^{\rho,E_1} \omega_{a_1}(\hat{q}_2) V_{a_2}^{\rho,E_2} \right. \\
&\quad \left. + V_{a_1}^{\rho,E_1} V_{b_1}^{E_2,E_1} \omega_{b_1}(\hat{q}_2) V_{b_2}^{\rho,E_2} \right] V_{12}^{\rho,E_2} \frac{d\Omega_1}{4\pi} \frac{d\Omega_2}{4\pi} dt_1 dt_2 \\
\Sigma_2^{VR} &= - \int_{\text{out}} V_{ab}^{E_2,Q} \omega_{ab}(\hat{q}_1) \omega_{ab}(\hat{q}_2) V_{a_1}^{\rho,E_2} V_{b_1}^{\rho,E_2} \frac{d\Omega_1}{4\pi} \frac{d\Omega_2}{4\pi} dt_1 dt_2 \\
\Sigma_2^{RV} &= - \int_{\text{out}} V_{ab}^{E_1,Q} \omega_{ab}(\hat{q}_1) \left[V_{a_1}^{E_2,E_1} V_{b_1}^{\rho,E_1} \omega_{a_1}(\hat{q}_2) V_{a_1}^{\rho,E_2} \right. \\
&\quad \left. + V_{a_1}^{\rho,E_1} V_{b_1}^{E_2,E_1} \omega_{b_1}(\hat{q}_2) V_{b_1}^{\rho,E_2} \right] \frac{d\Omega_1}{4\pi} \frac{d\Omega_2}{4\pi} dt_1 dt_2 \\
\Sigma_2^{VV} &= \int_{\text{out}} V_{ab}^{\rho,Q} \omega_{ab}(\hat{q}_1) \omega_{ab}(\hat{q}_2) \frac{d\Omega_1}{4\pi} \frac{d\Omega_2}{4\pi} dt_1 dt_2, \tag{2.87}
\end{aligned}$$

where we label the hard partons a and b and $t_i = (N_c \alpha / \pi) \ln(E_i / \rho)$. These Σ_n can also be obtained by iteratively solving the BMS equation, where our observable corresponds to

$$\Sigma(\rho) = G_{ab}(t_Q), \tag{2.88}$$

where $t_Q = (N_c \alpha_s / \pi) \ln(Q / \rho)$. As in [112], we first note that the distribution can be factorised into two pieces

$$G_{ij}(t) = V_{ij}^{\rho,E} g_{ij}(t). \tag{2.89}$$

The first is the Sudakov factor given by bremsstrahlung emission from the primary hard partons, whilst the second is the result of successive soft emission. Rewriting the BMS equation in terms of the latter, we have an evolution equation

$$\frac{\partial g_{ab}(t)}{\partial t} = \int_{\text{out}} \frac{d\Omega_k}{4\pi} \omega_{ab}(k) \left[\frac{V_{ak}^{\rho,E} V_{kb}^{\rho,E}}{V_{ab}^{\rho,E}} g_{ak}(t) g_{kb}(t) - g_{ab}(t) \right], \tag{2.90}$$

where the initial condition $G_{ab}(0) = 1$ means that $g_{ab}(0) = 1$. We can see that

Eq. 2.90 returns Σ_1 if we set $g_{ij}^{(0)}(t) = 1$ and integrate over the range $0 < t < t_Q$,

$$\int_0^{t_Q} \frac{\partial g_{ab}^{(1)}(t_1)}{\partial t_1} dt_1 = \int \int_{\text{out}} \frac{d\Omega_1}{4\pi} \omega_{ab}(\hat{q}_1) \left[\frac{V_{a1}^{\rho,E_1} V_{1b}^{\rho,E_1}}{V_{ab}^{\rho,E_1}} - 1 \right] dt_1. \quad (2.91)$$

The next iteration gives Σ_2 if we substitute $g_{ij}(t)$ on the RHS of Eq. 2.90 by $g_{ij}^{(1)}(t)$:

$$\begin{aligned} \frac{\partial g_{ab}^{(2)}(t_1)}{\partial t_1} = \int_{\text{out}} \frac{d\Omega_1}{4\pi} \omega_{ab}(\hat{q}_1) & \left[\frac{V_{a1}^{\rho,E_1} V_{1b}^{\rho,E_1}}{V_{ab}^{\rho,E_1}} \left(g_{a1}^{(1)}(t_1) g_{1b}^{(0)}(t_1) \right. \right. \\ & \left. \left. + g_{a1}^{(0)}(t_1) g_{1b}^{(1)}(t_1) \right) - g_{ab}^{(1)}(t_1) \right], \end{aligned} \quad (2.92)$$

where we have left $g_{ak}^{(0)} = g_{kb}^{(0)} = 1$ explicit for clarity. Inserting the form of $g_{ij}^{(1)}(t)$ into Eq. 2.92, we find

$$\begin{aligned} G_{ab}^{(2)}(t_Q) = V_{ab}^{\rho,Q} \int_{\text{out}} \omega_{ab}(\hat{q}_1) \omega_{a1}(\hat{q}_2) & \frac{V_{a1}^{\rho,E_1} V_{1b}^{\rho,E_1}}{V_{ab}^{\rho,E_1}} \left[\frac{V_{a2}^{\rho,E_2} V_{21}^{\rho,E_2}}{V_{a1}^{\rho,E_2}} - 1 \right] \\ & + \omega_{ab}(\hat{q}_1) \omega_{1b}(\hat{q}_2) \frac{V_{a1}^{\rho,E_1} V_{1b}^{\rho,E_1}}{V_{ab}^{\rho,E_1}} \left[\frac{V_{12}^{\rho,E_2} V_{2b}^{\rho,E_2}}{V_{1b}^{\rho,E_2}} - 1 \right] \\ & - \omega_{ab}(\hat{q}_1) \omega_{ab}(\hat{q}_2) \left[\frac{V_{a2}^{\rho,E_2} V_{2b}^{\rho,E_2}}{V_{ab}^{\rho,E_2}} - 1 \right] \frac{d\Omega_1}{4\pi} \frac{d\Omega_2}{4\pi} dt_1 dt_2, \end{aligned} \quad (2.93)$$

where by splitting contributions appropriately and using the identity

$$V_{ij}^{E_3,E_2} \times V_{ij}^{E_2,E_1} = V_{ij}^{E_3,E_1}, \quad (2.94)$$

we can see that $V_{ab}^{\rho,Q} g_{ab}^{(2)}(t_Q) = \Sigma_2^{RR} + \Sigma_2^{VR} + \Sigma_2^{RV} + \Sigma_2^{VV}$. We have shown that, at leading-colour, our algorithm generates the iterative solution to the BMS equation.

2.3.3 Subleading-Colour Contributions

Subleading-colour contributions are substantially more difficult to compute and describe in a systematic way, particularly as corrections to the leading-colour result. In this section we shall discuss the first subleading-colour corrections. We begin by collating our knowledge of colour-charge products dis-

cussed in Section 2.3. Using Eq. 2.66 one can write a general form for the anomalous dimension matrix element, $[\tau | \Gamma | \sigma \rangle$, as

$$[\tau | \Gamma | \sigma \rangle = -N_c \delta_{\tau\sigma} \Gamma_\sigma + \Sigma_{\tau\sigma} + \frac{1}{N_c} \delta_{\tau\sigma} \rho, \quad (2.95)$$

where

$$\begin{aligned} \Gamma_\sigma &= -\frac{\alpha_s}{\pi} \sum_{i < j} \int \left(\lambda_i \bar{\lambda}_j \delta_{c_i, \sigma^{-1}(\bar{c}_j)} + \lambda_j \bar{\lambda}_i \delta_{c_j, \sigma^{-1}(\bar{c}_i)} \right) \omega_{ij}(\hat{k}) \frac{d\Omega_k}{4\pi}, \\ \rho &= \frac{\alpha_s}{\pi} \sum_{i < j} \int (\lambda_i - \bar{\lambda}_i) (\lambda_j - \bar{\lambda}_j) \omega_{ij}(\hat{k}) \frac{d\Omega_k}{4\pi}, \end{aligned} \quad (2.96)$$

and

$$\begin{aligned} \Sigma_{\tau\sigma} &= -\frac{\alpha_s}{\pi} \sum_{i < j} \int \sum_{(ab)} \delta_{\tau(ab), \sigma} \left(\lambda_i \lambda_j \delta_{(ab), (c_i c_j)} + \bar{\lambda}_i \bar{\lambda}_j \delta_{(ab), (\sigma^{-1}(\bar{c}_i) \sigma^{-1}(\bar{c}_j))} \right. \\ &\quad \left. - \lambda_i \bar{\lambda}_j \delta_{(ab), (c_i, \sigma^{-1}(\bar{c}_j))} - \lambda_j \bar{\lambda}_i \delta_{(ab), (c_j, \sigma^{-1}(\bar{c}_i))} \right) \omega_{ij}(\hat{k}) \frac{d\Omega_k}{4\pi}. \end{aligned} \quad (2.97)$$

As we shall be considering multiple insertions of these operators in the following discussion, it is worth noting that each of the contributions to the anomalous dimension matrix element, Γ , Σ and ρ are of order α_s .

The leading colour contributions in the Sudakov operator are contained in the Γ_σ factor and are enhanced by powers of $\alpha_s N_c$. Owing to the fact that this term is diagonal (as indicated by the $\delta_{\tau\sigma}$ in Eq. 2.95) it can be accounted for to all orders in an exponential. This evolution does not induce additional transpositions between the basis tensors in the amplitude and conjugate-amplitude. These terms are depicted in the light-blue boxes of Figure 2.8. If only this term is considered in each invocation of the Sudakov operator, and supplemented by those contributions in the emission operator that also leave colour structures in both the amplitude conjugate intact, we recover the leading- N_c results of Section 2.3.1. In particular, this corresponds to the first row of real emission contributions in the light-blue section of Figure 2.8b.

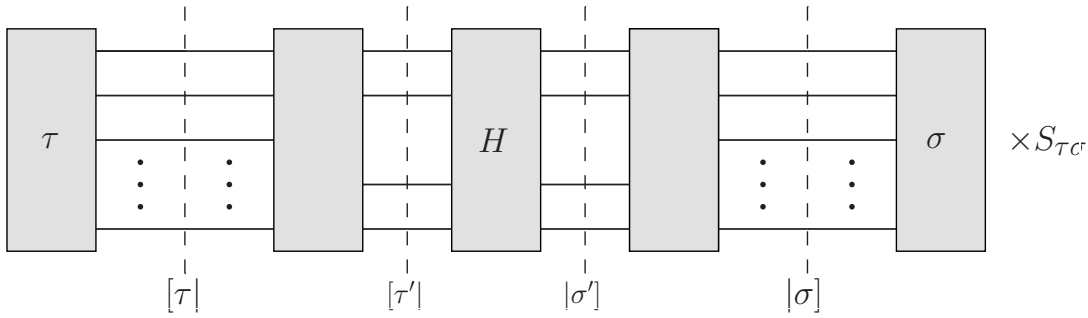
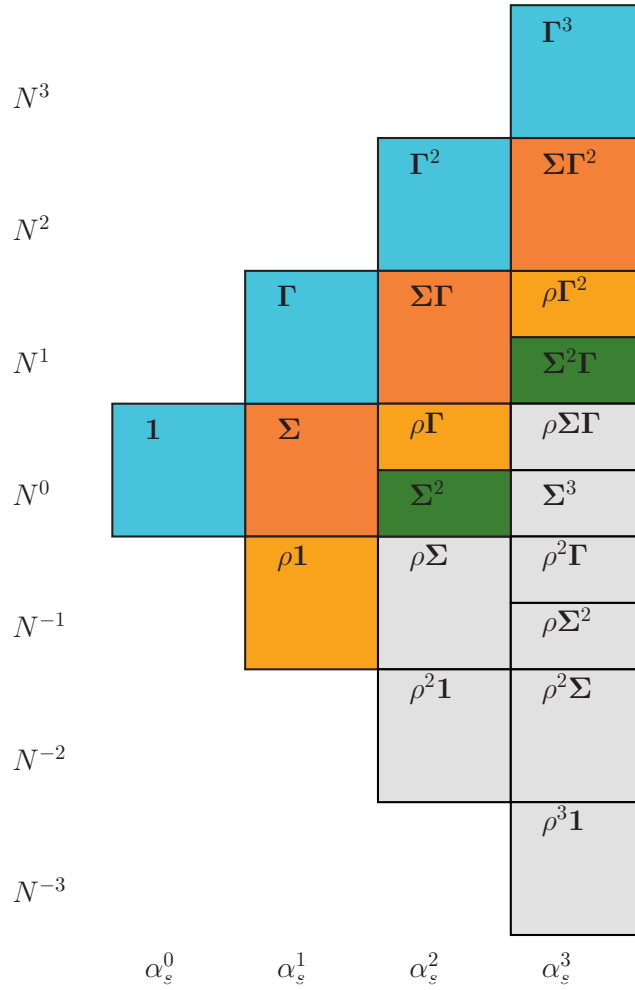


FIGURE 2.7: Depiction of the general structure of a calculation which can involve subleading-colour contributions. Figure 2.5 is a specific example involving leading-colour contributions. Figure from [99].

There are subleading-colour contributions arising from numerous sources: the hard scattering matrix, terms explicitly $1/N_c$ and $1/N_c^2$ suppressed in the emission operator and anomalous dimension matrix operator and from off-diagonal matrix elements in the scalar product matrix (see Eq. 2.42). Figure 2.7 illustrates the general structure of a calculation involving subleading-colour contributions. In order to calculate a correction of order $1/N_c^k$ we must consider final colour arrangements σ and τ which differ by $k - l$ transpositions, where $0 \leq l \leq k$. This accounts for the colour suppression resulting from the scalar product matrix, we must then determine the remaining terms which contribute $1/N_c^l$ corrections from the soft-gluon evolution and hard scattering matrix. As an example, an insertion of a Σ contribution is accompanied by a factor of $1/N_c$ relative to the leading-colour contribution. In addition to this it results in a relative single flip between the colour arrangements in the amplitude and conjugate amplitude, inducing an additional factor of $1/N_c$. It is worth noting that purely $1/N_c$ corrections (i.e. after the scalar product matrix element and soft-gluon evolution have been accounted for) can only originate from the hard scattering matrix via interference contributions. Hence, such contributions shall be ignored in the following discussion and can be easily accounted for in any case. Figure 2.7 indicates the intermediate colour arrangements after the action of an operator by dashed lines. We keep track of the number of transpositions (or flips) by which the colour arrangements in the amplitude and conjugate differ in the table of Figure 2.8b.



(A)

	virtuals	reals
	$(0 \text{ flips}) \times 1 \times (\alpha_s N)^n$	$(\mathbf{t}[\dots]\mathbf{t} _{0 \text{ flips}})^{r-1} \mathbf{t}[\dots]\mathbf{t} _{2 \text{ flips}} \times 1$ $(\mathbf{t}[\dots]\mathbf{t} _{0 \text{ flips}})^{r-1} \mathbf{t}[\dots]\mathbf{s} _{1 \text{ flip}} \times N^{-1}$ $(\mathbf{t}[\dots]\mathbf{t} _{0 \text{ flips}})^{r-1} \mathbf{s}[\dots]\mathbf{s} _{0 \text{ flips}} \times N^{-2}$
	$(1 \text{ flip}) \times \alpha_s \times (\alpha_s N)^n$	$(\mathbf{t}[\dots]\mathbf{t} _{0 \text{ flips}})^r$ $(\mathbf{t}[\dots]\mathbf{t} _{0 \text{ flips}})^{r-1} \mathbf{t}[\dots]\mathbf{s} _{1 \text{ flip}} \times N^{-1}$
	$(0 \text{ flips}) \times \alpha_s N^{-1} \times (\alpha_s N)^n$	$(\mathbf{t}[\dots]\mathbf{t} _{0 \text{ flips}})^r$
	$(0 \text{ flips}) \times \alpha_s^2 \times (\alpha_s N)^n$ $(2 \text{ flips}) \times \alpha_s^2 \times (\alpha_s N)^n$	$(\mathbf{t}[\dots]\mathbf{t} _{0 \text{ flips}})^r$ $(\mathbf{t}[\dots]\mathbf{t} _{0 \text{ flips}})^{r-1} \mathbf{t}[\dots]\mathbf{t} _{2 \text{ flips}}$

(B)

FIGURE 2.8: The next-to-leading colour contributions at varying powers of N_c and α_s . Each box in (A) corresponds to a contribution from the virtual evolution operator with increasing powers of α_s from left to right and decreasing powers of N_c from top to bottom, with N_c^0 in the middle. The effect of r real emissions and the $1/N_c^k$ suppression resulting from the scalar product matrix (indicated by the number of flips) is presented in the reals column of the table in (B). Figure modified from [99].

We begin our discussion with the subleading contributions, suppressed by $1/N_c^2$ relative to the leading contribution, originating from the real emission operator. They arise as a result of three possibilities. Firstly are contributions of the form $[\sigma | \mathbf{t}_\alpha \mathbf{A} \mathbf{t}_\beta | \tau]$, where $\sigma(\alpha) \neq \tau(\beta)$. This induces two flips, one in both the amplitude and conjugate-amplitude, accompanied by no explicit $1/N_c$ factor, leading to an overall $1/N_c^2$ suppression from the scalar product matrix. Secondly, are contributions of the form $[\sigma | \mathbf{t}_\alpha \mathbf{A} \mathbf{s} | \tau]$ and $[\sigma | \mathbf{s} \mathbf{A} \mathbf{t}_\alpha | \tau]$ which induces one flip and an explicit factor of $1/N_c$ through the use of an \mathbf{s} operator. Lastly are terms of the type $[\sigma | \mathbf{s} \mathbf{A} \mathbf{s} | \tau]$ which simply induce an explicit factor of $1/N_c^2$ with no flips. When these contributions act alongside the leading colour virtual contributions (only the Γ term in the anomalous dimension matrix element), they all contribute to the first overall subleading-colour corrections (see the light-blue row of Figure 2.8b). We remark that emissions never reduce the number of flips by which the colour arrangement in the amplitude and its conjugate differ.

Our discussion now continues onto subleading virtual corrections. An insertion of a perturbation $\Sigma_{\tau,\sigma}$ induces a flip between the amplitude and conjugate-amplitude colour arrangements. This leads to a $1/N_c$ suppression in the scalar product matrix element. However, the fixed-order $\Sigma_{\tau,\sigma}$ contribution, when combined with the all-order summation of contributions from Γ is suppressed by a factor of $\alpha_s N_c / N_c$ relative to the leading-colour contribution. If this is accompanied by a leading emission contribution, there is an overall factor of $1/N_c^2$. The flip can also undo a transposition that has already been induced by an emission operator, i.e. from terms like $[\sigma | \mathbf{t}_\alpha \mathbf{A} \mathbf{s} | \tau]$ and $[\sigma | \mathbf{s} \mathbf{A} \mathbf{t}_\alpha | \tau]$. However, due to the presence of an \mathbf{s} operator in such terms, an additional $1/N_c$ factor is introduced. Therefore, both of these fixed-order contributions are $1/N_c^2$ suppressed relative to the leading contributions. They correspond to the dark orange boxes in Figure 2.8.

Two $\Sigma_{\tau\sigma}$ insertions are proportional to α_s^2 and are therefore suppressed by at least $1/N_c^2$ relative to the leading contributions. If these insertions combine in such a way that the net number of flips is zero, and are accompanied by the leading emission contributions, they will contribute to terms exactly suppressed by $1/N_c^2$. Additionally, each Σ can induce a flip which exactly counteracts that induced by a real emission term of the form $[\sigma | \mathbf{t}_\alpha \mathbf{A} \mathbf{t}_\beta | \tau]$, when $\sigma(\alpha) \neq \tau(\beta)$. The net result is that the amplitude and its conjugate differ by zero transpositions and there is no additional suppression from the scalar product matrix. These two possibilities are pictorially represented in the dark

green boxes in Figure 2.8.

The ρ terms in Eq. 2.95 come with a factor of $(\alpha_s N_c) / N_c^2$ relative to the leading contributions and so are suppressed by $1 / N_c^2$ at each order of α_s . They describe singlet-gluon contributions and so have no effect on the colour arrangement. This in-turn means they generate zero flips and lie on the colour diagonal. A single ρ perturbation accompanied by a Γ insertion for each order of α_s above one, and the leading contribution to the emission operator, contributes at the same order as the contributions discussed above. These contributions are illustrated by the light-orange boxes in Figure 2.8. It is worth noting that due to their residence on the colour diagonal, ρ terms can also be exponentiated to all orders. This shall be discussed further in Chapter 4. The remaining grey boxes lead to a factor of $(\alpha_s N_c)^2 / N_c^4$ and are beyond the next-to-leading colour approximation.

In this chapter we have presented a general evolution algorithm which describes the full-colour recursive definitions of QCD amplitudes in the soft approximation. We have reviewed the colour flow basis, and used it to explore the colour structures encountered when solving the evolution equations. Using these equations, we expressed the evolution algorithm in the leading- N_c limit and showed its equivalence with the well-known BMS equation. Lastly, we presented some initial steps towards a systematic approach of including $1 / N_c^k$ corrections to the leading colour result, discussing in particular the first subleading-colour corrections. In Chapter 4 we shall study a Monte Carlo implementation of the general evolution algorithm, which will include the full-colour emission operator dependence, and provide a systematic way of expanding the Sudakov operator by ‘colour order’. Whilst the author has not endeavoured in this, we note that it would be an interesting project to write a Monte Carlo implementation of the general evolution algorithm, including just the organised leading and sub-leading contributions discussed in this chapter. It may reveal that the first subleading colour corrections offer a substantial improvement at little extra computation cost.

Chapter 3

Monte Carlo Methods

A Monte Carlo method is one of a broad class of computational algorithms which make use of repeated random sampling (a facet which led to the ‘Monte Carlo’ name) to obtain numerical results. Monte Carlo methods were historically introduced in studies of neutron diffusion (as far back as 1946) [113]; where it seems natural to employ random numbers to describe random processes. The numerical results were in fact ‘deterministic’ and could be solved, in principle, via integration. However, this proved difficult using conventional mathematical methods and Monte Carlo methods were utilised.

In more modern times, there are many fields of physics which rely upon Monte Carlo methods. In particle physics, Monte Carlo techniques are used to evaluate hard cross sections, simulate radiation, model hadronisation, and simulate the response of the detector to name a few applications. These tasks fall under the remit of general purpose event generators, such as **Herwig** [10–12], **Pythia** [13–15] and **Sherpa** [16]. To highlight the prevalence of Monte Carlo methods, we list just some of the main event generator-related projects:

- Fixed-order matrix element generation and matching; **GoSam** [114, 115], **MadGraph** [116], **NJet** [117, 118], **OpenLoops** [119], **VBFNLO** [120], **HJets** [121]
- Parton showers; angular-ordered shower [122], dipole shower [52, 53]
- Non-perturbative modelling (e.g. hadronisation) [54, 123–125]

A more comprehensive list of projects can be found on **HEPForge** [126].

In this chapter, we shall give an introduction to Monte Carlo methods, beginning with a probabilistic formulation of integrals in terms of averages, and their associated certainties. Subsequently, we discuss strategies for sampling from probability distributions and techniques for reducing the variance and improving the convergence of Monte Carlo integrals. Lastly, we briefly consider an angular-ordered parton branching algorithm, or basic parton shower, and outline the veto and competition Monte Carlo algorithms used to solve it.

3.1 Integration and Variance

We wish to employ Monte Carlo techniques to solve the integral

$$I = \int_{x_1}^{x_2} f(x)dx, \quad (3.1)$$

for a function $f(x)$ in the domain (x_1, x_2) . The principle behind the Monte Carlo approach is to substitute the issue of performing a numerical integration with one of calculating the expectation of the integrand. The expectation of a function $f(x)$ is defined as the average value of the function:

$$\langle f(x) \rangle = \int f(x') dG(x'), \quad (3.2)$$

where $G(x')$ is a distribution function describing the uniform distribution of x between x_1 and x_2 , so that $dG(x') = dx' / (x_2 - x_1)$ (we shall discuss this more later). The expectation can be written more explicitly as

$$\langle f(x) \rangle = \frac{1}{(x_2 - x_1)} \int f(x') dx' = \frac{1}{(x_2 - x_1)} I. \quad (3.3)$$

So if we take enough values of x , distributed on the domain (x_1, x_2) , the average value of $f(x)$ is a reasonable estimator for our integral, I . This estimator is written as

$$\langle f(x) \rangle \simeq \frac{1}{N} \sum_{i=1}^N f(x_i), \quad (3.4)$$

where x_i is a uniformly sampled value over the domain and N is the number of values of x we evaluate. The law of large numbers (LLN) tells us about the behaviour of the sum of a large number of random variables, as in Eq. 3.4. Specifically, it tells us that if x_i are the values of N independent and identically distributed random variables, their average (on the RHS of Eq. 3.4) converges to the exact value of $\langle f(x) \rangle$ (and therefore of I) as $N \rightarrow \infty$.

In reality, our integral in Eq. 3.1 is often over a multi-dimensional phase space (as we have seen in Chapter 2) and Eq. 3.4 can be extended to an arbitrary number of dimensions, d . Suppose that we write $f(x)$ now as $f(\mathbf{x})$ to denote a matrix element-squared which is a function of a d -component vector \mathbf{x} , which we wish to integrate over a region V of \mathbf{x} -space. Then, Eq. 3.1 becomes [127]

$$I = \int_V f(\mathbf{x}) d\Phi, \quad (3.5)$$

and the expectation of $f(\mathbf{x})$ is given by

$$\langle f(\mathbf{x}) \rangle = \frac{1}{\Phi(V)} \int_V f(\mathbf{x}) d\Phi \simeq \frac{1}{N} \sum_{i=1}^N f(\mathbf{x}_i), \quad (3.6)$$

where $\Phi(V)$ is the volume of V and each evaluation of $f(\mathbf{x})$ now requires the

sampling of d -components.

Since we are practically restricted to computing with finite N , we are naturally led to the question: ‘how accurate is our Monte Carlo estimator for a given, finite N ?’. To answer this, we turn to the central limit theorem (CLT). The CLT tells us approximately how our Monte Carlo estimate is distributed for a large number of samples. It establishes that the sum of a large number of independent and identically distributed random variables is itself a random variable, whose distribution converges to a normal distribution, provided N is ‘sufficiently large’. This statement relies on the individual random variable distributions having finite expectations and variances.

The variance of a random variable, X , is a measure of the expected deviation from the mean, or, expected value:

$$\text{var}(X) = \langle (X - \langle X \rangle)^2 \rangle = \langle X^2 \rangle - \langle X \rangle^2. \quad (3.7)$$

In order to compute the variance of our Monte Carlo estimator, we can rewrite Eq. 3.4 in terms of the independent random variables, X_i (which are distributed according to the $G(x)$ distribution), as

$$f_N = \frac{1}{N} \sum_{i=1}^N f(X_i), \quad (3.8)$$

where f_N denotes the estimator for N samples. If we identify the values of x_i as the random variate from each of the identically distributed random variables, X_i , we can see that, $\langle f(X_i) \rangle = \langle f(x) \rangle$, and the estimator has the same expectation value as that of the function, i.e. $\langle f_N \rangle = \langle f(x) \rangle$. Our estimator also has a variance, which by virtue of the CLT, will tend to a Gaussian with a standard deviation:

$$\sigma_{\text{MC}}^2 = \text{var}(f_N) = \text{var} \left(\frac{1}{N} \sum_{i=1}^N f(X_i) \right). \quad (3.9)$$

We can compute the variance of the sum over random variables using the identity

$$\text{var} \left(\sum_{i=1}^N a_i Z_i \right) = \sum_{i=1}^N a_i^2 \text{var}(Z_i) + 2 \sum_{i < j} a_i a_j \text{cov}(Z_i, Z_j), \quad (3.10)$$

where $\text{cov}(Z_i, Z_j)$ denotes the covariance between the random variables Z_i and Z_j , and a_i, a_j are the corresponding numerical coefficients. If the covariance is

positive, Z_i and Z_j are said to be positively correlated, and if negative, Z_i and Z_j are negatively correlated. Most importantly, if the two random variables are independent $\text{cov}(Z_i, Z_j) = 0$; which is indeed the case for $f(X_i)$. Additionally, each of the $f(X_i)$ share a common variance, $\text{var}(f(X_i)) = \text{var}(f(x)) = \sigma_f^2$. As such, we can write

$$\sigma_{\text{MC}}^2 = \frac{1}{N^2} \sum_{i=1}^N \text{var}(f(x_i)) = \frac{1}{N^2} \sum_{i=1}^N \text{var}(f(x)) = \frac{\sigma_f^2}{N}. \quad (3.11)$$

The standard error σ_{MC} is a measure of discrepancy between the value of the estimator and the true mean. As the estimator approaches a Gaussian for sufficiently large N , as per the CLT, σ_{MC} adopts a probabilistic interpretation: that the quantity $\langle f_N \rangle \pm \sigma_f / \sqrt{N}$ represents the value of our integral with a confidence interval of 68.3% (or 95.4% and 99.7% within two and three standard deviations respectively).

This advertises a big selling point of Monte Carlo techniques: for a d -dimensional integral, the convergence rate is still governed by the CLT and so the expected error does not depend on the dimension of the integral at all, only on the number of sampling points, as $1/\sqrt{N}$. This is in stark contrast to alternatives such as the trapezium and Simpson's rule (which rely on variations of Eq. 3.4). These quadrature rules converge as $N^{-2/d}$ and $N^{-4/d}$ respectively [128]. We can see that the convergence rate of Monte Carlo integration grants us an advantage for integrals with dimensions above $d = 4$ and $d = 8$; dimensions which are rapidly reached in the phase space integral for a reaction producing as few as three or four particles.

A second practicality of Monte Carlo techniques is in their flexibility. Whereas alternative numerical integration methods set out to calculate an integral - and that integral only - Monte Carlo methods can produce any desired distribution from a set of phase-space points. We simply 'book' a histogram for the quantity in question as a function of a phase-space variable, with the numerical value of the integrand evaluation (typically multiplied by a weight, corresponding to the particular techniques used in sampling the integrand) [129].

With this generality in-mind, and given that we seldom know the analytic form of σ_f , the variance of the Monte Carlo integration can be estimated using the

sample values themselves, with

$$\sigma_{\text{MC}} \simeq \frac{1}{\sqrt{N}} \sqrt{\frac{1}{N} \sum_{i=1}^N f(x_i)^2 - \left(\frac{1}{N} \sum_{i=1}^N f(x_i) \right)^2}. \quad (3.12)$$

It should be noted however, that whilst this formula is simple enough, it can lead to numerical difficulties, particularly when $\sigma_{\text{MC}} \ll |I|$. In this case there can be large round-off errors from ‘catastrophic cancellation’, where one subtracts two nearly equal numbers.

3.1.1 Hit-or-Miss Monte Carlo

The Hit-or-Miss Monte Carlo method is the simplest Monte Carlo integration technique. In essence, we estimate the area under a function $f(x)$ by integrating over some other function, $ck(x)$ (where c is a constant), with a larger but known area - usually a hyperrectangle. These functions need only satisfy the condition

$$0 < f(x) \leq ck(x), \quad (3.13)$$

for all values of x in the domain of integration. In order to show how hit-or-miss integration works, we first note that

$$I = \int_{x_1}^{x_2} f(x) dx = \int_{x_1}^{x_2} \int_0^{f(x)} dy dx. \quad (3.14)$$

Thus, sampling x according to the density $f(x)$ is the same as a uniform selection of (x, y) in the area $x_1 < x < x_2$, $0 < y < f(x)$. If we randomly choose uniformly distributed (x, y) points such that they lie under the curve $y = ck(x)$, then a fraction of these points will also lie under $y = f(x)$. This fraction will be equivalent to the ratio of the areas under $f(x)$ and $ck(x)$. If we identify $ck(x)$ with the maximum value of $f(x)$, $\max(f(x)) \equiv f_{\text{max}}$, we have

$$I = \int_{x_1}^{x_2} \int_0^{f(x)} dy dx = \int_{x_1}^{x_2} \int_0^{f_{\text{max}}} \Theta(f(x) - y) dy dx, \quad (3.15)$$

where $\Theta(f(x) - y)$ is the Heaviside step function, constraining $f(x)$ to be larger than y . We have therefore rephrased our original integration of $f(x)$, to be a two-dimensional integration of a Heaviside step function over the region $(x_1, x_2) \times (0, ck(x) = f_{\text{max}})$. Then, using Eq. 3.6, we can estimate I by determining the volume of our sampling region and $\langle \Theta(f(x) - y) \rangle$. The volume of

our sampling region is simply the area under the curve $ck(x)$,

$$\int_{x_1}^{x_2} \int_0^{f_{\max}} dy dx = (x_2 - x_1) f_{\max}. \quad (3.16)$$

The expected value of our Heaviside step function is

$$\langle \Theta(f(x) - y) \rangle = \frac{N_{\text{accepted}}}{N} \equiv H, \quad (3.17)$$

where N_{accepted} is the number of sampled points, (x, y) , for which the argument of our Heaviside step function is satisfied and N is the number of 'attempted' points. Then we can write down the estimate for the integral, I , along with its associated error, as

$$I_{\text{HM}} = (x_2 - x_1) f_{\max} \left[H \pm \sqrt{\frac{H - H^2}{N}} \right], \quad (3.18)$$

where we have used the fact that

$$\langle \Theta(f(x) - y)^2 \rangle = \langle \Theta(f(x) - y) \rangle. \quad (3.19)$$

As an example let's consider the integral [130]

$$I = \int_0^1 \frac{4}{1+x^2} dx = \left[4 \tan^{-1}(x) \right]_0^1 = \pi, \quad (3.20)$$

where $f(x) = 4/(1+x^2)$, on the domain $x \in [0, 1]$, which integrates to π . With this integrand we can rewrite Eq. 3.18 as

$$\begin{aligned} I_{\text{HM}} &= (x_2 - x_1) \left[\langle f(x) \rangle \pm \sqrt{\frac{\frac{(x_2 - x_1) f_{\max}}{(x_2 - x_1)} \langle f(x) \rangle - \langle f(x) \rangle^2}{N}} \right], \\ &= \pi \pm \sqrt{\frac{f_{\max} \pi - \pi^2}{N}} \simeq 3.14 \pm \frac{1}{\sqrt{N}} 1.64 \end{aligned} \quad (3.21)$$

where we have used the relation,

$$H = \frac{(x_2 - x_1)}{(x_2 - x_1) f_{\max}} \langle f(x) \rangle, \quad (3.22)$$

to replace the expected value of our Heaviside step function with that of the integrand. We can see that the accuracy of the hit-or-miss integration technique

depends not only on the expectation of the integrand, but on the area of our overestimate, $ck(x)$. This is clearly not an efficient way to calculate the value of π , as roughly 100 times more samples are needed to reduce the error of our estimate by one decimal place. We shall see in the next section, that the Crude Monte Carlo method has an improved accuracy.

3.1.2 Crude Monte Carlo

Crude Monte Carlo is a more direct application of Eq. 3.3 and Eq. 3.4. If we once again consider the integral in Eq. 3.20, we can see

$$\begin{aligned}
 I &= \int_{x_1}^{x_2} \frac{4}{1+x^2} dx = (x_2 - x_1) \int_{x_1}^{x_2} \frac{4}{1+x^2} \frac{1}{(x_2 - x_1)} dx \\
 &= (x_2 - x_1) \int f(x)g(x) dx = (x_2 - x_1) \langle f(x) \rangle \\
 &\simeq (x_2 - x_1) \frac{1}{N} \sum_{i=1}^N f(x_i), \tag{3.23}
 \end{aligned}$$

where $g(x)$ is the probability density function (PDF) corresponding to the $G(x)$ distribution function introduced in Eq. 3.2, $f(x) = 4/(1+x^2)$ and $x_1 = 0$, $x_2 = 1$. From this we can see that Crude Monte Carlo integration of Eq. 3.20 involves repeatedly sampling values of x randomly and uniformly across the domain of integration, and subsequently taking the average of all integrand evaluations. The Crude Monte Carlo estimate for the integral, with its associated error, is

$$\begin{aligned}
 I_{CMC} &= (x_2 - x_1) \left[\langle f(x) \rangle \pm \sqrt{\frac{\langle f(x)^2 \rangle - \langle f(x) \rangle^2}{N}} \right] \\
 &= \pi \pm \sqrt{\frac{2(2+\pi) - \pi^2}{N}} \simeq 3.14 \pm \frac{1}{\sqrt{N}} 0.64. \tag{3.24}
 \end{aligned}$$

It is important to note that unlike with the hit-or-miss Monte Carlo technique, the Crude Monte Carlo error only depends on the integrand itself. We can see from Eq. 3.21 and Eq. 3.24 that the Crude Monte Carlo technique will be more efficient than the hit-or-miss method if $f_{\max} > 2(2+\pi)/\pi$. This is indeed true, and furthermore we see from the definition of our overestimate in Eq. 3.13, that for a rectangular integration area, f_{\max} is the minimum value that $ck(x)$ can take. For this particular integral, the Crude Monte Carlo method requires a factor of about 6.5 fewer samples to reach the same accuracy.

3.2 Sampling

In the previous section we discussed calculating integrals using Monte Carlo methods, and in particular, the notion of recasting an integral as the average of its integrand. During this discussion we spoke loosely of sampling, i.e. generating points according to a distribution (see for instance Eq. 3.2). With this in-mind it is instructive to write the $f(x)$ mean with the sampling distribution, $p(x)$, made explicit:

$$\langle f(x) \rangle = \int f(x) dP(x) = \int f(x) p(x) dx, \quad (3.25)$$

where $p(x) = dP(x)/dx$. The basic building block of Monte Carlo methods is a reliable source of uniform random numbers on the domain $[0, 1]$, which we shall denote as \mathcal{R} throughout this work. Accordingly, the rest of this section will be concerned with utilising such a source to explore sampling strategies, in particular to acquire non-uniform random variables. We will focus on sampling by inversion, acceptance-rejection sampling and sampling from discrete distributions.

3.2.1 Sampling by Inversion

The method of sampling by inversion is a way to generate values according to a probability density function (PDF), such as $p(x)$ [131]. This is achieved by integrating the PDF and inverting the corresponding cumulative distribution function (CDF), $P(x)$.

The PDF of a continuous variable is related to the CDF by

$$P(x) = \int_{-\infty}^x p(x') dx' = \mathcal{P}(X \leq x), \quad (3.26)$$

where the distribution of the random variable X is completely specified through its CDF and $\mathcal{P}(X \leq x)$ is the probability that X is less than or equal to x . For a proper distribution, $P(\infty) = 1$ and $P(-\infty) = 0$, which results if $p(x)$ is appropriately normalised and by its nature as a PDF, $p(x)$ satisfies $p(x) \geq 0$ for all values of x . It follows from these stipulations that $P(x)$ is monotonically non-decreasing. If we generate a random number \mathcal{R} and put $X = P^{-1}(\mathcal{R})$, then

$$\mathcal{P}(X \leq x) = \mathcal{P}(P(P^{-1}(\mathcal{R})) \leq P(x)) = \mathcal{P}(\mathcal{R} \leq P(x)) = P(x), \quad (3.27)$$

i.e. the random variable X has the same distribution as $p(x)$, and by extension, $P(x)$.

More generally, one can generate the distribution of a $p(x)$ which is not explicitly normalised to unity. We first notice that if $p(x)$ is defined for x in the domain $[x_1, x_2]$, and is positive-definite, the probability $\mathcal{P}(x_1 \leq X < x)$ should be a fraction of the total probability $\mathcal{P}(x_1 \leq X < x_2)$ ¹. Then, we can determine x using [13]

$$\int_{x_1}^x p(x') dx' = \mathcal{R} \int_{x_1}^{x_2} p(x') dx' = \mathcal{R}(P(x_2) - P(x_1)) = P(x) - P(x_1), \quad (3.28)$$

which can be solved for x in terms of the inverse of the CDF:

$$x = P^{-1}(P(x_1) + \mathcal{R}[P(x_2) - P(x_1)]). \quad (3.29)$$

It is clear that through this Monte Carlo procedure of randomly generating an x value, the normalisation (which makes $p(x)$ a true PDF) is implicit in the result. Namely, $P(x_2) - P(x_1)$ normalises $p(x)$. If we write the normalised form of $P(x)$ in Eq. 3.28 as $\bar{P}(x) = (P(x) - P(x_1)) / (P(x_2) - P(x_1))$, i.e. $\bar{P}(x)$ is a proper cumulative distribution, then we see that

$$x = P^{-1}(P(x_1) + \mathcal{R}[P(x_2) - P(x_1)]) = \bar{P}^{-1}(\mathcal{R}), \quad (3.30)$$

such that we obtain a sample for x distributed according to $p(x)$.

We have already seen one example of a normalised distribution in Eq. 3.2, with the PDF

$$\bar{g}(x) = \frac{1}{x_2 - x_1}, \quad (3.31)$$

defined on the interval x_2 to x_1 , such that $g(x) = 0$ everywhere else. The CDF, $\bar{G}(x)$, has the form

$$\bar{G}(x) = \int_{x_1}^x \bar{g}(x') dx' = \frac{x - x_1}{x_2 - x_1}, \quad (3.32)$$

and is equal to unity if we integrate $\bar{g}(x)$ over the entire interval. This result can be inverted (after setting $\bar{G}(x) = \mathcal{R}$ as per Eq. 3.27) to obtain x ,

$$x = \bar{G}^{-1}(\mathcal{R}) = x_1 + \mathcal{R}(x_2 - x_1), \quad (3.33)$$

¹Another way of phrasing this, is that we can construct a distribution from any positive-definite function, which are commonly encountered when performing an integration.

so that we can use \mathcal{R} to sample values from a uniform distribution between $[x_1, x_2]$. This shows that uniform distributions are related by a rescaling and subsequent translation (as \mathcal{R} is itself a uniform distribution on $[0, 1]$). It is also worth noting that in the aforementioned discussions, we can equally replace \mathcal{R} by $1 - \mathcal{R}$, which is useful for inverting some distributions.

3.2.2 Rejection Sampling

Whilst the technique of sampling by inversion may at first seem all-encompassing, it relies on our PDF having an invertible integral. Often, finding an explicit formula for $x = F^{-1}(\mathcal{R})$, for the CDF of a density $f(x)$, is not possible. Rejection sampling can be viewed as an extension to the hit-or-miss Monte Carlo method, where we do not specify $ck(x) = f_{\max}$, but allow $ck(x)$ to take a more general form. The target and overestimate distributions must satisfy Eq. 3.13:

$$f(x) \leq ck(x), \quad (3.34)$$

with $c \geq 1$; this condition on the constant, c , arises as a result of the target and overestimate density normalisations². In practice we would like $k(x)$ to be ‘close’ to $f(x)$ and for c to be as close to unity as possible for efficiency. Akin to hit-or-miss Monte Carlo, rejection sampling chooses a value for x according to the overestimate, $k(x)$, and ‘accepts’ this value with a probability $f(x)/ck(x)$. It is the action of accepting / rejecting the generated value which corrects the sampling to our target distribution, $f(x)$. The rejection sampling algorithm to generate x , distributed as $f(x)$, is stated in Algorithm 1 below.

Algorithm 1: Rejection Sampling Algorithm

- 1 Generate a random variable, X , according to the PDF, $k(x)$, using \mathcal{R}_1
 - 2 **if** $\mathcal{R}_2 \leq f(x)/ck(x)$ **then**
 - 3 | Accept x as sampled value
 - 4 **else**
 - 5 | Goto line 1
-

In order to prove the validity of Algorithm 1, we must show that the conditional distribution of X , given the sampled value of x is accepted, reproduces

²We could just set $c = 1$, however we would rather maintain that $k(x)$ be a PDF in the true sense, with a normalisation equal to unity.

the distribution of our target PDF, $F(x)$. In other words, that

$$\mathcal{P}\left(X \leq x \mid \mathcal{R}_2 \leq \frac{f(X)}{ck(X)}\right) = F(x). \quad (3.35)$$

Using Bayes' theorem, this is equal to

$$\mathcal{P}\left(X \leq x \mid \mathcal{R}_2 \leq \frac{f(X)}{ck(X)}\right) = \frac{\mathcal{P}\left(\mathcal{R}_2 \leq \frac{f(X)}{ck(X)} \mid X \leq x\right) \mathcal{P}(X \leq x)}{\mathcal{P}\left(\mathcal{R}_2 \leq \frac{f(X)}{ck(X)}\right)}. \quad (3.36)$$

Looking at Algorithm 1, the number of times, N_{accepted} , that lines 1 and 3 need to be iterated, is itself a random variable which follows a geometric distribution: $\mathcal{P}(N_{\text{accepted}} = n) = p \times (1 - p)^{n-1}$, where we define p to be the probability that we accept the sampled x -value, $p = \mathcal{P}(\mathcal{R}_2 \leq f(X)/ck(X))$. This probability can be obtained by first conditioning on $X = x$. Then, integrating to obtain the marginal distribution, we find

$$p = \mathcal{P}\left(\mathcal{R}_2 \leq \frac{f(X)}{ck(X)}\right) = \int_{-\infty}^{\infty} \frac{f(x')}{ck(x')} k(x') dx' = \frac{1}{c}. \quad (3.37)$$

Following a geometric distribution, the random variable N_{accepted} has an expectation value of $1/p$, which highlights the associated inefficiency with this approach; that one typically has to cycle through c iterations of Algorithm 1 before accepting a sampled value. It is then clearly advisable to choose our overestimate density, $k(x)$, so as to minimise the constant c whilst retaining its invertibility. Furthermore, one can show that

$$\mathcal{P}\left(\mathcal{R}_2 \leq \frac{f(X)}{ck(X)} \mid X \leq x\right) = \frac{F(x)}{cK(x)}, \quad (3.38)$$

where $F(x)$ and $K(x)$ are the CDFs corresponding to $f(x)$ and $k(x)$ respectively. Using Eq. 3.36, we find

$$\begin{aligned} \mathcal{P}\left(X \leq x \mid \mathcal{R}_2 \leq \frac{f(X)}{ck(X)}\right) &= \mathcal{P}\left(\mathcal{R}_2 \leq \frac{f(X)}{ck(X)} \mid X \leq x\right) \times \frac{K(x)}{1/c} \\ &= F(x), \end{aligned} \quad (3.39)$$

proving that the recipe of Algorithm 1 recovers the desired distribution.

3.2.3 Sampling Discrete Distributions

A commonly encountered situation when using Monte Carlo methods is the need to sample one of a finite set of elements. We stated in Section 3.2.1 that a given CDF is related to its corresponding PDF through

$$P(x) = \int_{-\infty}^x p(x') dx', \quad (3.40)$$

for a continuous variable. The situation of a discrete distribution is contained in this as a special case. If we say the variable X takes discrete values x_1, \dots, x_n and that $X = x_i$ with probability p_i , then we can write

$$p(x) = \sum_i^n p_i \delta(x - x_i). \quad (3.41)$$

Then the probability that X is below or equal to a value x_k is

$$\mathcal{P}(X \leq x_k) \equiv P_k = \sum_{i=1}^k p_i, \quad (3.42)$$

where P_k is the discrete analogue of the cumulative distribution function. In the case that p_i are normalised, their sum is equal to unity, and each element of the set x_i can be chosen with a corresponding selection weight, p_i . Consequently, a method for sampling a given element from this set is to attribute a portion of the range $[0, 1]$ to each element, with a size directly proportional to its weight. Then using a uniform random number, \mathcal{R} , we can choose one of these portions. Specifically, if we represent the portion i by R_i , we can iterate through all of the portions using

$$R_{i+1} = R_i - p_{i+1}, \quad (3.43)$$

where $R_0 = \mathcal{R}P_n$, until $R_{i+1} < 0$. It is then the $(i + 1)$ -th element that is selected. Written another way, we choose i such that

$$\frac{P_i}{P_n} < \mathcal{R} < \frac{P_{i+1}}{P_n}, \quad (3.44)$$

which corresponds to an \mathcal{R} generated within the portion associated with the $(i + 1)$ -th element. Written in this form, Eq. 3.44 holds even for cumulative distribution functions with unnormalised weights (where $P_n = 1$ if they are normalised).

The ability to sample from discrete distributions is especially pertinent in the context of Section 2.3. We saw that the trace of the amplitude operator can be written as a sum of complex matrix elements. Each term of this sum can be identified by a pair of colour flow basis tensors. As the total number of basis tensors increases factorially with each emission, the set of tensors over which we sum quickly becomes intractable, and we can approximate the summation using Monte Carlo methods, as we shall discuss further in Chapter 4.

3.3 Importance Sampling

In Section 3.1.1 and 3.1.2 we reviewed the hit-or-miss and Crude Monte Carlo methods. We noted how, at least for the example function $f(x) = 4/(1 + x^2)$, the Crude Monte Carlo method was superior with a lower variance.

The integral we considered was simple, however other functions can have large variations in their value, which lead to a large uncertainty in the Monte Carlo estimate. The issue with large variations in the value of our function is tied to our sampling density. If we consider a function $f(x)$ with multiple peaks, then in uniformly sampling x values, we spend a great deal of time sampling regions which do not contribute significantly to the total integral estimate. On the other hand, if we sample from a density which closely describes $f(x)$, we will choose a large number of points in regions of the sampling space where the function is largest.

Doing this mathematically corresponds to a change of integration variables. If we consider Eq. 3.25, we can write

$$\langle f(x) \rangle_p = \int f(x)p(x)dx = \int \frac{f(x)p(x)}{k(x)}k(x)dx = \langle w(x)f(x) \rangle_k, \quad (3.45)$$

where $w(x) = p(x)/k(x)$ and the subscript on our averages denotes the chosen sampling distribution. In other words, we can recast the expectation of our integrand according to a different distribution. Then, by choosing $k(x)$ wisely, we will sample more points in regions where $f(x)$ is largest, which is then compensated for by reducing the function values in these regions. Ideally, these reweighted function values are close to a constant value, for which we would have zero variance. But at the very least, we have to choose $k(x)$ in such a way that the product of the Jacobian (of our change of integration variable) and the integrand itself, result in a smaller variance than the Crude Monte

Carlo method.

The estimate function $k(x)$ must fulfill certain conditions to be of practical use. Firstly, $k(x)$ must be non-negative everywhere in the integration region, whenever $f(x)p(x) \neq 0$. Looking at Eq. 3.45, one would be concerned about the eventuality that $k(x) = 0$, however as our change of variables indicates that we sample x according to $g(x)$, these points are never generated. There is however, still the risk that $k(x)$ is very small in a region where $f(x)p(x)$ is not, which results in large contributions to the average and in general to the variance as well.

Secondly, the integral of $k(x)$ (its CDF) must be known analytically and be invertible. The class of functions which satisfy this need is quite small - mainly trigonometric functions, exponentials, logarithms and low-degree polynomials. Failing this, we must be able to use alternate methods to generate random numbers according to the distribution of $k(x)$. However, in doing so, one must be careful not to introduce a large variance as a consequence. All of this serves to highlight the problem-dependent art of choosing a sensible form for $k(x)$.

The variance of our importance-sampled average is

$$\text{var} (w(x)f(x))_k = \langle (w(x)f(x))^2 \rangle_k - \langle w(x)f(x) \rangle_k^2, \quad (3.46)$$

where from Eq. 3.45 we can see $\langle w(x)f(x) \rangle_k^2 = \langle f(x) \rangle_p^2$. This demonstrates that in order to obtain better accuracy using importance sampling, we require $\langle (w(x)f(x))^2 \rangle_k < \langle f(x)^2 \rangle_p$.

The importance-sampled estimate for the integral, with its associated error, is

$$I_{IS} = (x_2 - x_1) \left[\langle w(x)f(x) \rangle_k \pm \sqrt{\frac{\langle (w(x)f(x))^2 \rangle_k - \langle w(x)f(x) \rangle_k^2}{N}} \right] \quad (3.47)$$

Returning once again to our example integration - where we wish to integrate $f(x) = 4/(1+x^2)$ between $x_1 = 0$ and $x_2 = 1$ - we can choose a sampling function with the form $k(x) = \frac{1}{3}(4-2x)$, which is a reasonable estimate of the shape of $f(x)$. Indeed, $\langle (w(x)f(x))^2 \rangle_k < \langle f(x)^2 \rangle_p$, and with this choice, the integral and estimate are given by

$$I_{IS} = 3.14 \pm \frac{1}{\sqrt{N}} 0.08. \quad (3.48)$$

This is a substantial improvement on the hit-or-miss and Crude Monte Carlo methods, requiring a factor of 64 fewer points to achieve the same accuracy as Crude Monte Carlo.

3.4 Random Number Generators

Thus far in our discussion of Monte Carlo methods, we have repeatedly used a source of uniform random numbers, \mathcal{R} . However, we have done so without defining how it can actually be implemented. One way of obtaining random numbers is to use natural random processes, for example measuring radioactive particle emission or thermal noise - a fun example being Cloudflares' lava-lamp wall used for `LavaRand` [132]. Measurements of such processes would have to be subject to the removal of any detection biases. And any remaining biases could be sufficient to cause the resulting physical numbers to fail tests for randomness. In addition to this, the rate of producing a stream of random numbers in this way is sufficiently slow that they are not really practical for Monte Carlo purposes. Owing to these setbacks, pseudorandom sequences are used in practice.

These sequences of numbers are generated by pseudo-random number generators (PRNG) and are deterministic, by their nature of being produced in software. The quality of randomness in the number sequences can be assessed by tests: two examples being the frequency test and gap test [133]. There is no one standard assessment to check this, and the requirements of a PRNG can depend greatly on the context in which they are used. A basic definition of a random number sequence, is that it is uniformly distributed over all possible values with each number being independent of those generated before it [134]. In the context of Monte Carlo techniques, the deterministic nature of PRNG's is actually one of their key assets. It means we can produce reliably fast and reproducible sequences of numbers. The latter point is vital in developing tools which rely on a source of randomness, whilst still allowing the user to distinguish internal errors. The majority of modern random number generators take a seed value as input (which is what enables the aforementioned reproducibility) and are based on recursions using modular arithmetic. One of the simplest and well-known forms of PRNG are the Linear Congruential Generators (LCGs). These are defined by the recurrence [135]

$$x_i = (a + b \times x_{i-1}) \bmod M. \quad (3.49)$$

This algorithm determines a sequence of at most M random numbers (known as the PRNG's period, whereafter the sequence starts to repeat itself), where the values of a , b and the modulus, M , specify the algorithm. The value of x_0 is the chosen seed; which is the only source of randomness in an LCG. If the a , b and M parameters are poorly chosen (with a particularly illustrative example being `RANDU` [136]), the period can be significantly less than M . Nevertheless, this algorithm badly violates the independence of successive groups of random numbers, i.e. there is a high degree of correlation between successive elements and its use has been heavily discouraged. This approach has since been surpassed and there are a number of very good and thoroughly tested generators. They quickly produce many random numbers and have portable implementations. One such PRNG is the Mersenne Twister [137], MT19937, which has a period of $P = 2^{19937} - 1$. This is the random number generator used by `CVolver`, which we shall discuss in Chapter 4.

3.5 Parton Showers

Event generators play a key role in particle physics, acting as the phenomenological bridge between the theoretical ideal and experimental reality. To do this, they make heavy use of the Monte Carlo methods we have outlined thus far.

The large phase space at the LHC can typically lead to the creation of $\mathcal{O}(100)$ particles. With their aim of simulating such processes, event generators must produce high multiplicity final states. Indeed, a fundamental component of event generators is their parton shower, which does just this, by performing approximate calculations of cross sections in the most dominant regions of phase space. To exemplify this, we shall briefly review the phenomenon of angular ordering, which gives rise to a parton branching process. Moreover, we shall outline the Monte Carlo algorithms used to simulate this branching process.

3.5.1 Angular Ordering

We showed in Section 1.4 how, in the soft limit, the terms associated with the emission of a real gluon off a quark anti-quark pair factorised from the Born

process, resulting in

$$d\sigma_1 = d\sigma_0 \frac{2\alpha_s}{\pi} \frac{dE_k}{E_k} \frac{d\Omega_k}{4\pi} C_F \omega_{q\bar{q}}(k), \quad (3.50)$$

where $d\Omega_k$ is the solid angle element for the emitted parton with four-momentum k and energy E_k . Furthermore, in Section 1.4.2 we showed that the eikonal approximation is valid for both the $q \rightarrow qg$ and $g \rightarrow gg$ splittings with the same effective vertex Feynman rule. The corresponding expression for the one-emission cross section is identical, with a colour factor of C_A instead of C_F . Consequently, the general differential cross section for a process with n hard external partons, and a real eikonal gluon emission can be written as

$$d\sigma_{n+1} = d\sigma_n \frac{\alpha_s}{\pi} \frac{dE_k}{E_k} \frac{d\Omega_k}{4\pi} \sum_{i,j} C_{ij} \omega_{ij}(k), \quad (3.51)$$

where we sum over all pairs of n coloured hard partons, $\{i, j\}$ and C_{ij} is the colour factor associated with each pair. For three or fewer coloured particles, these colour factors can be rewritten in terms of Casimir operators. We write the dipole function as

$$\omega_{ij}(k) = \frac{1 - \cos \theta_{ij}}{(1 - \cos \theta_{ik})(1 - \cos \theta_{jk})}, \quad (3.52)$$

where θ_{ab} is the separating angle between partons a and b . Our dipole function can be separated into two parts, each containing a leading collinear singularity, by adding and subtracting pole-like terms:

$$\omega_{ij}(k) = \omega_{ij}^{[i]}(k) + \omega_{ij}^{[j]}(k), \quad (3.53)$$

where

$$\omega_{ij}^{[i]}(k) = \frac{1}{2} \left(\omega_{ij}(k) + \frac{1}{1 - \cos \theta_{ik}} - \frac{1}{1 - \cos \theta_{jk}} \right), \quad (3.54)$$

and $\omega_{ij}^{[j]}(k)$ can be obtained by swapping the i and j parton labels in the above equation. Suppose we substitute the dipole function in Eq. 3.51 with Eq. 3.52 and write the solid angle element in terms of the polar and azimuthal angles with respect to the direction of parton i , $d\Omega_k = d \cos \theta_{ik} d\phi_{ik}$. Carrying out the azimuthal integration first, we find

$$\int_0^{2\pi} \omega_{ij}^{[i]}(k) \frac{d\phi_{ik}}{2\pi} = \frac{1}{1 - \cos \theta_{ik}} \Theta(\theta_{ij} - \theta_{ik}). \quad (3.55)$$

This means that each of the two terms, $\omega_{ij}^{[i]}$ and $\omega_{ij}^{[j]}$, describe radiation which is confined to a cone. The first is a cone centred on the direction of parton i , which extends to parton j . After instead averaging over ϕ_{jk} , the term $\omega_{ij}^{[j]}$ is a cone centered on j , extending to i . Using this we can rewrite Eq. 3.51 as

$$d\sigma_{n+1} \simeq d\sigma_n \frac{\alpha_s}{2\pi} \frac{dE_k}{E_k} \sum_{i,j} C_{ij} \left[\frac{d \cos \theta_{ik}}{1 - \cos \theta_{ik}} \Theta(\theta_{ij} - \theta_{ik}) + \frac{d \cos \theta_{jk}}{1 - \cos \theta_{jk}} \Theta(\theta_{ij} - \theta_{jk}) \right]. \quad (3.56)$$

We can see that the cross section possesses the property of angular ordering, i.e. that the soft emission pattern from each leg i and j is confined to a cone which has an angle less than their pairwise opening angle. This characteristic ordering is an example of a coherence effect which is common to all gauge theories (known as the Chudakov effect in QED [138]; the effect of decreased ionisation losses for narrow electron-positron pairs). Angular ordering in QCD is a direct result of colour coherence. In words, if we consider an emission off a pair of coloured partons i and j which are close in angle, their azimuthally-averaged incoherent radiation is limited to cones of half-angle θ_{ij} . In the wide angle limit, i and j give a coherent contribution proportional to the total colour charge of the pair. The physical interpretation is that the emitted gluon does not have sufficient resolving power to differentiate i and j , and hence can be computed as if it were emitted from their parent parton.

Eq. 3.56 can be interpreted as arising from a parton branching process, where the successive emission angles are ordered in a sequence of decreasing angles. The factorised form of Eq. 3.56 means one can iteratively generate any number of final-state emissions, accounting for the leading soft gluon enhancements to all orders. This process is known as a parton shower.

One finds a similar pattern of factorisation, of the matrix and phase-space elements, in the collinear limit. This can also be developed into a parton branching formalism, albeit describing collinear enhancements to all orders. In fact, one can show that these collinear enhancements can be incorporated into Eq. 3.56 [49, 139], by considering a single leg, i or j , and replacing

$$\frac{dE_k}{E_k} \rightarrow C_{li} P_{li}(z) dz, \quad (3.57)$$

where $P_{li}(z)$ are the set of universal, but flavour-dependent, azimuthally-

averaged unregularised Altarelli-Parisi (AP) splitting functions [140]. The function $P_{li}(z)$ reflects the collinear splitting of a parton $i \rightarrow l + k$, where z is defined as the energy fraction E_k/E_i , and C_{li} is the corresponding colour factor. This results in the following differential distribution [141, 142]:

$$d\sigma_{n+1} \simeq d\sigma_n \frac{\alpha_s}{2\pi} \frac{d\tilde{\zeta}}{\tilde{\zeta}} C_{li} P_{li}(z) dz, \quad (3.58)$$

where $\tilde{\zeta}$ is an ordering variable, proportional to $1 - \cos \theta_{lk}$. So that each emission can be treated independently, it is necessary to strongly order in $\tilde{\zeta}$. One would naively expect a parton shower built on Eq. 3.58 to only accurately describe collinear radiation. However, using the opening angle between l and k as our ordering variable, Eq. 3.58 treats both the leading-colour soft and collinear enhancements correctly. Of course, extending the treatment of soft-gluons to full-colour was the subject of Chapter 2 and its Monte Carlo implementation will be discussed in Chapter 4.

We notice that the integral over the $d\sigma_{n+1}$ differential cross section can contain divergences in both $\tilde{\zeta}$ and z . In order to iteratively generate emissions, we must tame such divergences to produce a well-defined probability distribution. The singular regions occur where partons are infinitely collinear or soft. But these scenarios are degenerate with the one in which an emission did not occur at all. One can then introduce the notion of resolvable and unresolvable emissions, segregated by resolution criteria. Then the contribution from resolvable radiation is finite, whilst the as-of-yet uncalculated virtual corrections ensure that their combination with unresolvable emissions is also finite. The two contributions are related through unitarity [142]:

$$\mathcal{P}(\text{resolvable}) + \mathcal{P}(\text{unresolvable}) = 1. \quad (3.59)$$

Denoting the cutoff limits on z as z^+ and z^- , we can use Eq. 3.58 to write down the probability that parton i will undergo a branching to $l + k$, within the range $\tilde{\zeta}$ to $\tilde{\zeta} + d\tilde{\zeta}$ as

$$d\mathcal{P}_{\text{res}} = \sum_l \frac{d\tilde{\zeta}}{\tilde{\zeta}} \int_{z^-}^{z^+} \frac{\alpha_s}{2\pi} C_{li} P_{li}(z) dz, \quad (3.60)$$

which is the distribution for resolvable emissions. The sum, indexed by l , runs over all possible branchings of particle i . The complement of $d\mathcal{P}_{\text{res}}$ is the probability of no branching in an infinitesimal increment of the evolution variable. In the limit that $d\tilde{\zeta} \rightarrow 0$, this exponentiates and we can define $\Delta(\tilde{\zeta}|\tilde{\zeta}_H)$ as the probability of no emission between $\tilde{\zeta}_H$ and $\tilde{\zeta}$. This follows the differential

equation

$$\frac{d\Delta(\zeta|\zeta_H)}{d\zeta} = \Delta(\zeta|\zeta_H) \frac{d\mathcal{P}_{\text{res}}}{d\zeta}. \quad (3.61)$$

Solving the above equation gives us the form of the exponential function [13]:

$$\Delta(\zeta|\zeta_H) = \exp \left[- \int_{\zeta}^{\zeta_H} \frac{d\zeta'}{\zeta'} \int_{z^-}^{z^+} \frac{\alpha_s}{\pi} \sum_l C_{li} P_{li}(z) dz \right], \quad (3.62)$$

which is the well-known Sudakov form factor [143]. Thus, to generate the first emission we use the probability distribution in Eq. 3.61 to write the probability that a branching occurs at ζ , as

$$\frac{d\mathcal{S}_P(\zeta|\zeta_H)}{d\zeta} = - \frac{d\Delta(\zeta|\zeta_H)}{d\zeta} = \Delta(\zeta|\zeta_H) \frac{d\mathcal{P}_{\text{res}}}{d\zeta}. \quad (3.63)$$

This is what we would intuitively expect: the probability that the first resolvable emission should occur at ζ is the product of the probability of no emission between ζ_H and ζ , and the probability that an emission subsequently occurs at ζ . One could then theoretically sample an emission according to this distribution, using the methods of Section 3.2. In particular, we could sample by inversion, and solve:

$$\int_{\zeta}^{\zeta_H} \frac{d\mathcal{S}_P(\zeta'|\zeta_H)}{d\zeta'} d\zeta' = \Delta(\zeta|\zeta_H) = \mathcal{R}. \quad (3.64)$$

However, in practice, obtaining a solution to the above equation is not straightforward as it requires the integrated splitting kernels in the exponent to be inverted. An alternative involves generating an emission according to a crude Sudakov form factor, with an overestimated splitting kernel which is invertible. To correct the sampling distribution back to the nominal Sudakov form factor, we use rejection sampling methods. This process of sampling is the Sudakov veto algorithm and shall be discussed in the next section.

3.5.2 Veto Algorithm

In the previous section, we started with the form for the soft gluon one-emission cross section and showed how it could lead to a coherent parton branching formalism, culminating in a statement of the Sudakov form factor used in traditional partons showers. The formulation of these showers is intrinsically Markovian, where each branching depends only on the emitted parton and its parent, which as we have seen is well-suited to Monte Carlo

techniques. We wish to generate an ordered sequence of values for the evolution variable according to the Sudakov form factor distribution function. The veto algorithm, a variant of the rejection sampling technique, is useful in achieving this [13, 108, 144].

Written simply, we wish to generate emissions according to a distribution of the form

$$P_f(q) = f(q) \exp \left[- \int_q^Q f(q') dq' \right] = f(q) \Delta_f(q|Q), \quad (3.65)$$

where $f(q)$ is the emission kernel, typically the AP splitting kernels, and q is a generic evolution variable. Given a hard scale, Q , we wish to generate a value $q < Q$. If $f(q)$ has a primitive function with a known inverse, the problem is straightforward, and we can simply adopt the methods of Section 3.2.1 to obtain

$$q = F^{-1}(\ln(\mathcal{R}) + F(Q)). \quad (3.66)$$

Of course, life is rarely so simple and $f(q)$ is often not invertible. In this case, we adopt the approach of Section 3.2.2 and find an overestimate kernel, $k(x)$ (where we have set $c = 1$ for simplicity sake), which can be solved using the inverse transform method, where

$$P_k(q) = k(q) \Delta_k(q|Q), \quad (3.67)$$

and $f(q) \leq k(q)$ for all $q \geq 0$. However, a straightforward application of the rejection sampling algorithm would not correctly take into account the effects of the exponential in $P_f(q)$. Instead, one can use the veto algorithm depicted in Algorithm 2.

Algorithm 2: Veto Algorithm

```

1  $i \leftarrow 0$ 
2  $q_i \leftarrow Q$ 
3 Loop
4    $i \leftarrow i + 1$ 
5    $q_i \leftarrow K^{-1}(\ln(\mathcal{R}) + K(q_{i-1}))$ , i.e. according to  $k(q)$ , but with the
   constraint that  $Q > q_i > q_{i-1}$ 
6   if  $\mathcal{R} \leq f(x)/k(x)$  then
7      $q \leftarrow q_i$ 
8   return  $q$ 

```

Considering the first few steps in this algorithm is instructive and will help us

see that sampling in this fashion reproduces the distribution in Eq. 3.65. The probability that q is accepted on the first sampling attempt, is given by

$$P_{k,1}(q) = k(q) \Delta_k(q|Q) \frac{f(q)}{k(q)} = f(q) \Delta_k(q|Q). \quad (3.68)$$

This is simply the probability that a value of q is chosen according to the distribution $P_k(q)$ multiplied by the probability, $f(q)/k(q)$, that this value is accepted. If we now consider the case where one intermediate scale, q_1 , is rejected, we find

$$P_{k,2}(q) = \int_q^Q k(q_1) \Delta_k(q_1|Q) \left[1 - \frac{f(q_1)}{k(q_1)}\right] k(q) \Delta_k(q|q_1) \frac{f(q)}{k(q)} dq_1, \quad (3.69)$$

which is the following probabilities multiplied together: the probability that q_1 is the first selected value, the probability that q_1 is subsequently rejected (the terms in-between square brackets), the probability that q is selected starting with a hard scale, q_1 , and the probability that q is accepted. We must also integrate over all possibilities for the intermediate scale, q_1 . Utilising the identity, $\Delta_k(q_1|Q) \Delta_k(q|q_1) = \Delta_k(q|Q)$, $P_{k,2}(q)$ simplifies to

$$P_{k,2}(q) = P_{k,1}(q) \int_q^Q [k(q_1) - f(q_1)] dq_1. \quad (3.70)$$

More generally we have to consider $n - 1$ intermediate times, $q \leq q_{n-1} \leq \dots \leq q_1 \leq Q$, where we write the result for $P_{k,n}$, as

$$\begin{aligned} P_{k,n}(q) &= P_{k,1}(q) \times \prod_{i=0}^{n-1} \int_q^{q_i} [k(q_{i+1}) - f(q_{i+1})] dq_{i+1} \\ &= \frac{1}{(n-1)!} \left(\int_q^Q [k(q') - f(q')] dq' \right)^{(n-1)} P_{k,1}(q). \end{aligned} \quad (3.71)$$

The last equality is due to the symmetry of the integrand, which allows us to recast the limits of integration. We can see the simplest example of this by considering $P_{k,3}$: the integral limits are $q < q_2 < q_1$ and $q_2 < q_1 < Q$. This is equivalent to integrating over the region $q < q_2 < Q$, $q < q_1 < Q$ and including an over-counting symmetry factor of $1/2$, such that the integrals over q_1 and q_2 decouple and become equal. This extends to any value of n , carrying a corresponding symmetry factor of $1/n!$.

Remembering that $P_{k,n}$ is the probability to accept a sampled q value after the n th attempt, the total probability to accept q at any iteration of the algorithm is the sum over all possible n values. With the aforementioned generalisation to hand, we can write the total probability as

$$\begin{aligned}
 P(q) &= \sum_{i=1}^{\infty} P_{k,i}(q) = P_{k,1}(q) \sum_{i=1}^{\infty} \frac{1}{(n-1)!} \left(\int_q^Q [k(q') - f(q')] dq' \right)^{(n-1)} \\
 &= f(q) \exp \left[- \int_q^Q k(q') dq' \right] \exp \left[\int_q^Q (k(q') - f(q')) dq' \right] \\
 &= f(q) \Delta_f(q|Q), \tag{3.72}
 \end{aligned}$$

showing that the veto algorithm samples q values according to the target distribution in Eq. 3.65. Whilst we have exhibited the veto algorithm for one variable, $f(q)$ is often a multivariable function, $f(q, z)$. The methods described here are easily generalised if one can find an overestimate function $k(q, z)$ which encapsulates both variables. The $k(q)$ function used in Algorithm 2 can be obtained as the marginal distribution of $k(q, z)$.

3.5.3 Competition Algorithm

In the previous section, we laid down the Sudakov veto algorithm for a single emission kernel, $f(q)$. We can see from Eq. 3.60 that for each emission, its progenitor can evolve down multiple branching channels, each characterised by their own branching kernel, $f_i(q)$. Including competing processes in the veto algorithm requires a modification known as the competition algorithm [145].

The overall probability of branching at some scale q is the sum of these kernels:

$$f(q) = \sum_i f_i(q). \tag{3.73}$$

One can then write a distribution for selecting the scale, q , of the next branching as

$$P_f(q) = \sum_i f_i(q) \exp \left[- \int_q^Q \sum_i f_i(q') dq' \right], \tag{3.74}$$

and each separate branching process follows the distribution

$$P_f^i(q) = f_i(q) \exp \left[- \int_q^Q f_i(q') dq' \right] = f_i(q) \Delta_{f_i}(q|Q), \quad (3.75)$$

which has the same form as Eq. 3.65. The competition algorithm involves generating a scale, q_i , for each competing process and selecting the highest. Showing then proceeds, using this scale and emitting according to the process i . Algorithm 3 summarises this process.

Algorithm 3: Competition Algorithm

- 1 Generate $\{q_1, \dots, q_m\}$ from $P_f^i(q)$, where $i = 1, \dots, m$, e.g. using the veto algorithm
 - 2 $q \leftarrow q_j = \max\{q_1, \dots, q_m\}$
 - 3 Evolve shower using the scale q and the process j
-

In order to see why Algorithm 3 produces the distribution in Eq. 3.74, we recall that the Sudakov form factor, $\Delta_{f_i}(q|Q)$, is the probability that an emission has not occurred between the scales Q and q . Consequently, the probability that we sample a scale q_j from $P_f^j(q)$, for each of m possible processes, and the i -th process produces the highest scale, is

$$\sum_{i=1}^m \left[\int_0^Q \prod_{j=1}^m dq_j f_j(q_j) \Delta_{f_j}(q_j|Q) \right] \prod_{k \neq i} \Theta(q_i > q_k) \delta(q - q_i), \quad (3.76)$$

where the sum over m is present, as any one of the processes could produce the largest sampled value of q_i . This reduces to

$$\begin{aligned} & \sum_{i=1}^m f_i(q) \Delta_{f_i}(q|Q) \prod_{j \neq i} \Delta_{f_j}(q|Q) \\ &= \sum_i f_i(q) \exp \left[- \int_q^Q \sum_i f_i(q') dq' \right] \\ &= P_f(q), \end{aligned} \quad (3.77)$$

reproducing the target distribution for q .

Equipped with the knowledge of this chapter, we shall move on to discuss **CvO1ver**: the Monte Carlo implementation of the general evolution algorithm explored in Chapter 2.

Chapter 4

CVolver

Chapter 2 presented a general evolution algorithm which encapsulates algorithmic and recursive definitions of QCD amplitudes, describing the full-colour radiation of multiple soft gluons, including virtual corrections to all orders. Subsequently, we explored the colour structures one encounters when solving the evolution equations, in the context of the colour flow basis. This culminated in expressions for the matrix elements of colour charge and colour charge product operators (for given external legs i and j , see Eq. 2.62 and 2.66) that are essential in determining contributions from emission and Sudakov operators. Using these results, the equivalence of the aforementioned general evolution algorithm (in the leading- N_c limit) to the BMS equation was shown. Furthermore, we organised contributions to the cross section into a series of powers in N_c to make manifest the large- N_c limit and successive corrections to it.

There have been numerous efforts in recent years to address subleading colour contributions in the context of parton shower algorithms [146–152] in an effort to improve on the accuracy of existing simulations [10, 11, 15, 153]. The work [146] for instance, modifies the leading- N_c dipole shower algorithm implementation within Herwig [53] to include colour suppressed contributions by an iterative use of so-called colour matrix element corrections. As opposed to a leading- N_c dipole shower, any pair of partons are allowed to radiate. This amounts to a correction of the emissions to include the exact colour correlations and is performed for the first handful of emissions, resorting to a traditional leading- N_c shower afterwards.

In this chapter, we shall bring together the concepts and results established in previous chapters, to present the practical implementation of a new Monte Carlo code, `CVolver`¹. This code simulates high-energy particle collisions including colour correlations beyond the leading-colour approximation. It currently showers electron-positron collision events in the context of a specific non-global observable: the ‘jet veto’ observable. However, the framework is more robust and can be readily extended to more general observables.

We shall begin in Section 4.1 with a review of the general evolution algorithm in Chapter 2 and describe how one can use Monte Carlo techniques to sample over intermediate colour states, through the insertion of the unit operator between successive real emission and virtual correction operators. A great deal

¹CVolver stands for Colour Virtual Evolver and originates from the studies first presented in [154].

of thought has been devoted to writing `CVolver` in a maximally modularised fashion, largely to reflect the structure of the evolution algorithm itself, but also with the view to generalising `CVolver` to a multi-purpose event generator. As such, we will devote a good deal of time in Section 4.2 to reviewing the C++ class structure of `CVolver` and describing how the colour index book-keeping in the colour flow basis of Section 2.2.1 is implemented (in Section 4.2.2). This will form the basis for defining an archetype C++ class of a colour evolution operator, e.g. a Sudakov or emission operator, in Section 4.2.3. These building blocks form the foundation for a shower evolution algorithm, which will be outlined in its most general form in Section 4.2.4. Much of Section 4.2 will be discussed in an observable-independent way, with the aim of providing a broad overview of both the `CVolver` code, and the numerous challenges of implementing the results of Chapter 2. These challenges are addressed analytically, alongside their concrete implementations in subsequent sections. In particular, the colour charge operator and colour product matrix elements (pertaining to the anomalous dimension matrix and emission operators) from Chapter 2 shall be reformulated into the colour flow basis in Sections 4.3.1 and 4.3.4. Most importantly, we shall review how the soft anomalous dimension matrix can be approximately exponentiated through the summation of subsequent towers of large- N_c contributions in Section 4.3.1. There is an inherent need, when sampling over intermediate colour states, to perform this in an efficient manner. We shall therefore dedicate Section 4.4 to discussing how colour states are selected for Sudakov matrix elements. Lastly, after all of the vital components of `CVolver` have been discussed, its two modus operandi (denoted as Variant A and Variant B) are covered in-detail in Sections 4.5.3 and 4.5.4. Where code is directly commented on, the reader may find it useful to refer to the `CVolver` UML diagrams provided in Appendix A.

In order to make the rest of this chapter more readable, we would like to remind the reader of nomenclature. In the following, roman letters are used to denote indices of external legs, whilst greek letters, those of colour or anti-colour lines (the letters are barred in the latter case). When colour indices are discussed in a context in which an anti-colour index would also be applicable, only one will be described with the implications for the other left implicit. If a distinction between a colour and anti-colour line is necessary, it will be provided to the reader. The mapping operator, providing the correspondence between an external leg, i , and a colour index, α , is written as c_i , whilst the inverse mapping is c_α^{-1} . The greek letters σ , τ and ρ are reserved to represent the

colour state before and after the action of a colour operator. In the case where amplitude and conjugate-amplitude matrix elements are discussed concomitantly, these tensors will be barred to denote the latter. An example of this is $[\tau | \mathbf{T}_i | \sigma] \langle \bar{\sigma} | \mathbf{T}_j | \bar{\tau} \rangle$. The object N_c is reserved to denote the number of colours, whilst N and n are used in the context of summations to represent the number of partons and the number of colour flows respectively. The values of these context-dependent quantities will be specified where necessary.

4.1 Algorithmic Overview

In Chapter 2 we presented an iterative algorithm for summing the leading soft-gluon logarithms to all orders for a general scattering process. We begin this section by recapitulating the key results of Chapter 2. The differential cross section for n soft-gluon emissions can be written as

$$d\sigma_n = \text{Tr} \mathbf{A}_n d\Pi_n, \quad (4.1)$$

where the operators \mathbf{A}_n satisfy the recurrence relation

$$\mathbf{A}_n(E) = \mathbf{V}_{E,E_n} \mathbf{D}_n^\mu \mathbf{A}_{n-1}(E_n) \mathbf{D}_{n\mu}^\dagger \mathbf{V}_{E,E_n}^\dagger \Theta(E \leq E_n), \quad (4.2)$$

and $\Theta(E \leq E_n)$ denotes the Heaviside function imposing energy ordering. For hard scattering processes with two or more coloured particles in both the initial and final state, the inclusion of Coulomb exchanges is necessary. However, in this chapter we only consider two-jet production off a colour singlet. As such, the Sudakov operator takes on a simpler form (than Eq. 2.6) and is given by

$$\mathbf{V}_{a,b} = \exp \left[-\frac{\alpha_s}{\pi} \ln \left(\frac{b}{a} \right) \sum_{i < j} (-\mathbf{T}_i \cdot \mathbf{T}_j) \int \frac{d\Omega_k}{4\pi} \frac{n_i \cdot n_j}{(n_i \cdot n_k)(n_j \cdot n_k)} \right], \quad (4.3)$$

where the vector, n_i , is light-like with a spatial part that is the unit vector in the direction in which particle i travels. The integral is over the direction of the, similarly light-like, vector n_k . A subset of terms in the Sudakov exponent is the soft anomalous dimension matrix:

$$\mathbf{\Gamma} = \frac{\alpha_s}{\pi} \sum_{i < j} (-\mathbf{T}_i \cdot \mathbf{T}_j) \int \frac{d\Omega_k}{4\pi} \frac{n_i \cdot n_j}{(n_i \cdot n_k)(n_j \cdot n_k)}. \quad (4.4)$$

The value of α_s is taken to be fixed throughout this chapter and the real emission operator is identical to that stated in Eq. 2.3,

$$\mathbf{D}_i^\mu = \sum_j \mathbf{T}_j \frac{n_j^\mu}{n_j \cdot n_i} \quad (4.5)$$

and the phase-space element is

$$d\Pi_n = \prod_{i=1}^n \left(-\frac{\alpha_s}{\pi} \frac{dE_i}{E_i} \frac{d\Omega_i}{4\pi} \right). \quad (4.6)$$

We remind the reader that the sum over partons in the operator definitions of $\mathbf{V}_{a,b}$ and \mathbf{D}_i^μ are context-specific, running over all prior soft-gluon emissions and the partons of the original hard scattering (the colour charge operator, \mathbf{T}_j , is in a representation of $SU(3)_c$ dependent on this multiplicity). The soft-gluon evolution described by Eq. 4.2 proceeds iteratively, starting from the hard-scattering operator $\mathbf{H} = |\mathcal{M}\rangle \langle \mathcal{M}|$, such that

$$\mathbf{A}_0(E) = \mathbf{V}_{E,Q_H} \mathbf{H} \mathbf{V}_{E,Q_H}^\dagger. \quad (4.7)$$

We restate that the trace of the amplitude operator in colour-space, Eq. 4.1, is

$$\text{Tr} \mathbf{A}_n = \sum_{\sigma, \tau} [\tau | \mathbf{A}_n | \sigma] \langle \sigma | \tau \rangle, \quad (4.8)$$

and that a general observable, Σ , can be computed using

$$\Sigma(\mu) = \int \sum_n d\sigma_n u_n(\{k\}_n), \quad (4.9)$$

where n is the multiplicity of emitted soft-gluons and u_n are the observable-dependent measurement functions with $\{k\}_n$ denoting the set of soft-gluon momenta. Whilst we have adopted energy-ordering throughout this work, the algorithm can be adapted to account for a different ordering variable. The infrared regulator μ should be taken to 0 in Eq. 4.9, however we showed in Section 2.1 that if the observable is fully inclusive over gluon emissions with the ordering-variable less than some scale $E < Q_0$, we can set $\mu = Q_0$.

It was shown in Section 2.2.2 that by using a dual basis, such that $\langle \alpha | \beta \rangle = |\alpha\rangle \langle \beta| = \delta_{\alpha\beta}$, we can insert the unit operator between successive real emission

and virtual correction operators to calculate the trace in Eq. 4.8. Particularly we showed $\mathbf{R}|\alpha\rangle = C_R^{\alpha,\beta}|\beta\rangle$, where \mathbf{R} is a colour-line or colour-line product operator, and $C_R^{\alpha,\beta} = [\beta|\mathbf{R}|\alpha\rangle$. This result can be used recursively to strip-off evolution operators leaving behind a string of C-coefficients and reduced matrix elements. Anticipating this pattern, we can also act in reverse and build an evolution cascade around the hard scattering matrix element by inserting these C-coefficients. The real emission and virtual correction operators contain multiple colour operators and as such, can map a given basis tensor to a multiplicity of others. One can then adopt Monte Carlo techniques to sample over these potential colour states. Figure 4.1 illustrates this process.

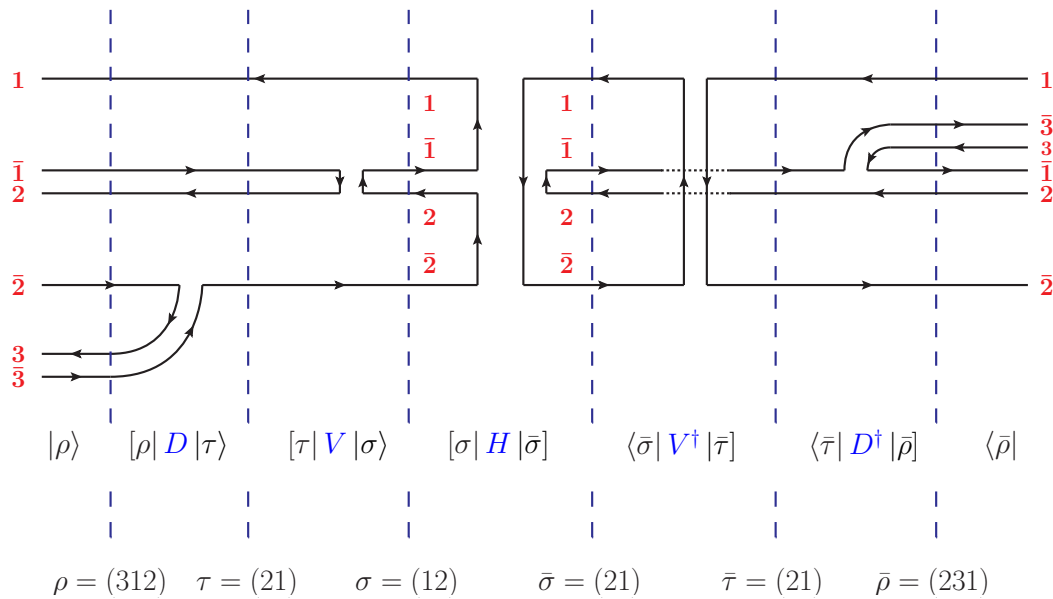


FIGURE 4.1: One contribution to the \mathbf{A}_1 operator, starting from the $|12\rangle [12] \mathbf{H} |21\rangle \langle 21|$ term in the $q\bar{q} \rightarrow q\bar{q}$ hard scattering. It corresponds to a single gluon emission and a single virtual gluon exchange in both the amplitude and conjugate-amplitude. The vertical dotted lines identify the intermediate colour states. The algorithm works iteratively outwards, starting from the hard process in the middle and multiplying emission and Sudakov matrix elements as it goes. Figure used in [155].

It is useful to walk through the evolution shown in Figure 4.1, working outwards from the hard process matrix element in the middle, to summarise the **CVolver** evolution strategy. We begin by selecting initial colour flows, σ and $\bar{\sigma}$ from the set of all possible basis tensors and compute the corresponding hard scattering matrix element $[\sigma|\mathbf{H}|\bar{\sigma}]$. In the case of the $q\bar{q} \rightarrow q\bar{q}$ process depicted in Figure 4.1, there are two potential colour arrangements in both the ampli-

tude and conjugate amplitude,

$$|\mathcal{M}\rangle \langle \mathcal{M}| = |12\rangle [12 | \mathbf{H} | 12] \langle 12| + |12\rangle [12 | \mathbf{H} | 21] \langle 21| \\ + |21\rangle [21 | \mathbf{H} | 12] \langle 12| + |21\rangle [21 | \mathbf{H} | 21] \langle 21|. \quad (4.10)$$

After computing the hard scattering matrix element, the momentum of the first real emission is chosen. In anticipation of inserting Sudakov operators that act in both the amplitude and the conjugate (which evolve from the hard scale Q_H down to the energy of the emitted gluon, E_1), we choose two new colour flows τ and $\bar{\tau}$. The flows τ and $\bar{\tau}$ are chosen from all possible tensors that can be accessed after the action of a Sudakov operator. Subsequently, the colour flows ρ and $\bar{\rho}$ are chosen from the set of all possible tensors that are accessible after the action of an emission operator. The hard process, Sudakov and emission matrix elements are then all multiplied together. This whole process repeats until the evolution terminates, which can be after having reached a predetermined maximum multiplicity or infrared cutoff². One last Sudakov operator evolves the last emission down to this cutoff scale. The final product of matrix elements must be further multiplied by the scalar product matrix $\langle \sigma_m | \bar{\sigma}_m \rangle$, where m labels the final colour flows.

One can rewrite Eq. 4.2 explicitly in terms of matrix elements, such that one step in the evolution (as depicted in Figure 4.1) is determined by

$$M_{\rho\bar{\rho}}(E) = -\frac{\alpha_s}{\pi} \frac{dE}{E} \frac{d\Omega}{4\pi} \sum_{\substack{\tau, \sigma \\ \bar{\tau}, \bar{\sigma}}} [\rho | \mathbf{D}_E | \tau] [\tau | \mathbf{V}_{E,E'} | \sigma] \\ \times M_{\sigma\bar{\sigma}}(E') \langle \bar{\sigma} | \mathbf{V}_{E,E'}^\dagger | \bar{\tau} \rangle \langle \bar{\tau} | \mathbf{D}_E^\dagger | \bar{\rho} \rangle. \quad (4.11)$$

In Eq. 4.11, E is the energy of the latest emission and E' is that of the previous one. This expression is the core of our implementation and it provides a map from a pair of colour flows $(\sigma, \bar{\sigma})$ to the pair $(\rho, \bar{\rho})$. The starting amplitude (before any emission or virtual exchange takes place) is $M_{\sigma\bar{\sigma}} = [\sigma | \mathbf{H}(Q_H) | \bar{\sigma}]$ and in the case of zero emissions,

$$M_{\rho\bar{\rho}}(\mu) = [\rho | \mathbf{V}_{\mu, Q_H} | \sigma] [\sigma | \mathbf{H}(Q_H) | \bar{\sigma}] \langle \bar{\sigma} | \mathbf{V}_{\mu, Q_H}^\dagger | \bar{\rho} \rangle. \quad (4.12)$$

In implementing Eq. 4.11 into a Monte Carlo code, there are a number of chal-

²It was shown in Section 2.1.1, that for certain observables, we can replace the infrared cutoff with a veto scale. This is true for the jet veto observable we consider here.

lenges that must be overcome. First, is the most obvious need to calculate the real emission and virtual gluon correction matrix elements which involves computing matrix elements of the forms $[\tau | \mathbf{T}_i | \sigma \rangle$ and $[\tau | \mathbf{T}_i \cdot \mathbf{T}_j | \sigma \rangle$. We have already expressed such elements in Section 2.3. However it is more convenient, for a code implementation, to express these matrix elements in terms of colour and anti colour indices as opposed to external leg indices. This translation is expressed analytically in Section 4.3. Secondly, is the challenge of computing the Sudakov matrix elements, $[\tau | \mathbf{V} | \sigma \rangle$, which involves the exponentiation of a possibly large and sparsely populated colour matrix. The evaluation can be considerably simplified if we are prepared to sum terms accurate only to order $1/N_c^d$, where d is a positive integer, while keeping the leading diagonal terms proportional to $(\alpha_s N_c)^n$ to all orders, n . Larger values of d will lead to more accurate calculations of the Sudakov matrix elements, at the cost of taking longer to compute. This challenge, along with the rephrasing of the anomalous dimension matrix elements as a sum over colour and anti colour indices, is addressed in Section 4.3.1. Additionally, there are algorithmic challenges associated with the calculation of Eq. 4.11. One is the way in which we choose the basis tensors that result from an evolution operator (be it a real emission or virtual exchange), i.e. the matrix elements or C-coefficients we wish to calculate. The set of all possible tensors that are accessible after the action of a Sudakov or emission operator is determinable. However, given the factorially increasing size of colour-space with the number of emissions, care must be taken to sample from this set in an efficient way. Particularly, sampling along the most important trajectories in colour-space. A method of sampling a basis tensor, $|\tau \rangle$, d swaps from $|\sigma \rangle$ is discussed in Section 4.4. As we shall see, this is particularly useful in determining matrix elements of the Sudakov operator, but is also used to determine emission matrix elements in Variant A of CVolver. An alternative emission matrix element sampling, which forms part of the Sudakov veto algorithm with competition, is presented for Variant B in Section 4.5.4.

The jet veto cross section is an interesting observable containing non-global logarithms, that is sensitive to wide-angle, soft-gluon production and thus provides a good test of the CVolver framework. It was the focus of [18, 19] and was discussed in the introduction to Chapter 2: one vetoes events that have one or more particles radiated into some fixed angular region with energy greater than the veto scale, Q_0 . It is part of the class of observables discussed in Section 2.1.1. Both Variant A and Variant B implementations focus on this observ-

able for the production of either a $q\bar{q}$ pair, or a pair of gluons (gg), with total energy $2Q_H$ in their zero momentum frame (ZMF). In this work, we shall apply the veto on particle production to the central in-gap region ($-\pi/4 < \theta < \pi/4$) in the zero momentum frame (ZMF) of the primary two-jet system. We refer to these as $V \rightarrow q\bar{q}$ (production off a colour singlet gauge boson) and $H \rightarrow gg$ (Higgs decay to gluons), throughout this work. It is worth noting that these cross sections are independent of the details of the initial state, so long as it is a colour singlet. And, that like most non-global observables, the summation of even the leading logarithms with full colour accuracy has not yet been achieved in parton showers.

Before we move onto discussing solutions to the aforementioned challenges, and the variant implementations, it is useful to take a detour and give a broad overview of the `CVolver` code structure so that the implementations of these solutions can be put into context.

4.2 CVolver Structure

Eq. 4.11 lies at the heart of our implementation and numerous challenges in computing Eq. 4.11 have been highlighted. This section aims to provide a broad overview of the `CVolver` structure so that solutions to these challenges in subsequent sections can be contextualised. As such, this section will discuss a number of representative functions without concrete definitions, with the knowledge that they shall be defined in later sections, namely in discussions of Variant A (in Section 4.5.3) and Variant B (in Section 4.5.4).

4.2.1 CVolver Overview

The `CVolver` code is a collection of C++ classes which implement colour flow arithmetic and map the correspondence between the physical and colour flow regimes. Suffice it to say, the physical regime refers to the paradigm of labelling objects with external leg indices, such as the operators $\mathbf{T}_i \cdot \mathbf{T}_j$ in Eq. 4.3. The colour flow regime on the other hand, regards each colour or anti colour line as labelling an independent particle species and the colour charge products can be written as $\mathbf{T}_\alpha \cdot \mathbf{T}_\beta$, i.e. each gluon has a colour and anti colour line which can evolve independently. This correspondence shall be defined more explicitly for these operators in Section 4.3.1. Moreover, the `CVolver` code designates classes which calculate matrix elements of the operators in Eq. 4.2, and a class which drives the shower evolution, necessary to perform the colour

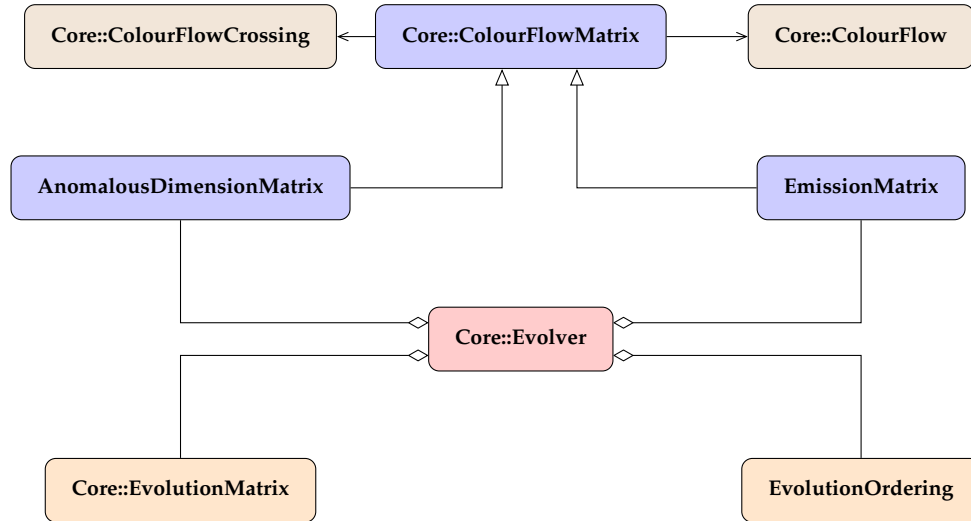
evolution in Eq. 4.11. The components of **CVolver** can be grouped into two sections, the **Core** and **Implementation** and both are needed to produce events. One can broadly think of the **Core** as implementing the colour algebra, whilst **Implementation** specifies kinematics and process-specific details. An example is the **Hemispheres**³ implementation of the jet veto observable, which will be discussed throughout this chapter.

Figure 4.2a provides a schematic overview of the components of **CVolver** which shall be discussed in this section. The blue boxes encapsulate the class hierarchy of the **AnomalousDimensionMatrix** and **EmissionMatrix** operator classes. It is the operator classes which tie **Core** to **Hemispheres**⁴, and as such we illustrate the entire inheritance hierarchy of the **Hemispheres::AnomalousDimensionMatrix** class in Figure 4.2b (which we shall discuss in more detail shortly). This inheritance hierarchy is typical of the class hierarchy for all four operator classes: the **AnomalousDimensionMatrix**, **EmissionMatrix**, **HardProcessMatrix** and **ScalarProductMatrix** classes (which shall be discussed in more depth in Section 4.2.3). **Core::ColourFlow** and **Core::ColourFlowCrossing** are classes associated with **Core::ColourFlowMatrix**. **Core::ColourFlowMatrix** delegates the responsibility of keeping track of colour flow permutations and the correspondence from the physical to colour flow regime to **Core::ColourFlow** and **Core::ColourFlowCrossing** respectively. The orange classes represent independent classes, for instance **Core::EvolutionMatrix**, which handles the Sudakov colour expansion (discussed in Section 4.3.1). The **EvolutionOrdering** box represents **Hemispheres::EvolutionOrdering**, which inherits from the abstract base class **Core::EvolutionOrdering**, and carries out the evolution scale selection (of which two variants are discussed in Section 4.5). The arrows in Figure 4.2a represent the relationships between classes. A black arrow represents an association, an open triangle denotes inheritance and an open diamond indicates an aggregation association. We refer to the reader to Appendix A for a more detailed discussion of these symbols.

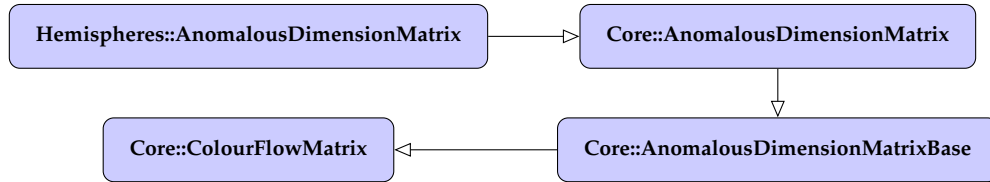
The **Core** implements observable-independent functionality, utilising abstract base classes to leave observable-dependent components as pure virtual methods to be defined within **Implementation**. An example of this dynamic polymorphism is exhibited in the **Hemispheres::AnomalousDimensionMatrix**

³This naming comes about, as the jet veto and (non-global part of the) hemisphere jet mass cross sections can be computed using the same **Implementation**; the veto region needs to be changed to $0 < \theta < \pi/2$ for the latter cross section.

⁴We shall distinguish classes sharing the same name in both **Core** and **Hemispheres** by using their scope, e.g. **Hemispheres::**, where necessary.



(A) The blue boxes denote the classes which represent the operators in Eq. 4.2 and their inheritance hierarchies. The beige and orange boxes represent independent classes which perform specific tasks, whilst the red box highlights the class, **Evolver**, which collates instantiations of all other classes, to conduct the shower evolution.



(B) The inheritance hierarchy of the **Hemispheres::AnomalousDimensionMatrix** class, represented by the **AnomalousDimensionMatrix** blue box in Figure (a). It is an example of the inheritance structure used for all operator classes in **Implementation**.

FIGURE 4.2: An overview of the **CVolver** code.

class within **Hemispheres**, which we shall look at in more detail, to get across the philosophy. **Hemispheres::AnomalousDimensionMatrix**, provides the definition for the pure virtual method **evaluate()**, which calculates the coefficients of the colour charge operators (in the physical regime) in Eq. 4.4, which we shall call Γ_{ij} for a pair of external legs (ij) for the time being (and which we will define in Section 4.3.1). **Hemispheres::AnomalousDimensionMatrix** inherits from another class, **Core::AnomalousDimensionMatrix**, which declares the pure virtual method **evaluate()** (as well as declaring all other observable-dependent methods). This way, **Core::AnomalousDimensionMatrix** has prototyped a necessary function to be defined in **Hemispheres**. The class **Core::AnomalousDimensionMatrix** is itself an abstract-base class which inherits from **Core::AnomalousDimensionMatrixBase**, defining observable-independent functionality⁵. **Core::AnomalousDimensionMatrix** implements the computation

⁵The distinction between the **Core::AnomalousDimensionMatrix** and **Core::AnomalousDimensionMatrixBase** classes has been highlighted here for completeness-sake, to explain their exact inheritance hierarchy. Specifically,

of soft-gluon anomalous dimension matrix elements and its components, Γ_σ , ρ and $\Sigma_{\tau\sigma}$ (which were schematically defined in the physical regime in Eq. 2.95, and shall be redefined in the colour flow regime in Section 4.3.1). These components are calculated by making use of the coefficients, Γ_{ij} , which are defined in `Hemispheres::AnomalousDimensionMatrix`.

The `Core::AnomalousDimensionMatrix` class inherits from `ColourFlowMatrix`; which is also part of `Core`. The `ColourFlowMatrix` class defines a template for all classes which represent an operator (such as the emission, Sudakov and scalar product matrix operators in Eq. 4.2). In particular, it provides (to all derived classes) the facility to make the correspondence between the physical and colour flow regime. For instance, it enables `Core::AnomalousDimensionMatrix` to make the correspondence between external leg indices and colour indices when calculating the $\gamma_{\alpha\beta}$ flow-decomposition coefficients (their relationship to Γ_{ij} is detailed in Section 4.3.1).

In addition to defining observable-dependent functionality, `Hemispheres` also defines global physical parameters, such as the QCD coupling, α_s (which we fix at 0.118), the infrared cutoff, μ , and the collinear cutoff, λ , which shall be placed into context in Section 4.5. Moreover, it specifies the event record (typed `EventRecordT`) and the random number generator (typed `RandomT`) to be used throughout the code. Additionally, the generation of new emission degrees of freedom and subsequent phase-space mapping, along with their sampling methods and the application of the measurement function are carried out in `Hemispheres::EmissionMatrix`.

Figure 4.2 also depicts the `Core::Evolver` class. It is the work horse of `CVolver`, driving the shower evolution. It collates instantiations of all the necessary classes and delegates tasks to them in the process of calculating each evolution step (of Eq. 4.11). Section 4.2.4 provides a walk-through of this process, denoting each task with a representative function. The point of this section is to link these functions to aspects of the code, whereas the actual forms of these functions shall be defined later in Sections 4.3.1, 4.3.4, 4.4 and 4.5 for two implementations of the jet veto observable: Variant A and Variant B.

With the above overview in-mind, a more detailed description of the

`Core::AnomalousDimensionMatrix` builds on `Core::AnomalousDimensionMatrixBase` to template the event record and random number generator class types, (`EventRecordT` and `RandomT`), and to declare the `evaluate()` pure virtual method. As they are both part of `Core`, this distinction is ultimately unnecessary and shall be dropped henceforth.

ColourFlow and **ColourFlowCrossing** classes is carried out in the following section. Subsequently, **ColourFlowMatrix** and its inheriting classes are detailed in Section 4.2.3, whilst the shower evolution algorithm (of **Evolver**) is outlined in Section 4.2.4.

4.2.2 Colour Flow Mapping And Arithmetic

In this section, we shall discuss the implementation of the **ColourFlowCrossing** and **ColourFlow** classes in the **Core** of **CVolver**. They keep track of and manipulate the correspondence between the colour flow and physical regime, and of the colour arrangement as the shower evolves. As such, the **EvolutionMatrix**, **EvolutionOrdering**, **Evolver** and all operator classes have access to them through their respective **crossing()** methods. We will closely follow the external leg, colour and anti colour index labelling conventions of Section 2.2.1.

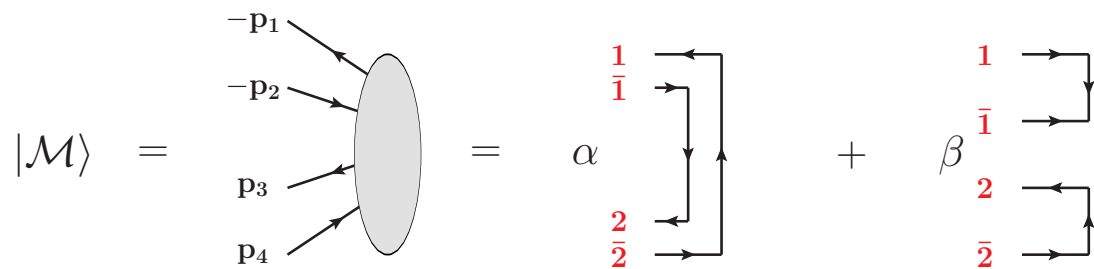


FIGURE 4.3: An example of the $q\bar{q} \rightarrow q\bar{q}$ process amplitude decomposed in the colour flow basis. Outgoing particles are represented by arrows to the left of the blob with positive momenta. Incoming particles are treated as if they were outgoing particles with negative momenta. Figure used in [155].

ColourFlowCrossing deals principally with two tables, **theReverseColourMap** and **theReverseAntiColourMap**. These tables map a particle index, i , to its corresponding colour (c_i) and/or anti colour index (\bar{c}_i). The constructor of this class takes two vectors of particle data as input, corresponding to incoming and outgoing particles. This data is then used by the method **fill()**, to populate these tables. To illustrate this process, Figure 4.3 depicts the amplitude for the $q\bar{q} \rightarrow q\bar{q}$ hard scattering process in the colour flow basis. Focusing on the blob-diagram, all particles are considered as outgoing, with negative momenta indicating incoming particles. The particle with incoming momentum p_1 is an anti-quark, that with incoming momentum p_2 is a quark whilst p_3 and p_4 label an outgoing quark and anti-quark respectively. Quarks and anti-quarks are represented by colour and anti-colour lines, whilst gluons are represented by

a pair of colour and anti-colour lines. Those particles which are incoming are treated as having a colour in the opposite representation, i.e. as pertaining to an anti colour line for an incoming quark. To account for the negative momenta of incoming particles, an appropriate crossing sign, $s_i = -1$ and /or $\bar{s}_i = -1$ for an incoming colour or anti colour line, is stored in `theColourCrossingSigns` and / or `theAntiColourCrossingSigns`. We note that in this work we do not consider initial-state radiation. The crossing signs are therefore always equal to 1 and shall henceforth be disregarded.

The populated tables `theReverseColourMap`, `theReverseAntiColourMap`, `theColourCrossingSigns` and `theAntiColourCrossingSigns` corresponding to this process are listed in Table 4.1. Two additional tables contained within `ColourFlowCrossing`, `theColourMap` and `theAntiColourMap`, are also listed. These tables act as inverse mappings of `theReverseColourMap` and `theReverseAntiColourMap` respectively.

<code>theReverseColourMap</code>		<code>theReverseAntiColourMap</code>	
i	c_i	\bar{i}	\bar{c}_i
1	1	2	1
3	2	4	2

<code>theColourCrossingSigns</code>		<code>theAntiColourCrossingSigns</code>	
c_i	s_i	\bar{c}_i	\bar{s}_i
1	-1	1	-1
2	1	2	1

<code>theColourMap</code>		<code>theAntiColourMap</code>	
c_i	i	\bar{c}_i	i
1	1	1	2
2	3	2	4

TABLE 4.1: Illustration of the tables contained within the `ColourFlowCrossing` class. They have been populated for the example process $q\bar{q} \rightarrow q\bar{q}$ presented in Figure 4.3. The label i denotes an external leg index, whilst c_i and \bar{c}_i specify the colour and anti colour indices to which i maps. s_i and \bar{s}_i denote the crossing sign attributed to a colour or anti colour index.

In order for external classes to interact with the mappings listed in Table 4.1, `ColourFlowCrossing` has a number of public access methods. These are listed, along with their function, in Table 4.2. As the shower evolves and gluons are

Method	Description of functionality
<code>colourLeg()</code>	Return the external leg index corresponding to a given colour index in <code>theColourMap</code> .
<code>antiColourLeg()</code>	Return the external leg index corresponding to a given anti colour index in <code>theAntiColourMap</code> .
<code>colourLine()</code>	Return the colour index corresponding to a given external leg index in <code>theReverseColourMap</code> .
<code>antiColourLine()</code>	Return the anti colour index corresponding to a given external leg index in <code>theReverseAntiColourMap</code> .
<code>coloured()</code>	Return true if the external leg index has a corresponding colour line index in <code>theReverseColourMap</code> .
<code>antiColoured()</code>	Return true if the external leg index has a corresponding anti colour line index in <code>theReverseAntiColourMap</code> .

TABLE 4.2: The public methods of the `ColourFlowCrossing` class, used by external classes to access the colour maps.

emitted, external classes require the facility to modify the tables contained within `ColourFlowCrossing`. This functionality is encoded through protected members, summarised in Table 4.3.

Method	Description of functionality
<code>addColourCrossing()</code>	Add a new colour index corresponding to a new external leg index in <code>theColourMap</code> , <code>theColourCrossingSigns</code> and <code>theReverseColourMap</code> .
<code>addAntiColourCrossing()</code>	Add a new anti colour index corresponding to a new external leg index in <code>theAntiColourMap</code> , <code>theAntiColourCrossingSigns</code> and <code>theReverseAntiColourMap</code> .
<code>addColourAntiColourCrossing()</code>	Add a new colour and anti colour index, both corresponding to the same new external leg index via <code>addColourCrossing()</code> and <code>addAntiColourCrossing()</code> .

TABLE 4.3: The protected methods of the `ColourFlowCrossing` class, used by external classes to manipulate the colour maps.

The `ColourFlow` class is used to describe a basis tensor and perform colour flow arithmetic on it. A basis tensor in the colour flow basis is labelled by a permutation, i.e. stating how all colour and anti colour lines are connected. Each

ColourFlow instantiation stores a permutation as a vector, `thePermutation`. This permutation can be represented as

$$|\sigma\rangle = \left| \begin{array}{ccc} 1 & \cdots & n \\ \sigma(1) & \cdots & \sigma(n) \end{array} \right\rangle, \quad (4.13)$$

where the vector index of `thePermutation` corresponds to a colour line (top row in Eq. 4.13) and the element contained at that vector index corresponds to the anti colour line (bottom row). The two basis tensors that describe the possible colour arrangements for the $q\bar{q} \rightarrow q\bar{q}$ hard process are illustrated on the right-hand side of Figure 4.3. In the first term, the incoming anti-quark is colour connected to the outgoing anti-quark and the incoming quark is colour connected to the outgoing quark. The second term is the only other possible colour arrangement. External classes utilise public methods in **ColourFlow** to perform colour flow arithmetic and access `thePermutation`. These are outlined in Table 4.4.

Method	Description of functionality
<code>scalarProduct()</code>	Determine the scalar product between the current basis tensor, $ \sigma\rangle$, and another, resulting in N_c^k . Return the power k .
<code>colour()</code>	Return the colour index that is connected to the given anti colour index in $ \sigma\rangle$.
<code>antiColour()</code>	Return the anti colour index that is connected to the given colour index in $ \sigma\rangle$.
<code>swap()</code>	Swap the two given anti colour indices in the permutation $ \sigma\rangle$.
<code>getTranspositionOf()</code>	Return the two anti colour indices that must be swapped to transform $ \sigma\rangle$ into a given basis tensor (that differs by at-most, one transposition).
<code>emitSinglet()</code>	Add another flow, labelled by $n + 1$, to $ \sigma\rangle$, such that $n + 1 = \overline{n + 1}$. See Figure 2.3b.
<code>emitFromColour()</code>	Emit a gluon from specified colour line in $ \sigma\rangle$. See Figure 2.3a.
<code>emitFromAntiColour()</code>	Emit a gluon from a specified anti colour line in $ \sigma\rangle$. See Figure 2.3a.

TABLE 4.4: The public methods of the **ColourFlow** class, used by external classes to manipulate colour flows and carry out colour flow arithmetic.

The **ColourFlow** class also provides comparison operators to test for equality between two basis tensors, and the functionality to produce the entire set of

basis tensors for a given number of colour flows.

4.2.3 Operator Classes

In the previous section we discussed the implementation of the `ColourFlowCrossing` and `ColourFlow` classes. The `ColourFlowMatrix` class utilises them to keep track of the correspondence between the physical colour flow regime and the colour flow arrangement throughout the shower evolution. Figure 4.1 illustrates how the operators in Eq. 4.11 can evolve this colour arrangement. Here, we will outline the `ColourFlowMatrix` class and all of its derived operator classes.

As an archetype for all operator classes, `ColourFlowMatrix` contains the method, `crossing()`, which is used to define (or access if it has already been defined) an instantiation of `ColourFlowCrossing`. Another method `includeCrossingSigns()` indicates whether crossing signs should be considered, i.e. if there are initial-state partons in the hard scattering.

Each operator in Eq. 4.11 has a corresponding abstract base class definition to enact the effect of the operator on colour flows. These are the `Core::AnomalousDimensionMatrix`, `Core::EmissionMatrix`, `Core::HardProcessMatrix` and `Core::ScalarProductMatrix` classes. They build on `ColourFlowMatrix` to define observable-independent methods which calculate matrix elements.

`Core::ScalarProductMatrix` implements the `exponent()` method to calculate the power, k , of the scalar product matrix element

$$S_{\sigma\bar{\sigma}} = \langle \sigma | \bar{\sigma} \rangle = N_c^k. \quad (4.14)$$

An additional method `element()` makes use of `exponent()` to return N_c^k itself.

The hard scattering process operator, \mathbf{H} , is inherently process-dependent. As such, `Core::HardProcessMatrix` only specifies pure virtual methods, to template the functionality that the inheriting class, `Hemispheres::HardProcessMatrix`, must define. These methods are `initialFlows() = 0`, `initialKinematics() = 0` and `element() = 0`. `initialFlows()` sets the starting flows of the evolution and `element()` calculates the initial matrix element corresponding to these flows. The basis tensors σ and $\bar{\sigma}$ and the matrix element, $[\sigma | \mathbf{H} | \bar{\sigma}]$, in Figure 4.1 are an example of this. The method `initialKinematics()` generates the degrees of freedom for the partons involved in the hard scattering. The pure virtual methods (denoted by $= 0$) are templates of observable-dependent

(and variant-dependent) functionality. Therefore, their precise forms will be discussed and expressed in Section 4.5.

Method	Description of functionality
<code>omega()</code>	Return the flow-decomposition coefficient for the given colour or anti colour lines (see the γ coefficients in Eq. 4.19) using <code>ColourFlowCrossing</code> .
<code>Omega()</code>	Calculate Γ_σ (see Eq. 4.23) for a given colour flow, σ .
<code>rho()</code>	Calculate ρ (see Eq. 4.24).
<code>Sigma()</code>	Calculate $\Sigma_{\tau\sigma}$ (see Eq. 4.25) for the given flows τ and σ .
<code>evaluate() = 0</code>	Evaluate the coefficients, Γ_{ij} , of each colour charge product in the Sudakov operator (see Eq. 4.16).
<code>evaluateNoScale() = 0</code>	Evaluate the coefficients of each colour charge product in the anomalous dimension matrix. These are the coefficients in <code>evaluate()</code> , with the energy-dependent terms neglected.
<code>nextFlows() = 0</code>	Generate the basis tensors to which the anomalous dimension matrix operator in the amplitude and conjugate evolve, i.e. which anomalous dimension matrix elements to calculate.

TABLE 4.5: The methods of the `Core::AnomalousDimensionMatrix` class.

The observable-independent functionality of `Core::AnomalousDimensionMatrix` and `Core::EmissionMatrix` is listed in Table 4.5 and 4.6. The analytic expressions for the objects that these methods calculate, such as Γ_σ and ρ , are postponed to Section 4.3.1 and 4.3.4 for a more in-depth discussion. Also listed are the pure virtual methods templating the observable-dependent functionality. Alike `Hemispheres::HardMatrix`, the precise forms for these methods are variant-dependent, and so shall be expressed in Section 4.5.

The `Core::AnomalousDimensionMatrix` class is templated with the type definitions for an event record, `EventRecordT`, and a random number generator, `RandomT`. This allows the event record and number generator implementations to be defined in `Hemispheres`, and subsequently specified in the `Hemispheres::AnomalousDimensionMatrix` derived class. `Core::EmissionMatrix`, being an operator class, follows the same construction as `Core::AnomalousDimensionMatrix` (the `Core::EmissionMatrix` class methods shall be discussed in Section 4.3.4). In practice, a single `ColourFlowCrossing`

instantiation is created to keep track of the colour maps in each event. This single instantiation is accessible (and initially set) in all operator classes via the inherited `crossing()` method from `ColourFlowMatrix`.

Method	Description of functionality
<code>omega()</code>	Return the flow decomposition coefficient in Eq. 4.42 for the given colour or anti colour line.
<code>omegaLR()</code>	Return the flow decomposition coefficient in Eq. 4.44 for the given pair of colour or anti colour lines.
<code>element()</code>	Calculate the emission matrix element in Eq. 4.40, in terms of flow decomposition coefficients, for the given colour flows σ and τ .
<code>elementLR()</code>	Calculate the cross section level emission matrix element in Eq. 4.45, in terms of flow decomposition coefficients, for the given colour flows σ , τ and $\bar{\sigma}$, $\bar{\tau}$.
<code>nextPhaseSpace() = 0</code>	Generate the new degrees of freedom for the next emission. If <code>element()</code> (and therefore <code>evaluate()</code> and <code>omega()</code>) are used, i.e. we are calculating amplitude-level matrix elements, also generate the polarisation vector.
<code>evaluate() = 0</code>	Evaluate the coefficients of each colour charge operator, $\omega_j(i)$, in the emission operator (see Eq. 4.42).
<code>evaluateLR() = 0</code>	Evaluate the coefficients of each colour charge product, $\omega_{ij}(k)$, resulting from the contraction of two emission operators at the level of the cross section. See Section 4.44
<code>nextFlowWeight() = 0</code>	Return the sum of weights, ζ_{ij} (see Eq. 4.94), for a given dipole (ij) and pair of basis tensors ($\tau, \bar{\tau}$ in Eq. 4.94) to emit from.
<code>nextFlows() = 0</code>	Generate the basis tensors to which the emission operator in the amplitude and conjugate evolve i.e. which emission matrix elements to calculate.
<code>updateCrossing() = 0</code>	Update the colour maps in the <code>colourFlowCrossing</code> instantiation to reflect the emission of a soft-gluon.

TABLE 4.6: The methods of the `Core::EmissionMatrix` class.

4.2.4 Shower Evolution

It is useful to pause and have a brief recap of the last two sections. With reference to Figure 4.2 and 4.3, we have discussed how a basis tensor, $|\sigma\rangle$,

is described by an instantiation⁶ of the `ColourFlow` class. Additionally, the correspondence between the physical and colour flow regime is mapped in an instantiation of the `ColourFlowCrossing` class. All operators in the evolution of Eq. 4.11 have their own class and through their inheritance from `ColourFlowMatrix`, can access a `ColourFlowCrossing` instantiation. Each operator class follows an inheritance hierarchy similar to that illustrated in Figure 4.2b for `Hemispheres::AnomalousDimensionMatrix`. We outlined the observable-independent methods of `Core::AnomalousDimensionMatrix`, which calculate matrix elements, and will be tied to analytic expressions in Section 4.3.1 and 4.3.4. The observable-dependence in `Hemispheres::AnomalousDimensionMatrix` will be detailed in Section 4.5.

In this section we shall discuss the `Evolver` class (the red box in Figure 4.2a), which is responsible for performing the shower evolution. We shall use a number of ‘reference functions’, such as E_n , W_{E_n} and α_n to denote separate tasks in carrying out one step of the evolution in Eq. 4.11. These will be related to class methods in this section, and to concrete implementations in subsequent sections. With this in-mind, let’s proceed to discussing the `Evolver` class.

Like `Core::AnomalousDimensionMatrix`, `Core::Evolver` is templated with the type definitions for the event record `EventRecordT` and a random number generator, `RandomT`. `Evolver` collates instantiations of the operator classes⁷ and utilises their methods to multiply chains of matrix elements as in Figure 4.1. It also orchestrates the sampling of kinematic parameters. The product of these matrix elements is stored using `currentAmplitude()` method. The weights produced through the use of Monte-Carlo techniques - sampling colour flows, scale generation or particle kinematics - is recorded in `currentWeight()`. A list of the `Evolver` class methods is presented in Table 4.7. The event evolution is conducted by two methods, `evolve()` and `evolveFull()`. The schematic outline of these methods is illustrated in Algorithm 4 and 5 respectively.

⁶i.e. to create an object of a given class.

⁷e.g. the `anomalousDimension()` method sets, or returns (if one has already been set) an instantiation of the `Hemisphere::AnomalousDimensionMatrix` class.

Method	Description of functionality
<code>crossing()</code>	Set or access the crossing, an instantiation of ColourFlowCrossing
<code>hardProcessMatrix()</code>	Set or access the hard process matrix operator class, an instantiation of HardProcessMatrix .
<code>evolutionMatrix()</code>	Set or access the evolution matrix operator class, an instantiation of EvolutionMatrix .
<code>anomalousDimension()</code>	Set or access the soft-gluon anomalous dimension matrix operator class, an instantiation of AnomalousDimensionMatrix .
<code>emissionMatrix()</code>	Set or access the emission operator class, an instantiation of EmissionMatrix .
<code>scalarProductMatrix()</code>	Set or access the scalar product matrix operator class, an instantiation of ScalarProductMatrix .
<code>maxEmissions()</code>	Set or access the maximum number of emissions.
<code>currentEvent()</code>	Set or return the event record (of type EventRecordT).
<code>currentAmplitude()</code>	Set or return the event amplitude.
<code>currentFlows()</code>	Set or return the outermost colour flows in the amplitude and conjugate-amplitude, considered in the event.
<code>currentWeight()</code>	Set or return the event weight.
<code>evolve()</code>	Generate an event, sampling over colour flows in Eq. 4.11, and return the resultant weight, amplitude and particle list.
<code>evolveFull()</code>	Generate an event, performing the full summation over tensors in Eq. 4.11, using numerical exponentiation of the soft-gluon anomalous dimension matrix and return the resultant weight, amplitude and particle list.

TABLE 4.7: The methods of the **Core::Evolver** class.

Algorithm 4: Overview of the `evolve()` algorithm in the `Evolver` class.

Input: `EventRecordT`: $\{\phi, w \in \mathbb{R}, E' \in \mathbb{R}, E \in \mathbb{R}, M \in \mathbb{C}, \sigma, \bar{\sigma}, \tau, \bar{\tau}, \rho, \bar{\rho}\}$

```

1  $\phi \leftarrow \phi_0, \{\sigma, \bar{\sigma}\} \leftarrow \{\alpha_0(\phi), \bar{\alpha}_0(\phi)\}, M_{\sigma, \bar{\sigma}} \leftarrow [\sigma | \mathbf{H} | \bar{\sigma}], E' \leftarrow Q_H, w \leftarrow w_{\text{hard}},$ 
    $n \leftarrow 0$ 
2 while  $n \leq n_{\text{max}}$  and  $u_n(\phi) > 0$  do
3    $E \leftarrow E_n(\phi, E', \{\sigma, \bar{\sigma}\})$ 
4    $w \leftarrow w \times W_{E_n}(\phi, E, E', \{\sigma, \bar{\sigma}\})$ 
5    $\{\tau, \bar{\tau}\} \leftarrow \{\alpha_n(\phi, \{\sigma, \bar{\sigma}\}), \bar{\alpha}_n(\phi, \{\sigma, \bar{\sigma}\})\}$ 
6    $w \leftarrow w \times W_{\alpha_n}(\phi, \{\sigma, \bar{\sigma}\}) \times W_{\bar{\alpha}_n}(\phi, \{\sigma, \bar{\sigma}\})$ 
7    $M_{\tau, \bar{\tau}} \leftarrow [\tau | \mathbf{V}_{E, E'} | \sigma] \times M_{\sigma, \bar{\sigma}} \times \langle \bar{\sigma} | \mathbf{V}_{E, E'}^\dagger | \bar{\tau} \rangle$ 
8   if  $n < n_{\text{max}}$  and  $E > \rho$  then
9      $\phi \leftarrow \Phi_{n+1}(\phi, \vec{g})$ 
10     $w \leftarrow w \times W_{\Phi_{n+1}}(\phi, \vec{g})$ 
11  if  $n = n_{\text{max}}$  or  $u_n(\phi) = 0$  or  $E = \rho$  then
12     $w \leftarrow w \times \text{Re}(M_{\tau, \bar{\tau}} S_{\tau, \bar{\tau}})$ 
13    return  $\{\phi, w\}$ 
14   $\{\rho, \bar{\rho}\} \leftarrow \{\alpha_{n+1}(\phi, \{\tau, \bar{\tau}\}), \bar{\alpha}_{n+1}(\phi, \{\tau, \bar{\tau}\})\}$ 
15   $w \leftarrow w \times W_{\alpha_{n+1}}(\phi, \{\tau, \bar{\tau}\}) \times W_{\bar{\alpha}_{n+1}}(\phi, \{\tau, \bar{\tau}\})$ 
16   $M_{\rho, \bar{\rho}} \leftarrow [\rho | \mathbf{D}_E | \tau] \times M_{\tau, \bar{\tau}} \times \langle \bar{\tau} | \mathbf{D}_E^\dagger | \bar{\rho} \rangle$ 
17   $E' \leftarrow E;$ 
18   $\sigma \leftarrow \rho, \bar{\sigma} \leftarrow \bar{\rho};$ 
19   $n \leftarrow n + 1;$ 

```

Output: $\{\phi, w\}$

Algorithm 4 outlines the generation of an event using the `evolve()` method. In addition to giving the reader a schematic overview of the event generation, the ‘representative functions’ take the place of method calls to conceal code. The idea being, that their definitions are variant-dependent and can be discussed in subsequent sections, unencumbered by code referencing. One cycle of Algorithm 4 represents Eq. 4.11 and as such, closely follows its nomenclature.

It is instructive to walk through the algorithm, upto the first emission. We shall explain what each function represents as we encounter it. Let’s begin: initially, all variables in the event record are set to their default values. These are 0 for the real-valued variables; w , E' and E . Here, w is the event weight. It is used to record the product of weights resulting from Monte Carlo sampling and represents the value accessed by the `currentWeight()` method. E and E' correspond to the scale of the latest emission (or the hard scale in the case of no emissions)

and that of the previous one (just as in Eq. 4.11). In the case that no further emissions are to occur, E takes the value of the infrared cutoff of the final Sudakov operator. The objects $\sigma, \bar{\sigma}, \tau, \bar{\tau}, \rho, \bar{\rho}$ are placeholders for the tensors describing the Sudakov and emission matrix elements and ϕ denotes a collection of particles: including the phase-space points which describe their momenta and their corresponding colour representation. The variable n counts the emission multiplicity and $M_{\kappa, \bar{\kappa}}$ is the multiplied chain of matrix elements with $\kappa, \bar{\kappa}$ being the outermost tensors.

Before the action of any Sudakov or emission operators, the variables pertaining to the hard process are defined in line 1. The phase space points for the particles in the hard process are generated and their colour representations determined (in `initialKinematics()` of the `Hemispheres::HardProcessMatrix` class). This process, along with the initialisation of the mappings in `Core::ColourFlowCrossing` is represented by ϕ_0 . The energy scale E' is set to be that of the hard process, Q_H , and the emission multiplicity, n , is set to 0. From the set of all possible colour arrangements of the particles in the hard process, the flows σ and $\bar{\sigma}$ are selected (in `Hemispheres::HardProcessMatrix::initialFlows()`). These colour flows are stored in `Core::Evolver::currentFlows`, which is generally represented in the algorithm by two curly brackets, $\{, \}$. The functions $\alpha_0, \bar{\alpha}_0$ represent the sampling process according to which the initial basis tensors in the amplitude and conjugate-amplitude are chosen. The weight associated with this sampling, and the generation of the hard process kinematics is w_{hard} and is stored in w . The amplitude, $M_{\sigma, \bar{\sigma}}$, is set to the hard matrix element corresponding to the sampled basis tensors σ and $\bar{\sigma}$ (by `Hemispheres::HardProcessMatrix::element()`). The details of this initial selection process are shared across both Variant A and B of the `CVolver` code and shall be discussed in Section 4.5. Specifically we will discuss the processes $V \rightarrow q\bar{q}$ and $H \rightarrow gg$.

We then enter the emitting loop. The next emission scale, E , is generated using the sampling function E_n , representing the `setNextScale()` method in `Hemispheres::evolutionOrdering`. In general, it can depend on ϕ , E' , and the most recent colour arrangements, $\{\sigma, \bar{\sigma}\}$. The resultant weight produced in the process of this scale generation is denoted by W_{E_n} , which can also depend on the newly generated scale. Throughout Algorithm 4, α_i and $\bar{\alpha}_i$ denote the process according to which the basis tensors in the amplitude and conjugate-amplitude are chosen, for the Sudakov and emission operators after

the i th emission. They correspond to the `nextFlows()` methods in both the `Hemispheres::AnomalousDimensionMatrix` and `Hemispheres::EmissionMatrix` classes. For instance, the colour flows to which the Sudakov operators evolve, $\{\tau, \bar{\tau}\}$, are selected by α_n and $\bar{\alpha}_n$ at a multiplicity, n . The weights corresponding to this selection are W_{α_n} and $W_{\bar{\alpha}_n}$.

Subsequently, $M_{\sigma, \bar{\sigma}}$ is multiplied by the corresponding Sudakov matrix elements in the amplitude and conjugate-amplitude. The process according to which the phase-space is mapped from ϕ to a new phase space including another emission, is represented by Φ_{n+1} (corresponding to `Hemispheres::EmissionMatrix::nextPhaseSpace()`). This can depend on the prior phase-space of all particles and the generated degrees of freedom of the new emission, \vec{g} . The weight generated by this process is $W_{\Phi_{n+1}}$ and contributes to w . A pair of colour flows, $\{\rho, \bar{\rho}\}$, are chosen by α_{n+1} and $\bar{\alpha}_{n+1}$ with weights W_{α_n} and $W_{\bar{\alpha}_n}$. The corresponding emission matrix elements multiply $M_{\tau, \bar{\tau}}$ and the resultant element, $M_{\rho, \bar{\rho}}$, is multiplied with the value held in `Evolver::currentAmplitude()`. This value will be the product of matrix elements from previous evolution steps. The hard scale, E' of the next step of the evolution is set to be the current soft scale, E , and the multiplicity of the event is incremented by 1. At this stage the colour maps in the `ColourFlowCrossing` instantiation are updated (using `ColourFlowCrossing::addColourAntiColourCrossing()` via the `updateCrossing()` method of the `Hemispheres::EmissionMatrix` class) to reflect the new soft-gluon. The details of the aforementioned sampling functions are one subject of discussion in Sections 4.4 and 4.5.

Once in the emitting while-loop, the algorithm will continue progressing through evolution steps until a termination criterion is met. This termination criterion can be reaching a pre-determined maximum multiplicity, violating the measurement function associated with the observable (described by $u_n(\phi)$) or generating an energy scale below the shower cutoff. When this is the case, the trace over the amplitude is taken, which for a product of matrix elements means multiplying by the scalar product matrix element, $S_{\tau, \bar{\tau}}$, and the event is returned. Each event contains the information specified by the `EventRecordT` class in `Hemispheres`: the particle four-momenta of the hard process partons and any subsequent emissions, their colour representation (i.e. fundamental, anti-fundamental or adjoint), the hardest and softest scale in the event and the event-weight. This is the same as in a typical event generator such as `Herwig` [10–12], `Pythia` [13–15] or `Sherpa` [16].

Looking back to our discussions of Monte Carlo methods in Chapter 3.6, the event-weight is an integrand evaluation (including additional weight factors due to sampling strategies). The integration we are performing corresponds to the observable we wish to calculate (which will be detailed in Section 4.5 for the jet veto cross section). When averaged over the number of attempted points (or events), the sum of these event-weights approximates this integral. Typically in ‘event generator’ mode, one would produce events, constraining the particle phase-space only for reasons of IR control. Then, any desired distribution can be produced from the set of phase-space points and event-weights. This mode of **CVolver** is still under development however.

Instead, in this work we focus on using **CVolver** to compute the class of observables which restrict angular regions between hard jets by a veto on the energy, as a testbed of the framework. We have tailored **CVolver** to be efficient for this particular observable, by terminating the evolution when emitting into the veto region. However, this is not a restriction on the general applicability of our approach, and the framework is much more general.

Algorithm 5: Overview of the `evolveFull()` algorithm in the **EvoLver** class.

Input: **EventRecordT:** $\{\phi, w \in \mathbb{R}, E' \in \mathbb{R}, E \in \mathbb{R}, \mathbf{M} \in \mathbb{C}^{m! \times m!}\}$

```

1  $\phi \leftarrow \phi_0, w \leftarrow w_{\text{hard}}, \mathbf{H} \leftarrow \mathbf{H}_{\text{hard}}, E' \leftarrow Q_H$ 
2 while  $n \neq n_{\text{max}}$  and  $u_n(\phi) > 0$  do
3    $E \leftarrow E_n(\phi, E')$ 
4    $w \leftarrow w \times W_{E_n}(\phi, E, E')$ 
5    $\mathbf{M} \leftarrow \mathbf{V}_{E, E'} \cdot \mathbf{M} \cdot \mathbf{V}_{E, E'}^\dagger$ 
6    $\phi \leftarrow \Phi_{n+1}(\phi, \vec{g})$ 
7    $w \leftarrow w \times W_{\Phi_{n+1}}(\phi, \vec{g}, E)$ 
8   if  $n = n_{\text{max}}$  or  $u_n(\phi) = 0$  then
9      $w \leftarrow w \times \text{Tr} [\mathbf{M} \cdot \mathbf{S}_n]$ ;
10    return  $\{\phi, w\}$ ;
11    $\mathbf{M} \leftarrow \mathbf{D}_E \cdot \mathbf{M} \cdot \mathbf{D}_E^\dagger$ 
12    $E' \leftarrow E$ ;
13    $n \leftarrow n + 1$ 

```

Output: $\{\phi, w\}$

Algorithm 5 presents the generation of an event using the `evolveFull()` method of **EvoLver**. The functions to generate the emission scale, phase space mapping, and their corresponding weights, are the same as those outlined in Algo-

rithm 4. Termination criteria are also the same. Instead of sampling basis tensors and products of matrix elements, the full Sudakov and emission operator matrices (represented in the colour flow basis) are used in each evolution step. The Sudakov operators preserve the representation of the amplitude in colour space and so are represented by $m! \times m!$ complex matrices (for an amplitude with m colour lines), whilst the emission operators increase the dimension and are represented by $m! \times (m + 1)!$ complex matrices. This enables one to cross-check the colour sampling techniques used in α_i and β_i , the results of which are presented in Chapter 5, at least for small numbers of emissions.

With the generalised shower algorithm of the **Evolver** class outlined, we are able to discuss two specific implementations of the aforementioned sampling functions in Section 4.5. Before we do this however, we will address the challenges of computing the approximated Sudakov matrix element in Section 4.3.1 and the full- N_c emission matrix element in Section 4.3.4. Approximating the Sudakov matrix elements, creates the need to be able to systematically sample a tensor $|\tau\rangle$, d swaps from $|\sigma\rangle$ (through α_n and $\bar{\alpha}_n$). The solution to this issue is subsequently addressed in Section 4.4.

4.3 Computation of Matrix Elements

In Section 2.3, we presented the matrix elements of the emission and virtual-exchange operators. Using these results we went on to begin a discussion of subleading-colour corrections in Section 2.3.3 and presented some initial steps towards systematically including $1/N_c^k$ corrections to the leading result. It is convenient however, in a Monte Carlo code, to express these results not in terms of external leg indices, but in terms of colour and anti colour indices; the distinction between the physical and colour flow regime. We therefore show the general form of the soft-gluon anomalous dimension matrix elements and emission matrix elements, in terms of summations over colour indices, in Sections 4.3.1 and 4.3.4. It was noted in Section 4.1 that a key challenge in computing Sudakov matrix elements, $[\tau | \mathbf{V} | \sigma]$, is the exponentiation of large and sparse colour matrices. Using the soft-gluon anomalous dimension matrix, we present and discuss the result of [154], which approximates the exponentiation of the anomalous dimension matrix by successive summation of towers of large- N_c contributions, in a systematic way. We shall see this Sudakov matrix element approximation also lends us a hand in solving the issue of sampling matrix element basis tensors.

4.3.1 Sudakov Matrix Elements

In this section we review the general form of the soft anomalous dimension matrix in the colour flow regime. Subsequently we illustrate the result presented in [154], which approximates the full exponentiation of the soft gluon anomalous dimension matrix.

Firstly, we remind the reader that in the following discussions, roman letters indicate external leg indices whilst greek letters indicate colour lines and barred greek letters, anti colour lines. The coefficients of the colour charge products in the soft anomalous dimension matrix in Eq. 4.4 shall be written as

$$\Gamma_{ij} = \frac{\alpha_s}{2\pi} \int_E^{E'} \frac{dE_k}{E_k} \int \frac{d\Omega_k}{4\pi} \frac{n_i \cdot n_j}{(n_i \cdot n_k)(n_j \cdot n_k)}, \quad (4.15)$$

where the energy dependent terms (with a minus sign) in the Sudakov operator in Eq. 4.3 (and their integral limits) have been absorbed into the definition of the anomalous dimension matrix coefficients with the hindsight that we shall be performing a colour-expansion of the Sudakov operator. The coefficients in Eq. 4.15 appear in the context that

$$\Gamma = \sum_{ij} \Gamma_{ij} \mathbf{T}_i \cdot \mathbf{T}_j. \quad (4.16)$$

Note that in Eq. 4.16, contrary to the ordered sum in Eq. 4.4, i and j run over all external leg combinations. This is the reason for the factor of $1/2$ in the definition of Γ_{ij} . Rather than work with the \mathbf{t} and \mathbf{s} color-line operators of Eq. 2.55, we wish to write an expression for Γ in the colour flow regime to facilitate a comparison with [154] and its implementation in `CVolver`. As such, we adopt a different notation here for the colour charge products, $\mathbf{T}_\alpha \cdot \mathbf{T}_\beta$, where we subsume the \mathbf{s} operator contribution into their definition such that

$$\mathbf{T}_i \cdot \mathbf{T}_j = \lambda_i \lambda_j \mathbf{T}_\alpha \cdot \mathbf{T}_\beta + \bar{\lambda}_i \bar{\lambda}_j \mathbf{T}_{\bar{\alpha}} \cdot \mathbf{T}_{\bar{\beta}} + \lambda_i \bar{\lambda}_j \mathbf{T}_\alpha \cdot \mathbf{T}_{\bar{\beta}} + \bar{\lambda}_i \lambda_j \mathbf{T}_{\bar{\alpha}} \cdot \mathbf{T}_\beta, \quad (4.17)$$

where $\alpha = c_i$ and $\bar{\alpha} = \bar{c}_i$ denote the colour and anti colour line corresponding to the external leg i whilst $\beta = c_j$ and $\bar{\beta} = \bar{c}_j$ denote the colour and anti colour line corresponding to j (reminding the reader that c and \bar{c} are the mapping operators). In the case that parton i is a quark, $\bar{\alpha}$ does not exist and the corresponding colour charge products vanish (enforced by $\bar{\lambda}_i = 0$). Similarly, when parton i is an anti-quark, terms involving α vanish. The same logic holds true for parton j . The colour charge products in the colour flow basis can be written

as [156]

$$\begin{aligned}\mathbf{T}_\alpha \cdot \mathbf{T}_\beta &= \left(\delta_\alpha^{\beta'} \delta_\beta^{\alpha'} - \frac{1}{N_c} \delta_\alpha^{\alpha'} \delta_\beta^{\beta'} \right), \\ \mathbf{T}_\alpha \cdot \mathbf{T}_{\bar{\beta}} &= - \left(\delta_\alpha^{\bar{\beta}} \delta_{\bar{\beta}'}^{\alpha'} - \frac{1}{N_c} \delta_\alpha^{\alpha'} \delta_{\bar{\beta}}^{\bar{\beta}'} \right),\end{aligned}\quad (4.18)$$

which effectively describe one-gluon exchange between two colour or anti colour lines or between a colour and an anti colour line (regardless of whether they correspond to a quark, anti-quark or gluon). The prime notation in Eq. 4.18 is used to distinguish a colour or anti colour index after the action of a colour charge product operator, from the same colour or anti colour index before its action. The reason for this distinction is clear if we look at the first term in $\mathbf{T}_\alpha \cdot \mathbf{T}_\beta$: the colour index initially associated with the i th particle, $\alpha = c_i$, is exchanged to the colour index, $\beta = \beta'$, whilst the colour index associated with the j th particle, $\beta = c_j$, is exchanged to $\alpha = \alpha'$. Examining the second term in $\mathbf{T}_\alpha \cdot \mathbf{T}_\beta$, we see that $c_i = \alpha = \alpha'$, i.e. this contribution to the $\mathbf{T}_\alpha \cdot \mathbf{T}_\beta$ operator does not change the colour index associated with the i th particle, and the same is true for the j th particle. An example of one-gluon exchange between a quark and gluon is presented in Figure 4.4.

One can define flow-decomposition coefficients, $\gamma_{\alpha\beta}$, as

$$\begin{aligned}\gamma_{\alpha,\beta} &= \Gamma_{c_\alpha^{-1}c_\beta^{-1}} + \Gamma_{c_\beta^{-1}c_\alpha^{-1}}, \\ \gamma_{\alpha,\bar{\beta}} &= \Gamma_{c_\alpha^{-1}\bar{c}_\beta^{-1}} + \Gamma_{c_\beta^{-1}\bar{c}_\alpha^{-1}}, \\ \gamma_{\bar{\alpha},\bar{\beta}} &= \Gamma_{\bar{c}_\alpha^{-1}\bar{c}_\beta^{-1}} + \Gamma_{\bar{c}_\beta^{-1}\bar{c}_\alpha^{-1}},\end{aligned}\quad (4.19)$$

where the c^{-1} operator in Eq. 4.19 was described in Section 2.2 and maps a colour or anti colour index onto the corresponding external leg index, and the Γ_{ij} are the soft gluon anomalous dimension coefficients in the physical regime (see Eq. 4.15). As an example, a selection of γ -coefficients in the case of the $q\bar{q} \rightarrow q\bar{q}$ process presented in Figure 4.3 are

$$\begin{aligned}\gamma_{1,2} &= \Gamma_{13} + \Gamma_{31}, \\ \gamma_{1,\bar{2}} &= \Gamma_{14} + \Gamma_{41}, \\ \gamma_{\bar{2},\bar{1}} &= \Gamma_{42} + \Gamma_{24}.\end{aligned}\quad (4.20)$$

Using Eq. 4.18 and 4.19, one can write the soft-gluon anomalous dimension

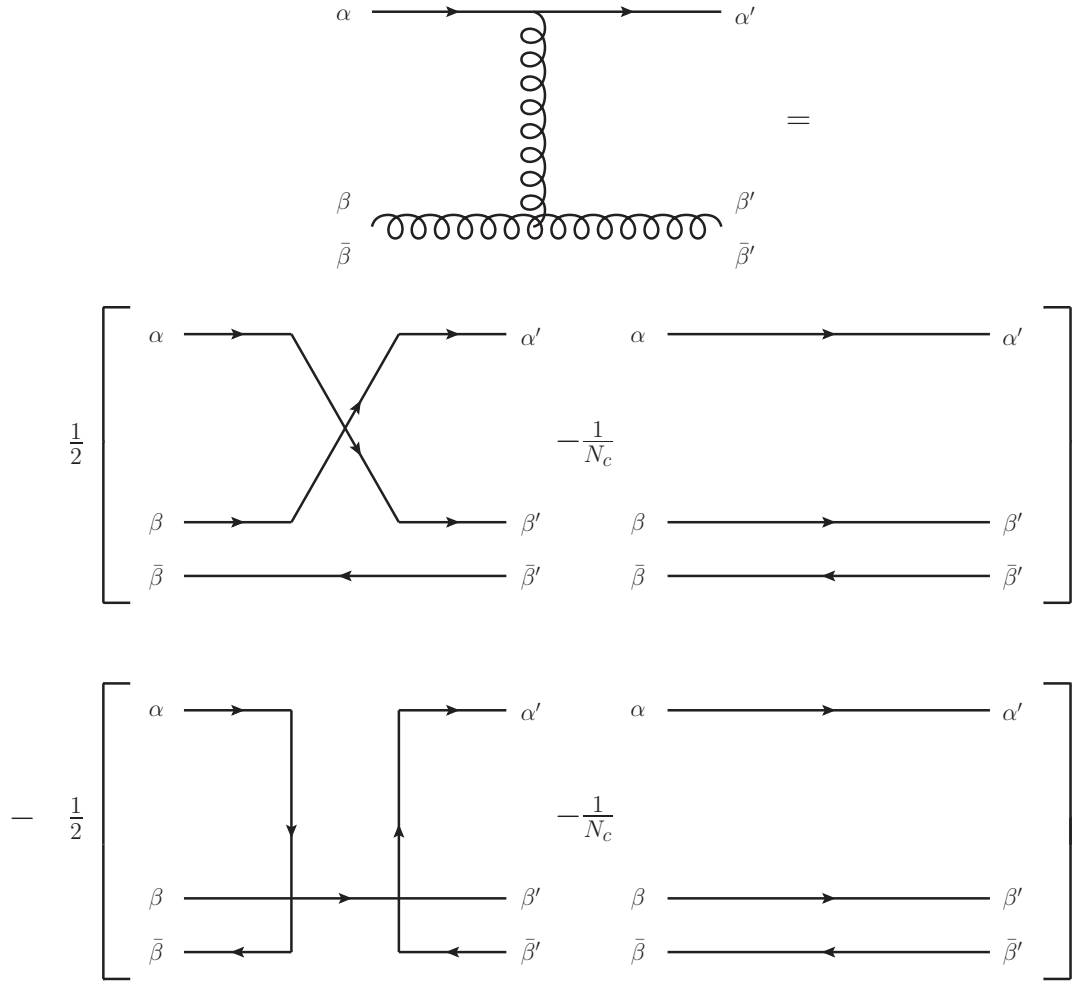


FIGURE 4.4: Illustration of the colour charge products in the colour flow basis which contribute to a single-gluon exchange between a quark (represented by a colour line α) and a gluon (represented by a colour line β and an anti colour line $\bar{\beta}$).

matrix in Eq. 4.16 as a sum over colour indices, as

$$\Gamma = \sum_{\alpha < \beta} \left(\gamma_{\alpha, \beta} \mathbf{T}_{\alpha} \cdot \mathbf{T}_{\beta} + \gamma_{\bar{\alpha}, \bar{\beta}} \mathbf{T}_{\bar{\alpha}} \cdot \mathbf{T}_{\bar{\beta}} \right) + \sum_{\alpha, \beta} \gamma_{\alpha, \bar{\beta}} \mathbf{T}_{\alpha} \cdot \mathbf{T}_{\bar{\beta}}, \quad (4.21)$$

where the sum over $\alpha < \beta$ denotes an ordered sum and that over α, β denotes an unordered sum over all colour indices. We remind the reader of the general form for anomalous dimension matrix elements stated in Eq. 2.95:

$$[\tau | \Gamma | \sigma] = \left(-N_c \Gamma_{\sigma} + \frac{1}{N_c} \rho \right) \delta_{\tau\sigma} + \Sigma_{\tau\sigma}. \quad (4.22)$$

By grouping the terms in Eq. 4.21 into leading-colour diagonal terms (Γ_{σ}), subleading-colour diagonal terms (ρ), and subleading-colour off-diagonal

terms $(\Sigma_{\tau\sigma})$, we can write expressions for the components of Eq. 4.22. The diagonal leading-colour contributions, are

$$\Gamma_{\sigma} = \frac{1}{2} \sum_{\alpha} \gamma_{\alpha, \overline{\sigma(\alpha)}}, \quad (4.23)$$

whilst the diagonal subleading-colour contributions can be written as

$$\rho = \frac{1}{2} \left(\sum_{\alpha, \beta} \gamma_{\alpha, \beta} - \sum_{\alpha < \beta} (\gamma_{\alpha, \beta} + \gamma_{\bar{\alpha}, \bar{\beta}}) \right). \quad (4.24)$$

Finally the off-diagonal elements are given by

$$\begin{aligned} \Sigma_{\tau\sigma} = & \frac{1}{2} \sum_{\alpha, \beta} \left(\gamma_{\alpha, \beta} + \gamma_{\overline{\tau(\alpha)}, \overline{\tau(\beta)}} - \gamma_{\alpha, \overline{\tau(\alpha)}} - \gamma_{\beta, \overline{\tau(\beta)}} \right) \\ & \times \delta_{\tau(\alpha)\sigma(\beta)} \delta_{\tau(\beta)\sigma(\alpha)} \prod_{\kappa \neq \alpha, \beta} \delta_{\tau(\kappa)\sigma(\kappa)}, \end{aligned} \quad (4.25)$$

where the Kronecker deltas serve to reduce the sum over all colour indices down to one term and ensure that the basis tensors σ and τ differ by exactly one transposition.

With a general form for the soft-gluon anomalous dimension matrix, we can address the challenge of computing Sudakov matrix elements, $[\tau | \mathbf{V} | \sigma]$, noted in Section 4.1. The difficulty lies in exponentiating the soft-gluon anomalous dimension matrix. This exponentiation in closed form is limited to processes in which there are only two colour flows. Past this, one can use numerical exponentiation methods, but they limit the production of high-multiplicity events in a timely manner. However, there is some light. The evaluation of the Sudakov matrix elements can be simplified if we are prepared to sum terms accurate only to an order $1/N_c^d$, where d is a positive integer, whilst keeping the leading diagonal terms proportional to $(\alpha_s N_c)^n$ to all orders n . It is the result presented in [154] which enables us to do this:

$$\begin{aligned} [\tau | \mathbf{V}_{E, E'} | \sigma] \simeq & \delta_{\tau\sigma} R(\{\sigma\}) + \sum_{l=1}^d \left(-\frac{1}{N_c} \right)^l \sum_{\{\sigma_0, \dots, \sigma_l\}} \delta_{\tau\sigma_0} \delta_{\sigma_l, \sigma} \\ & \times \left(\prod_{\alpha=0}^{l-1} \Sigma_{\sigma_{\alpha}, \sigma_{\alpha+1}} \right) R(\{\sigma_0, \dots, \sigma_l\}). \end{aligned} \quad (4.26)$$

This equation is going to need some unpacking. In doing so, we shall first review the structure of the contributions to the soft-gluon anomalous dimension matrix and the consequences of exponentiating them. It is then instructive to walk-through the form of Eq. 4.26 for the first two colour orders, $d = 0$ and $d = 1$, as an illustrative example. We refer to the $d = 0$ approximation as our leading colour virtuals (LC'_V) approximation and $d = 1$ as next-to-leading (NLC'_V). We then finish with a more general discussion of the Sudakov matrix element approximation and how it is implemented in **CVolver**.

We noted that the off-diagonal contributions of the soft-gluon anomalous dimension matrix, $\Sigma_{\tau\sigma}$ are only non-zero if $\#(\sigma, \tau) = 1$, whilst the contributions Γ_σ are leading colour-diagonal and ρ are subleading colour-diagonal. In other words, each virtual gluon exchange can either leave a basis tensor unchanged or induce a single swap (through a Σ -contribution). Exponentiating this to produce the Sudakov matrix element produces the possibility for many swaps. Importantly, this is manageable since each swap comes at a price of a factor of $1/N_c$. This is what allows us to truncate our sum over l , at a small colour order d (meaning our $N^d LC'_V$ approximation involves at most d swaps for each application of the Sudakov operator).

When $d = 0$, we only consider colour-diagonal contributions, described by the first term on the RHS of Eq. 4.26. The object

$$R(\{\sigma\}) = \exp(-N_c \Gamma'_\sigma), \quad (4.27)$$

is, suffice it to say for the time being, one example of a kinematic R function. The primed notation, $\Gamma'_\sigma = \Gamma_\sigma - \rho/N_c^2$, indicates we have trivially summed the Γ_σ and ρ contributions to all orders, so that we exponentiate the leading colour contributions, improved by the colour-diagonal subleading terms.

Now, when $d = 1$, we sum over all contributions with a single swap between σ and τ . This involves summing over chains of basis tensors in general, indicated by lists of the form $\{\sigma_0, \dots, \sigma_l\}$. The first and last tensors in this list identify the matrix element in Eq. 4.26 and each tensor in this list is one swap away from its adjacent tensors (corresponding to each swap by a Σ -contribution). In the case $d = 1$ there is only one such list, $\{\tau, \sigma\}$, that contributes. The NLC'_V Sudakov matrix elements are then

$$[\tau | \mathbf{V}_{E,E'} | \sigma \rangle = \delta_{\tau\sigma} \exp(-N_c \Gamma'_\sigma) - \frac{1}{N_c} \Sigma_{\tau\sigma} R(\{\tau, \sigma\}), \quad (4.28)$$

where

$$R(\{\tau, \sigma\}) = \frac{\exp(-N_c \Gamma'_\tau) - \exp(-N_c \Gamma'_\sigma)}{\Gamma'_\tau - \Gamma'_\sigma}, \quad (4.29)$$

and if it is the case that $\Gamma_\sigma = \Gamma_\tau$, then Eq. 4.29 reverts to its degenerate form

$$R(\{\tau, \sigma\}) = -N_c \exp(-N_c \Gamma'_\sigma). \quad (4.30)$$

As a further illustrative example, all of the lists summed over, in the case $d = 2$ with $\sigma = |312\rangle, \tau = |123\rangle$ are

$$\begin{aligned} & \{|123\rangle, |132\rangle, |312\rangle\}, \\ & \{|123\rangle, |213\rangle, |312\rangle\}, \\ & \{|123\rangle, |321\rangle, |312\rangle\}. \end{aligned} \quad (4.31)$$

It is important to point out that our $N^d \text{LC}'_V$ approximation involves at most d swaps for each application of the Sudakov operator and as such we have managed to kill two challenges with one stone. As we only have to consider basis tensors, τ , up to d swaps away from σ , the task of Monte Carloing over accessible colour states is now a tractable one. This will be the focus of our discussion in Section 4.4. However, before that we turn our attention back to discussing the most general form of Eq. 4.26.

If we choose not to exponentiate the ρ contributions of Eq. 4.22 to all orders, we can include them in our $1/N_c$ summation and write

$$\begin{aligned} [\tau | \mathbf{V}_{E,E'} | \sigma] & \simeq \delta_{\tau\sigma} R(\{\sigma\}) + \sum_{l=1}^d \frac{(-1)^l}{N_c^l} \sum_{k=0}^l \frac{(-\rho)^k}{k!} \sum_{\{\sigma_0, \dots, \sigma_{l-k}\}} \delta_{\tau\sigma_0} \delta_{\sigma_{l-k}, \sigma} \\ & \times \left(\prod_{\alpha=0}^{l-k-1} \Sigma_{\sigma_\alpha, \sigma_{\alpha+1}} \right) R(\{\sigma_0, \dots, \sigma_{l-k}\}). \end{aligned} \quad (4.32)$$

We refer to this as our unprimed, $N^d \text{LC}_V$ approximation. Results for both our primed and unprimed notation will be presented and compared in Chapter 5. In addition to the $1/N_c$ factor that occurs with each swap (i.e. with each factor of Σ), another $1/N_c$ factor now appears for every occurrence of the diagonal subleading-colour contributions, ρ . Each $1/N_c^l$ subleading-colour contribution is then a combination of k , ρ -contributions and $l - k$, Σ -contributions. Of course, only the terms in which $\#(\tau, \sigma) = l - k$ have a non-zero contribution.

Let's investigate Eq. 4.32 by looking back and comparing to our discussion of the first $1/N_c^2$ corrections in Section 2.3.3. To remind the reader, we considered $1/N_c^2$ corrections to the leading-colour trace which arose from emission and virtual contributions, treating ρ independently of Γ_σ . For the virtual contributions we need to consider the next-to-next-to-leading colour approximation ($N_c^2\text{LC}_V$) for the evolution operator

$$\begin{aligned} [\tau | \mathbf{V}_{E,E'} | \sigma \rangle &= \delta_{\tau\sigma} e^{-N_c \Gamma_\sigma} + \delta_{\tau\sigma} \frac{\rho}{N_c} e^{-N_c \Gamma_\sigma} - \frac{1}{N_c} \Sigma_{\tau\sigma} R(\{\tau, \sigma\}) \\ &+ \frac{1}{N_c^2} \left(\sum_{\{\tau, \rho, \sigma\}} \Sigma_{\tau\rho} \Sigma_{\rho\sigma} R(\{\tau, \rho, \sigma\}) \right. \\ &\quad \left. - \rho \Sigma_{\tau\sigma} R(\{\tau, \sigma\}) + \frac{\rho^2}{2} e^{-N_c \Gamma_\sigma} \delta_{\tau\sigma} \right). \end{aligned} \quad (4.33)$$

The sum over $\{\tau, \rho, \sigma\}$ denotes a sum over all possible lists where ρ represents a basis tensor such that $\#(\tau, \rho) = \#(\rho, \sigma) = 1$. The $1/N_c^2$ subleading corrections which come from terms in Eq. 4.33 containing Σ factors, contribute when σ and τ are identical or differ by a single flip. The latter case comes from the term with a single Σ -contribution in Eq. 4.33 (in the first line) which can occur in either the amplitude or conjugate-amplitude. This term comes with an explicit $1/N_c$ factor and induces an additional $1/N_c$ from the scalar product matrix (due to the swap). It can also undo a flip induced by a previous real emission (containing an \mathbf{s} operator, and therefore a factor of $1/N_c$) in either the amplitude or conjugate. This accounts for the dark orange boxes in Figure 2.8. Additionally, we may include either two Σ -contributions in the amplitude or conjugate-amplitude (presented in the second line of Eq. 4.33) or one in each, in such a way as to undo the effect of a two-flip real emission. In the case that σ and τ are identical, we can have two flips (one from each Σ) which cancel each other out. These contributions are represented by the green boxes in Figure 2.8. Lastly, the ρ term in Eq. 4.33 contributes to the $1/N_c^2$ virtual corrections (represented by the light-orange boxes in Figure 2.8) in the case that there is no additional suppression from any emission contribution. The last line of Eq. 4.33 is beyond the next-to-leading colour approximation at the level of the cross section and account for a subset of the grey boxes in Figure 2.8.

The lists of basis tensors over which $\{\tau, \rho, \sigma\}$ sums was presented in Eq. 4.31, when $\sigma = |312\rangle$ and $\tau = |123\rangle$. It is the `makeSummationSequences()` method in the `EvolutionMatrix` class which generates these sets of lists for general σ , τ and $l - k$. Succinctly, it operates in a brute-force manner: if lists, $\{\sigma_0, \dots, \sigma_{l-k}\}$,

of length $l - k$ are required, it starts from $\sigma_0 = \tau$, and sequentially swaps pairs of anti-colour indices. Each anti-colour index swap seeds a new list, $\{\sigma_0, \sigma_{0(ij)}, \dots, \sigma_{l-k}\}$, where ij denote the swapped anti-colour indices. This algorithm then acts recursively on $\sigma_{0(ij)}$ in each list until the set of all lists of length $l - k$ are found. The lists in which each of the $l - k$ tensors are only one swap apart from their adjacent tensors are retained, and the rest are discarded. This can obviously be very inefficient, particularly for larger $l - k$, i.e. a larger colour order. In this work however, we focus on a maximum value of $l - k = 2$. In Eq. 4.33, each of the $\{\tau, \rho, \sigma\}$ lists has a corresponding kinematic function, $R(\{\tau, \rho, \sigma\})$. We refer the reader to [154] for their derivation and their explicit forms, up to the $N^3\text{LC}_V$ approximation. It is these forms which are implemented in **CVolver**.

Having finished our comparison with Section 2.3.3, we can see that Eq. 4.32 goes beyond the first $1/N_c^2$ corrections to the leading-colour trace in the $N_c^2\text{LC}_V$ approximation, and in the context of full- N_c emission matrix elements. Infact, we compare the primed (Eq. 4.26) and unprimed (Eq. 4.32) Sudakov approximations in Chapter 5, and find remarkable accuracy using only the LC'_V approximation for the jet veto observable, in the case of the $V \rightarrow q\bar{q}$ hard process. Before we get there however, let's go back to our discussion of the Sudakov approximation and its implementation in **CVolver**.

The approximation to the Sudakov matrix element in Eq. 4.26 and 4.32 is used to calculate the matrix elements in the amplitude and conjugate amplitude in Algorithm 4, line 7,

$$M_{\tau, \bar{\tau}} \leftarrow [\tau | \mathbf{V}_{E, E'} | \sigma \rangle \times M_{\sigma, \bar{\sigma}} \times \langle \bar{\sigma} | \mathbf{V}_{E, E'}^\dagger | \bar{\tau} \rangle. \quad (4.34)$$

Whether we use the primed or unprimed form of the Sudakov approximation is set in the `lcPrime()` method of the `EvolutionMatrix` class. The components of the soft-gluon anomalous dimension matrix and correspondingly, the Sudakov matrix element approximation, all depend (through the γ -coefficients) on the Γ_{ij} coefficients in Eq. 4.15. These are defined in `Hemispheres` and will be written explicitly in Section 4.5, in the context of a collinear cutoff prescription.

We would also like to write a short comment on the topic of Coulomb gluons in the context of **CVolver**: whilst much effort has been placed on the inclusion of subleading-colour effects in recent years, often, attention has focused on processes with no coloured particles in the initial state, not least to avoid Coulomb gluon contributions that result in coherence-violation beyond the large- N_c ap-

proximation. Coulomb exchanges are of particular interest due to the realisation that they are the origin of the super-leading logarithms discovered to exist in the gaps-between-jets observable [18, 19]. They also affect almost all observables in hadron-hadron collisions [92, 157, 158] and are the origin of the breakdown of collinear factorisation in hadron-hadron collisions [77, 78]. The work [20] showed their inclusion in Eq. 2.6 is correct up to two real gluon emissions, to one-loop accuracy, using full Feynman-gauge calculations for the Drell-Yan process, if we use the emission transverse momentum as our ordering variable. The work [103] went one step further to account for collinear emissions in Eq. 2.1, where it was also showed that collinear factorisation occurs below the scale of the last Coulomb exchange. We focus on colour-neutral initial-state processes in this work (and can therefore neglect Coulomb gluon contributions) to hone our colour machinery. However, the `CVolver` algorithm can be readily adapted to account for different ordering variables, and the facility for the inclusion of Coulomb gluons has already been implemented with [103] in-mind.

To summarise this section, we have presented the general form of the soft-gluon anomalous dimension matrix elements in the colour flow regime in Eq. 4.22. To tackle the key challenge of computing Sudakov matrix elements, $[\tau | \mathbf{V} | \sigma \rangle$, we adopted the result of [154], which approximates the exponentiation of the anomalous dimension matrix by successive summation of large- N_c contributions. This approximation also helps us to develop a method for sampling matrix elements, as our $N_c^d \text{LC}_V$ approximation limits us to basis tensors τ that differ from σ by at most d swaps. This sampling will be discussed in Section 4.4. However we shall first review the implementation of Eq. 4.26 and 4.32 in `CVolver` in the next section. We shall then outline the numerical exponentiation methods alluded to at the beginning of this section and used by the `evolveFull()` method.

4.3.2 Sudakov Operators

The calculation of the components of the soft-gluon anomalous dimension matrix elements in 4.22 is carried out by the `Core::AnomalousDimensionMatrix` class. The relevant public methods of this class were listed in Table 4.5.

The `omega()` method calculates the γ coefficients, in Eq. 4.19, for a given pair of colour or anti colour lines. To do this, it accesses the crossing maps of the `ColourFlowCrossing` instantiation, through its inheritance from

ColourFlowMatrix, to determine the corresponding Γ_{ij} coefficients. These coefficients are defined in the **Hemispheres::AnomalousDimensionMatrix** class using the **evaluate()** method. Their general form was written in Eq. 4.15. However, this contains collinear divergences which must be tamed in any numerical implementation. Accordingly, Γ_{ij} coefficients with a collinear cutoff prescription shall be defined in Section 4.5 for each variant.

The independent class, **Core::EvolutionMatrix**, handles the calculation of Eq. 4.26 and Eq. 4.32. It has an aggregation association to an instantiation of **Hemispheres::AnomalousDimensionMatrix** to which it delegates the calculation of components of the soft-gluon anomalous dimension matrix elements, Γ_σ , ρ and $\Sigma_{\tau\sigma}$ and through which it accesses a **ColourFlowMatrix** instantiation. The public methods of **EvolutionMatrix** are listed in Table 4.8.

The calculation of the Sudakov matrix element to a given colour-order, d , is carried out by the **element()** method in **EvolutionMatrix**. This method provides three alternatives: **lcPrimeElement()**, which calculates Eq. 4.26 using the primed ρ contributions; **lcElement()**, which calculates Eq. 4.32 using the unprimed ρ contributions and **exactElement()**, which shall be discussed in Section 4.3.3. For each l and k combination in Eq. 4.32 (where k is always 0 in the case of Eq. 4.26), both **lcElement()** and **lcPrimeElement()** delegate the generation of lists of basis tensors and the onward calculation of Σ -contributions and R functions to the **sigmaSum()** method. This method in-turn utilises **makeSummationSequences()** to produce the tensor lists, as already discussed. The product of Σ -coefficients multiplied by the corresponding R function, is calculated by **sigmaSummand()** for each of these tensor lists. The R functions are computed in the **R()** method. Their degenerate form is used if any two Γ coefficients, Γ_σ and Γ_τ , are equal to within the value of **cutParameter()**.

4.3.3 Numerical Exponentiation

In this section we shall outline the numerical exponentiation methods that are used by the **evolveFull()** method, as a cross-check of the Sudakov matrix element approximation in the previous section and of the colour flow sampling method which shall be presented in Section 4.4.

The **evolveFull()** method (outlined in Algorithm 5) in the **Evolver** class provides an alternative shower evolution algorithm to that of **evolve()**. In particular, it removes the need to sample basis tensors, by multiplying together the full Sudakov, emission and scalar product matrices represented in the colour

Method	Description of functionality
<code>lcPrime()</code>	Return true if the primed resummation is performed, i.e. if we adopt Γ'_σ in Eq. 4.26.
<code>defaultOrder()</code>	Return the colour order d to which we calculate the Sudakov matrix elements.
<code>element()</code>	Calculate the Sudakov matrix element using primed (Eq. 4.26) or unprimed (Eq. 4.32) ρ contributions for a given pair of colour flows τ and σ and colour order <code>defaultOrder()</code> .
<code>lcElement()</code>	Return the Sudakov matrix element using unprimed ρ contributions up to the $N^d\text{LC}_V$ approximation (see Eq. 4.32).
<code>lcPrimeElement()</code>	Return the Sudakov matrix element using primed ρ contributions up to the $N^d\text{LC}'_V$ approximation (see Eq. 4.26).
<code>exactElement()</code>	Return the exact or numerically exponentiated anomalous dimension matrix element (see Section 4.3.3).
<code>sigmaProduct()</code>	Calculate the product of $\Sigma_{\sigma_\alpha, \sigma_{\alpha+1}}$ contributions (see Eq. 4.26 and 4.32).
<code>sigmaSummand()</code>	Calculate the summand in the sum over the list of flows. This is the product of <code>sigmaProduct()</code> multiplied by the corresponding R-function.
<code>makeSummationSequences()</code>	Generate the lists of basis tensors, $\{\sigma_0, \dots, \sigma_{l-k}\}$, in Eq. 4.26 and 4.32.
<code>sigmaSum()</code>	Calculate the sum over lists of basis tensors, $\sum_{\{\sigma_0, \dots, \sigma_{l-k}\}}$, in Eq. 4.26 and 4.32, for a fixed colour order <code>defaultOrder()</code> .
<code>R()</code>	Calculate the R-function with a provided list of colour flows. This is carried out using hard-coded R-functions, presented in [154].
<code>cutParameter()</code>	The value below which two Gamma factors, Γ_σ and Γ_τ , are considered to be degenerate.
<code>nextFlows()</code>	Generate the next basis tensors for the Sudakov matrix elements in the amplitude and the conjugate amplitude.

TABLE 4.8: The methods of the `EvolutionMatrix` class.

flow basis, as opposed to multiplying individual sampled matrix elements. It thus provides a useful validation on the basis tensor sampling used by the `evolve()` method.

`evolveFull()` utilises the `ExactEvolutionMatrix` class, which inherits from `EvolutionMatrix`, solely to implement the `exactElement()` method. The use of this method is signified in `CVolver` when `defaultOrder()` (or the variable d in the parlance of Section 4.4) is set to `inf`. In the case that the evolution involves only one or two colour flows, analytic solutions are available and are computed by `exactElement()`. These solutions are

$$\exp(\Gamma) = \exp\left(-N_c \Gamma_{|1\rangle} + \frac{\rho}{N_c}\right), \quad (4.35)$$

in the case of one flow, and

$$\begin{aligned} \exp(\Gamma) = & \frac{\exp(\rho/N_c) \exp(-\frac{N_c}{2}(\Gamma_{|12\rangle} + \Gamma_{|21\rangle}))}{\kappa} \\ & \times \begin{pmatrix} -\Delta \sinh \frac{\kappa}{2} + \kappa \cosh \frac{\kappa}{2} & 2\Sigma_{|12\rangle,|12\rangle} \sinh \frac{\kappa}{2} \\ \Sigma_{|12\rangle,|21\rangle} \sinh \frac{\kappa}{2} & \Delta \sinh \frac{\kappa}{2} + \kappa \cosh \frac{\kappa}{2} \end{pmatrix}, \end{aligned} \quad (4.36)$$

in the case of two [154], where

$$\Delta = N_c(\Gamma_{|12\rangle} - \Gamma_{|21\rangle}), \quad \kappa = \sqrt{\Delta^2 + 4\Sigma_{|12\rangle,|12\rangle}\Sigma_{|12\rangle,|21\rangle}}. \quad (4.37)$$

Where the evolution involves more than two colour flows, the `exactElement()` method populates a matrix container with the elements of the anomalous dimension matrix (using the methods in `AnomalousDimensionMatrixBase` to calculate Eq. 2.95). This matrix is subsequently numerically exponentiated using the Padé approximation [159, 160].

4.3.4 Emission Matrix Elements

This section shall focus on the calculation of the emission operator matrix elements at the level of both the amplitude and the cross section, expressing them as a sum over colour indices. Unlike Sudakov matrix elements, real emissions are sufficiently simple that we can always include their full colour dependence. To remind the reader, the emission operator is

$$\mathbf{D}_i^\mu = \sum_j \mathbf{T}_j \frac{n_j^\mu}{n_j \cdot n_i}, \quad (4.38)$$

where the sum over j is context-specific, running over all prior soft-gluon emissions and the partons of the original hard scattering. As it appears here, each occurrence of an emission operator (in the amplitude and conjugate-

amplitude) comes with a phase-space factor, which was written in Eq. 4.6. This factor, contains a minus sign for each emission, which is a reflection of having already summed over the emitted gluon polarisation states. However, in Variant A, we insist on an amplitude-level description of operators, and therefore use explicit polarisation vectors, $\epsilon_{\mu,i}$ (in-place of this minus sign). In the context of Eq. 4.38, this means the numerator would be replaced with the inner-product, $n_j \cdot \epsilon_i$. This added complication is necessary if we wish to consider contributions beyond the soft-gluon approximation, including collinear emissions, the inclusion of spin-dependence and kinematic recoil effects. Variant B is an attempt to improve on the accuracy of Variant A cross section results. As we only consider soft-gluon emissions in this work, we can perform cross section-level contractions of the emission operators where possible, removing the need for explicit polarisation vectors (which we shall discuss below). In this case the minus sign in Eq. 4.6 is included explicitly. This cross section-level contraction is done for Variant B, which grants the additional benefit of more efficient sampling strategies (to be discussed in Section 4.5.4).

The colour charge operator, associated to each leg j in Eq. 4.38, can be decomposed as

$$\mathbf{T}_j = \lambda_j \mathbf{t}_{c_j} - \bar{\lambda}_j \bar{\mathbf{t}}_{\bar{c}_j} - \frac{1}{N_c} (\lambda_j - \bar{\lambda}_j) \mathbf{s}. \quad (4.39)$$

These colour-line operators were discussed in Section 2.3. As a review: the colour-line operator \mathbf{s} acts to add a new colour flow, with a colour line labelled $n+1$ and anti colour line labelled $\overline{n+1}$, to a basis tensor, σ , with n existing colour flows. \mathbf{t}_α acts first with an \mathbf{s} operator, reconnecting the new colour flow such that the colour line α is now connected to $\overline{n+1}$ and $n+1$ to $\overline{\sigma(\alpha)}$. The action of the anti colour-line operator, $\bar{\mathbf{t}}_{\bar{\alpha}}$, is defined through the relation $\bar{\mathbf{t}}_{\bar{\alpha}} |\sigma\rangle = \mathbf{t}_{\sigma^{-1}(\bar{\alpha})} |\sigma\rangle$. Consequently, an emission operator, \mathbf{T}_j , can do one of two things: add a new colour line to a basis tensor, $|\sigma\rangle$, without changing any of the existing colour connections, or add a new colour line and make a single swap. On the level of the cross section, an emission in the amplitude and conjugate-amplitude changes the number of transpositions by which the colour flows (in the amplitude and conjugate) differ, by at most two, $\#(\sigma_{n+1}, \bar{\sigma}_{n+1})$. The singlet gluons from the \mathbf{s} operator contributions are sub-leading in colour and inert with respect to any subsequent evolution.

Rephrasing the sum over external legs in Eq. 4.38 to a sum over colour flows,

the matrix elements, $[\tau | \mathbf{D}_i | \sigma \rangle$, become

$$[\tau | \mathbf{D}_i | \sigma \rangle = \sum_j [\tau | \mathbf{T}_j | \sigma \rangle \omega_j(i) = \left(1 - \delta_{|\sigma\rangle, |\tau \setminus n\rangle}\right) \frac{1}{\sqrt{2}} \left(\omega_{c^{-1}(\beta)}(i) - \omega_{\bar{c}^{-1}(\sigma(\beta))}(i)\right) - \delta_{|\sigma\rangle, |\tau \setminus n\rangle} \sum_\alpha \frac{1}{\sqrt{2N_c}} \left(\omega_{c^{-1}(\alpha)}(i) - \omega_{\bar{c}^{-1}(\bar{\alpha})}(i)\right). \quad (4.40)$$

The notation in Eq. 4.40 needs some explanation: the colour line β in Eq. 4.40 is defined such that $|\tau\rangle = \mathbf{t}_\beta |\sigma\rangle$. The variable α is a dummy summation over the number of colour flows in σ . The first contribution, $\omega_{c^{-1}(\beta)}$, corresponds to an emission off the colour line β , whilst the second contribution, $\omega_{\bar{c}^{-1}(\sigma(\beta))}$, is from an emission off the anti colour line which forms a colour flow with β in σ . The sum over α corresponds to the possibility to emit a singlet gluon off every colour flow in σ . Differing from Chapter 2 but using the same notation, the object $\tau \setminus n$ denotes the permutation in which the colour flow involving n and $\tau(n)$ is removed. The Kronecker delta, $\delta_{|\sigma\rangle, |\tau \setminus n\rangle}$ acts as a switch and is equal to 1 if $|\sigma\rangle = |\tau \setminus n\rangle$, i.e. if the latest emission is a singlet,

$$|\sigma\rangle = \left| \begin{array}{cccccc} 1 & \dots & \beta & \dots & n-1 \\ \sigma(1) & \dots & \sigma(\beta) & \dots & \sigma(n-1) \end{array} \right\rangle = |\tau \setminus n\rangle = \left| \begin{array}{cccccc} 1 & \dots & \beta & \dots & n-1 \\ \tau(1) & \dots & \tau(\beta) & \dots & \tau(n-1) \end{array} \right\rangle, \quad (4.41)$$

and 0 otherwise. The ω_j factors are the kinematic part of Eq. 4.38, including the explicit polarisation vectors, defined as

$$\omega_j(i) = \frac{n_j \cdot \epsilon_i^\pm}{n_j \cdot n_i}, \quad (4.42)$$

where \pm denotes the two possible helicities (± 1) of the gluon. The explicit form of the gluon polarisation vector, ϵ_i^\pm , is a matter of choice, upto respecting the usual properties: $\epsilon_i^\pm \cdot n_i = 0$ (transversality with respect to the gluon momentum), $(\epsilon_{i,\mu}^+)^* = \epsilon_{i,\mu}^-$ (reversal of helicity under complex conjugation), $\epsilon_i^+ \cdot \epsilon_i^- = -1$ and $\epsilon_i^+ \cdot \epsilon_i^+ = 0$. The representation used in Variant A is outlined in Section 4.5.3.

Variant B adopts a cross section-level description of emission matrix elements. As we have seen in Eq. 4.11, emission operators occur in pairs, one in the amplitude and the other in the conjugate-amplitude. If we contract the Lorentz index in Eq. 4.40 with its conjugate counterpart, the object of interest at the

cross section level is

$$[\tau | \mathbf{D}_k^\mu | \sigma \rangle \langle \bar{\sigma} | \mathbf{D}_{\mu,k}^\dagger | \bar{\tau} \rangle = \sum_{i,j} [\tau | \mathbf{T}_i | \sigma \rangle \langle \bar{\sigma} | \mathbf{T}_j | \bar{\tau} \rangle \omega_{ij}(k). \quad (4.43)$$

This cross section level emission matrix element eliminates the need for gluon polarisation vectors and the dipole factors are related by

$$\omega_{ij}(k) = -\sum_{\epsilon_k^\pm} \omega_i(k) (\omega_j(k))^* = \frac{n_i \cdot n_j}{(n_i \cdot n_k)(n_j \cdot n_k)}. \quad (4.44)$$

The cross section level emission operator matrix elements can be written as a sum over colour flows as

$$\begin{aligned} \sum_{i,j} [\tau | \mathbf{T}_i | \sigma \rangle \langle \bar{\sigma} | \mathbf{T}_j | \bar{\tau} \rangle \omega_{ij}(k) &= \left[\delta_{|\sigma\rangle,|\tau\rangle n} \delta_{\langle \bar{\sigma}|, \langle \bar{\tau} | n} \right. \\ &\times \frac{1}{2N_c^2} \sum_{\alpha,\beta} \left(\omega_{c^{-1}(\alpha),c^{-1}(\beta)} - \omega_{c^{-1}(\alpha),\bar{c}^{-1}(\bar{\beta})} \right. \\ &\quad \left. \left. - \omega_{\bar{c}^{-1}(\bar{\alpha}),c^{-1}(\beta)} + \omega_{\bar{c}^{-1}(\bar{\alpha}),\bar{c}^{-1}(\bar{\beta})} \right) \right] \\ &- \left[(1 - \delta_{|\sigma\rangle,|\tau\rangle n}) \delta_{\langle \bar{\sigma}|, \langle \bar{\tau} | n} \right. \\ &\times \frac{1}{2N_c} \sum_{\alpha} \left(\omega_{c^{-1}(\rho),c^{-1}(\alpha)} - \omega_{c^{-1}(\rho),\bar{c}^{-1}(\bar{\alpha})} \right. \\ &\quad \left. \left. - \omega_{\bar{c}^{-1}(\sigma(\rho)),c^{-1}(\alpha)} + \omega_{\bar{c}^{-1}(\sigma(\rho)),\bar{c}^{-1}(\bar{\alpha})} \right) \right] \\ &- (\rho \leftrightarrow \gamma, \sigma, \tau \leftrightarrow \bar{\sigma}, \bar{\tau}) \\ &+ \left[(1 - \delta_{|\sigma\rangle,|\tau\rangle n}) (1 - \delta_{\langle \bar{\sigma}|, \langle \bar{\tau} | n} \right) \\ &\times \frac{1}{2} \left(\omega_{c^{-1}(\rho),c^{-1}(\gamma)} - \omega_{c^{-1}(\rho),\bar{c}^{-1}(\bar{\sigma}(\gamma))} \right. \\ &\quad \left. \left. - \omega_{\bar{c}^{-1}(\sigma(\rho)),c^{-1}(\gamma)} + \omega_{\bar{c}^{-1}(\sigma(\rho)),\bar{c}^{-1}(\bar{\sigma}(\gamma))} \right) \right]. \quad (4.45) \end{aligned}$$

The greek letters ρ and γ in Eq. 4.45 are defined such that $|\tau\rangle = \mathbf{t}_\rho |\sigma\rangle$ and $\langle \bar{\tau} | = \mathbf{t}_\gamma \langle \bar{\sigma} |$ whilst the Kronecker deltas are defined just as in Eq. 4.41. They act to isolate terms which originate from the gluon-singlet contributions in the colour charge operators \mathbf{T}_i and \mathbf{T}_j . The object $(\rho \leftrightarrow \gamma, \sigma, \tau \leftrightarrow \bar{\sigma}, \bar{\tau})$ indicates a repeat of the terms between the previous square-brackets, but with the colour indices ρ and γ swapped and the basis tensors σ, τ exchanged with $\bar{\sigma}, \bar{\tau}$.

The emission matrix element in Eq. 4.40 and 4.45 is used to calculate the matrix

elements in the amplitude and conjugate amplitude in Algorithm 4, line 16:

$$M_{\rho,\bar{\rho}} \leftarrow [\rho | \mathbf{D}_E | \tau \rangle \times M_{\tau,\bar{\tau}} \times \langle \bar{\tau} | \mathbf{D}_E^\dagger | \bar{\rho} \rangle. \quad (4.46)$$

Whilst the calculation of these elements is carried out in `Core::EmissionMatrix`, the dipole factors $\omega_j(i)$ and $\omega_{ij}(k)$ are variant-dependent. Accordingly, they are defined in `Hemispheres` and will be written explicitly in Section 4.5 when we discuss the collinear cutoff prescription.

We have so far tackled two of the challenges discussed in Section 4.1: the computation of the Sudakov and emission matrix elements. The operator class `Core::EmissionMatrix` carries out the computation of the amplitude-level matrix elements in Eq. 4.40 and the cross section-level elements in Eq. 4.45 through the `element()` and `elementLR()` public methods respectively. A list of all the `Core::EmissionMatrix` methods was presented in Table 4.6. The external leg indices of the $\omega_j(i)$ and $\omega_{ij}(k)$ factors in Eq. 4.42 and 4.44 are translated from the physical regime to the colour flow regime using the `omega()` and `omegaLR()` methods. In order to do this, `omega()` and `omegaLR()` have access to the crossing maps of the `ColourFlowCrossing` instantiation, accessible to `Core::EmissionMatrix` through its inheritance from `ColourFlowMatrix`. The `evaluate()` and `evaluateLR()` pure virtual methods are declared in `Core::EmissionMatrix`. They are subsequently defined in `Hemispheres::EmissionMatrix` and evaluate the $\omega_j(i)$ and $\omega_{ij}(k)$ factors. Their general form was written in Eq. 4.42 and Eq. 4.44, however these contain divergences which are controlled in `CVolver` through the use of a cutoff prescription. These shall be defined in Section 4.5.3 (for $\omega_j(i)$) and Section 4.5.4 (for $\omega_{ij}(k)$). In the next section, we move on to solving the algorithmic issue of sampling the basis tensors that result from an evolution operator, in an efficient way.

4.4 Colour Flow Sampling

In this section we shall address the challenge of sampling the intermediate colour states in Eq. 4.11. This sampling will be used to determine Sudakov matrix elements in both Variant A and B of `CVolver`, and emission matrix elements in Variant A. As the Sudakov operator matrix is generally both large and sparsely populated, it is crucial that non-zero matrix elements can be identified and sampled efficiently. Beyond rendering the calculation of Sudakov matrix elements tractable, our $N_c^d \text{LC}_V$ approximation in Section 4.3.1 has the advan-

tage of limiting the set size of all basis tensors that can be reached after the action of a Sudakov operator.

The key point is that the $N^d LC'_V$ approximation involves at most d swaps for each application of the Sudakov operator. Our task is then to find all distinct basis tensors, τ , that are d transpositions away from σ .

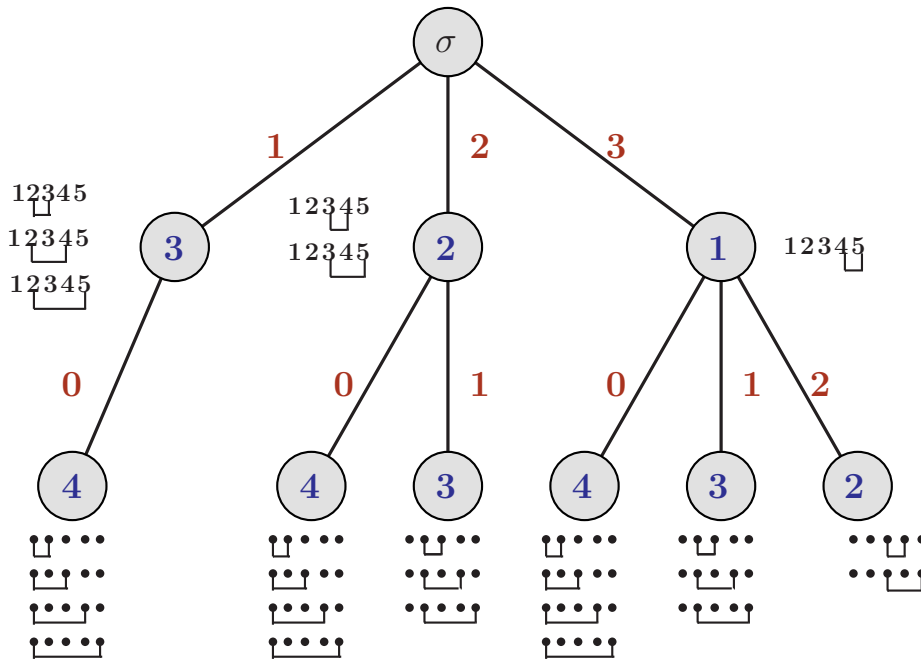


FIGURE 4.5: A pictorial representation of the algorithm determining all basis tensors which are exactly two swaps away from σ . In this example, $|\sigma\rangle = |12345\rangle$, a tensor with five colour flows. Figure used in [161].

Figure 4.5 presents a pictorial representation of the algorithm which determines all basis tensors which are exactly two swaps away from the tensor $|\sigma\rangle = |12345\rangle$. Let's walk through this diagram layer-by-layer from top to bottom. Note that in Figure 4.5 and for the following discussion, we adopt C-counting, i.e. all indices run from 0. Firstly, we begin by considering the basis tensor σ to be a list of numbers. This list denotes the permutation of anti colour indices with respect to the colour line with which they form a colour flow, i.e. the representation $|\sigma\rangle = |12345\rangle$. The first layer of branches in Figure 4.5 shows a subset of the basis tensors which are one swap away from σ . This subset consists of the intermediate tensors, which with the addition of particular swaps, produce all accessible tensors that are two swaps from σ (these particular swaps will be explained shortly). Each layer of swaps is achieved by first picking an index i (denoted by the red numbers above each branch) as the colour index (or position index) corresponding to one of the

pair of anti colour indices we wish to swap. The values of i range from $d' - l$ to $i_{l-1} - 1$, where d' is the target number of swaps, n is the number of colour flows in σ and l denotes the layer of the branching we are on. i_{l-1} indicates the i value of the branch in the layer above the current one being considered (where $i_0 = n - 1$). The second of the pair of indices we wish to swap, $i + k$, can take any value above index i (k takes a value in the range $[1, n - 1 - i]$). Each value of i results in a new branch in the current layer whilst the bubble at the end of each branch in Figure 4.5 indicates the number of values that k can take. For the first layer, the possible anti colour index swaps are indicated explicitly next to each bubble, whilst for the second layer the black dots represent one of these single-swap permutations. This pattern continues down the branches until we reach the d' -th layer, or in other words have found all distinct permutations, τ , which differ from σ by exactly d' swaps. Algorithm 6 outlines this process.

Algorithm 6: The level-swap algorithm, determining all basis tensors, d' swaps away from σ (as depicted in Figure 4.5).

Input: basis tensor: σ , number of swaps to carry out: d'

```

1  $n \leftarrow$  number of colour flows in  $\sigma$ 
2  $L \leftarrow d'$ 
3  $\{\}_L \leftarrow$  initialise list of swapped tensors
4  $i_0 \leftarrow n - 1$ 
5 // Recursive definition of level-swap
6 Function levelSwap(target level:  $L$ , current level:  $l$ , swap index:  $i_{l-1}$ ,  $\sigma$ ):
7   for  $i_l \leftarrow L - l$  to  $i_{l-1} - 1$  do
8     for  $k \leftarrow 1$  to  $n - i_l - 1$  do
9       if  $L = l$  then
10         $\{\}_L \leftarrow \sigma_{(i_l, i_l+k)}$ 
11       else
12        levelSwap( $L, l + 1, i_l, \sigma_{(i_l, i_l+k)}$ )
13 levelSwap( $L, 1, i_0, \sigma$ )
14 return  $\{\}_L$ 

```

In order to illustrate this process, Table 4.9 lists all of the basis tensors at each layer of the algorithm for the left-most branch in Figure 4.5. The total multiplicity of tensors at the d th layer is the sum over k indices (the blue number in each bubble) for each i index, multiplied by all k indices in the previous layer. This particular branch produces 12 tensors, whilst totalling all branches results in a total of 35 tensors that differ from σ by two swaps.

$ \sigma\rangle$	tensors with one swap (first layer)	tensors with two swaps (second layer)
$ 12345\rangle$	$ 13245\rangle$	$ 31245\rangle$
		$ 23145\rangle$
		$ 43215\rangle$
		$ 53241\rangle$
	$ 14325\rangle$	$ 41325\rangle$
		$ 34125\rangle$
		$ 24315\rangle$
		$ 54321\rangle$
	$ 15342\rangle$	$ 51342\rangle$
		$ 35142\rangle$
		$ 45312\rangle$
		$ 25341\rangle$

TABLE 4.9: A walk-through of the basis tensors which are generated at each layer along the left-most branch in Figure 4.5. Three tensors result in the first layer, and from each those, a further four tensors in the second layer.

In order to sample from the set of all basis tensors that can be reached after d' swaps in an unbiased manner, we must be able to determine the total multiplicity of permutations in each branch. This is achieved through summing the total number of k values at each layer of the branch, and multiplying these totals:

$$M_{n,d'}(l, i_l) = \sum_{j=d'-l}^{i_l-1} (n-1-j) \times M_{n,d'}(l+1, j), \quad (4.47)$$

where $M_{n,d'}(l, i_l)$ is the multiplicity of permutations d' swaps away from σ in a branch starting at a layer l and at an i index of i_l . This recursion follows down each branch until it reaches $M_{n,d'}(d'+1, j) = 1$. Note the total multiplicity of Figure 4.5 is determined by $M_{n,d'}(1, n-1)$, where $n = 5$ and $d' = 2$. It is useful

to show this explicitly:

$$\begin{aligned}
M_{5,2}(1,4) &= \sum_{j=1}^3 (4-j) M_{5,2}(2,j) \\
&= 3 \times \left\{ \sum_{k=0}^0 4 M_{5,2}(3,0) \right\} + 2 \times \left\{ \sum_{k=0}^1 (4-k) M_{5,2}(3,k) \right\} \\
&\quad + \left\{ \sum_{k=0}^2 (4-k) M_{5,2}(3,k) \right\} \\
&= 3 \times \{4\} + 2 \times \{4+3\} + \{4+3+2\} = 35, \tag{4.48}
\end{aligned}$$

where the last line corresponds to the numbered bubbles in Figure 4.5. The bubbles at each layer of each branch are summed together and multiplied by the bubble in the layer above, totalling 35 tensors which differ from σ by two swaps. This is equal to the magnitude of the Stirling number of the first kind, $|S(n, n-d')|$; a well-known result which counts permutations according to their number of cycles [162, 163].

Armed with Eq. 4.47, one can recursively sample values of i and k to choose a basis tensor at each layer depicted in Figure 4.5. At each layer we:

- Pick a value for i from the distribution

$$P_{n,d',l}(i) = \frac{(n-i-1)M_{n,d'}(l+1,i)}{M_{n,d'}(l,i)}. \tag{4.49}$$

- Choose k uniformly from the range of valid values: 1 to $n-i-1$.
- Swap the indices i and $i+k$ in σ , resulting in $\sigma_{(i,i+k)}$.

This process continues until a basis tensor is selected at the d' -th level. We call this our level-swap algorithm.

Let's take a moment to relate this sampling procedure to our shower evolution in Algorithm 4. We stated that the representative sampling functions for the Sudakov matrix elements, $[\tau | \mathbf{V} | \sigma]$ and $\langle \bar{\sigma} | \mathbf{V} | \bar{\tau} \rangle$, were $\alpha_n(\phi, \{\sigma, \bar{\sigma}\})$ and $\beta_n(\phi, \{\sigma, \bar{\sigma}\})$ respectively. These functions represent the selection of τ and $\bar{\tau}$ using the aforementioned sampling process. Since the level-swap algorithm is

biased we must apply a weight, i.e.

$$\begin{aligned} W_{\alpha_n}(\phi, \{\sigma, \bar{\sigma}\}) &\leftarrow M_{n_\sigma, d'}(1, n_\sigma - 1), \\ W_{\beta_n}(\phi, \{\sigma, \bar{\sigma}\}) &\leftarrow M_{n_{\bar{\sigma}}, d'}(1, n_{\bar{\sigma}} - 1), \end{aligned} \quad (4.50)$$

where $n_\sigma = n_{\bar{\sigma}}$ represents the number of colour flows in the tensors $|\sigma\rangle$ and $|\bar{\sigma}\rangle$.

This could be the end of the story for the sampling of our Sudakov matrix elements. However, looking at the wider computation, our sampling of matrix elements can be made more efficient by considering the effect of the scalar product matrix. The scalar product matrix elements increasingly contribute N_c -suppressed terms the further they are from the matrix diagonal. Owing to this, we wish to more frequently sample those colour flows that result in matrix elements closer to the colour-diagonal. To do this, we sample the number of swaps that we wish to make between σ and τ (which we have so far been referring to as d'), from an exponentially falling distribution

$$P(x) = \frac{1 - N_c^{d_{min} - x}}{1 - N_c^{d_{min} - d_{max}}}, \quad (4.51)$$

where $d_{max} = \min(d, n_\sigma)$ and $d_{min} = 0$. d_{max} is the minimum between the colour order, d , to which we wish to approximate the calculation of Sudakov matrix elements and the number of colour flows in σ . The need for this upper limit is due to the following logic: the colour order, d , to which we calculate our $N_c^d \text{LC}'_V$ approximation (for all Sudakov matrix elements) is in fact a globally set value in `CVolver` (in the method `defaultOrder()` of the `Evolver` class). However, for smaller numbers of emissions, this value can exceed the number of colour flows in σ (which would place a limit on the number of swaps we can make).

The distribution in Eq. 4.51 is continuous however, whilst a sampled colour order, d' , must be of integer value. We set $d' = \lfloor x \rfloor$, the floor of the sampled x value. This modifies the distribution in Eq. 4.51 to be

$$P(d') = \frac{N_c^{-d'-1} (N_c - 1)}{N_c^{-d_{min}} - N_c^{-d_{max}}}. \quad (4.52)$$

We sample the value of d' according to the distribution in Eq. 4.52 before the determination of τ and $\bar{\tau}$ through the level-swap algorithm. The process that

$\alpha_n(\phi, \{\sigma, \bar{\sigma}\})$ and $\beta_n(\phi, \{\sigma, \bar{\sigma}\})$ represent (i.e. the level-swap algorithm using our newly sampled d') now includes this initial step and the corresponding sampling weights are

$$\begin{aligned} W_{\alpha_n}(\phi, \{\sigma, \bar{\sigma}\}) &\leftarrow \frac{M_{n_\sigma, d'}(1, n_\sigma - 1)}{P(d')}, \\ W_{\beta_n}(\phi, \{\sigma, \bar{\sigma}\}) &\leftarrow \frac{M_{n_{\bar{\sigma}}, d'}(1, n_{\bar{\sigma}} - 1)}{P(d')}. \end{aligned} \quad (4.53)$$

Beyond serving as a manageable way to calculate Sudakov matrix elements, we can see that our $N_c^d \text{LC}_V$ approximation has the added advantage that it limits the number of basis tensors that can be reached after the action of a Sudakov operator.

The orchestration of determining d_{max} , sampling a value of d' and subsequently sampling a basis tensor τ from σ using the level-swap algorithm is executed by the `nextFlows()` method in the `EvolutionMatrix` class. The process of sampling values for the i and k indices down a branch in the level-swap algorithm, is carried out by an independent function `randomLevelSwap()`. In particular, the sampling over i indices according to the distribution in Eq. 4.49 is conducted in `nextIlevel()`. For this, the multiplicity of permutations described in Eq. 4.47 is implemented as a recursive function in `levelSwapMultiplicity()`. The sampling of emission matrix element basis tensors is determined by the `nextFlows()` method in the `EmissionMatrix` class. The `nextFlows()` implementation differs for Variant A and B: Variant A utilises the sampling method of this chapter, to ensure that the chosen basis tensors for the amplitude and conjugate-amplitude differ by no more than two transpositions. Variant B samples tensors according to the distribution of emission matrix element values weighted by their scalar product matrix elements. These will be explained in Section 4.5.

4.5 The Implementation

In Section 4.1 we recapitulated the iterative algorithm for summing the leading soft-gluon logarithms to all orders, introduced in Chapter 2. Outlining how we could Monte Carlo over intermediate colour states, by inserting the unit operator between successive real emission and virtual correction operators, we rewrote our iterative algorithm explicitly in terms of matrix elements. This was expressed in Eq. 4.11 for one step in the evolution. A number of

challenges in implementing this equation into a Monte Carlo code were noted. Among them were, expressing the emission and Sudakov matrix elements in the colour flow regime (which was discussed in Section 4.3.1 and 4.3.4), computing an approximation of the Sudakov matrix element (discussed in Section 4.3.1) and sampling intermediate colour states along the most important trajectories in colour space (discussed in Section 4.4). We outlined some of the components necessary to implement Eq. 4.11 into a general shower evolution algorithm, Algorithm 4 in Section 4.2.4, representing each of these components by a ‘reference function’. The explicit forms of the matrix elements $[\tau | \mathbf{V}_{E,E'} | \sigma \rangle$ and $[\rho | \mathbf{D}_E | \tau \rangle$ in Algorithm 4 were stated in Section 4.3.1 and 4.3.4, whilst the reference functions $\alpha_n, \bar{\alpha}_n$, representing the sampling of Sudakov matrix elements at a multiplicity n , were determined in Section 4.4. All of these implementations reside in **Core**, with a dependence on **Hemispheres** for the exact definition of Γ_{ij} and ω_i or ω_{ij} .

Hemispheres is an example of **Implementation**, which generates events corresponding to the jet veto cross section. In what follows, we will present two implementations (Variant A and B) of the **Hemispheres** components. In doing so, we shall elucidate the emission scale selection (represented by the function E_n in Algorithm 4), the phase-space mapping (represented by Φ_{n+1}) and the details of the shower initialisation, including the hard process matrices. We shall also discuss the variant-dependent emission matrix element sampling method (represented by α_{n+1} and $\bar{\alpha}_{n+1}$), implemented in **Hemispheres::EmissionMatrix**. The development of variants A and B were carried out in close collaboration with S. Plätzer, and as such parts of this section are based heavily on unpublished notes from S. Plätzer, particularly the direction sampling implemented in Variant B.

Variant A was our initial approach to implementing the evolution algorithm in Eq. 4.11. It adopts an ‘ideal’ approach, which maintains an inherently amplitude-level description, using the emission matrix element in Eq. 4.40 with explicit polarisation vectors, and a corresponding basis tensor sampling scheme. In Chapter 5, we present jet veto cross section results for Variant A, where we shall see that this implementation suffers from increasingly large weights (at higher emission multiplicities), which contaminate the total cross section result. In an attempt to remedy this, Variant B was developed. This implementation performs cross section-level contractions of the emission operators. Consequently, this enables us to utilise the Sudakov veto algorithm with competition, in order to simultaneously sample the emission scale,

emission matrix basis tensors, and to choose the parents of the emitted gluon, which aids us in sampling emission degrees of freedom.

We begin our discussions by defining the implementations common to both variants of **Hemispheres**. This shall begin with a definition of the $V \rightarrow q\bar{q}$ and $H \rightarrow gg$ matrix elements, followed by a discussion of the emission scale sampling and termination criteria.

4.5.1 Hard Process Matrix Elements

We start this section by writing the hard process matrix for $q\bar{q}$ production:

$$\mathbf{H}_{q\bar{q}} = |1\rangle [1 | \mathbf{H}_{q\bar{q}} |1] \langle 1|, \quad (4.54)$$

where $[1 | \mathbf{H}_{q\bar{q}} |1] = 1$ such that we neglect contributing factors from the initial process, V (see Section 1.4.1 for the details of one possible form of V). The basis tensor $|1\rangle$ corresponds to a single colour flow between the two final-state primary jets. For gg production,

$$\mathbf{H}_{gg} = |21\rangle \langle 21| - \frac{1}{N_c} |12\rangle \langle 21| - \frac{1}{N_c} |21\rangle \langle 12| + \frac{1}{N_c^2} |12\rangle \langle 12|. \quad (4.55)$$

We shall denote the corresponding veto cross section as $\Sigma(\rho)$ throughout the rest of this work, where $\rho = Q_0/Q_H$, i.e. we consider energies to be normalised to the hard scale of the primary jets. The inclusive cross section is then $\Sigma_{q\bar{q}}(1) = \text{Tr}\mathbf{H}_{q\bar{q}} = N_c$ for $q\bar{q}$ production and $\Sigma_{gg}(1) = N_c^2 - 1$ for gg production.

The initial σ and $\bar{\sigma}$ basis tensors in Algorithm 4, line 1 specify the hard process matrix element. In the case of $q\bar{q}$ production, the single colour flow between the final-state primary partons means that we choose the tensor $|1\rangle$ in both the amplitude and conjugate-amplitude with unit probability and unit weight, i.e.

$$\{\sigma, \bar{\sigma}\} \leftarrow \{\alpha_0 = |1\rangle, \bar{\alpha}_0 = \langle 1|\}, \quad M_{\sigma, \bar{\sigma}} \leftarrow [1 | \mathbf{H}_{q\bar{q}} |1], \quad w_{\text{hard}} \leftarrow 1, \quad (4.56)$$

where α_0 and $\bar{\alpha}_0$ are the reference functions in Algorithm 4 which represent the process according to which we choose σ and $\bar{\sigma}$. In the case of gg production, there are two colour flows between the primary partons, $|12\rangle$ and $|21\rangle$. The

basis tensors σ and $\bar{\sigma}$ are selected at the same time, with a probability

$$P_{H_{gg}}(\sigma, \bar{\sigma}) = \frac{[\sigma | \mathbf{H}_{gg} | \bar{\sigma}] N_c^2}{(N_c + 1)^2}. \quad (4.57)$$

With σ and $\bar{\sigma}$ chosen, the corresponding hard matrix element and weight, take on the values

$$M_{\sigma, \bar{\sigma}} \leftarrow [\sigma | \mathbf{H}_{gg} | \bar{\sigma}], \quad w_{\text{hard}} \leftarrow \frac{1}{P_{H_{gg}}(\sigma, \bar{\sigma})}. \quad (4.58)$$

Cvolver has been designed with a view to being generalised into a multi-purpose event generator. One example where this manifests itself is that we sample the directions of the two primary particles for both the $V \rightarrow q\bar{q}$ and $H \rightarrow gg$ processes⁸ in **Hemispheres** (represented by ϕ_0 in Algorithm 4). In this simple case, the direction of the first primary parton (e.g. a quark or gluon) is sampled uniformly across the solid angle in the lab-frame: specifically, the azimuthal angle, ϕ_1 , is chosen uniformly between 0 and 2π and the polar angle, $\cos \theta_1$, between -1 and 1 . The polar and azimuthal angles of the other primary parton are $\cos \theta_2 = -\cos \theta_1$ and $\phi_2 = \Theta(\phi_1 - \pi)(\phi_1 - \pi) + \Theta(\pi - \phi_1)(\phi_1 + \pi)$, i.e. the two partons are back-to-back. We shall use the terms lab-frame and di-jet ZMF interchangeably in the following discussions, as they are identical, up to a rotation.

Whilst we have provided explicit expressions for the hard process matrix elements, colour flow selection and initial kinematics of the hard partons, the class methods implementing these could be readily interfaced to a fully-fledged matrix element generator, such as **MadGraph** [116].

4.5.2 Observable Cross Section

In Eq. 4.9 we wrote the cross section for a general observable:

$$\Sigma(\mu) = \int \sum_n d\sigma_n u_n(\{k\}_n). \quad (4.59)$$

⁸For the purposes of this work, their corresponding matrix elements have no kinematic dependence. But more generally, this sampling would amount to an integration over initial-state particles.

The jet veto cross section is part of the class of observables discussed in Section 2.1.1. As such the measurement function can be written as

$$u_n(\{k\}_n) = \prod_{i=1}^n u_i(k_i), \quad (4.60)$$

where $u_i(k_i)$ denotes the measurement function of parton i and depends on its momentum k_i ,

$$u_i(k_i) = \Theta_{\text{out}}(k_i) + \Theta_{\text{in}}(k_i)\Theta(\rho > E_i), \quad (4.61)$$

where ρ is the veto scale of any real emission for the jet veto observable. The Heaviside functions Θ_{in} and Θ_{out} , separate the observable phase-space into an in- and out-of-gap region. We noted in Section 2.1.1, that for such observables, their inclusivity for energies less than the veto scale, leads to a complete cancellation of the real emission and virtual exchange contributions. Thus, we can set $\mu = \rho$ in Eq. 4.9 and set $u_i(k_i) = \Theta_{\text{out}}(k_i)$. This is exactly the measurement function, u_n , in Algorithm 4 for **Hemispheres**, and means we only sample emitted gluon directions in the out-region. Unlike in Section 2.1, we do not split apart the virtual loop-integral into two parts to perform an out-of-gap expansion. We instead integrate the kinematic variables in the soft-gluon anomalous dimension matrix over the entire angular phase-space.

In our shower evolution, we also wish to allow particles to freely cascade and only stop once particular termination criteria are met: we want to be able to limit the multiplicity of an event to a value n_{max} or sample evolution energy scales until we reach our veto scale, ρ , whichever occurs first. It is then useful to breakdown the total cross section, $\Sigma(\rho)$, by multiplicity,

$$\Sigma(\rho) = \sum_n \Sigma_n(\rho), \quad (4.62)$$

where $\Sigma_n(\rho)$ is the cross section after n emissions. This can be written explicitly, as

$$\begin{aligned} \Sigma_n(\rho) = & \int_0^1 dE_{n+1} \int_{E_{n+1}}^1 \frac{\alpha_s dE_n}{\pi E_n} \int_{\text{out}} \frac{d\Omega_n}{4\pi} \cdots \int_{E_2}^1 \frac{\alpha_s dE_1}{\pi E_1} \int_{\text{out}} \frac{d\Omega_1}{4\pi} \\ & \times \sum_{\substack{\sigma, \bar{\sigma} \\ \rho, \bar{\rho}}} [\sigma | \mathbf{V}_{E_{n+1}, E_n} | \rho \rangle M_{\rho, \bar{\rho}}(E_n) \langle \bar{\rho} | \mathbf{V}_{E_{n+1}, E_n}^\dagger | \bar{\sigma} \rangle \langle \sigma | \bar{\sigma} \rangle \delta(E_{n+1} - \rho), \end{aligned} \quad (4.63)$$

where $M_{\rho, \bar{\rho}}(E_n)$ is the recursively defined matrix element in Eq. 4.11. The re-

cursive phase-space factors have been extracted and explicitly integrated over; we have written the energies in units of Q_H , the hard process scale. Also note, that we have neglected the minus sign in each phase-space factor. For Variant A, these are accounted for by the completeness relation of the gluon polarisation vectors. In Variant B however, we calculate the emission operators in the amplitude and conjugate-amplitude at the cross section-level. The minus signs are then included in the definition of our dipole factors, ω_{ij} , as per Eq. 4.44.

Eq. 4.63 highlights the emission direction and scale sampling that takes place at each evolution step, including the potential sampling of our veto scale (in the integral over E_{n+1}). With both of our termination criteria in-mind, we adopt a scale sampling strategy similar to the Sudakov veto algorithm, discussed in Chapter 3. Succinctly, emission scales are sampled at each step according to the distribution,

$$dS_P(E|E') = P(E) \exp\left(-\int_E^{E'} P(q)dq\right) dE = P(E)\Delta_P(E|E')dE \quad (4.64)$$

which is the probability for an emission to occur at E , given the last emission scale is E' . dE in the above equation represents each of the dE_i (where $i = 1, \dots, n+1$) elements in Eq. 4.63, with $E' = E_{i-1}$. $P(E)$ represents the emission probability, whilst the exponential is the Sudakov form factor, or the non-emission probability. As is argued in [108], Eq. 4.64 alone is not sufficient to sample energies in the presence of a lower cutoff scale, μ . The relevant probability density is

$$dS_P(\mu, E|E') = \Delta_P(\mu|E')\delta(E - \mu)dE + \Theta(E' - E)\Theta(E - \mu)P(E)\Delta_P(E|E')dE, \quad (4.65)$$

where we identify the cutoff μ , with our veto scale ρ for the jet veto observable. In order to constrain our events to a maximum multiplicity, n_{max} , we can extend Eq. 4.65 and write the density

$$dS_P(\rho, E|E') = \Delta_P(\rho|E')\delta(E - \rho)dE + (1 - \Delta_P(\rho|E'))\delta_{n, n_{max}}\delta(E - \rho)dE + P(E)\Delta_P(E|E')(1 - \delta_{n, n_{max}})\Theta(E' - E)\Theta(E - \rho)dE, \quad (4.66)$$

where $\delta_{n, n_{max}}$ is a Kronecker delta which is equal to 1 if $n = n_{max}$ and 0 otherwise. One can see that Eq. 4.66 describes a density from which we can sample emission scales, and which accounts for three scenarios:

- When we have not yet reached our maximum multiplicity n_{max} , and we have not emitted below our veto scale, ρ (third line).
- When we have reached our maximum multiplicity, and we therefore evolve down to our veto scale, ρ (second line).
- And, when we have not yet reached our maximum multiplicity n_{max} , but we terminate at fewer emissions because we have emitted below our veto scale, ρ (first line).

It is the third line of Eq. 4.66 which conducts the ‘standard’ Sudakov veto algorithm discussed in Chapter 3 and we can see that Eq. 4.66 reverts back to Eq. 4.65 in the case that we do not wish to limit the multiplicity. Both variants adopt the sampling density in Eq. 4.66: Variant A exploits the imposed cutoff prescription (which shall be discussed in the next section) to isolate the colour-diagonal terms of the Sudakov operator which are cutoff-dependent. These terms are described by the kernel $P(E)$ in Eq. 4.66 so that $\Delta_P(E|E')$ constitutes the collinear part of the Sudakov operator. Eq. 4.66 can easily be extended to include the competition algorithm as done in Section 3.5.3, by writing $P(E)$ as a sum over its constituent species:

$$P(E) = \sum_{ij} P_{ij}(E), \quad (4.67)$$

where each of the species is indexed by an ij pair. One can simultaneously sample a scale E and choose a process ij using Algorithm 3. Variant B adopts Eq. 4.66 with competition to sample emission scales at the same time as treating the accessible emission matrix elements, indexed by the external particles ij , as competing processes. The act of choosing two parent partons ij , also facilitates a direction sampling strategy (which shall be discussed in Section 4.5.4).

In the rest of the chapter, we will discuss the Variant A and B implementations. For each, we shall present the phase-space mapping (represented by Φ_n in Algorithm 4), the emission matrix element sampling (represented by α_{n+1} and $\bar{\alpha}_{n+1}$), emission direction sampling, and a cutoff prescription used to tame collinear divergences in the dipole factors (which instructs the form of Γ_{ij} , ω_i and ω_{ij}). The evolution scale sampling for each variant (represented by E_n) uses the density in Eq. 4.66 to sample evolution energy scales. However, the exact form of the kernel, $P(E)$, differs for both variants: in Variant A, the kernel describes the cutoff dependent part of the Sudakov operator exponent

after applying a collinear cutoff to the dipole factor. Variant B on the other hand utilises the Sudakov veto algorithm with competition to simultaneously sample evolution scales and the parent partons (ij) of the next emission.

4.5.3 Variant A

We begin with our first implementation of the shower evolution in Algorithm 4, Variant A⁹. As our first attempt at implementing the general evolution algorithm in Eq. 4.11, this variant adopts a strictly amplitude-level description. In particular, it uses the amplitude-level emission matrix elements in Eq. 4.40. In this section, we will express the form of ω_i used in these, including the cutoff prescription and explicit four-vector representation of the polarisation vectors. Additionally, we explain the emission matrix element tensor sampling and emission direction sampling procedures.

For the jet veto observable we consider in this work, there are only wide-angle, soft logarithms. There still remain however intermediate collinear singular terms, which whilst they cancel analytically, are numerically problematic. As a stringent test that the algorithm correctly handles the cancellation of these singular terms, and to facilitate numerical computation, we cut out small cones in phase-space around each real emission:

$$\frac{n_i \cdot \epsilon_k^\pm}{(n_i \cdot n_k)} \rightarrow \frac{n_i \cdot \epsilon_k^\pm}{(n_i \cdot n_k)} \Theta_{\text{cut}}(n_k), \quad (4.68)$$

where

$$\Theta_{\text{cut}}(n_k) = \prod_i \Theta(n_i \cdot n_k - \lambda). \quad (4.69)$$

Specifically, we impose that $n \cdot n_i > \lambda$, where λ is a collinear cutoff, for each parton i in the evolution, i.e. the emitted gluon resides outside a small conical region, of extent λ , about each parton in the lab-frame. Correspondingly, for the loop integrals we regulate using the replacement

$$\begin{aligned} \frac{n_i \cdot n_j}{(n_i \cdot n)(n_j \cdot n)} \Theta_{\text{cut}} &= \left(\frac{n_i \cdot n_j}{(n_i \cdot n)(n_j \cdot n)} - S_{ij} - S_{ji} \right) + (S_{ij} + S_{ji}) \Theta_{\text{cut}} \\ &\quad - (1 - \Theta_{\text{cut}}) \frac{n_i \cdot n_j}{(n_i \cdot n)(n_j \cdot n)} + (1 - \Theta_{\text{cut}}) (S_{ij} + S_{ji}), \end{aligned} \quad (4.70)$$

where the last two terms are collinear-finite, encapsulating the complementary

⁹Variant A is based on revision `f5365a90d98d` (the changeset signature within the `CVolver` Mercurial repository) of the `CVolver` code.

phase-space region within the cones about each parton. One would anticipate that these terms cancel against corresponding real-emission contributions, and so we disregard them in the ensuing discussions. The subtraction terms S_{ij} and S_{ji} are defined as

$$\begin{aligned} S_{ij} &= \frac{1}{n_i \cdot n} - \frac{n_j \cdot n - n_i \cdot n_j}{(n_i \cdot n_j)(n_i \cdot n)} \\ S_{ji} &= \frac{1}{n_j \cdot n} - \frac{n_i \cdot n - n_i \cdot n_j}{(n_i \cdot n_j)(n_j \cdot n)}, \end{aligned} \quad (4.71)$$

such that after the subtraction of these terms, the dipole factor remains finite in the limit that either i or j are collinear with the emission, i.e. when $n_i \cdot n$ or $n_j \cdot n$ approach 0. After integrating over solid angle,

$$\begin{aligned} \int \left[\left(\frac{n_i \cdot n_j}{(n_i \cdot n)(n_j \cdot n)} - S_{ij} - S_{ji} \right) + (S_{ij} + S_{ji}) \Theta_{\text{cut}} \right] \frac{d\Omega}{4\pi} \\ = \ln \left(\frac{2}{\lambda} \right) + \ln \left(\frac{n_i \cdot n_j}{2} \right) + \mathcal{O}(\lambda). \end{aligned} \quad (4.72)$$

It is worth noting that the finite integral involving the subtracted terms is similar to that used to derive angular ordering [164], which we showed in Chapter 3. Since the $\ln \lambda$ term is independent of i and j we can exploit colour conservation to write

$$\sum_{i < j} (-\mathbf{T}_i \cdot \mathbf{T}_j) = \frac{1}{2} \sum_i \mathbf{T}_i^2, \quad (4.73)$$

which is colour diagonal. This leads to the well-known result that the collinear region has trivial colour and it means that all of the collinear cutoff dependence is in the abelian sector [103]. We can exploit this to extract the collinear cutoff dependent terms of the Sudakov operator at each step of the evolution, in both the amplitude and conjugate-amplitude, and use these contributions to sample the evolution scale. As such we set the kernel, $P(E)$, in Eq. 4.66 to be

$$P(E) = \frac{1}{E} \frac{\alpha_s}{\pi} \sum_i C_i \ln \left(\frac{2}{\lambda} \right), \quad (4.74)$$

resulting in

$$\Delta_P(E|E') = \exp \left(-\frac{\alpha_s}{\pi} \sum_i C_i \ln \left(\frac{2}{\lambda} \right) \ln \left(\frac{E'}{E} \right) \right), \quad (4.75)$$

for the form of $\Delta_P(E|E')$. Here, i is a sum over all partons and C_i is the Casimir

operator associated with parton i . That is, $C_i = C_A = N_c$ if i is a gluon and $C_i = C_F = (N_c^2 - 1)/2N_c$ if i is a quark or antiquark. Algorithm 7 below represents the action of the scale generating function, E_n , in our shower evolution (Algorithm 4) and corresponds to sampling by inversion from the probability density in Eq. 4.66 with $P(E)$ and $\Delta_P(E|E')$ as defined above. Provided we have not reached the maximum multiplicity, n_{max} , and the energy sampled in Algorithm 7 is not smaller than ρ , this act of sampling is as if we multiplied the weight by

$$\frac{\alpha_s}{\pi} \frac{1}{E} \sum_i C_i \ln \left(\frac{2}{\lambda} \right) \exp \left(-\frac{\alpha_s}{\pi} \sum_i C_i \ln \left(\frac{2}{\lambda} \right) \ln \left(\frac{E'}{E} \right) \right). \quad (4.76)$$

This is exactly the part of the phase-space factor, $(\alpha_s/\pi)dE/E$, in each evolution step of Eq. 4.11, combined with the collinear part of the corresponding Sudakov operators in the amplitude and conjugate-amplitude. The additional $\sum_i C_i \ln(2/\lambda)$ factor is removed as a weight using the emission scale selection weight, W_{E_n} (in line 12 of Algorithm 7). In the case that we have reached maximum multiplicity, or our sampled energy scale is below ρ , our event terminates. In the former case, the collinear part of the final Sudakov operators is included as a weight, $W_{E_n} = \Delta_P(\rho|E')$.

Algorithm 7: The modified Sudakov veto algorithm for Variant A, accounting for the presence of a lower cutoff, ρ , and a potential constraint on the maximum multiplicity, n_{max} . It outlines the emission scale sampling, represented by E_n . This, the hard scale, E' , and the scale sampling weight, W_{E_n} are introduced in Algorithm 4.

```

solve  $\mathcal{R} = \Delta_P(E|E')\theta(E - \rho)$ 
1 if  $E < \rho$  then
2    $E \leftarrow \rho$ 
3   if  $n = n_{max}$  then
4      $W_{E_n}(\phi, E, E', \{\sigma, \bar{\sigma}\}) \leftarrow \Delta_P(E|E')$ 
5     return  $E$ 
6 else
7   if  $n = n_{max}$  then
8      $E \leftarrow \rho$ 
9      $W_{E_n}(\phi, E, E', \{\sigma, \bar{\sigma}\}) \leftarrow \Delta_P(E|E')$ 
10    return  $E$ 
11  else
12     $W_{E_n}(\phi, E, E', \{\sigma, \bar{\sigma}\}) \leftarrow 1 / (\sum_i C_i \ln(2/\lambda))$ 
13    return  $E$ 

```

The remaining contributions to the Sudakov operator matrix elements are included at each evolution step manually, as per line 7 in Algorithm 4,

$$M_{\tau\bar{\tau}} \leftarrow [\tau | \mathbf{V}_{E,E'} | \sigma \rangle M_{\sigma\bar{\sigma}} \langle \bar{\sigma} | \mathbf{V}_{E,E'}^\dagger | \bar{\tau} \rangle]. \quad (4.77)$$

These matrix elements are approximated as discussed in Section 4.3.1, using Eq. 4.26 or Eq. 4.32. They rely on the corresponding soft-gluon anomalous dimension matrix coefficients, which are

$$\Gamma_{ij} = \frac{\alpha_s}{2\pi} \ln \left(\frac{E'}{E} \right) \ln \left(\frac{n_i \cdot n_j}{2} \right), \quad (4.78)$$

i.e. the part of the Sudakov exponent corresponding to the i, j dependent term in Eq. 4.72.

We now move our discussion onto the sampling and evaluation of the emission operator matrix elements in Algorithm 4, line 16,

$$M_{\rho,\bar{\rho}} \leftarrow [\rho | \mathbf{D}_E | \tau \rangle \times M_{\tau,\bar{\tau}} \times \langle \bar{\tau} | \mathbf{D}_E^\dagger | \bar{\rho} \rangle]. \quad (4.79)$$

The sampling of the basis tensors, ρ and $\bar{\rho}$, is represented by α_{n+1} and $\bar{\alpha}_{n+1}$ in line 14. The process according to which they are chosen, follows a similar logic as was presented in Section 4.4, i.e. we choose tensors which differ by at most d' swaps, favouring smaller values of d' . Specifically, we know from Section 2.3 that, $0 \leq \#(\rho, \bar{\rho}) - \#(\tau, \bar{\tau}) \leq 2$, which constrains $\rho, \bar{\rho}$ to being at most two additional swaps from each other than $\tau, \bar{\tau}$. Our sampling procedure is then as follows:

- Choose either of the basis tensors post-emission, ρ or $\bar{\rho}$, with equal probability.
- Set the chosen basis tensor, say ρ , to be one of the $n_q + n_g + 1$ tensors that are accessible after the action of an emission operator (on τ) (n_q and n_g are the number of quarks and gluons in the event). These tensors are sampled with uniform probability. This choice is represented by the function α_{n+1} in Algorithm 4, line 14. Note that the $n_q + n_g + 1$ tensors come about due to the following logic: the colour charge operator maps τ onto three other, unique tensors. They correspond to an emission off the colour line (c_i) corresponding to parton i , anti colour line (\bar{c}_i), or a singlet gluon emission. The operator \mathbf{D} sums over the colour charge operators corresponding to all partons.

- $\bar{\rho}$ can then be sampled using the level-swap algorithm, starting with ρ and determining a basis tensor d' swaps away. This value of d' is itself sampled as outlined in Section 4.4, using a value of $d_{\max} = \min(n_\tau, n_\tau - \#(\tau, \bar{\tau}) + 2)$, where n_τ is the number of colour flows in the basis tensors τ and $\bar{\tau}$. Sampling of $\bar{\rho}$ is represented by the function $\bar{\alpha}_{n+1}$ in Algorithm 4.

The weights corresponding to the sampling of ρ and $\bar{\rho}$ are then

$$\begin{aligned} W_{\alpha_{n+1}} &\leftarrow (n_q + n_g + 1) \\ W_{\bar{\alpha}_{n+1}} &\leftarrow \frac{1 - N_c^{-d_{\max}}}{N_c^{-d'-1}(N_c - 1)} M_{n_\tau, d'}(1, n_\tau - 1) \end{aligned} \quad (4.80)$$

where $M_{n, d'}(1, n_\tau - 1)$ is the multiplicity of all permutations d' swaps from τ . If we had instead chosen $\bar{\rho}$ in the first step, the overall resultant weight $W_{\alpha_{n+1}} \times W_{\bar{\alpha}_{n+1}}$ would be the same, with

$$\begin{aligned} \alpha_{n+1} &\leftrightarrow \bar{\alpha}_{n+1}, \\ W_{\alpha_{n+1}} &\leftrightarrow W_{\bar{\alpha}_{n+1}}. \end{aligned} \quad (4.81)$$

Having established which emission operator matrix elements are to be calculated, we turn our attention to their actual evaluation. Firstly, the phase-space point for the next emission, k , is generated. Variant A is tailored to be efficient for the jet veto observable and as such samples gluon directions uniformly in the out-region. With the sampled emission scale, the momentum of k is defined entirely by $\cos \theta_k$ and ϕ_k which are sampled according to the distributions

$$\begin{aligned} dP_{\cos \theta}(\cos \theta_k) &= \frac{1}{2} \frac{(\Theta(\cos \theta_k - c_0) + \Theta(-c_0 - \cos \theta_k))}{(\cos \theta_k - c_0)} d \cos \theta_k, \\ dP_\phi(\phi_k) &= \frac{1}{2\pi} d\phi_k, \end{aligned} \quad (4.82)$$

where $c_0 = \cos(\pi/4)$. The emitted gluon azimuth, ϕ_k , is sampled uniformly from the range of possible values $[0, 2\pi]$. We can see that these sampling distributions are exactly the normalised solid angle integrations for each emission in Eq. 4.63, whilst the Heaviside step functions in $dP_{\cos \theta}$ constrain each emission to the out-region, ensuring our measurement function is always equal to unity. This means that Variant A never terminates due to an emission into the in-gap region, but only due to either evolving to a maximum multiplicity, n_{\max} , or sampling an emission scale below the veto scale, ρ . The direction sampling

is performed (in general) by Φ_{n+1} , whilst the weight corresponding to this selection is $W_{\Phi_{n+1}} \leftarrow (1 - c_0)$. Moreover, Φ_{n+1} updates ϕ with the newly added particle momenta and its colour representation. It is important to note that the aforementioned sampling efficiency, in which we uniformly sample gluon directions in the out-region, is not a restriction on the general applicability of our approach and in general, Φ_{n+1} would also represent the action of a kinematic recoil prescription.

In Variant A we calculate the emission matrix elements using the amplitude-level emission operators in Eq. 4.40, and must specify the form of the dipole factors,

$$\omega_i(k) = \frac{n_i \cdot \epsilon_k^\pm}{n_i \cdot n_k} \Theta_{\text{cut}}(n_k). \quad (4.83)$$

In particular, this means providing a representation for the emitted gluon polarisation vector. To do this we use the spinor-helicity formalism [165]. The spinor representation for a gluon polarisation vector of definite helicity, ± 1 , is

$$\epsilon_\mu^\pm(k, q) = \pm \frac{\langle q^\mp | \gamma_\mu | k^\mp \rangle}{\sqrt{2} \langle q^\mp | k^\pm \rangle}. \quad (4.84)$$

The γ^μ are the Dirac matrices (written explicitly in Chapter 1) and $\langle q^\mp | k^\pm \rangle$ are Lorentz-invariant Weyl products. q is an auxiliary massless vector (the so-called reference momentum), reflecting the freedom of on-shell gauge transformations. It is light-like and not parallel to k , the gluon momentum. A polarisation vector defined in this way obeys the completeness relation of a gluon in the light-cone gauge:

$$\sum_{\lambda=\pm 1} \epsilon_\mu^\lambda(k, q) (\epsilon_\nu^\lambda(k, q))^* = -\eta_{\mu\nu} + \frac{k_\mu q_\nu + k_\nu q_\mu}{k \cdot q}. \quad (4.85)$$

Using Eq. 4.84 and [166], the explicit four-vector representation of the polarisation vector can be written as

$$\epsilon_\mu^+(k, q_x) = \begin{pmatrix} k^+ \\ k^+ \\ -ik^- \\ k^- \end{pmatrix}, \quad \epsilon_\mu^+(k, q_z) = \begin{pmatrix} k^+ \\ k^- \\ -ik^- \\ k^+ \end{pmatrix}, \quad (4.86)$$

for a reference momentum along the x - and z -axis respectively. These two forms of the polarisation vectors are related by the Schouten identity [166].

The reference momenta, q_x and q_z , and gluon momenta, are defined as

$$\begin{aligned} q_x &= (1, 1, 0, 0), & q_z &= (1, 0, 0, 1), \\ n_k &= (1, \sin(\theta) \cos(\phi), \sin(\theta) \sin(\phi), \cos(\theta)), \end{aligned} \quad (4.87)$$

whilst the k^+ and k^- variables have the form

$$\begin{aligned} \text{sgn} &= 1 - 2\Theta(c_0 - |\cos(\theta)|), \\ k^+ &= \frac{1 + \cos(\theta) + \cos(\phi) \sin(\theta) - i \sin(\phi) \sin(\theta)}{\sqrt{2}(1 + \text{sgn} \cos(\theta) - \text{sgn} \cos(\phi) \sin(\theta) - i \sin(\phi) \sin(\theta))}, \\ k^- &= \frac{1 + \text{sgn} \cos(\theta) - \text{sgn} \cos(\phi) \sin(\theta) + i \sin(\phi) \sin(\theta)}{\sqrt{2}(1 + \text{sgn} \cos(\theta) - \text{sgn} \cos(\phi) \sin(\theta) - i \sin(\phi) \sin(\theta))}. \end{aligned} \quad (4.88)$$

The Variant A **Hemispheres** implementation uses the $\epsilon_\mu^+(k, q_x)$ polarisation vector defined in Eq. 4.86, by default. They are determined in Φ_{n+1} , so that the ω_i factors can be subsequently evaluated in `Hemispheres::EmissionMatrix::evaluate()`. When using explicit polarisation vectors, one must sum over all helicities of each soft-gluon emission to account for the minus-sign in the phase-space element of Eq. 4.6, as per Eq. 4.85. As written in Eq. 4.86, these polarisation vectors have +1 helicity, and are related to their -1 helicity counterpart through complex conjugation, $\epsilon_\mu^-(k, q) = (\epsilon_\mu^+(k, q))^*$. The helicity sum is handled in Variant A using Monte Carlo methods, by assigning each emitted gluon a helicity of +1 or -1 with equal probability during the generation of the gluon degrees of freedom. The event is weighted accordingly with a factor of 2, i.e. $W_{\Phi_{n+1}} \leftarrow 2$. Generally, we are free to choose a different reference momentum for each gluon momentum in an amplitude, and by-default we use one oriented along the x -axis, q_x . However, one encounters numerical instabilities in the case that the sampled emitted gluon direction is sufficiently close to this axis. In such a case, we should adopt a different quantisation axis, along the z -axis. Specifically, if the generated emission direction lay outside a cone, of extent c_0 , about the xy -plane, Variant A uses $\epsilon_\mu^+(k, q_z)$ as the polarisation vector for that emission instead of $\epsilon_\mu^+(k, q_x)$. This choice is reflected in the sgn variable in Eq. 4.88.

As a check on the form of the polarisation vectors in Eq. 4.86, we see that they obey the required transversality with respect to both the gluon and reference

momenta,

$$\begin{aligned}
\epsilon_x^\pm(k, q_x) \cdot q_x &= \epsilon_x^\pm(k, q_x) \cdot k = \epsilon_x^\pm(k, q_x) \cdot \epsilon_x^\pm(k, q_x) = 0, \\
\epsilon_z^\pm(k, q_z) \cdot q_z &= \epsilon_z^\pm(k, q_z) \cdot k = \epsilon_z^\pm(k, q_z) \cdot \epsilon_z^\pm(k, q_z) = 0, \\
\epsilon_x^\pm(k, q_x) \cdot \epsilon_x^\mp(k, q_x) &= \epsilon_z^\pm(k, q_z) \cdot \epsilon_z^\mp(k, q_z) = -1. \quad (4.89)
\end{aligned}$$

We have now described all of the components of Variant A. In Chapter 5 we will present the Variant A individual-multiplicity jet veto cross section results for both the `evolve()` and `evolveFull()` algorithms. For low multiplicities we shall analytically calculate the jet veto cross section, adopting the cutoff prescription in Eq. 4.68. These calculations show agreement with the results of Variant A. Additionally, we compare the `evolve()` and `evolveFull()` algorithms, which provides a validation of the emission and Sudakov matrix element sampling implemented in `evolve()`. Lastly, we exhibit the total cross section, $\Sigma(\rho)$, in Section 5.1.6, with contributions from multiplicities up to 10 emissions. We shall see that the Variant A total cross section contains large weight fluctuations which dominate the results. In the next section, we shall outline our attempt at ameliorating this issue, with Variant B.

4.5.4 Variant B

Variant B¹⁰ was designed with the large weight fluctuations of Variant A in mind. As such, Variant B performs cross section-level contractions of the emission operators where possible. This in-turn enables us to use the Sudakov veto algorithm with competition to sample the emission scale, determine the parents of the emitted gluon and to choose emission matrix elements, at the same time. This ameliorates the issue of large fluctuating weights to some extent, by only introducing two sources of sampling weights: the Sudakov matrix element sampling (as outlined in Section 4.4) and by dividing out exponential factors related to the Sudakov veto algorithm.

Like in Variant A, we deal with the collinear region by cutting out small cones around each real emission. By virtue of the Sudakov veto algorithm with competition, we choose two parent partons, ij , from which we emit, at each step of

¹⁰Variant B is based on revision `b8d7734d94d9` of the `CVolver` code.

the evolution. We impose that $n \cdot n_{i,j} > \lambda$ for emission off the ij pair:

$$\frac{n_i \cdot n_j}{(n_i \cdot n)(n_j \cdot n)} \rightarrow \frac{n_i \cdot n_j}{n \cdot n_i + n \cdot n_j} \left(\frac{\Theta(n \cdot n_i - \lambda)}{n \cdot n_i} + \frac{\Theta(n \cdot n_j - \lambda)}{n \cdot n_j} \right). \quad (4.90)$$

The loop integrals are regulated using the same replacement, where

$$\int \frac{d\Omega}{4\pi} \frac{n_i \cdot n_j}{n \cdot n_i + n \cdot n_j} \left(\frac{\Theta(n \cdot n_i - \lambda)}{n \cdot n_i} + \frac{\Theta(n \cdot n_j - \lambda)}{n \cdot n_j} \right) \approx \ln \frac{n_i \cdot n_j}{\lambda}, \quad (4.91)$$

after integration over the solid angle. As before, we ignore terms which are suppressed by powers of the collinear cutoff, λ .

Similar to how standard parton showers describe the large- N_c emission probability through the use of the Sudakov veto algorithm with competition, Variant B uses it to include the full-colour emission probability:

$$dR(E_k) = \frac{\alpha}{\pi} \frac{dE_k}{E_k} \sum_{i,j} [\rho | \mathbf{T}_i | \tau] \langle \bar{\tau} | \mathbf{T}_j | \bar{\rho} \rangle \omega_{ij}(k) \frac{d\Omega_k}{4\pi}. \quad (4.92)$$

In the above equation, the emission operators in the amplitude and conjugate-amplitude for the k th emission, have been contracted as per Eq. 4.43. Also included, are the phase-space element terms in Eq. 4.63 corresponding to the k th emission. The sum over i, j runs over all external legs which do not form a singlet-gluon in the colour arrangements τ or $\bar{\tau}$ respectively, i.e. $\tau(c_i) \neq c_i$ and $\bar{\tau}(c_j) \neq c_j$. Such terms are excluded for efficiency purposes, as they inevitably cancel for emitted gluons. It is convenient to rewrite Eq. 4.92 into the form

$$dR(E_k) = \frac{\alpha_s}{\pi} \frac{dE_k}{E_k} \sum_{i,j} \tilde{\zeta}_{ij} \Omega_{ij} \times \left(\frac{\omega_{ij}(k) d\Omega_k}{\Omega_{ij} 4\pi} \right) \times \left(\frac{[\rho | \mathbf{T}_i | \tau] \langle \bar{\tau} | \mathbf{T}_j | \bar{\rho} \rangle}{|[\rho | \mathbf{T}_i | \tau] \langle \bar{\tau} | \mathbf{T}_j | \bar{\rho} \rangle|} \right) \times \left(\frac{\langle \rho | \bar{\rho} \rangle}{\langle \tau | \bar{\tau} \rangle} \frac{|[\rho | \mathbf{T}_i | \tau] \langle \bar{\tau} | \mathbf{T}_j | \bar{\rho} \rangle|}{\tilde{\zeta}_{ij}} \right), \quad (4.93)$$

where $\Omega_{ij} = \int \omega_{ij}(k) d\Omega_k$ is the dipole factor integrated over the solid angle, and the object $\tilde{\zeta}_{ij}$ is defined as

$$\tilde{\zeta}_{ij} = \sum_{\rho', \bar{\rho}'} \frac{\langle \rho' | \bar{\rho}' \rangle}{\langle \tau | \bar{\tau} \rangle} |[\rho' | \mathbf{T}_i | \tau] \langle \bar{\tau} | \mathbf{T}_j | \bar{\rho}' \rangle|. \quad (4.94)$$

The sum $\rho', \bar{\rho}'$ is over all basis tensors that can be reached through the action of the emission operators, and we have introduced a ratio of scalar product matrices (corresponding to the tensors before and after the action of the emission operator). Normalised quantities in Eq. 4.93 have been delimited by parenthesis. Written in this way, we highlight the sampling densities for the direction sampling (in the first pair of parenthesis) and emission matrix element sampling (in the third), and expose the structure of the competition algorithm. We shall move on to discuss this latter point.

Variant B uses the density in Eq. 4.66 (used for Variant A), extended by the competition algorithm, to sample emission scales. The competing processes are each of the terms contributing to the emission probability, i.e. the competition algorithm accounts for each i, j combination in the sum of Eq. 4.93. We sample an energy E_{ij} for each emission species, according to the distribution

$$dS_{P_{ij}}(\rho, E|E') = P_{ij}(E_{ij})\Delta_{P_{ij}}(E_{ij}|E') dE_{ij}, \quad (4.95)$$

where we identify the kernel as

$$P_{ij}(E_{ij}) = \frac{\alpha_s}{\pi} \frac{1}{E_{ij}} \xi_{ij} \Omega_{ij}, \quad \Delta_P = \prod_{i,j} \Delta_{P_{ij}} \quad (4.96)$$

which contains the first three terms of Eq. 4.93. Following the procedure of the competition algorithm, and the density in Eq. 4.66, we sample E_{ij} for each kernel P_{ij} , such that the chosen emission energy is $E = \max(\{E_{ij}\}, \rho)$. This process also determines the parent partons, ij , of the emission. The chosen ij will instruct the exact form of the parenthesised sampling densities in Eq. 4.66. Eq. 4.95 corresponds to the last line of the density in Eq. 4.66. If the chosen E is below ρ , or we have reached the maximum desired multiplicity, the shower evolution is terminated (corresponding to the first and second line of Eq. 4.66 respectively), as discussed in Section 4.5.2.

Algorithm 8 below outlines the process of sampling evolution scales (in E_n of Algorithm 4). Whereas in a typical shower, Δ_P would encapsulate the non-emission probability, we wish to use the Sudakov matrix element approximation outlined in Section 4.3.1, and therefore must divide Δ_P out in the scale sampling weight:

$$W_{E_n} \leftarrow \frac{1}{\Delta_P(E|E')}. \quad (4.97)$$

Following the density in Eq. 4.66, this only occurs when we have not reached

Algorithm 8: The modified Sudakov veto algorithm with competition Variant B, accounting for the presence of a lower cutoff, ρ , and a potential constraint on the maximum multiplicity, n_{max} . It outlines the emission scale sampling, represented by E_n . This, the hard scale, E' , and the scale sampling weight, W_{E_n} are introduced in Algorithm 4.

```

for  $i, j$  in  $\phi$  where  $\tau(c_i) \neq c_i$  and  $\bar{\tau}(c_j) \neq c_j$  do
  | solve  $\mathcal{R} = \Delta_{P_{ij}}(E_{ij}|E')\theta(E_{ij} - \rho)$  for each  $E_{ij}$ 
  |  $\{E_{ij}\} \leftarrow \text{dS}_{P_{ij}}(E_{ij}|E')$ 
  |  $E \leftarrow \mathbf{max}\{E_{ij}\}$ 
1 if  $E < \rho$  then
2   |  $E \leftarrow \rho$ 
3   | if  $n \neq n_{max}$  then
4     |  $W_{E_n}(\phi, E, E', \{\sigma, \bar{\sigma}\}) \leftarrow 1/\Delta_P(E|E')$ 
5     | return  $E$ 
6 else
7   | if  $n = n_{max}$  then
8     |  $E \leftarrow \rho$ 
9     | return  $E$ 
10  | else
11    |  $W_{E_n}(\phi, E, E', \{\sigma, \bar{\sigma}\}) \leftarrow 1/\Delta_P(E|E')$ 
12    | return  $E$ 

```

maximum multiplicity and is one of only two sources of weight in Variant B.

Before proceeding to a discussion of the direction and emission matrix element sampling, we turn our attention to the Sudakov matrix elements and the second parenthesised quantity in Eq. 4.93. The approximated Sudakov matrix elements are evaluated at each evolution step, identically to Variant A, as per line 7 in Algorithm 4. We introduced a ratio of scalar product matrices in Eq. 4.93 corresponding to the emission matrix elements, and must include a complementary term to accompany the Sudakov matrix elements:

$$M_{\tau\bar{\tau}}(E) \leftarrow [\sigma | \mathbf{V}_{E,E'} | \tau] M_{\sigma\bar{\sigma}} [\bar{\sigma} | \mathbf{V}_{E,E'} | \bar{\tau}] \times \frac{\langle \tau | \bar{\tau} \rangle}{\langle \sigma | \bar{\sigma} \rangle}. \quad (4.98)$$

Just as in Variant A, the basis tensors τ and $\bar{\tau}$ are chosen (in α_n and $\bar{\alpha}_n$ respectively) using the level-swap algorithm discussed in Section 4.4. This sampling contributes a weight, $W_{\alpha_n} \times W_{\bar{\alpha}_n}$, which is the second source of weights in Variant B. The anomalous dimension matrix element coefficients pertaining to the

Sudakov matrix elements are

$$\Gamma_{ij} = \frac{\alpha_s}{\pi} \ln \left(\frac{E'}{E} \right) \Omega_{ij}, \quad (4.99)$$

where

$$\Omega_{ij} = \frac{1}{2} \ln \left(\frac{n_i \cdot n_j}{\lambda} \right) \Theta(n_i \cdot n_j - \lambda), \quad (4.100)$$

following the collinear cutoff prescription outlined in Eq. 4.91. In addition to the ratio of scalar product matrix elements in Eq. 4.93 and 4.98, an additional scalar product matrix element must be included in the hard matrix element, e.g. $M_{\sigma\bar{\sigma}}(Q_H) = [\sigma | \mathbf{H}(Q_H) | \bar{\sigma}] \langle \sigma | \bar{\sigma} \rangle$. This chain of scalar product matrix elements will multiply for each evolution step, and ultimately reduce to a single element, $S_{\sigma_n \bar{\sigma}_n}$, where n labels the final colour flows.

In order to compute the sum over emission matrix elements using the Sudakov veto algorithm with competition, the emission kernels used, $\zeta_{ij} \Omega_{ij}$, must be positive-definite. Consequently, the sign of the selected emission matrix element (for the chosen ij), must be corrected. The second parenthesised object in Eq. 4.93,

$$\frac{[\rho | \mathbf{T}_i | \tau] \langle \bar{\tau} | \mathbf{T}_j | \rho \rangle}{|[\rho | \mathbf{T}_i | \tau] \langle \bar{\tau} | \mathbf{T}_j | \bar{\rho} \rangle|}, \quad (4.101)$$

corrects for this, to attain the right sign in each evolution step. This factor is evaluated using the cross section-level emission matrix elements in Eq. 4.45.

Turning now to the emission matrix element sampling, we focus on the last parenthesised quantity in Eq. 4.93:

$$P(\rho, \bar{\rho}) = \frac{1}{\zeta_{ij}} \frac{\langle \rho | \bar{\rho} \rangle}{\langle \tau | \bar{\tau} \rangle} |[\rho | \mathbf{T}_i | \tau] \langle \bar{\tau} | \mathbf{T}_j | \bar{\rho} \rangle|. \quad (4.102)$$

It is with this probability that we select the basis tensors ρ and $\bar{\rho}$, which determine the emission matrix element in Eq. 4.101, and the starting flows for the next evolution step.

The selection of ρ and $\bar{\rho}$ is represented in Algorithm 4, by α_{n+1} and $\bar{\alpha}_{n+1}$, assuming an amplitude-level implementation. This was carried out in Variant A, whereby ρ was chosen randomly (from the set of tensors accessible after the action of an emission operator), and $\bar{\rho}$ was subsequently selected using the level-swap algorithm, to be at-most two swaps away. Whilst functional, this approach lacks the ability to choose tensors following the most important trajectories in colour space, and can result in potentially large weights (for a

larger sampled colour order, d' , in $W_{\bar{\alpha}_{n+1}}$ of Eq. 4.80). A key advantage of the Variant B cross section-level formulation, lies in the fact that both ρ and $\bar{\rho}$ can be sampled at the same time using Eq. 4.102. This cross section-level description is also what has enabled us to weight the probability of selecting a given ρ and $\bar{\rho}$, by the ratio of scalar product matrix elements. This helps to steer the evolution of the shower along the most importance trajectories in colour space.

It also has the advantage of simplifying the sampling process: we can show that the contributions to ξ_{ij} , i.e. the weights by which we are choosing a given emission matrix element in Eq. 4.102 (and therefore basis tensors $\rho, \bar{\rho}$), are largely determinable and result in factors of N_c or $1/N_c$. Emitting off the ij parton pair, chosen in the competition algorithm, a predetermined map of accessible $\rho, \bar{\rho}$ to their corresponding weights, greatly speeds up the sampling process.

To see this, we can define each term of the sum in ξ_{ij} by its identifying basis tensors, as $\xi_{ij}^{\rho', \bar{\rho}'}$:

$$\begin{aligned} \xi_{ij}^{\rho', \bar{\rho}'} &= \frac{\langle \rho' | \bar{\rho}' \rangle}{\langle \tau | \bar{\tau} \rangle} [\rho' | \mathbf{T}_i | \tau \rangle \langle \bar{\tau} | \mathbf{T}_j | \bar{\rho}' \rangle] = \frac{\langle \rho' | \bar{\rho}' \rangle}{\langle \tau | \bar{\tau} \rangle} \delta_{\tau, \rho' \setminus n} \times \\ &\quad \left[\left(\lambda_i \lambda_j \delta_{c_i, \rho'^{-1}(\bar{c}_n)} \delta_{c_j, \bar{\rho}'^{-1}(\bar{c}_n)} + \bar{\lambda}_i \bar{\lambda}_j \delta_{\bar{c}_i, \rho'(c_n)} \delta_{\bar{c}_j, \bar{\rho}'(c_n)} \right) \right. \\ &\quad + \left(-\lambda_i \bar{\lambda}_j \delta_{c_i, \rho'^{-1}(\bar{c}_n)} \delta_{\bar{c}_j, \bar{\rho}'(c_n)} - \bar{\lambda}_i \lambda_j \delta_{\bar{c}_i, \rho'(c_n)} \delta_{c_j, \bar{\rho}'^{-1}(\bar{c}_n)} \right) \\ &\quad - \frac{1}{N_c} \left(\lambda_i \delta_{c_i, \rho'^{-1}(\bar{c}_n)} - \bar{\lambda}_i \delta_{\bar{c}_i, \rho'(c_n)} \right) (\lambda_j - \bar{\lambda}_j) \delta_{c_n, \bar{\rho}'^{-1}(\bar{c}_n)} \\ &\quad - \frac{1}{N_c} \left(\lambda_i \delta_{c_i, \rho'^{-1}(\bar{c}_n)} - \bar{\lambda}_i \delta_{\bar{c}_i, \rho'(c_n)} \right) (\lambda_j - \bar{\lambda}_j) \delta_{c_n, \bar{\rho}'^{-1}(\bar{c}_n)} \\ &\quad \left. + \frac{1}{N_c^2} (\lambda_i - \bar{\lambda}_i) (\lambda_j - \bar{\lambda}_j) \delta_{c_n, \rho'^{-1}(\bar{c}_n)} \delta_{c_n, \bar{\rho}'^{-1}(\bar{c}_n)} \right] \delta_{\bar{\tau}, \bar{\rho}' \setminus n}. \end{aligned} \quad (4.103)$$

The right-hand side of Eq. 4.103 is just the expression for the matrix elements of the colour charge operators, described in Eq. 2.65. It is a result of decomposing each of the colour charge operators, \mathbf{T}_i , into three colour-line operators: \mathbf{t}_{c_i} , $\bar{\mathbf{t}}_{\bar{c}_i}$ and \mathbf{s} , which emit off the colour line, c_i (represented by each occurrence of λ_i), off the anti colour line, \bar{c}_i (represented by $\bar{\lambda}_i$) and a singlet-gluon (represented by $\lambda_i - \bar{\lambda}_i$). In order to efficiently sample ρ and $\bar{\rho}$, i.e. our choice of emission matrix element, we examine the values that $\xi_{ij}^{\rho, \bar{\rho}}$ can take for a given ij and arrangement of colour flows in τ and $\bar{\tau}$. To do this, we shall study each of the terms on the right-hand side of Eq. 4.103 in terms of their corresponding

colour-line operators, \mathbf{t} , $\bar{\mathbf{t}}$ and \mathbf{s} . We henceforth write these operators without the index subscript, understanding that any operator in the amplitude is off the external leg i , and any operator in the conjugate-amplitude is off leg j . It turns out that the values of all $\zeta_{ij}^{\rho, \bar{\rho}}$ can be determined in five scenarios:

- The action of a \mathbf{t} (or equally $\bar{\mathbf{t}}$) in both the amplitude and conjugate, acting on the same colour flow in both.
- The action of a \mathbf{t} (or equally $\bar{\mathbf{t}}$) in the amplitude and conjugate, acting on differing colour flows, but the same colour line.
- The action of a \mathbf{t} (or equally $\bar{\mathbf{t}}$) in the amplitude (or conjugate) and an \mathbf{s} in the other.
- The action of an \mathbf{s} in both the amplitude and conjugate.
- The action of a \mathbf{t} in the amplitude and conjugate, acting on two colour flows which share no colour or anti-colour index.

The first four of these scenarios are determinable, in the sense that each scenario unambiguously results in a factor of either N_c or $1/N_c$. On the other hand, the last scenario is not determinable: it can result in both N_c or $1/N_c$ depending on the specific colour arrangement within τ and $\bar{\tau}$. The weight corresponding to these contributions must be calculated as they are needed.

Let's begin by examining the first of these scenarios. Figure 4.6 illustrates two possibilities for the action of a \mathbf{t} operator on both $|\tau\rangle$ and $\langle\bar{\tau}|$ in $\zeta_{ij}^{\rho, \bar{\rho}}$ (in the second and third lines of Eq. 4.103); the very same logic always holds for a $\bar{\mathbf{t}}$ operator due to the relation $\bar{\mathbf{t}}_{\bar{c}_i} = \mathbf{t}_{\sigma^{-1}(\bar{c}_i)}$. Red lines denote the new colour flow created by the \mathbf{t} operators, whilst the grey boxes represent the wider context of additional colour flows in $|\tau\rangle$ and $\langle\bar{\tau}|$; we shall see that these contextual flows are unaffected by emissions, except for the contributions illustrated in Figure 4.8. In both Figure 4.6a and 4.6b, the \mathbf{t} operators emit off the same colour line (represented by the black dots). Figure 4.6a presents the scenario in which the anti colour lines connected to these colour lines are also identical. The resultant scalar product matrix element, relative to any N_c factors that would come from the contextual flows, are written below each diagram. Figure 4.6b on the other hand represents the case in which the emitting colour line in the amplitude and conjugate-amplitude are connected to different anti colour lines. We find that both of these contributions to $\zeta_{ij}^{\rho, \bar{\rho}}$ are proportional to N_c .

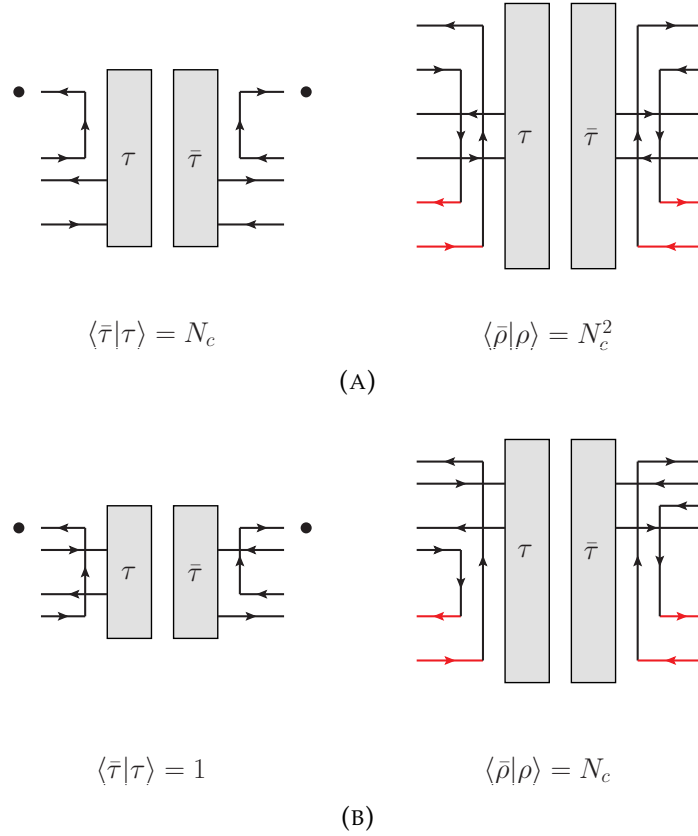
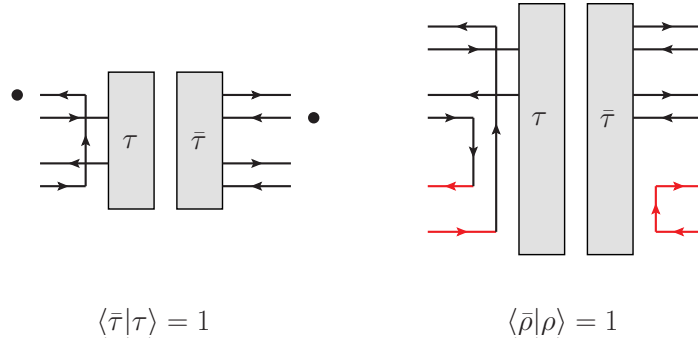


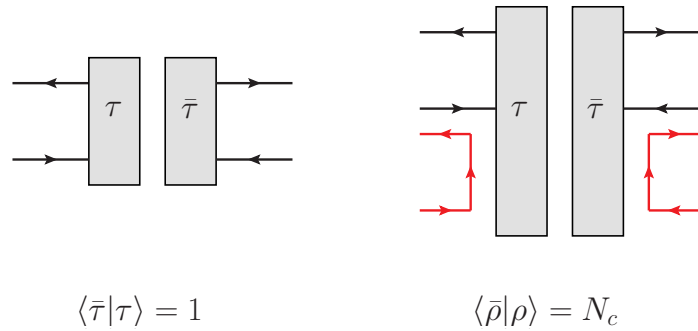
FIGURE 4.6: Diagrammatic representation of the action of a \mathbf{t} ($\bar{\mathbf{t}}$) operator, acting on the same colour (anti colour) line (highlighted by a black dot) in the amplitude and conjugate amplitude. Figure (A) presents the case in which the same anti colour line is connected to the emitting colour line in both the amplitude and conjugate, whilst in Figure (B) the connecting anti colour lines differ. Newly emitted colour and anti colour lines are red. The N_c factor contributed to the scalar product matrix element in contracting the emitting flows is written below each diagram.

Figure 4.7 shows the colour flows that result from those terms in $\zeta_{ij}^{\rho', \bar{\rho}'}$ that contain an \mathbf{s} operator (in the fourth and fifth lines of Eq. 4.103). Figure 4.7a illustrates the case in which a \mathbf{t} (or $\bar{\mathbf{t}}$) operator acts on a colour line in τ , whilst an \mathbf{s} operator is applied to $\bar{\tau}$. This combination of operators results in no change to the relative scalar product matrix element. Figure 4.7b demonstrates the effect of an \mathbf{s} operator in both the amplitude and conjugate-amplitude. A relative N_c factor in the scalar product matrix element results.

Using the results depicted in Figures 4.6 and 4.7, Table 4.10 presents a comprehensive list of contributions to $\zeta_{ij}^{\rho', \bar{\rho}'}$. An important set of contributions that are omitted, are those of the form $[\sigma | \mathbf{t} | \alpha] \langle \beta | \mathbf{t} | \tau \rangle$ in which the emitting colour flows in the amplitude and conjugate-amplitude have no colour or anti-colour



(A) The action of a \mathbf{t} ($\bar{\mathbf{t}}$) operator in the amplitude and \mathbf{s} operator in the conjugate amplitude. Whilst it has been specified that the \mathbf{s} operator acts on the first anti colour line in the conjugate, it is agnostic to colour and anti colour indices and results in the same new singlet-gluon colour flow regardless.



(B) The action of an \mathbf{s} operator in both the amplitude and conjugate amplitude.

FIGURE 4.7: Diagrammatic representation of the action of \mathbf{t} ($\bar{\mathbf{t}}$) and \mathbf{s} operators. Newly emitted colour and anti colour lines are coloured red. The black dots denote the colour line on which \mathbf{t} or \mathbf{s} acts and the N_c factor contributed to the scalar product matrix element in contracting the emitting flows is written below each diagram.

lines in-common. Contributions of this type are illustrated in Figure 4.8, where the bottom two diagrams show the pictorial representation of the arrangement of colour flows in the scalar product matrix element, $\langle \bar{\tau} | \tau \rangle$. The contributions to $\tilde{\xi}_{ij}$ are still N_c or $1/N_c$ but are dependent on the contextual colour flow arrangement. In particular, one can see that the relative difference in powers of N_c , is dependent on how m, \bar{n}, k and \bar{l} are connected: if the colour flow arrangement in $\langle \bar{\tau} | \tau \rangle$ connects the colour line m to the anti colour line \bar{n} and l to \bar{k} ,

$$\tilde{\xi}_{ij}^{\rho', \bar{\rho}'} = \frac{1}{N_c}, \tag{4.104}$$

Operator	α, β connections	λ_i	λ_j	$\bar{\lambda}_i$	$\bar{\lambda}_j$	Contribution to $\zeta_{ij}^{\rho', \bar{\rho}'}$
$\mathbf{t} \alpha\rangle\langle\beta \mathbf{t}$	$c_i = c_j, \alpha(c_i) = \beta(c_j)$	1	1	0	0	$\frac{N_c^2}{N_c} \times 1$
	$\bar{c}_i = \bar{c}_j, \alpha^{-1}(\bar{c}_i) = \beta^{-1}(\bar{c}_j)$	0	0	1	1	$\frac{N_c^2}{N_c} \times 1$
	$c_i = \beta^{-1}(\bar{c}_j), \alpha(c_i) = \bar{c}_j$	1	0	0	1	$-\frac{N_c^2}{N_c} \times 1$
	$\bar{c}_i = \beta(c_j), \alpha^{-1}(\bar{c}_i) = c_j$	0	1	1	0	$-\frac{N_c^2}{N_c} \times 1$
$\mathbf{t} \alpha\rangle\langle\beta \mathbf{t}$	$c_i = c_j$	1	1	0	0	$\frac{N_c}{1} \times 1$
	$\bar{c}_i = \bar{c}_j$	0	0	1	1	$\frac{N_c}{1} \times 1$
	$c_i = \beta^{-1}(\bar{c}_j)$	1	0	0	1	$-\frac{N_c}{1} \times 1$
	$\bar{c}_i = \beta(c_j)$	0	1	1	0	$-\frac{N_c}{1} \times 1$
$\mathbf{t} \alpha\rangle\langle\beta \mathbf{s}$		1	1	0	0	$\frac{1}{1} \times \frac{1}{N_c}$
		1	0	0	1	$-\frac{1}{1} \times \frac{1}{N_c}$
		0	1	1	0	$-\frac{1}{1} \times \frac{1}{N_c}$
		0	0	1	1	$\frac{1}{1} \times \frac{1}{N_c}$
$\mathbf{s} \alpha\rangle\langle\beta \mathbf{t}$		1	1	0	0	$\frac{1}{1} \times \frac{1}{N_c}$
		1	0	0	1	$-\frac{1}{1} \times \frac{1}{N_c}$
		0	1	1	0	$-\frac{1}{1} \times \frac{1}{N_c}$
		0	0	1	1	$\frac{1}{1} \times \frac{1}{N_c}$
$\mathbf{s} \alpha\rangle\langle\beta \mathbf{s}$		1	1	0	0	$\frac{N_c}{1} \times \frac{1}{N_c^2}$
		1	0	0	1	$-\frac{N_c}{1} \times \frac{1}{N_c^2}$
		0	1	1	0	$-\frac{N_c}{1} \times \frac{1}{N_c^2}$
		0	0	1	1	$\frac{N_c}{1} \times \frac{1}{N_c^2}$

TABLE 4.10: List of all possible colour-line operator combinations in Eq. 4.103. Each of these is a contribution to a single term in the sum of Eq. 4.94. The relevant colour-line operator matrix element in the amplitude and conjugate-amplitude are presented with unspecified external leg indices. Conditions on the colour arrangement in τ and $\bar{\tau}$ for each contribution are also listed. The contribution itself is presented in the last column.

whilst if it connects m to l and \bar{n} to \bar{k} ,

$$\zeta_{ij}^{\rho', \bar{\rho}'} = N_c. \quad (4.105)$$

For an emission off any given parent partons, ij , we have therefore ascertained all contributions to the sum in Eq. 4.94. In particular, we know all of the possible $\rho, \bar{\rho}$ combinations which can be reached by an emission off partons i and

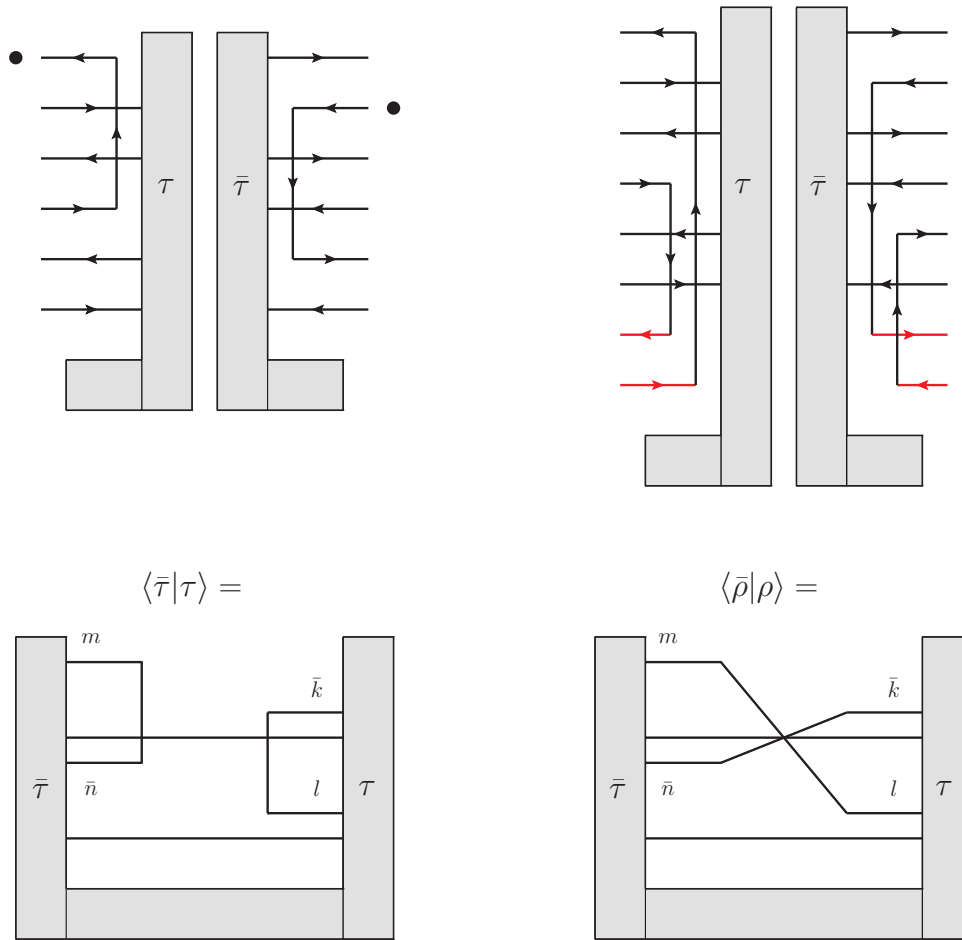


FIGURE 4.8: Diagrammatic representation of the action of a \mathbf{t} ($\bar{\mathbf{t}}$) operator, acting in both the amplitude and conjugate amplitude. In the top two illustrations, the colour flows on which \mathbf{t} ($\bar{\mathbf{t}}$) act share no colour or anti colour indices in common. Newly emitted colour and anti colour lines are coloured red and the black dots denote an example colour line on which \mathbf{t} acts in the amplitude and an anti colour line on which $\bar{\mathbf{t}}$ acts in the conjugate. The lower two diagrams present the scalar product matrix elements before and after the emission has occurred. \bar{n} and n denote the emitting anti colour line in the conjugate and its connecting colour line, whilst l and \bar{k} are the emitting colour line and connecting anti colour line in the amplitude.

j , and the relative probabilities, $\zeta_{ij}^{\rho, \bar{\rho}} / \zeta_{ij}$, with which they occur; these are all factors of N_c or $1/N_c$.

It is the `nextFlowWeight()` method in the `Core::EmissionMatrix` class which implements the results of Table 4.10. And where contributions of the type presented in Figure 4.8 are encountered, `nextFlowWeight()` defers the ‘manual’ calculation of the scalar product matrix to the `scalarProduct()` method in `Core::ColourFlow`. `nextFlowWeight()` is used in both the scale sampling, E_n ,

to calculate each ξ_{ij} , and `nextFlows()` in `Core:EmissionMatrix`, to sample ρ and $\bar{\rho}$ (represented by α_{n+1} and $\bar{\alpha}_{n+1}$) according to the distribution in Eq. 4.102. As this distribution is normalised, the weights corresponding to the sampling of ρ and $\bar{\rho}$, are unity:

$$W_{\alpha_{n+1}} \leftarrow 1, \quad W_{\bar{\alpha}_{n+1}} \leftarrow 1. \quad (4.106)$$

Lastly, let us consider the first parenthesised quantity in Eq. 4.93,

$$dP(\theta_k, \phi_k) = \frac{\omega_{ij}(k) d\Omega_k}{\Omega_{ij} 4\pi}. \quad (4.107)$$

Using this probability density, we sample the polar and azimuthal angles of the gluon, emitted off the ij parent partons.

In Variant A we adopted a more rudimentary direction sampling, wherein we chose the gluon direction uniformly in the out-region. This approach carries with it three problems. First, we do not necessarily sample the regions of phase-space which are most dominant to the cross section. Second, our sampling density contributes a weight, $W_{\Phi_{n+1}} \leftarrow (1 - c_0)$. And finally, as each emission is in the out-region, the shower evolution always emits up to our maximum multiplicity, n_{\max} ; this is in-contrast to a more general approach, where the evolution terminates, only after emitting into the veto region. Variant B resolves these issues by sampling from the density in Eq. 4.107. Firstly, Eq. 4.107 is a normalised quantity and so there are no weights associated with sampling from it, i.e. $W_{\Phi_{n+1}} \leftarrow 1$; minimising sampling weights was a key focus in the formulation of Variant B. Secondly, sampling directions according to a density describing the emission dipole factor, will focus on regions of phase-space which more-significantly contribute to the cross section. Lastly, sampling according to Eq. 4.107 is more general and allows the evolution to emit into the in-region.

Sampling by inversion from Eq. 4.107 requires that it is integrable and invertible. The form of $\omega_{ij}(k)$ makes this difficult to achieve. However, we can exploit the fact that we have selected a pair of parent partons ij , and sample the emission direction in Φ_{n+1} , in the zero-momentum frame of the partons i and j with a subsequent Lorentz boost back to the lab-frame. If we write the i and

j momenta such that n_i lies along the lab-frame z -axis, then

$$\begin{aligned} n_i^\mu &= (1, 0, 0, 1) \\ n_j^\mu &= (1, \sin \theta_{ij}, 0, \cos \theta_{ij}), \end{aligned} \quad (4.108)$$

where θ_{ij} is the angle between partons i and j and we have oriented the particles such that the azimuthal angle is $\phi_{ij} = 0$. In the lab-frame, n_i and n_j will typically not be oriented in this way and so a rotation matrix will be necessary to correct any emission direction sampled in the ZMF. The momentum n_j can be rewritten as

$$n_j^\mu = (1, \sqrt{-(n_i \cdot n_j - 2)n_i \cdot n_j}, 0, 1 - n_i \cdot n_j), \quad (4.109)$$

such that a Lorentz boost from the zero-momentum frame of the parent partons i and j , back to the rotated lab-frame defined by Eq. 4.108, is

$$\Lambda_v^\mu(n_i, n_j) = \begin{pmatrix} \sqrt{\frac{2}{n_{ij}}} & \sqrt{\frac{(2-n_{ij})}{n_{ij}}} & 0 & 0 \\ \sqrt{\frac{(2-n_{ij})}{2}} & 1 & 0 & -\sqrt{\frac{(2-n_{ij})}{2}} \\ 0 & 0 & 1 & 0 \\ -\frac{n_{ij}-2}{\sqrt{2n_{ij}}} & \sqrt{\frac{(2-n_{ij})}{2}} & 0 & \sqrt{\frac{n_{ij}}{2}} \end{pmatrix}, \quad (4.110)$$

where for notational brevity we have defined $n_{ij} = n_i \cdot n_j$. Eq. 4.110 is such that in the ZMF, the parent partons (ij) have the momenta

$$\begin{aligned} \hat{n}_i^\mu &= \sqrt{\frac{n_{ij}}{2}} (1, 0, 0, 1) = \left(\Lambda^{-1}(n_i, n_j) \right)_v^\mu n_i^v, \\ \hat{n}_j^\mu &= \sqrt{\frac{n_{ij}}{2}} (1, 0, 0, -1) = \left(\Lambda^{-1}(n_i, n_j) \right)_v^\mu n_j^v, \end{aligned} \quad (4.111)$$

whilst that of the emitted gluon is

$$\hat{n}_k^\mu = (1, \sin \theta \cos \phi, \sin \theta \sin \phi, \cos \theta). \quad (4.112)$$

The dipole factor and integration measure in Eq. 4.107 in the lab-frame and

ij -ZMF frame respect the relation

$$\omega(n_{ik}, n_{jk}, n_{ij}) \frac{d\Omega_k}{4\pi} = \omega\left(\frac{\hat{n}_{ik}}{(\Delta\hat{n}_k)^0}, \frac{\hat{n}_{jk}}{(\Delta\hat{n}_k)^0}, \hat{n}_i \cdot \hat{n}_j\right) \frac{1}{[(\Delta\hat{n})^0]^2} \frac{d\hat{\Omega}_k}{4\pi}, \quad (4.113)$$

where we have made the dipole factor dot-product dependence explicit:

$$\omega_{ij}(k) \equiv \omega(n_{ik}, n_{jk}, n_{ij}) = \frac{n_{ij}}{n_{ik} + n_{jk}} \left(\frac{\Theta(n_{ik} - \lambda)}{n_{ik}} + \frac{\Theta(n_{jk} - \lambda)}{n_{jk}} \right), \quad (4.114)$$

including the collinear cutoff prescription in Eq. 4.90. A careful analysis of the integration over the first term in Eq. 4.114 in the ij -ZMF frame, shows that

$$\begin{aligned} & \int_{-1}^1 \int_0^{2\pi} \frac{\hat{n}_{ij}}{(\hat{n}_{ik} + \hat{n}_{jk}) \hat{n}_{ik}} \frac{1}{(\Delta\hat{n}_k)^0} \Theta\left(\frac{\hat{n}_{ik}}{(\Delta\hat{n}_k)^0} - \lambda\right) \frac{1}{[(\Delta\hat{n}_k)^0]^2} \frac{d\cos\theta}{2} \frac{d\phi}{2\pi} \\ &= \int_{-1}^1 \frac{1}{1 - \cos\theta} \left(\Theta(a - b) + \Theta(b - |a|) \left(1 - \frac{\arccos\left(\frac{a}{b}\right)}{\pi}\right) \right) \frac{d\cos\theta}{2}, \end{aligned} \quad (4.115)$$

where a and b are defined such that

$$\begin{aligned} a &= \frac{n_{ij}}{2} (1 - \cos\theta) - \lambda, \\ b &= \lambda \sqrt{1 - \frac{n_{ij}}{2} \sin\theta \cos\phi}. \end{aligned} \quad (4.116)$$

The remaining integration over the polar angle of the emitted gluon, θ , in Eq. 4.115 is then non-zero in three distinct regions of phase-space: $\cos\theta \in [-1, c_-]$, $\cos\theta \in [c_-, c_1]$ and $\cos\theta \in [c_1, c_+]$, and

$$\begin{aligned} c_1 &= 1 - \frac{2\lambda}{n_{ij}}, \\ c_{\pm} &= \frac{(n_{ij})^2 - 2n_{ij}\lambda \pm 2\sqrt{(2 - n_{ij})(2 - \lambda)}\lambda^3 n_{ij}}{(n_{ij})^2 - 2n_{ij}\lambda^2 + 4\lambda^2}. \end{aligned} \quad (4.117)$$

In the limit that our collinear cutoff, λ , is sufficiently small,

$$c_{\pm} \simeq c_1 + \mathcal{O}\left(\left(\frac{\lambda}{n_{ij}}\right)^{3/2}\right) \quad (4.118)$$

and Eq. 4.115 reduces to

$$\int_{-1}^{c_-} \left(\frac{1}{1-\cos\theta}\right) \Theta(n_{ij}-\lambda) \frac{d\cos\theta}{2} \simeq \frac{1}{2} \ln\left(\frac{n_{ij}}{\lambda}\right). \quad (4.119)$$

The same logic follows for the second term of the dipole factor in Eq. 4.114 in the ij -ZMF frame,

$$\int_{-1}^1 \int_0^{2\pi} \frac{\hat{n}_{ij}}{(\hat{n}_{ik} + \hat{n}_{jk})} \frac{1}{\hat{n}_{jk}} \Theta\left(\frac{\hat{n}_{jk}}{(\Lambda \hat{n}_k)^0} - \lambda\right) \frac{1}{[(\Lambda \hat{n}_k)^0]^2} \frac{d\hat{\Omega}_k}{4\pi} \simeq \frac{1}{2} \ln\left(\frac{n_{ij}}{\lambda}\right). \quad (4.120)$$

All of this means we can sample the emitted gluon azimuth uniformly across the interval $\phi \in [0, 2\pi]$ and the gluon polar angle can be sampled with a probability density

$$dP(\cos\theta) = \left(\frac{\alpha_s}{\pi} \ln\left(\frac{n_{ij}}{\lambda}\right)\right)^{-1} \left(\frac{1}{1-\cos\theta}\right) d\cos\theta. \quad (4.121)$$

The sampled polar angle is then flipped, i.e. $\cos\theta \rightarrow -\cos\theta$, with half-probability. Finally, we must rotate our emitted gluon direction, so that the azimuth is correct in the lab-frame:

$$\begin{aligned} n_i^{\mu} &= (1, \sin\theta_i \cos\phi_i, \sin\theta_i \sin\phi_i, \cos\theta_i), \\ n_j^{\mu} &= (1, \sin\theta_j \cos\phi_j, \sin\theta_j \sin\phi_j, \cos\theta_j). \end{aligned} \quad (4.122)$$

This is achieved using the following rotation matrix:

$$R(n_i, n_j) = \begin{pmatrix} \frac{(n_{ij}-1)\bar{c}_i s_i + \bar{c}_j s_j}{\sqrt{(2-n_{ij})n_{ij}}} & \frac{c_j s_i \bar{s}_i - c_i s_j \bar{s}_j}{\sqrt{(2-n_{ij})n_{ij}}} & \bar{c}_i s_i \\ \frac{(n_{ij}-1)s_i \bar{s}_i + s_j \bar{s}_j}{\sqrt{(2-n_{ij})n_{ij}}} & \frac{c_i \bar{c}_j s_j - c_j \bar{c}_i s_i}{\sqrt{(2-n_{ij})n_{ij}}} & s_i \bar{s}_i \\ \frac{(n_{ij}-1)c_i + c_j}{\sqrt{(2-n_{ij})n_{ij}}} & -\frac{\sqrt{-c_i^2 - c_j^2 - 2(n_{ij}-1)c_i c_j - (n_{ij}-2)n_{ij}}}{\sqrt{(2-n_{ij})n_{ij}}} & c_i \end{pmatrix}, \quad (4.123)$$

where $c_k = \cos\theta_k$, $s_k = \sin\theta_k$, $\bar{c}_k = \cos\phi_k$ and $\bar{s}_k = \sin\phi_k$. As is the case in

Variant A, the direction sampling of each emitted gluon is performed by Φ_{n+1} (but with a corresponding selection weight of $W_{\Phi_{n+1}} \leftarrow 1$). Again, Φ_{n+1} also updates ϕ with a newly added particle momenta and its colour representation. Unlike in Variant A however, we can see that the process of sampling the gluon direction in the ij -ZMF and the subsequent Lorentz boost to the lab-frame, allows for gluon emission into the in-gap region. Whereas the event evolution in Variant A can terminate by either evolving to a maximum multiplicity, n_{max} , or sampling an emission scale below the veto scale ρ , the Variant B evolution can also terminate if the condition of the measurement function is violated (i.e. the gluon emission is in-gap). In this sense, a Variant A event will always contain n_{max} emissions (modulo the veto scale termination criteria), whilst Variant B will contain n emissions, where $n \leq n_{max}$.

Chapter 5

Results

In the last chapter, we brought together the concepts and results of Chapters 2 and 3, to present a practical implementation into a Monte Carlo code, `Cvolver`. We outlined the `Cvolver` code structure, including the general `Core` framework which handles full- N_c colour manipulation of the hard process, emission and scalar product operators in the colour flow basis, for a general observable. The full-colour Sudakov operators are approximated according to the work [154]. In subsequent sections we outlined two implementations of the jet veto observable using this framework. These are denoted Variant A and Variant B.

Variant A was the initial ‘ideal’ approach to implementing the algorithm of Chapter 2. It maintains an inherently amplitude-level description, to reflect that of the general evolution algorithm, mainly by using amplitude-level emission matrix elements and a corresponding basis tensor sampling scheme. Such a description will be useful for the future inclusion of collinear emissions and spin dependence [103]. We shall see, in Section 5.1.6, that this implementation suffers from increasingly large weights at higher multiplicities, which contaminate the total cross section result. To redress this situation, Variant B was developed, whereby cross section-level contractions of the emission operators have been carried out, where possible. This facilitated an emission scale and direction sampling closer to that used in conventional showers, using the Sudakov veto algorithm with competition. By treating the accessible (at any given stage of the shower) emission matrix elements as our competing processes, we were also able to develop a more efficient emission matrix basis tensor sampling strategy.

In this chapter we will present the jet veto cross section results using both Variant A and Variant B. For Variant A we compare these results with an independently largely analytic fixed-order cross section calculation presented in Section 5.1.1. We first compare these results, neglecting all Sudakov operators, providing a validation of Variant A components related to real emissions. Then, we check the Sudakov basis tensor sampling strategy by comparing results of the two running modes of Variant A: `evolve` and `evolveFull`. Lastly, we compare the jet veto cross sections for 0, 1 and 2 emissions, $\Sigma_0(\rho)$, $\Sigma_1(\rho)$ and $\Sigma_2(\rho)$, against our analytic calculations and examine the total summed cross section, $\Sigma(\rho)$. This provides validation of all components of Variant A. For Variant B, changes were made to the `Cvolver` code, to allow for a general value of N_c and to account for a $1/N_c$ -breakdown. Utilising this, we present cross sections results for Variant B, which supplement those of Variant A to further validate the shared `Core` colour machinery. In addition, these results

verify Variant B as an alternative implementation. Furthermore, we compare the Variant B 20-emission total cross section result with the work [167] and find agreement.

The results presented in the following sections have been created using the histogramming package `myStatistics`, written by S. Plätzer as part of the Herwig Collaboration [11]. They have been subsequently plotted using `Gnuplot` [168].

5.1 Variant A

In this section, we present numerical results of the `CVolver` Variant A implementation discussed in Section 4.5.3 for the jet veto observable. We shall use the $V \rightarrow q\bar{q}$ process as a testbed to isolate and validate components of the `CVolver` implementation.

To start, we carry out fixed order calculations of the jet veto cross section, $\Sigma_n(\rho)$, for the first two soft gluon emissions, $n = 0, 1, 2$, in Section 5.1.1. These calculations adopt the same collinear cutoff as Variant A (as written in Eq. 4.68) and have been implemented into an independent test code, `FixedOrderA`, to make a straightforward comparison with `CVolver`. We subsequently show that the total (summed) cross section, $\Sigma(\rho)$, is independent of the aforementioned cutoff, if we include all contributions upto order α_s^2 .

As an initial test of `CVolver`, we present the emission cross sections, $\Sigma_n^R(\rho)$, in which all Sudakov matrix elements are set to unity, for $n = 1, 2$. We compare these results with those of `FixedOrderA`, with each Sudakov operator set to the unit matrix for two values of the collinear cutoff. This provides a good test of the `CVolver` components related to emissions. Then, we compare the `CVolver` cross sections produced by the two running modes `evolve()` and `evolveFull()` in Section 5.1.4, which validate both the emission and Sudakov basis tensor sampling. Further to this, we present the jet veto cross section results of `FixedOrderA` and `CVolver` for the first two gluon multiplicities in Section 5.1.5. Lastly, we show the emission spectra for the shower evolution, including the first 20 emissions, in Section 5.1.6. Here, we observe the large weight fluctuations that afflict the cross sections produced by Variant A, and explore their cause.

`CVolver` Variant A was the first attempt to implement the results of Chapter 2. To remedy the aforementioned weight fluctuations, Variant B was developed,

which was then used to produce the results for [22].

5.1.1 Fixed Order Calculation

We shall begin by computing the $V \rightarrow q\bar{q}$ jet veto cross section explicitly in the colour flow basis, for gluon multiplicities upto two emissions. The phase-space integration and non-trivial matrix exponentiation, of the one and two-emission cross sections, is carried out in an independent code, **FixedOrderA**.

To remind the reader, the hard scattering matrix is written as $\mathbf{H}_{q\bar{q}} = \mathbf{1}$, whilst the Sudakov operator can quite generally be written as

$$\mathbf{V}_{a,b} = \exp \left[-\frac{\alpha_s}{\pi} \ln \left(\frac{b}{a} \right) \sum_{i < j} (-\mathbf{T}_i \cdot \mathbf{T}_j) \int \frac{d\Omega_k}{4\pi} \omega_{ij}(k) \Theta_{\text{cut}} \right], \quad (5.1)$$

where

$$\omega_{ij}(k) = \frac{n_i \cdot n_j}{(n_i \cdot n_k)(n_j \cdot n_k)}, \quad \Theta_{\text{cut}} = \prod_i \Theta(n_i \cdot n - \lambda). \quad (5.2)$$

We write the parton momenta of the hard partons q , \bar{q} and the first two emissions as

$$\begin{aligned} n_q &= (1, 0, 0, 1), \\ n_{\bar{q}} &= (1, 0, 0, 1), \\ n_1 &= (1, 0, \sin \theta_1, \cos \theta_1), \\ n_2 &= (1, \sin \theta_2 \cos \phi_2, \sin \theta_2 \sin \phi_2, \cos \theta_2). \end{aligned} \quad (5.3)$$

The integration over solid angle of the kinematic terms in the Sudakov exponent can be written as

$$\int \frac{d\Omega}{4\pi} \frac{n_i \cdot n_j}{(n_i \cdot n)(n_j \cdot n)} \Theta_{\text{cut}} \simeq \ln \left(\frac{n_i \cdot n_j}{2} \right) + \ln \left(\frac{2}{\lambda} \right), \quad (5.4)$$

where the only approximation is to ignore all terms of order the collinear cut-off. The cross section for zero emissions is

$$\Sigma_{q\bar{q},0}(\rho) = \text{Tr}(\mathbf{V}_{\rho,1} \mathbf{V}_{\rho,1}^\dagger \mathbf{S}_0). \quad (5.5)$$

Note that in Eq. 5.5 and for the rest of this section, the operators are understood to be matrices in the colour flow basis and therefore equivalent to their

calligraphic counterparts in Eq. 2.54. Correspondingly, the scalar product matrix corresponding to the relevant colour space dimensionality will be included in the trace. In the case of zero emissions, the scalar product matrix and the colour charge product are

$$\begin{aligned}\mathbf{T}_a^0 \cdot \mathbf{T}_b^0 &= -C_F \mathbf{1}, \\ \mathbf{S}_0 &= N_c \mathbf{1},\end{aligned}\tag{5.6}$$

whilst the Sudakov factor in the amplitude and conjugate-amplitude combine to give

$$\mathbf{V}_{\rho,1} \mathbf{V}_{\rho,1}^\dagger = \exp\left(-\frac{2\alpha_s}{\pi} \ln\left(\frac{1}{\rho}\right) C_F \mathbf{1} \ln\left(\frac{2}{\lambda}\right)\right).\tag{5.7}$$

In the context of zero emissions and a hard scattering with only a $q\bar{q}$ pair, there is only one colour flow. The trace over the one-dimensional basis is trivial and results in

$$\Sigma_{q\bar{q},0}(\rho) = N_c \exp\left(-\frac{2\alpha_s}{\pi} \ln\left(\frac{1}{\rho}\right) \left(\frac{N_c^2 - 1}{2N_c}\right) \ln\left(\frac{2}{\lambda}\right)\right).\tag{5.8}$$

The one-emission cross section is

$$\begin{aligned}\Sigma_{q\bar{q},1}(\rho) &= -\frac{\alpha_s}{\pi} \int_\rho^1 \frac{dE_1}{E_1} \int \frac{d\Omega_1}{4\pi} \text{Tr}(\mathbf{V}_{\rho,E_1} \mathbf{D}_1^\mu \mathbf{V}_{E_1,1} \mathbf{V}_{E_1,1}^\dagger \mathbf{D}_{1\mu}^\dagger \mathbf{V}_{\rho,E_1}^\dagger \mathbf{S}_1) \\ &= -\frac{\alpha_s}{\pi} \int_\rho^1 \frac{dE_1}{E_1} \int \frac{d\Omega_1}{4\pi} \text{Tr}(\mathbf{V}_{\rho,E_1} \mathbf{D}_1^\mu \mathbf{D}_{1\mu}^\dagger \mathbf{V}_{\rho,E_1}^\dagger) \\ &\quad \times \exp\left[-\frac{2\alpha_s}{\pi} \ln\left(\frac{1}{E_1}\right) C_F \ln\left(\frac{2}{\lambda}\right)\right],\end{aligned}\tag{5.9}$$

where the second line of Eq. 5.9 incorporates the results of Eq. 5.8, and again the trivial nature of the hard scattering means that an abelian factor can be extracted. Combining the emission operators in the amplitude and conjugate-amplitude, we find

$$\mathbf{D}_1^\mu \mathbf{D}_{1\mu}^\dagger = \omega_{q\bar{q}}(n_1) \left(\mathbf{T}_q^1 \mathbf{T}_{\bar{q}}^{1,\dagger} + \mathbf{T}_{\bar{q}}^1 \mathbf{T}_q^{1,\dagger}\right).\tag{5.10}$$

The outermost Sudakov operators can also be simplified to abelian factors after exploiting colour conservation, where $\sum_i \mathbf{T}_i = 0$. We find $\mathbf{T}_q^1 \cdot \mathbf{T}_{\bar{q}}^1 = C_A/2 - C_F$

and $\mathbf{T}_q^1 \cdot \mathbf{T}_1^1 = \mathbf{T}_{\bar{q}}^1 \cdot \mathbf{T}_1^1 = -C_A/2$ and can therefore write

$$\mathbf{V}_{\rho, E_1} = \exp \left[-\frac{\alpha_s}{\pi} \ln \left(\frac{E_1}{\rho} \right) \left(\left(C_F + \frac{C_A}{2} \right) \ln \left(\frac{2}{\lambda} \right) - \frac{C_A}{2} \ln \left(\frac{4}{(n_q \cdot n_1)(n_{\bar{q}} \cdot n_1)} \right) \right) \right]. \quad (5.11)$$

In the colour flow basis, the colour charge operators corresponding to the hard partons and the scalar product matrix after one emission are represented as

$$\begin{aligned} \mathbf{T}_q^0 &= \begin{pmatrix} -\frac{1}{\sqrt{2}N_c} \\ \frac{1}{\sqrt{2}} \end{pmatrix}, \\ \mathbf{T}_{\bar{q}}^0 &= \begin{pmatrix} \frac{1}{\sqrt{2}N_c} \\ -\frac{1}{\sqrt{2}} \end{pmatrix}, \\ \mathbf{S}_1 &= \begin{pmatrix} N_c^2 & N_c \\ N_c & N_c^2 \end{pmatrix}, \end{aligned} \quad (5.12)$$

which enables us to evaluate the remaining trace:

$$\text{Tr}((\mathbf{T}_q^1 \mathbf{T}_{\bar{q}}^{1,\dagger} + \mathbf{T}_{\bar{q}}^1 \mathbf{T}_q^{1,\dagger}) \mathbf{S}_1) = -2C_F C_A. \quad (5.13)$$

The one emission cross-section is thus

$$\begin{aligned} \Sigma_{q\bar{q},1}(\rho) &= 4C_F C_A \frac{\alpha_s}{\pi} \int_{\rho}^1 \frac{dE_1}{E_1} \int_{c_0}^{1-\lambda} \frac{d \cos \theta_1}{1 - \cos^2 \theta_1} \\ &\times \exp \left[-\frac{2\alpha_s}{\pi} \left(\frac{N_c^2 - 1}{2N_c} \right) \ln \left(\frac{1}{\rho} \right) \ln \left(\frac{2}{\lambda} \right) \right] \\ &\times \exp \left[-\frac{\alpha_s}{\pi} N_c \left(\ln \left(\frac{E_1}{\rho} \right) \ln \left(\frac{2}{\lambda} \right) - \ln \left(\frac{4}{1 - \cos^2 \theta_1} \right) \right) \right], \end{aligned} \quad (5.14)$$

where the angular phase-space region of integration is within the cone along the positive thrust axis, $c_0 < \cos \theta_1 < 1 - \lambda$. An additional factor of 2 has been included to account for gluon emissions into the cone centered about the negative thrust axis.

Lastly, we wish to compute the two-emission cross section. As we shall see, this provides a non-trivial test on colour charge products in the Sudakov ex-

ponents. The cross section is

$$\begin{aligned}
\Sigma_{q\bar{q},2}(\rho) &= \left(\frac{\alpha_s}{\pi}\right)^2 \int_{\rho}^1 \frac{dE_1}{E_1} \int_{\text{out}} \frac{d\Omega_1}{4\pi} \int_{\rho}^{E_1} \frac{dE_2}{E_2} \int_{\text{out}} \frac{d\Omega_2}{4\pi} \\
&\quad \times \text{Tr}(\mathbf{V}_{\rho,E_2} \mathbf{D}_2^{\nu} \mathbf{V}_{E_2,E_1} \mathbf{D}_1^{\mu} \mathbf{D}_{1\mu}^{\dagger} \mathbf{V}_{E_2,E_1}^{\dagger} \mathbf{D}_{2\nu}^{\dagger} \mathbf{V}_{\rho,E_2}^{\dagger} \mathbf{S}_2), \\
&= \left(\frac{\alpha_s}{\pi}\right)^2 \int_{\rho}^1 \frac{dE_1}{E_1} \int_{\text{out}} \frac{d\Omega_1}{4\pi} \int_{\rho}^{E_1} \frac{dE_2}{E_2} \int_{\text{out}} \frac{d\Omega_2}{4\pi} \\
&\quad \times \text{Tr}(\mathbf{V}_{\rho,E_2} \mathbf{D}_2^{\nu} \mathbf{D}_1^{\mu} \mathbf{D}_{1\mu}^{\dagger} \mathbf{D}_{2\nu}^{\dagger} \mathbf{V}_{\rho,E_2}^{\dagger} \mathbf{S}_2) \\
&\quad \times \exp \left[-\frac{\alpha_s}{\pi} C_A \ln \left(\frac{E_1}{E_2} \right) \left(\ln \left(\frac{2}{\lambda} \right) - \ln \left(\frac{4}{(n_q \cdot n_1)(n_{\bar{q}} \cdot n_1)} \right) \right) \right] \\
&\quad \times \exp \left[-\frac{2\alpha_s}{\pi} C_F \ln \left(\frac{1}{E_2} \right) \ln \left(\frac{2}{\lambda} \right) \right], \tag{5.15}
\end{aligned}$$

where we have again subsumed the results of Eq. 5.14 into our current calculation. The relevant colour charge operators and scalar product matrix are

$$\begin{aligned}
\mathbf{T}_q^2 &= \begin{pmatrix} -\frac{1}{\sqrt{2N_c}} & 0 \\ 0 & 0 \\ 0 & -\frac{1}{\sqrt{2N_c}} \\ 0 & 0 \\ 0 & \frac{1}{\sqrt{2}} \\ \frac{1}{\sqrt{2}} & 0 \end{pmatrix}, & \mathbf{T}_{\bar{q}}^2 &= \begin{pmatrix} \frac{1}{\sqrt{2N_c}} & 0 \\ 0 & 0 \\ 0 & \frac{1}{\sqrt{2N_c}} \\ 0 & -\frac{1}{\sqrt{2}} \\ 0 & 0 \\ -\frac{1}{\sqrt{2}} & 0 \end{pmatrix}, & \mathbf{T}_1^2 &= \begin{pmatrix} 0 & 0 \\ 0 & 0 \\ 0 & 0 \\ 0 & \frac{1}{\sqrt{2}} \\ 0 & -\frac{1}{\sqrt{2}} \\ 0 & 0 \end{pmatrix}, \\
\mathbf{S}_2 &= \begin{pmatrix} N_c^3 & N_c^2 & N_c^2 & N_c & N_c & N_c^2 \\ N_c^2 & N_c^3 & N_c & N_c^2 & N_c^2 & N_c \\ N_c^2 & N_c & N_c^3 & N_c^2 & N_c^2 & N_c \\ N_c & N_c^2 & N_c^2 & N_c^3 & N_c & N_c^2 \\ N_c & N_c^2 & N_c^2 & N_c & N_c^3 & N_c^2 \\ N_c^2 & N_c & N_c & N_c^2 & N_c^2 & N_c^3 \end{pmatrix}. \tag{5.16}
\end{aligned}$$

The chain of emission operators in both the amplitude and conjugate-amplitude can easily be deduced using Eq. 5.16 and results in a symmetric

matrix of the form

$$\mathbf{D}_2^\nu \mathbf{D}_1^\mu \mathbf{D}_{1\mu}^\dagger \mathbf{D}_{2\nu}^\dagger = \omega_{q\bar{q}}(n_1) \times \begin{pmatrix} \frac{\omega_{q\bar{q}}}{N_c^4} & 0 & -\frac{\omega_{q\bar{q}}}{N_c^3} & \frac{\omega_{q\bar{q}} + \omega_{\bar{q}1} - \omega_{q1}}{2N_c^2} & \frac{\omega_{q\bar{q}} + \omega_{q1} - \omega_{\bar{q}1}}{2N_c^2} & -\frac{\omega_{q\bar{q}}}{N_c^3} \\ \cdot & 0 & 0 & 0 & 0 & 0 \\ \cdot & \cdot & \frac{\omega_{q\bar{q}}}{N_c^2} & \frac{-\omega_{q\bar{q}} - \omega_{\bar{q}1} + \omega_{q1}}{2N_c} & \frac{-\omega_{q\bar{q}} - \omega_{q1} + \omega_{\bar{q}1}}{2N_c} & \frac{\omega_{q\bar{q}}}{N_c^2} \\ \cdot & \cdot & \cdot & \omega_{\bar{q}1} & \frac{\omega_{q\bar{q}} - \omega_{q1} - \omega_{\bar{q}1}}{2} & \frac{-\omega_{q\bar{q}} - \omega_{\bar{q}1} + \omega_{q1}}{2N_c} \\ \cdot & \cdot & \cdot & \cdot & \omega_{q1} & \frac{-\omega_{q\bar{q}} - \omega_{q1} + \omega_{\bar{q}1}}{2N_c} \\ \cdot & \cdot & \cdot & \cdot & \cdot & \frac{\omega_{q\bar{q}}}{N_c^2} \end{pmatrix}, \quad (5.17)$$

where for notational brevity we have written all occurrences of $\omega_{ij}(n_2)$ as ω_{ij} . In the case of the outermost Sudakov operator, the colour algebra can no longer be simplified to just abelian factors. However, rather than work with six different colour matrices, we can again exploit colour conservation to find

$$\begin{aligned} \mathbf{T}_q^2 \cdot \mathbf{T}_1^2 &= \mathbf{T}_{\bar{q}}^2 \cdot \mathbf{T}_2^2, \\ \mathbf{T}_{\bar{q}}^2 \cdot \mathbf{T}_1^2 &= \mathbf{T}_q^2 \cdot \mathbf{T}_2^2, \\ \mathbf{T}_1^2 \cdot \mathbf{T}_2^2 &= (C_F - C_A)\mathbf{1} + \mathbf{T}_q^2 \cdot \mathbf{T}_{\bar{q}}^2, \\ \mathbf{T}_q^2 \cdot \mathbf{T}_2^2 &= -C_F\mathbf{1} - \mathbf{T}_q^2 \cdot \mathbf{T}_{\bar{q}}^2 - \mathbf{T}_{\bar{q}}^2 \cdot \mathbf{T}_1^2, \end{aligned} \quad (5.18)$$

which greatly simplifies the exponent of the Sudakov factor. We choose to express the entire exponent in terms of factors of $\mathbf{T}_q^2 \cdot \mathbf{T}_{\bar{q}}^2$, $\mathbf{T}_{\bar{q}}^2 \cdot \mathbf{T}_1^2$ and $\mathbf{1}$:

$$\begin{aligned} \mathbf{V}_{\rho, E_2} &= \exp \left[-\frac{\alpha_s}{\pi} \ln \left(\frac{E_2}{\rho} \right) \left\{ (C_A + C_F)\mathbf{1} \ln \frac{2}{\lambda} \right. \right. \\ &\quad + \mathbf{T}_q^2 \cdot \mathbf{T}_1^2 \ln \left(\frac{(n_{\bar{q}} \cdot n_1)(n_q \cdot n_2)}{(n_q \cdot n_1)(n_{\bar{q}} \cdot n_2)} \right) - \mathbf{T}_q^2 \cdot \mathbf{T}_{\bar{q}}^2 \ln \left(\frac{2(n_1 \cdot n_2)}{(n_{\bar{q}} \cdot n_1)(n_q \cdot n_2)} \right) \\ &\quad \left. \left. - C_F\mathbf{1} \ln \left(\frac{2(n_1 \cdot n_2)}{(n_{\bar{q}} \cdot n_1)(n_q \cdot n_2)} \right) - C_A\mathbf{1} \ln \left(\frac{2}{n_1 \cdot n_2} \right) \right\} \right]. \end{aligned} \quad (5.19)$$

In the case of two emissions, these colour charge products have the following

form

$$\begin{aligned}
\mathbf{T}_q^2 \cdot \mathbf{T}_{\bar{q}}^2 &= \begin{pmatrix} -\frac{N_c^2-1}{2N_c} & 0 & -\frac{1}{2} & 0 & 0 & -\frac{1}{2} \\ 0 & -\frac{N_c^2-1}{2N_c} & 0 & -\frac{1}{2} & -\frac{1}{2} & 0 \\ 0 & 0 & \frac{1}{2N_c} & 0 & 0 & 0 \\ 0 & 0 & 0 & \frac{1}{2N_c} & 0 & 0 \\ 0 & 0 & 0 & 0 & \frac{1}{2N_c} & 0 \\ 0 & 0 & 0 & 0 & 0 & \frac{1}{2N_c} \end{pmatrix}, \\
\mathbf{T}_q^2 \cdot \mathbf{T}_1^2 &= \begin{pmatrix} 0 & 0 & \frac{1}{2} & 0 & 0 & 0 \\ 0 & 0 & 0 & 0 & \frac{1}{2} & 0 \\ 0 & 0 & -\frac{N_c}{2} & 0 & -\frac{1}{2} & 0 \\ 0 & -\frac{1}{2} & 0 & -\frac{N_c}{2} & 0 & 0 \\ 0 & \frac{1}{2} & 0 & 0 & 0 & 0 \\ 0 & 0 & 0 & \frac{1}{2} & 0 & 0 \end{pmatrix}. \tag{5.20}
\end{aligned}$$

We can see from the above that the Sudakov exponent in Eq. 5.19 cannot be straightforwardly exponentiated. For this we will adopt numerical exponentiation methods that we shall describe later. Firstly however, we turn our attention to examining the order-by-order cancellation of the collinear cutoff parameter, λ .

5.1.2 Cutoff independence

Before presenting the `FixedOrderA` implementation of the cross sections calculated in the previous section, it is interesting to deviate and examine the order-by-order results to confirm independence from our imposed collinear cutoff, to order α_s^2 .

We therefore begin by denoting the order α_s^p contribution to the n -emission cross section as $\Sigma_{q\bar{q},n}^{(p)}$, such that

$$\Sigma_{q\bar{q},n} = \sum_{p=n}^{\infty} \Sigma_{q\bar{q},n}^{(p)} \tag{5.21}$$

where the lowest order contribution of any σ_n is $p = n$ due to the emission phase-space factors. Whilst we expand the Sudakov operators, we shall undo the angular integrals carried out in Eq. 5.8, 5.14 and 5.19 in order to make the collinear cancellation between emissions and virtual exchanges more explicit.

Expanding the zero-emission cross-section, Eq. 5.8, we find

$$\begin{aligned}
\Sigma_{q\bar{q},0}^{(0)}(\rho) &= C_A, \\
\Sigma_{q\bar{q},0}^{(1)}(\rho) &= -C_A \left(\frac{\alpha_s}{\pi} \ln \left(\frac{1}{\rho} \right) \right) 2C_F \int_0^{1-\lambda} d(\cos \theta_1) \omega_{q\bar{q}}(n_1), \\
\Sigma_{q\bar{q},0}^{(2)}(\rho) &= C_A \left(\frac{\alpha_s}{\pi} \ln \left(\frac{1}{\rho} \right) \right)^2 2C_F^2 \int_0^{1-\lambda} d(\cos \theta_1) \omega_{q\bar{q}}(n_1) \\
&\quad \times \int_0^{1-\lambda} d(\cos \theta_2) \omega_{q\bar{q}}(n_2). \tag{5.22}
\end{aligned}$$

The order α_s and α_s^2 results in the case of one-gluon emission are

$$\begin{aligned}
\Sigma_{q\bar{q},1}^{(1)}(\rho) &= C_A \left(\frac{\alpha_s}{\pi} \ln \left(\frac{1}{\rho} \right) \right) \int_c^{1-\lambda} d(\cos \theta_1) \omega_{q\bar{q}}(n_1), \\
\Sigma_{q\bar{q},1}^{(2)}(\rho) &= -C_A \left(\frac{\alpha_s}{\pi} \ln \left(\frac{1}{\rho} \right) \right)^2 C_F \int_c^{1-\lambda} d(\cos \theta_1) \int_{-1+\lambda}^{1-\lambda} d(\cos \theta_2) \frac{d\phi}{2\pi} \omega_{q\bar{q}}(n_1) \\
&\quad \times \left[\frac{C_A}{2} (\omega_{q1}(n_2) + \omega_{\bar{q}1}(n_2)) - \left(\frac{C_A}{2} - 2C_F \right) \omega_{q\bar{q}}(n_2) \right] \\
&\quad \times \Theta(n_1 \cdot n_2 - \lambda). \tag{5.23}
\end{aligned}$$

There is only one result in which $\Sigma_2(\rho)$ contributes at order α_s^2 . This is the case in which there are two emissions with no virtual exchanges, the result of which is

$$\begin{aligned}
\Sigma_{q\bar{q},2}^{(2)}(\rho) &= C_A \left(\frac{\alpha_s}{\pi} \ln \left(\frac{1}{\rho} \right) \right)^2 C_F \left[\int_c^{1-\lambda} d(\cos \theta_1) \int_{-1+\lambda}^{-c} d(\cos \theta_2) \int_0^{2\pi} \frac{d\phi}{2\pi} \omega_{q\bar{q}}(n_1) \right. \\
&\quad \times \left[\frac{C_A}{2} (\omega_{q1}(n_2) + \omega_{\bar{q}1}(n_2)) - \left(\frac{C_A}{2} - C_F \right) \omega_{q\bar{q}}(n_2) \right] \Theta(n_1 \cdot n_2 - \lambda) \\
&\quad + \int_c^{1-\lambda} d(\cos \theta_1) \int_c^{1-\lambda} d(\cos \theta_2) \int_0^{2\pi} \frac{d\phi}{2\pi} \omega_{q\bar{q}}(n_1) \\
&\quad \times \left. \left[\frac{C_A}{2} (\omega_{q1}(n_2) + \omega_{\bar{q}1}(n_2)) - \left(\frac{C_A}{2} - C_F \right) \omega_{q\bar{q}}(n_2) \right] \Theta(n_1 \cdot n_2 - \lambda) \right], \tag{5.24}
\end{aligned}$$

where we have used the result

$$\begin{aligned}
\text{Tr} \left(\mathbf{D}_2^\nu \mathbf{D}_1^\mu \mathbf{D}_{1\mu}^\dagger \mathbf{D}_{2\nu}^\dagger \mathbf{S}_2 \right) &= 2C_A C_F \omega_{q\bar{q}}(n_1) \left[C_A (\omega_{q1}(n_2) + \omega_{\bar{q}2}(n_2)) \right. \\
&\quad \left. - (C_A - 2C_F) \omega_{q\bar{q}}(n_2) \right]. \tag{5.25}
\end{aligned}$$

If we add all of the contributions together, order-by-order, we find

$$\begin{aligned}\Sigma_{q\bar{q},0}^{(1)} + \Sigma_{q\bar{q},1}^{(1)} &= -C_A \left(\frac{\alpha_s}{\pi} \ln \left(\frac{1}{\rho} \right) \right) 2C_F \int_0^c d(\cos \theta_1) \omega_{q\bar{q}}(n_1) \\ &= -C_A \left(\frac{\alpha_s}{\pi} \ln \left(\frac{1}{\rho} \right) \right) 2C_F \ln \left(\frac{1+c}{1-c} \right),\end{aligned}\tag{5.26}$$

where we see cancellation of the collinear cutoff, and

$$\begin{aligned}\Sigma_{q\bar{q},0}^{(2)} + \Sigma_{q\bar{q},1}^{(2)} + \Sigma_{q\bar{q},2}^{(2)} &= C_A \left(\frac{\alpha_s}{\pi} \ln \left(\frac{1}{\rho} \right) \right)^2 \\ &\times \left[2C_F \int_0^c d(\cos \theta_1) \int_0^c d(\cos \theta_2) \omega_{q\bar{q}}(n_1) \omega_{q\bar{q}}(n_2) \right. \\ &- \frac{C_A}{2} \int_c^{1-\lambda} d(\cos \theta_1) \int_{-c}^c d(\cos \theta_2) \int_0^{2\pi} \frac{d\phi}{2\pi} \omega_{q\bar{q}}(n_1) \\ &\left. \times (\omega_{q_1}(n_2) + \omega_{\bar{q}_1}(n_2) - \omega_{q\bar{q}}(n_2)) \Theta(n_1 \cdot n_2 - \lambda) \right].\end{aligned}\tag{5.27}$$

The second integral initially appears to have a residual cutoff dependence. We can see this cancels as the integrand is zero in the limit that $n_1 \rightarrow n_a$. Indeed, if we numerically integrate Eq. 5.27, we find cutoff independence below values of $\lambda = 10^{-3}$ [169]. We can therefore see that the veto cross section, given the initial hard process $V \rightarrow q\bar{q}$ and using the cutoff prescription in Eq. 5.2, is independent of this cutoff including contributions upto order α_s^2 .

We now explain the implementation of **FixedOrderA**. The code implements the $\Sigma_n(\rho)$ cross sections in Eq. 5.8, Eq. 5.14 and Eq. 5.15 (where $n = 0, 1, 2$). To do this it utilises the **GSL** [170] implementation of the **VEGAS** Monte Carlo algorithm [171] to perform the angular and energy integrations. The emission and scalar product matrix operators are written as matrices represented in the colour flow basis. Their manipulation is carried out using the **Armadillo** library [172]. Whilst the colour structure of the $\Sigma_{q\bar{q},1}$ Sudakov exponents can be simplified to Casimir operators, this is not true of the ultimate Sudakov operator in $\Sigma_{q\bar{q},2}$. For this we employ numerical exponentiation methods implemented in **Armadillo**.

5.1.3 Testing Real Emissions

As the first test of the Variant A implementation, we focus on its components related to real emissions. In particular, we wish to validate the methods which

carry out the amplitude-level emission matrix element calculation, the basis tensor sampling which determines such matrix elements and the sampling of emitted gluon directions. As such, we hone in on the emission cross section, $\Sigma_{q\bar{q},n}^R$, which results from setting all Sudakov matrix elements in **CVolver** to unity. This is controlled by the **no-virtuals** run-time toggle (which we set to 1 in this case). In Section 4.5.3, we outlined how the collinear Casimir contributions to the Sudakov operators in the amplitude and conjugate-amplitude, at each evolution step, factorise. Indeed, such contributions are used as the sampling density from which we draw emission scales in Variant A. As we wish to ignore all Sudakov operator contributions, the results of this section are instead generated using emission scales sampled uniformly in the range $[0, E']$ (with E' being the previous emission scale, or the hard scale Q in the case of no emissions). The emission cross sections produced using this setup of **CVolver** can be validated against **FixedOrderA**.

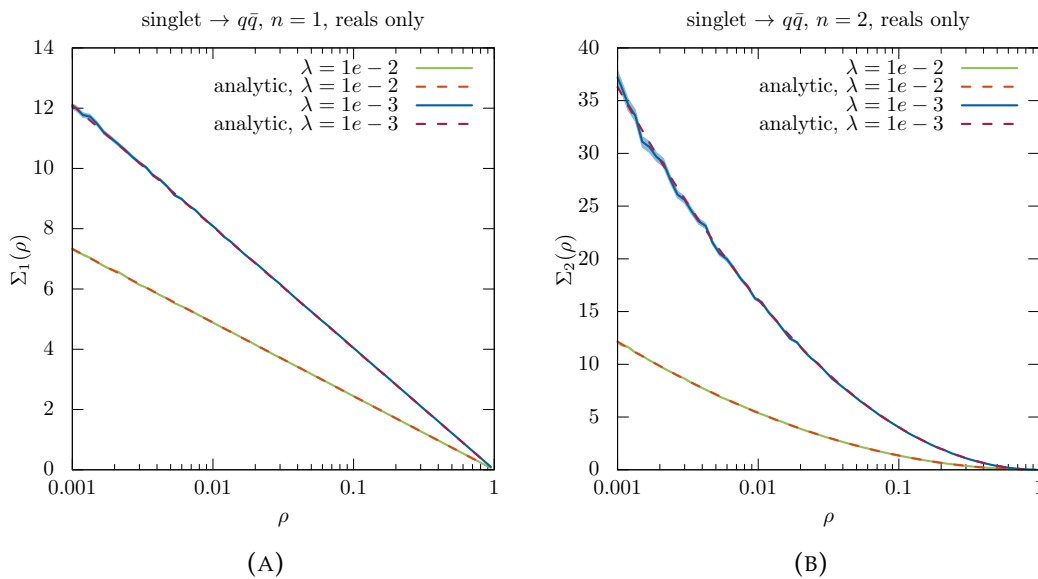


FIGURE 5.1: The jet veto emission cross section as a function of the veto scale ρ , for $V \rightarrow q\bar{q}$. Figure (A) presents the cross section for a gluon multiplicity of one and Figure (B) for two. The solid curves pertain to those generated with **CVolver** for two values of the collinear cutoff, $\lambda = 10^{-2}$ and $\lambda = 10^{-3}$. The light-blue shading indicates the error band for these results, whilst the broken lines labelled ‘analytic’ correspond to the independent **FixedOrderA** results (see text for details).

Figure 5.1 shows the jet veto emission cross section dependence on the veto scale, ρ , for different gluon multiplicities, $n = 1, 2$. Each cross section is presented for two values of the collinear cutoff: $\lambda = 10^{-2}$ and $\lambda = 10^{-3}$. The solid green and blue curves depict the results produced by Variant A, using

the aforementioned setup and the errors on these results are represented by light-green and light-blue shading around each curve. **FixedOrderA** results are denoted by broken lines and labelled as ‘analytic’. We observe good agreement between the **CVolver** and **FixedOrderA** curves. For $n = 1$, the $\lambda = 10^{-2}$ results are within 0.2% of each other and their ratio is consistent with unity to within two standard deviations. Whilst for a cutoff value of $\lambda = 10^{-3}$, the curves are within 0.4% and their ratio is equal to one, within one standard deviation. In the case of two emissions, the **CVolver** and **FixedOrderA** curves, for both cutoff values, are within 2% and their ratios are equivalent to unity to within two standard deviations.

The close agreement between **CVolver** and **FixedOrderA** provides a good validation of all of the components in **CVolver** related to emissions. This includes the calculation of amplitude-level emission matrix elements, along with the evaluation of the gluon polarisation vectors stated in Eq. 4.86. In addition, the sampling strategy of the basis tensors identifying these matrix elements and the emission direction sampling is verified.

5.1.4 Numerical Exponentiation

We shall now examine the full cross section to verify the sampling of Sudakov matrix element basis tensors. In order to do this we will compare the jet veto cross section generated by the two **CVolver** running modes, **evolve()** and **evolveFull()**. The **evolve** run-time toggle chooses between the two modes (set to 0 for **evolve()** and 1 for **evolveFull()**). The **evolve()** and **evolveFull()** methods carry out each evolution step according to Algorithm 4 and 5 respectively. The latter conducts the full matrix multiplication of the emission, Sudakov and scalar product operators decomposed in the colour flow basis. To carry out the matrix multiplication and transposition (for conjugate operators) we use the **Boost uBlas** library [173] matrix container classes.

These matrix containers are populated using the **element()** method in the respective classes. The Sudakov operator matrix is calculated in one of two ways: if the colour order, d , is set to a finite integer, each element of the Sudakov operator matrix is calculated using the primed or unprimed approximation outlined in Section 4.3.1. If instead d is set to **inf**, we utilise the numerical exponentiation methods outlined in Section 4.3.3, which are contained in the **exactElement()** method of the **EvolutionMatrix** class. For one or two colour flows this method calculates hard-coded analytic expressions for ele-

ments of the exponentiated anomalous dimension matrix. In the case of additional colour flows, the anomalous dimension matrix is first determined and numerically exponentiated (NE) using the Padé approximation [159, 160].

When the numerical exponentiation methods are used, we must adopt the same uniform scale sampling as described in Section 5.1.3. The anomalous dimension matrix coefficients, Γ_{ij} , are then defined as

$$\Gamma_{ij} = \frac{\alpha_s}{2\pi} \ln\left(\frac{E'}{E}\right) \left(\ln\left(\frac{n_i \cdot n_j}{2}\right) + \ln\left(\frac{2}{\lambda}\right) \right), \quad (5.28)$$

to account for the Casimir collinear terms. The reason being, that by default, Variant A as outlined in Section 4.5.3, extracts the Casimir collinear part of the Sudakov operators (the term proportional to $\ln(2/\lambda)$ in Eq. 5.28) in the amplitude and conjugate-amplitude to be used as a density from which to sample emission scales. As this contribution cannot be extracted from the numerically exponentiated Sudakov operator matrix, we employ a flat sampling to avoid double-counting the collinear part.

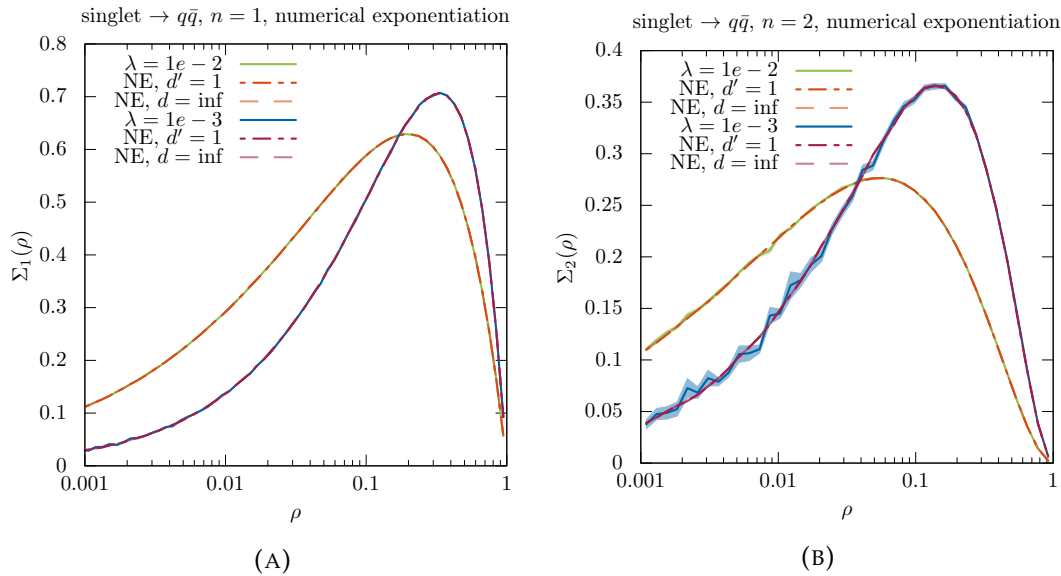


FIGURE 5.2: The jet veto cross section dependence on ρ for the $V \rightarrow q\bar{q}$ process. Gluon multiplicities are presented for upto two emissions ($n = 1, 2$). The solid curves denote the results of the `evolve()` method and the dashed curves to `evolveFull()`.

Figure 5.2 shows the results of Variant A using the `evolve()` and the `evolveFull()` methods, for gluon multiplicities up to two emissions $n = 1, 2$. The solid green and blue curves denote the results of `evolve()` for two different values of the collinear cutoff: $\lambda = 10^{-2}$ and 10^{-3} , at a colour order $d' = 1$.

One can see from Section 5.1.1 that calculating the Sudakov operator to this colour order, is sufficient to determine all subleading-colour contributions to the two-emission cross section. Also plotted in Figure 5.2, are the `evolveFull()` results with dotted-dashed lines for $d' = 1$ and dashed lines for d symbolically set to `inf`. The red dashed curves correspond to a collinear cutoff value of $\lambda = 10^{-2}$, whilst the magenta dashed curves to $\lambda = 10^{-3}$.

From Figure 5.2, we see good agreement between the `evolve()` and `evolveFull()` methods. Specifically, the one-emission cross section results agree to within 0.15% and 0.5% for the collinear cutoff values $\lambda = 10^{-2}$ and 10^{-3} respectively. The ratio between the results of the two methods are equal to 1 within two standard deviations. Similarly, the two-emission cross sections agree to within 0.6% for a cutoff value of $\lambda = 10^{-2}$. In the case that $\lambda = 10^{-3}$, the cross sections are within 1.5% down to ρ values of 0.01 and 4.5% below. This larger uncertainty is caused by increasing weight fluctuations in the `evolve()` method, which we can see worsen with a larger number of emissions and a smaller collinear cutoff.

5.1.5 Fixed Order Validation

The self-consistency between the two running modes `evolve()` and `evolveFull()` of `CVolver` provides a good check on the basis tensor sampling for both the emission and Sudakov matrix elements, in addition to the evaluation of these elements and the Sudakov approximation. We now want to provide further validation of the $n = 0, 1$ and 2 cross sections, by comparing them with the independent `FixedOrderA` code.

Figure 5.3 presents the veto cross section as a function of ρ for gluon multiplicities up to $n = 2$, and for two collinear cutoff values, $\lambda = 10^{-2}$ and $\lambda = 10^{-3}$. Each Sudakov matrix element occurrence is computed in the NNLC'_V approximation¹. The Variant A results correspond to the solid curves, whilst the dotted curves, denoted ‘analytic’, represent the results of `FixedOrderA`. We see that for $n = 0, 1$, the Variant A and `FixedOrderA` cross sections are within 0.6% and agree to within one standard deviation across the entire range of ρ . This is true

¹We remind the reader that the NNLC'_V approximation refers to the accuracy to which we sum terms in each Sudakov matrix element (in both the amplitude and conjugate-amplitude). The N^dLC_V approximation sums terms accurate only to order $1/N_c^d$, where d is the specified colour order (see Eq. 4.32). This approximation sums the leading colour-diagonal terms to all orders. This summation can be improved by including the colour-diagonal subleading terms to all orders, which we dub our primed notation (see Eq. 4.26). NNLC'_V uses the primed approximation with $d = 2$.

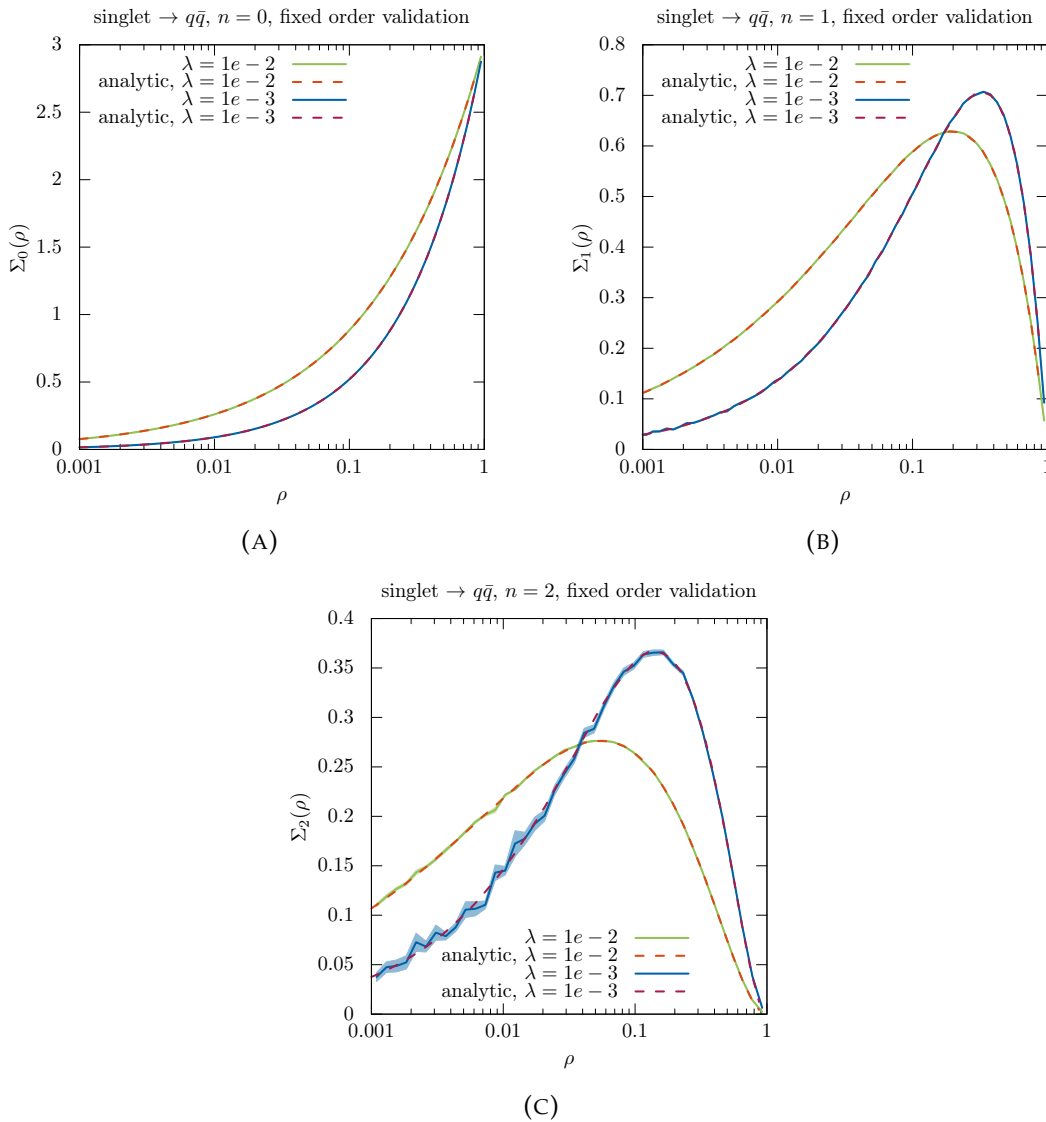


FIGURE 5.3: The jet veto cross section dependence on ρ for the $V \rightarrow q\bar{q}$ process. Gluon multiplicities are presented for upto two emissions ($n = 0, 1, 2$). The solid curves denote the results of the **CVolver** Variant A, where the shaded region on the green and blue lines demarcates the corresponding errors. The dashed curves present the results of **FixedOrderA**.

for both values of the collinear cutoff. In the case of the $\Sigma_2(\rho)$ cross sections, Variant A and **FixedOrderA** agree to within 0.55% for $\lambda = 10^{-2}$ and 3% for $\lambda = 10^{-3}$. Above $\rho = 10^{-2}$, this reduces to $\leq 1\%$. The results are consistent to within two standard deviations across the entire ρ -range. The larger band of errors necessary for agreement of the $\Sigma_2(\rho)$ cross sections at a lower collinear cutoff, is due to increasing weight fluctuations in the Variant A cross section. In the next section, we shall see that such fluctuations worsen with increasing multiplicity, rendering a comparison of the $\lambda = 10^{-2}$ and $\lambda = 10^{-3}$ total cross

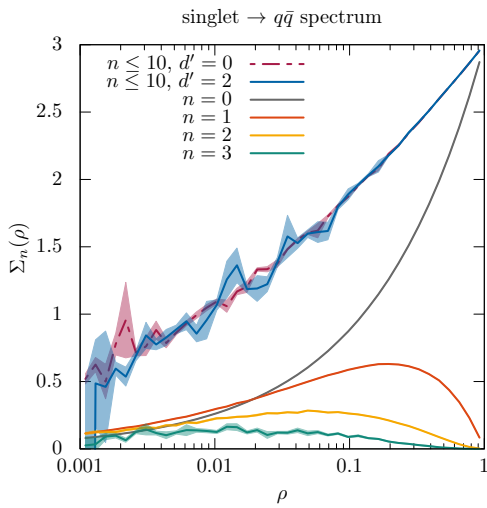
section results difficult. However, for $n \leq 2$ they are sufficiently tame, that Figure 5.3 provides an excellent validation for all components of Variant A at low multiplicities.

5.1.6 Emission Spectra

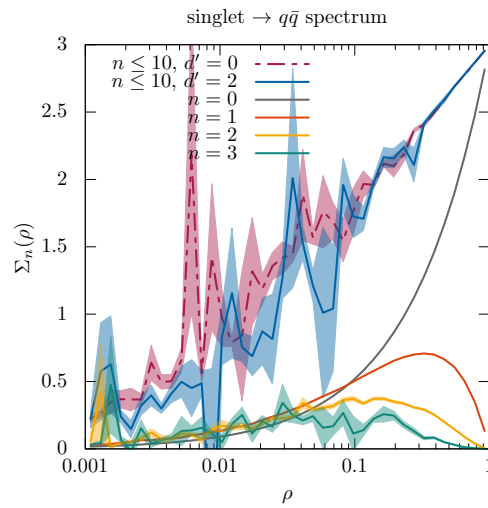
In this section, we shall present the total cross section result, $\Sigma(\rho)$, including contributions from the first 10 emissions.

Figure 5.4a and Figure 5.4b show the total cross section, $\Sigma(\rho)$, which results from summing over contributions from the first ten emissions, for both cutoffs $\lambda = 10^{-2}$ and $\lambda = 10^{-3}$ respectively. This summation is denoted by $n \leq 10$. The dashed curve exhibits the total full- N_c cross section, with all Sudakov operators calculated in the LC'_V approximation. Also displayed are the $NNLC'_V$ total cross section results, and the cross sections for the first few contributing multiplicities. The shaded region in each plot of Figure 5.4 represents the one standard deviation Monte Carlo error (determined as per Eq. 3.11). Figure 5.4c and Figure 5.4d show how the total cross section is built up from these individual multiplicity cross sections, for $\lambda = 10^{-2}$ and $\lambda = 10^{-3}$ respectively.

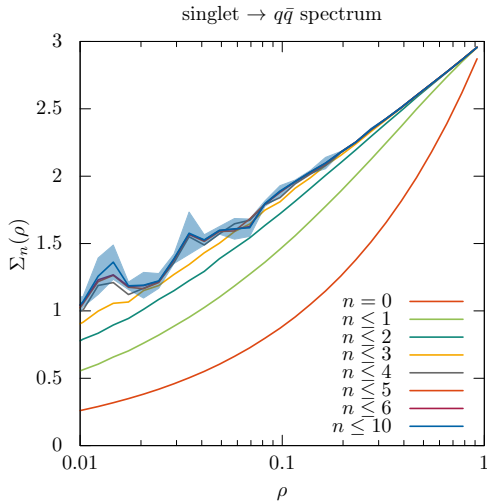
The plots in Figure 5.4 exhibit some key features: the $n = 0$ curves are described solely by an exponential function; these would be a straight line if we plotted our cross section value logarithmically. Additionally, the $n = 0$ curves for different cutoffs have the same values at $\rho = 1$, and the lower collinear cutoff curve falls faster as ρ gets smaller. Figures 5.4a and 5.4b illustrate how the $n > 0$ curves become more peaked closer to $\rho = 1$ for lower cutoff values, and how higher multiplicities contribute relatively little to the total cross section at larger ρ , but have similar contributions (to lower multiplicities) at smaller ρ . Therefore, a higher number of real emissions are necessary to reach a convergent answer, given a smaller collinear cutoff. We would expect there to be an ‘optimal’ combination of cutoff and number of emissions, which provide a good approximation to the limit of zero cutoff and an infinite number of emissions. However, as can be seen from Figures 5.4b and 5.4d in particular, Variant A develops large fluctuations for higher multiplicities and smaller cutoffs, which source from the event weights. This makes determining the aforementioned point of convergence, impossible. If we present the total cross section on a linear ρ scale, and for both cutoff values, as in Figure 5.5a, we witness apparent cutoff-independence for much of the ρ -range $[0.1 : 1]$, although this cannot be confirmed below $\rho = 0.1$.



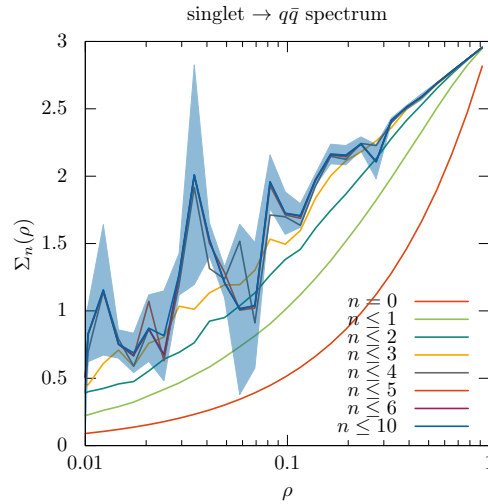
(A) Breakdown of the jet veto total cross section using $\lambda = 10^{-2}$ by multiplicity and colour order, for the process $\text{singlet} \rightarrow q\bar{q}$.



(B) Breakdown of the jet veto total cross section using $\lambda = 10^{-3}$ by multiplicity and colour order, for the process $\text{singlet} \rightarrow q\bar{q}$.



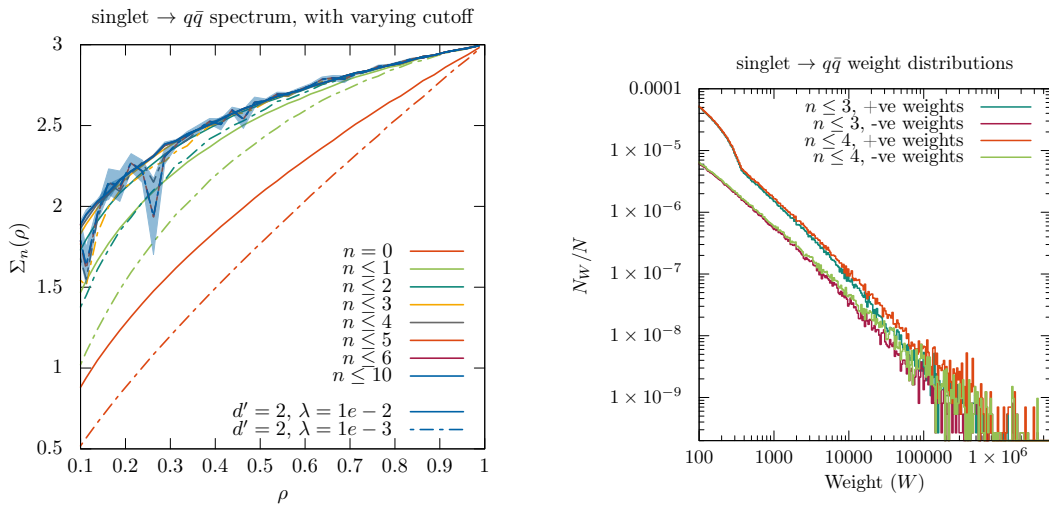
(C) The jet veto total cross section in (a), for summations over different gluon multiplicities ($n \leq 0, 1, 2, 3, 4, 5, 6$ and 10). Results are shown for $d' = 2$, and a collinear cutoff of $\lambda = 10^{-2}$.



(D) The jet veto total cross section in (b), for summations over different gluon multiplicities ($n \leq 0, 1, 2, 3, 4, 5, 6$ and 10). Results are shown for $d' = 2$, and a collinear cutoff of $\lambda = 10^{-3}$.

FIGURE 5.4: The jet veto total cross section (for $n \leq 10$) for the $V \rightarrow q\bar{q}$ process, using Variant A of `CVolver`. Results are shown for $d' = 0, 2$. The contributions from $n = 0$ up to 3 emissions are also presented in (a) and (b), and summed over in (c) and (d). The total cross section result is a summation over all emissions.

It is clear from Figure 5.4d, that the large weights, disrupting the stability of the total cross section, begin to appear after four emissions. Figure 5.5b presents the distribution of positive and negative event-weights which contribute to the $n \leq 4$ total cross section in Figure 5.4d, with the $n \leq 3$ cross section for comparison. We can see that with an increasing number of emissions, the weight dis-



(A) The jet veto total cross section presented for linearly scaled values of the veto energy. Included, are the summations over different gluon multiplicities ($n \leq 0, 1, 2, 3, 4, 5, 6$ and 10) for $\lambda = 10^{-2}$ (solid curves) and $\lambda = 10^{-3}$ (dashed curves).

(B) A subset of the event-weight distributions corresponding to the $n \leq 3, 4$ total cross section. Positive and negative event-weights have been plotted separately for $n \leq 4$.

FIGURE 5.5: The jet veto total cross section presented for linearly scaled values of the veto energy and the $n \leq 3, 4$ total cross section weight distributions for $\lambda = 10^{-3}$.

tributions broaden, with a higher population of larger weights. Importantly, the positive and negative weight distributions become more ‘erratic’ at larger weight-values, and there exist outlier event-weights which dominate the total cross section.

Table 5.1 is an event with a large overall weight ($W > 10^6$), contributing to the $n = 4$ cross section. The weights, matrix elements and sampled basis tensors corresponding to each evolution step are shown, represented by the ‘reference functions’ in Algorithm 4. We see that the Sudakov operator matrix elements (in the rows corresponding to $[\alpha_n | \mathbf{V}_{E,E'} | \alpha_{n-1}]$ and $\langle \alpha_{n-1}^\dagger | \mathbf{V}_{E,E'} | \alpha_n^\dagger \rangle$), and the weights from their basis tensor sampling (in the row $W_{\alpha_n} \times W_{\alpha_n^\dagger}$), are of $\mathcal{O}(1)$ - with an exception being the NLC'_V approximation used for $n = 4$ in the conjugate-amplitude. This exception is highlighted by the blue cells in Table 5.1. The basis tensor sampling weight is larger because of the choice to induce a single swap in the conjugate-amplitude basis tensors, from $|34512\rangle$ to $|34215\rangle$ (see Section 4.4 for a description of the colour order sampling process). However, the largest contributions to the event-weights come from the emission matrix elements and their tensor sampling (in the rows corresponding to $W_{\alpha_{n+1}} \times W_{\alpha_{n+1}^\dagger}$ and $[\alpha_{n+1} | \mathbf{D}_E | \alpha_n] \times \langle \alpha_n^\dagger | \mathbf{D}_E^\dagger | \alpha_{n+1}^\dagger \rangle$).

Object Value	$n = 0$	1	2
W_{E_n}	0.0493364	0.0232171	0.0151804
$W_{\alpha_n} \times W_{\alpha_n^\dagger}$	1	1.77778	2.08642
$\langle \alpha_n \alpha_n^\dagger \rangle$	$\langle 1 1 \rangle$	$\langle 21 21 \rangle$	$\langle 231 312 \rangle$
$[\alpha_n \mathbf{V}_{E,E'} \alpha_{n-1}]$	1	1.04243	1.15778
$\langle \alpha_{n-1}^\dagger \mathbf{V}_{E,E'} \alpha_n^\dagger \rangle$	1	1.04243	1.21939
$W_{\alpha_{n+1}} \times W_{\alpha_{n+1}^\dagger}$	2.66667	78	586.667
$\langle \alpha_{n+1} \alpha_{n+1}^\dagger \rangle$	$\langle 21 21 \rangle$	$\langle 231 312 \rangle$	$\langle 2413 3421 \rangle$
$[\alpha_{n+1} \mathbf{D}_E \alpha_n] \times \langle \alpha_n^\dagger \mathbf{D}_E^\dagger \alpha_{n+1}^\dagger \rangle$	2.77721	2.02518	10.7231
	$n = 3$	4	
	0.0112768	0.0451669	
	2.08642	62.5926	
	$\langle 2413 3421 \rangle$	$\langle 25134 34215 \rangle$	
	1.03913	1.39434	
	1.02595	-0.0428957	
	14520		
	$\langle 25134 34512 \rangle$		
	-29.684		

TABLE 5.1: An event with a large weight, of $> 10^6$, which contributes towards the $n = 4$ cross section. The object values column uses the ‘reference functions’ detailed in Algorithm 4, to indicate which part of the shower contributes the corresponding weight at the n th multiplicity. The total weight, 1.41074×10^6 , can be obtained by multiplying together all of the sampling weights W_{E_n} , $W_{\alpha_n} \times W_{\alpha_n^\dagger}$ and $W_{\alpha_{n+1}} \times W_{\alpha_{n+1}^\dagger}$, the matrix elements $[\alpha_n | \mathbf{V}_{E,E'} | \alpha_{n-1}]$, $\langle \alpha_{n-1}^\dagger | \mathbf{V}_{E,E'} | \alpha_n^\dagger \rangle$ and $[\alpha_{n+1} | \mathbf{D}_E | \alpha_n] \times \langle \alpha_n^\dagger | \mathbf{D}_E^\dagger | \alpha_{n+1}^\dagger \rangle$, the final scalar product matrix element, $\langle 25134 | 34215 \rangle = N_c^2$, and the direction sampling weights from all emissions, $W_{\Phi_{n+1}} \leftarrow 2^4 \times (1 - c_0)^4$.

In order to improve on the large weights contaminating Variant A, Variant B was devised. Primarily, the ambition of Variant A - to maintain an amplitude-level description of our general evolution algorithm - is replaced with cross section-level contractions, where possible. In particular, Variant B adopts the cross section-level emission matrix element formula (in Eq. 4.43). This fundamental change enables us to utilise the Sudakov veto algorithm with competition, where the competing processes are the scalar-product-element-weighted emission matrix elements. A further by-product of this algorithm is the selection of the parent partons to each emission, which allows for a more robust direction sampling. As was previously outlined, the Variant A direction sampling is constrained to the out-of-gap region, never triggering an in-gap

emission, and termination of the shower cascade through the measurement function. The shower can still of course terminate if it reaches a maximum number of emissions, n_{max} , or if the sampled emission scale is below the veto scale ρ . Variant B on the other hand implements a direction sampling which permits us to emit into the in-gap region, and therefore introduces an additional termination criterion (compared with Variant A). Variant B emits up to an arbitrary number of emissions, n , where $n \leq n_{max}$. In practice this means, that with Variant A, we generate each n -emission $\Sigma_{q\bar{q},n}$ cross section separately and sum the results. For Variant B however, we provide a maximum multiplicity, n_{max} , and the shower cascade simultaneously calculates the total cross section (summing all of the $\Sigma_{q\bar{q},n}$ contributions) and the individual n -emission cross sections. The more complex nature of the Variant B direction sampling warrants an analysis, which we carry out in Section 5.2.2.

We shall now progress the discussion onto verifying **CVolver** Variant B. In addition to changing the formulation of the shower for Variant B, many peripheral code changes were made. Among these, a generalised value for N_c was implemented throughout **CVolver**, a second test-bed hard process, $H \rightarrow gg$, was added, and an accurate book-keeping of the $1/N_c^k$ -breakdown was instated. This paved the way for a wider scope of analysis and cross-checks on Variant B, which will be discussed in the following section. Of course, the colour machinery of **CVolver**, the calculation of the Sudakov matrix element approximation and the Sudakov basis tensor sampling implementations are shared between the two variants. And so, the following cross-checks supplement the validations of Section 5.1.

5.2 Variant B

In this section, we present numerical results of the **CVolver** Variant B implementation discussed in Section 4.5.4 for the jet veto observable. In particular, we shall isolate components of the **CVolver** implementation for both the $V \rightarrow q\bar{q}$ and $H \rightarrow gg$ processes and compare their results with independent cross-checks. This section is based on work carried out for [22].

Firstly, we compare the colour coefficients of the emission cross sections in **CVolver** against analytic results in Section 5.2.1. Then, we examine the angular correlations between emitted particles in Section 5.2.2, in order to validate the sampling of particle directions and the calculation of emission matrix elements. As an initial test of the inclusion of both emission and Sudakov

operators, we present the value of the fully-inclusive cross section for numerous colour order and veto scale combinations, with fixed emission (ω_{ij}) and anomalous dimension matrix (Γ_{ij}) coefficients, as a function of N_c in Section 5.2.3. Subsequently in Section 5.2.4, we illustrate the jet veto cross section upto two emissions, including both emission and Sudakov operators, and compare with the fixed order calculation in Section 5.1.1 (modulo a change to the appropriate cutoff prescription). In Section 5.2.5 we show and discuss the N_c breakdown of the jet veto cross section for the first three emissions and we culminate in the emission spectra for the shower evolution, including up to 20 emissions, in Section 5.2.6.

Throughout the ensuing discussions, we shall adopt the schema of writing the cross section, subscripted by the multiplicity at which it is calculated. Additionally, we write the cross section, in terms of the different powers of N_c that contribute, as

$$\Sigma_n(\rho) = \sum_{k=k_n^{\min}}^{k_n^{\max}} N_c^k \Sigma_n^{(k)}(\rho). \quad (5.29)$$

The value of k_n^{\max} is equal to $n + 1$ for $q\bar{q}$ and $n + 2$ for gg production. It is important to note here that the $\Sigma_n^{(k)}$ coefficients include the Sudakov R-factors, as seen in Eq. 4.27 and 4.29. The exponents of which contain the leading diagonal entries in the anomalous dimension matrix and can also contain the sub-leading diagonal ones. As a reminder to the reader, this is the distinction between what we coin our primed and unprimed $N^d \text{LC}_V$ approximation. Therefore, Eq. 5.29 is not a strict expansion in powers of N_c , but rather, it keeps track of $1/N_c$ off-diagonal suppression that originates in the hard scattering matrix, the real emission operators, the successive colour orders in Eq. 4.26 or Eq. 4.32 and the scalar product matrix.

Where we discuss strictly leading-colour results, they are denoted by LC_{V+R} , and are composed of the $N_c^{k_n^{\max}}$ contribution in Eq. 5.29, with $\Sigma_n^{(k_n^{\max})}$ calculated in the $d = 0$ approximation.

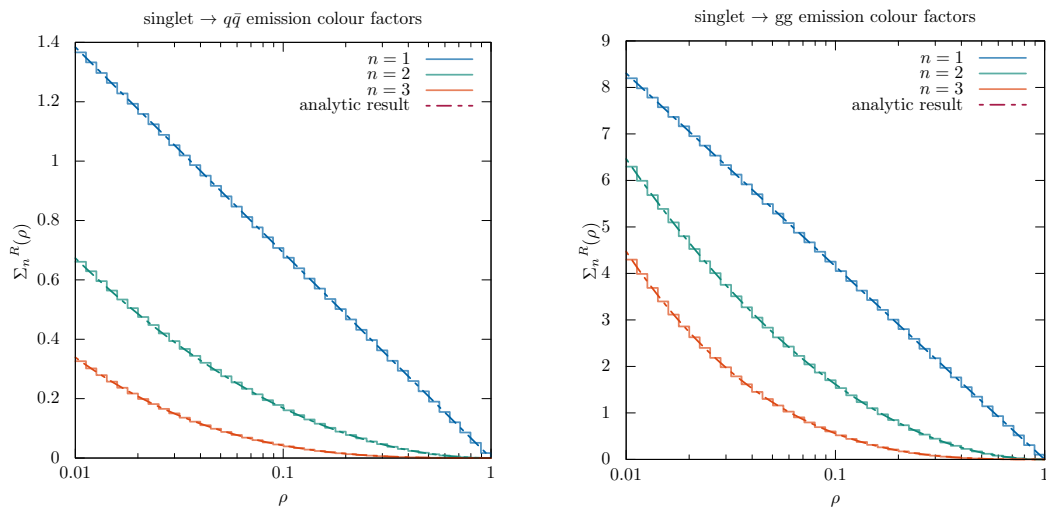
5.2.1 Emission Colour Factors

We begin our series of validation tests by looking at the components of Variant B that are related to emissions, namely, the calculation of cross section level emission matrix elements and the correct inclusion of emission contributions using the competition algorithm. In order to isolate the contributions to the cross section which arise from the emission operators, we set the Sudakov op-

erator matrix elements to unity. As such, we shall denote the cross section contribution, $\Sigma_n^{(k)}$, containing only emission contributions as $\Sigma_n^{R,(k)}$. The superscript (k) once again indicates that we are referring to the N_c^k contribution and we understand that its exclusion refers to the sum over all N_c^k terms.

So that we can test the emission components independently of our chosen emission direction sampling or cutoff prescription, we adopt a uniform emission direction sampling over all phase space. This unit radiation pattern has the effect of setting our direction sampling density (in Eq. 4.93), $\omega_{ij}d\Omega_k/\Omega_{ij}$, to 1. In addition, whilst the Sudakov matrix elements are all unity, the non-energy dependent part of their exponents (the coefficients Ω_{ij}) are still used in the competition algorithm. The value of Ω_{ij} for all partons i and j is set to $\alpha_s/2\pi$, so that **CVolver** will produce the emission cross section with all eikonal factors equal to unity.

The results of this procedure for gluon multiplicities upto three emissions ($n = 1, 2, 3$) are presented in Figures 5.6a and 5.6b for the $V \rightarrow q\bar{q}$ and $H \rightarrow gg$ processes respectively.



(A) Emission cross section in the case of 1, 2 and 3 emissions, for the process singlet $\rightarrow q\bar{q}$.

(B) Emission cross section in the case of 1, 2 and 3 emissions, for the process singlet $\rightarrow gg$.

FIGURE 5.6: The inclusive emission cross section for the processes $V \rightarrow q\bar{q}$ and $H \rightarrow gg$. Gluon multiplicities are presented upto three emissions ($n = 1, 2, 3$). The stepped results pertain to those, generated using **CVolver**, with all Ω_{ij} set to $\alpha_s/(2\pi)$ and adopting a uniform direction-sampling over the full angular phase-space. The broken curves correspond to the analytic result described in the text.

For comparison, the analytic forms of the simplified emission cross section for

each multiplicity, are plotted in Figure 5.6 with broken lines of the same colour. Looking at Eq. 5.13 and 5.25, we can determine the analytic expressions for the $V \rightarrow q\bar{q}$ emission cross sections by setting the Sudakov contributions to unity and eikonal factors to 1. Carrying out the energy integrals, we find

$$\begin{aligned}\Sigma_{q\bar{q},1}^R(\rho) &= \left(\frac{\alpha_s}{\pi}\right) (N_c^2 - 1) \ln\left(\frac{1}{\rho}\right), \\ \Sigma_{q\bar{q},2}^R(\rho) &= \left(\frac{\alpha_s}{\pi}\right)^2 \left(2N_c^3 - 3N_c + \frac{1}{N_c}\right) \frac{1}{2} \ln^2\left(\frac{1}{\rho}\right),\end{aligned}\quad (5.30)$$

whereas the cross section for three emissions is

$$\Sigma_{q\bar{q},3}^R(\rho) = \left(\frac{\alpha_s}{\pi}\right)^3 \left(6N_c^4 - 11N_c^2 - \frac{1}{N_c^2} + 6\right) \frac{1}{6} \ln^3\left(\frac{1}{\rho}\right). \quad (5.31)$$

In the case of $H \rightarrow gg$, there exists a general form for the emission cross section:

$$\Sigma_{gg,n}^R(\rho) = \left(\frac{\alpha_s}{\pi}\right)^n (n+1)! (N_c^2 - 1) N_c^n \frac{1}{n!} \ln^n\left(\frac{Q}{\rho}\right), \quad (5.32)$$

which is correct up to at least $n = 4$.

Figures 5.6a and 5.6b exhibit good agreement between Eq. 5.30 and 5.32 and the **CVolver** results. In particular, the analytic and numerical $q\bar{q}$ results are within 0.1%, 0.9% and 0.9% for $n = 1, 2$ and 3. For gg , they are within 0.3%, 0.6% and 1% for $n = 1, 2$ and 3. The ratio between the analytic and numerical results is consistent with unity to within two standard deviations for all multiplicities.

This agreement serves to validate the methods in **CVolver** which calculate the cross-section emission matrix element (outlined in Eq. 4.45) and its colour coefficients. Moreover, it is an affirmation that the sampling of basis tensors for emission matrix elements, selected with probability

$$P(\rho, \bar{\rho}) = \frac{1}{\xi_{ij}} \frac{\langle \rho | \bar{\rho} \rangle}{\langle \tau | \bar{\tau} \rangle} |[\rho | \mathbf{T}_i | \tau] \langle \bar{\tau} | \mathbf{T}_j | \bar{\rho} \rangle|, \quad (5.33)$$

(as discussed in Section 4.5.4) is correctly performed. In particular, the emission matrix elements of the form $[\rho | \mathbf{T}_i | \tau] \langle \bar{\tau} | \mathbf{T}_j | \bar{\rho} \rangle$, in which the emitting colour flows in the amplitude and conjugate share no common colour or anti colour lines contribute for processes with ≥ 4 colour flows. This corresponds to $n = 3$ for $V \rightarrow q\bar{q}$ and $n \geq 2$ for $H \rightarrow gg$ and so we see Figure 5.6 validates the inclusion of these contributions.

Additionally, the correct description of the emission cross section ρ -dependence, by `CVolver` in Figure 5.6, provides a good verification of the scale sampling density and the competition algorithm that implements it (discussed in Section 4.5.2).

5.2.2 Angular Correlations

In this section we continue our validation of `CVolver` components related to real emissions. Specifically, we shall examine the direction sampling outlined in Section 4.5.4 and the $1/N_c$ breakdown of the emission matrix elements, by focusing on the emission cross section.

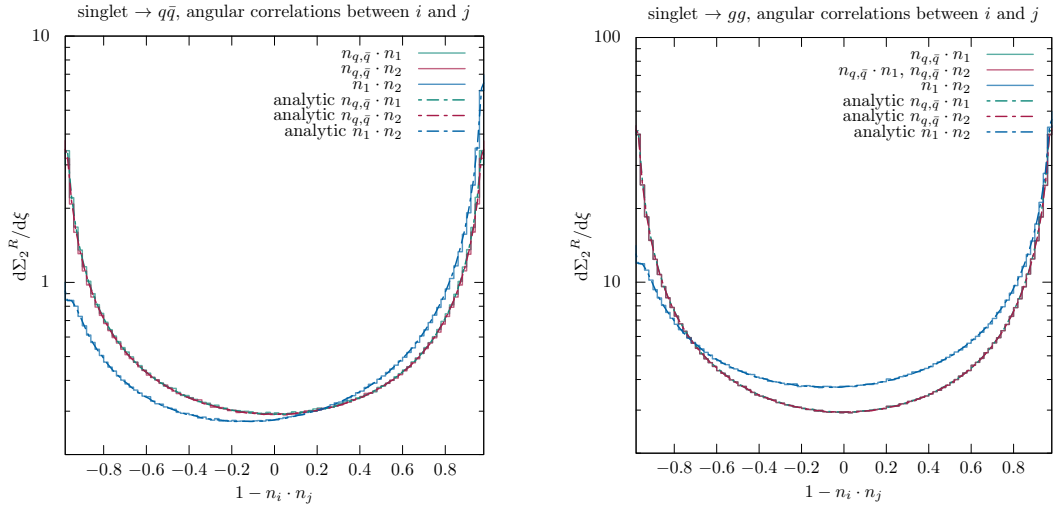
To remind the reader, generating emission directions in Variant B involves the inverse transform sampling of the eikonal factor

$$\omega_{ij}(k) = \frac{n_i \cdot n_j}{(n_i \cdot n_k + n_j \cdot n_k)} \left(\frac{\Theta(n_i \cdot n_k - \lambda)}{n_i \cdot n_k} + \frac{\Theta(n_j \cdot n_k - \lambda)}{n_j \cdot n_k} \right), \quad (5.34)$$

where the factor includes the cutoff prescription stated in Eq. 4.90, i.e. that $n_{i,j} \cdot n > \lambda$ for emission off the ij pair. This sampling is carried out in the ij zero-momentum frame and the resulting parton momenta are subsequently boosted back into the lab-frame. In inverting the normalised PDF, $\omega_{ij}(k) / \int \omega_{ij}(k)$, two approximations are made: to discard terms suppressed by powers of the cutoff λ and to approximate the bounds of integration over $\cos \theta_k$ in the small- λ limit.

In order to visualise the distribution of generated directions, we focus on the angular correlations between partons, $n_i \cdot n_j$. For each distinct pair of partons i and j in an event, we book the event-weight (corresponding to the integrand of $\Sigma_n^R(\rho)$) into the bin representing the value of $\xi = 1 - n_i \cdot n_j$. This corresponds to the distribution $d\Sigma_n^R(\rho) / d\xi$. So that we can test the employed direction sampling across the full angular phase-space, we remove the restriction of the jet veto measurement function. The collinear cutoff is of course intrinsically implemented in our sampling method and so is retained.

Figure 5.7 shows the angular correlation distributions for the two emission cross section. It compares the resultant angular correlations between partons i and j in `CVolver` (solid histograms) to those produced by an independent test code, `AngularCorrelations` (dashed curves, labelled ‘analytic’). This code performs a Crude Monte Carlo integration of the emission cross section over



(A) Angular correlations between particles i and j for the process $V \rightarrow q\bar{q}$. (B) Angular correlations between particles i and j for the process $H \rightarrow gg$.

FIGURE 5.7: The inclusive emission cross section as a function of the angular correlation between particles i and j , $\xi = 1 - n_i \cdot n_j$, for $V \rightarrow q\bar{q}$ and $H \rightarrow gg$. This cross section corresponds to a gluon multiplicity of two. The stepped results pertain to those generated with `CVolver`, whilst the broken lines to the independent test code `AngularCorrelations`. The legend specifies which $\xi = 1 - n_i \cdot n_j$ each coloured curve corresponds to.

the full angular phase space. Specifically, it calculates

$$A_2^R = \int \frac{d\Omega_2}{4\pi} \int \frac{d\Omega_1}{4\pi} \text{Tr}(\mathbf{D}_2^v \mathbf{D}_1^\mu \mathbf{H} \mathbf{D}_{1\mu}^\dagger \mathbf{D}_{2\nu}^\dagger \mathbf{S}_2), \quad (5.35)$$

where the form of the trace over operators depends on the hard process. In the case of $V \rightarrow q\bar{q}$,

$$\begin{aligned} \text{Tr}(\mathbf{D}_2^v \mathbf{D}_1^\mu \mathbf{H}_{q\bar{q}} \mathbf{D}_{1\mu}^\dagger \mathbf{D}_{2\nu}^\dagger \mathbf{S}_2) &= \left(\frac{\alpha_s}{\pi}\right)^2 \left(\frac{N_c^2 - 1}{N_c}\right) \omega_{q\bar{q}}(n_1) \\ &\times \left(N_c^2 (\omega_{q1}(n_2) + \omega_{\bar{q}1}(n_2)) - \omega_{q\bar{q}}(n_2)\right), \end{aligned} \quad (5.36)$$

and the eikonal factors include the cutoff prescription as written in Eq. 4.90 (in the lab-frame). The four momenta, n_i , of each emission is fully determined by $\cos\theta_i$ and ϕ_i , which are sampled uniformly over the domains $[-1, 1]$ and $[0, 2\pi]$ respectively. The same procedure is carried out for the $H \rightarrow gg$ process,

but with the trace over operators equal to

$$\begin{aligned} \text{Tr}(\mathbf{D}_2^\nu \mathbf{D}_1^\mu \mathbf{H}_{gg} \mathbf{D}_{1\mu}^\dagger \mathbf{D}_{2\nu}^\dagger \mathbf{S}_2) &= \left(\frac{\alpha_s}{\pi}\right)^2 2N_c^2 (N_c^2 - 1) \omega_{gg}(n_1) \\ &\times (\omega_{gg}(n_2) + \omega_{g1}(n_2) + \omega_{g1}(n_2)). \end{aligned} \quad (5.37)$$

We have distinguished between the object calculated by **AngularCorrelations**, A_2^R , and that calculated by **CVolver**, $\Sigma_2^R(\rho)$. This is because there is no sampling of emission energy scales in **AngularCorrelations**. However, as the angular correlations between partons are uncorrelated with the emission energy, the lack of such a sampling simply manifests itself as a difference in normalisation.

After normalising the results of **AngularCorrelations**, we find agreement between these and the distributions produced by **CVolver** for both processes $V \rightarrow q\bar{q}$ and $H \rightarrow gg$ in Figure 5.7, in the central portion of the distributions. Across the central portion ($-0.6 < \xi < 0.6$), the distributions are within 1.2% of each other for both a $q\bar{q}$ and gg final state. Outside of this region the distributions are within 3.5% for $V \rightarrow q\bar{q}$ process and within 3% for $H \rightarrow gg$.

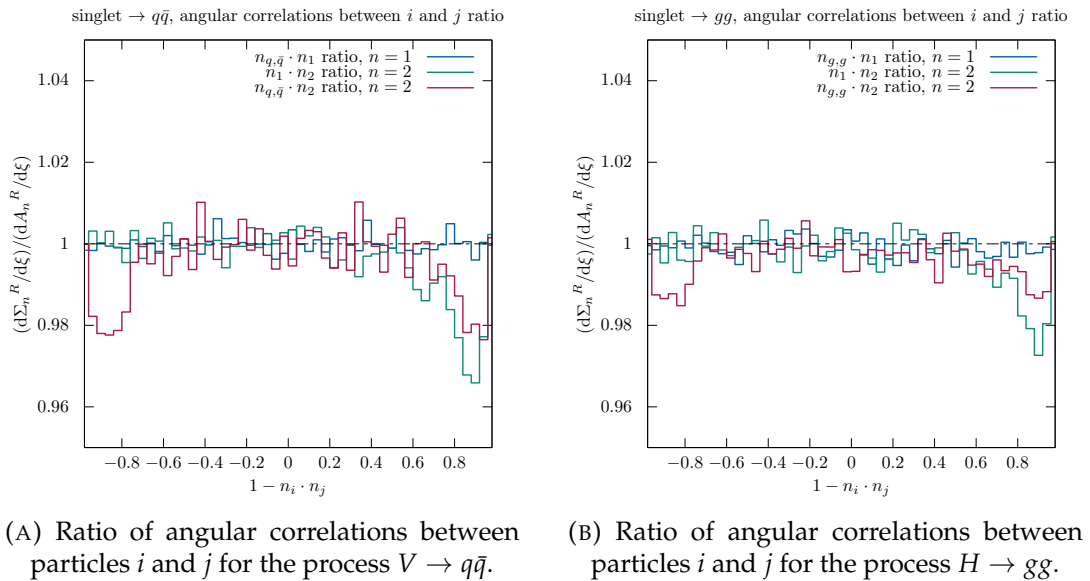


FIGURE 5.8: The ratio of inclusive cross sections between **CVolver** and **AngularCorrelations** as a function of the angular correlation between particles i and j , for $V \rightarrow q\bar{q}$ in (A) and $H \rightarrow gg$ in (B). This ratio corresponds to gluon multiplicities $n = 1, 2$. The black dashed line is for reference and takes a value of unity.

Figure 5.8 shows the ratio between the **CVolver** and **AngularCorrelations** distributions. It illustrates the angular correlation distributions for the $V \rightarrow q\bar{q}$ and $H \rightarrow gg$ processes for the gluon multiplicities $n = 1, 2$. In the case of

the one-emission cross sections, we see that this ratio fluctuates about unity, showing agreement between **CVolver** and **AngularCorrelations**. For the $V \rightarrow q\bar{q}$ emission cross sections above $n \geq 1$ however, we find that the angular correlations involving emissions beyond the first, deviate from unity as we approach values of $\zeta = -1$ and 1. These differences also exist in the angular correlation distributions for the $H \rightarrow gg$ process, although they are smaller. For both processes, these differences increase in magnitude for higher-emission cross sections. It is the case that **CVolver** and **AngularCorrelations** adopt slightly different cutoff prescriptions: **CVolver** applies Eq. 5.34 in the dipole-frame of the parent partons selected by the competition algorithm, whereas **AngularCorrelations** applies Eq. 5.34 in the lab-frame. However, one would expect any disparity between these regimes to be small, and Figure 5.8 points to an issue with our direction sampling method. One possible problem could be in the validity of the series expansion, in terms of the collinear cutoff λ , used in Eq. 4.118. To remind the reader, we sample the polar direction of each emission according to Eq. 5.34, after azimuthal averaging in the zero-momentum frame of its parents i and j . Inverse transform sampling requires that we are able to integrate and invert Eq. 5.34 over all values of the polar angle; we identified the valid regions of integration in Section 4.5.4, which we denoted c_1 , c^+ and c^- . Importantly, we noted that $c^\pm \simeq c_1$ in the limit that λ/n_{ij} is small, which allowed us to invert the integral. However, by the nature of the collinear cutoff, with a sufficient number of emissions there will be regions of angular phase-space where n_{ij} can approach λ , which could invalidate the integral-limit approximation. This is currently speculative and requires a more in-depth analysis.

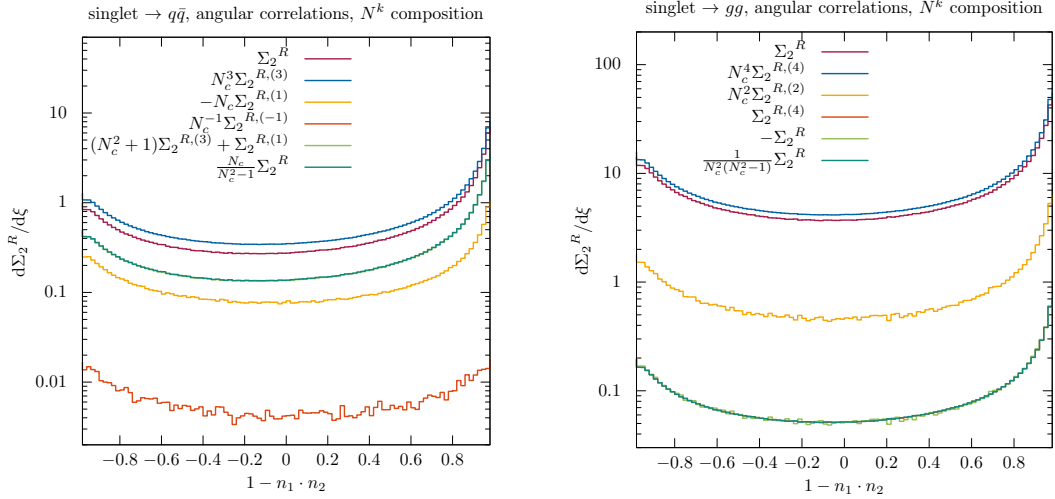
Despite the direction sampling issue, the angular correlation distributions in **CVolver** grant us an opportunity to test the $1/N_c$ breakdown of the emission matrix elements. We see from the colour factors in Eq. 5.35, that the N_c^k contributions to the angular correlation distributions produced by **CVolver** should be related by

$$\frac{N_c}{N_c^2 - 1} \sum_{k=-1}^3 N_c^k \Sigma_{q\bar{q},2}^{R,(k)} = \Sigma_{q\bar{q},2}^{R,(3)} + N_c^2 \Sigma_{q\bar{q},2}^{R,(3)} + \Sigma_{q\bar{q},2}^{R,(1)}, \quad (5.38)$$

for the $V \rightarrow q\bar{q}$ process. Similarly, in the case of $H \rightarrow gg$, the angular correla-

tion distributions should obey the relation

$$\frac{1}{N_c^2(N_c^2 - 1)} \sum_{k=2}^4 N_c^k \Sigma_{gg,2}^{R,(k)} = \Sigma_{gg,2}^{R,(4)} = -\Sigma_{gg,2}^{R,(2)}. \quad (5.39)$$



(A) Angular correlation between the two gluon emissions, for the process singlet $\rightarrow q\bar{q}$.

(B) Angular correlation between the two gluon emissions, for the process singlet $\rightarrow gg$.

FIGURE 5.9: The inclusive emission cross section as a function of the angular correlation between two gluon emissions, for the processes $V \rightarrow q\bar{q}$ and $H \rightarrow gg$. Also shown are the individual contributions at each order of N_c^k . A check on these contributions is illustrated, as described in the text.

Figure 5.9 shows the breakdown of the angular correlation distributions in terms of the powers of N_c^k that contribute. This is illustrated for both the $V \rightarrow q\bar{q}$ and $H \rightarrow gg$ process in Figure 5.9a and 5.9b respectively. In the former, there is agreement between the light-green and dark-green curves which shows that the relation in Eq. 5.38 holds. Similarly, there is agreement between the light-green, dark-green and red curves in Figure 5.9b which respects Eq. 5.39. This observation acts as a further check on the correctness of the emission matrix element calculation, basis tensor sampling of these elements and the handling of the emission colour mechanics.

5.2.3 N_c Dependence

We have so far presented results pertaining to the components of `CVolver` related to emissions. In this section, we build on this to provide an initial validation of the fully-inclusive cross section, including both emission and virtual

operators, up to three emissions.

To do this we use artificially chosen values for the colour charge and colour charge product coefficients in the emission and virtual operators. This removes the need for a direction sampling method and the density, $\omega_{ij}d\Omega_k/\Omega_{ij}$ (in Eq. 4.93), is equal to unity. Specifically, the anomalous dimension matrix coefficients used in the Sudakov operator exponents, Γ_{ij} , and those used in the competition algorithm, Ω_{ij} , are ascribed constant predetermined values in the range 0.01 to 0.1 for each i, j pair. Importantly, the energy dependence in Γ_{ij} is left untouched. These coefficients take the form,

$$\begin{aligned}\Gamma_{ij}^k &= \frac{1}{2} \ln \left(\frac{E'}{E} \right) C_{ij}^{\Gamma,k}, \\ \Omega_{ij}^k &= \frac{1}{2} C_{ij}^{\Omega,k},\end{aligned}\tag{5.40}$$

where $C_{ij}^{\Gamma,k}$ and $C_{ij}^{\Omega,k}$ are the aforementioned fixed values and we have included the index k to denote the multiplicity context in which they appear. In the normal running of **CVolver**, these coefficients are related according to

$$\Gamma_{ij} = \ln \left(\frac{E'}{E} \right) \Omega_{ij}.\tag{5.41}$$

However, for the purposes of this cross-check they are given values independent of each other. The coefficients Ω_{ij} can then be equivalently viewed as the coefficients of the emission operators, ω_{ij} , i.e. the eikonal factors. In addition, the nature of evolving soft gluons dictates that these coefficients remain unchanged if we swap the indices $i \leftrightarrow j$. As a more robust test of **CVolver**, we assign different fixed values to all coefficients under this interchange of indices (as might be necessary for the future inclusion of recoil effects or contributions along the lines of dipole subtraction terms).

The specification of the coefficients $C_{ij}^{\Gamma,k}$ and $C_{ij}^{\Omega,k}$ as fixed values essentially predetermines a single point in angular phase-space for each emission, although these points differ for the same emission between $C_{ij}^{\Gamma,k}$ and $C_{ij}^{\Omega,k}$. As such, we can regard our cutoff prescription as having been absorbed into the coefficient values. This also means that there is no notion of any angular region in which the veto is enforced and no restriction on emission angles. Table 5.2 specifies the coefficients used to produce the results in Figures 5.10 and 5.11.

Figure 5.10 presents cross section values generated using **CVolver** at a fixed

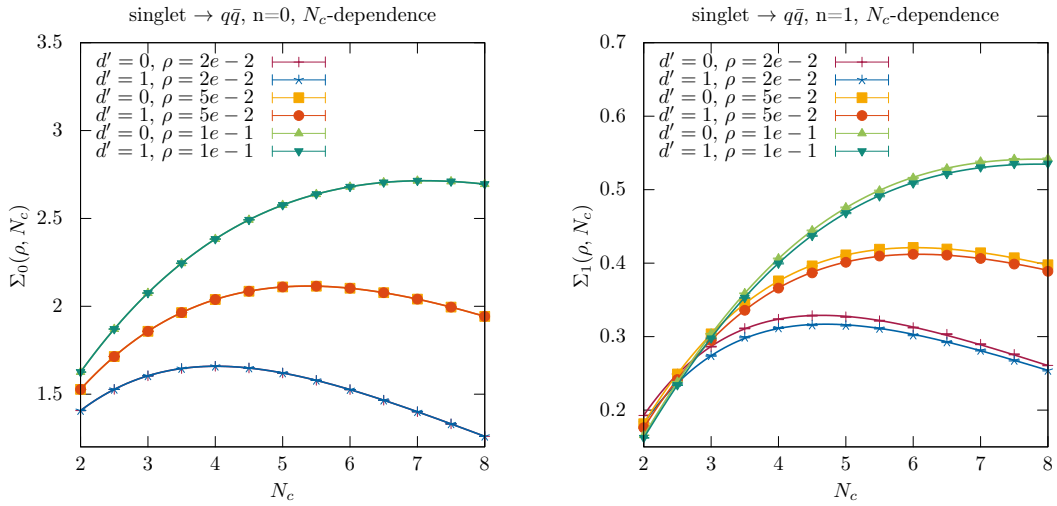
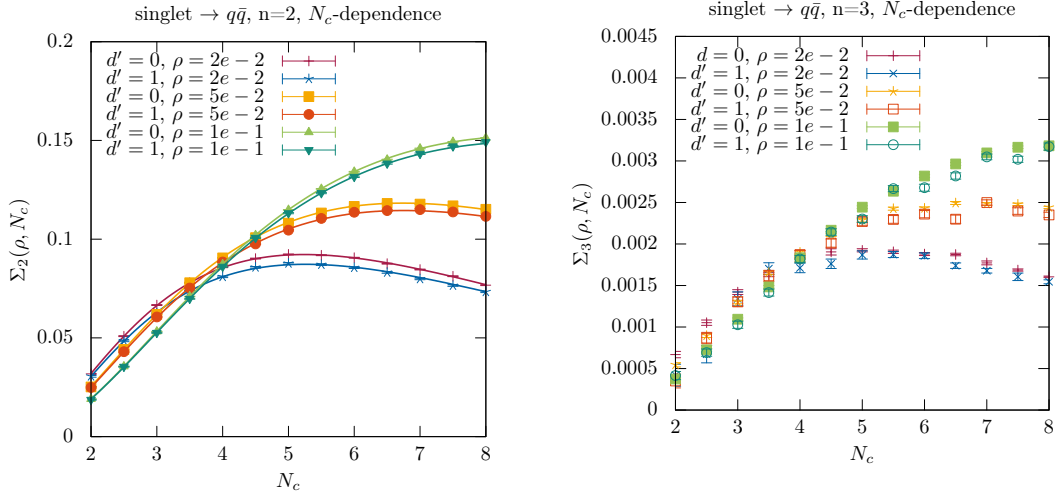
(A) Inclusive cross section in the case of zero emissions, for the process $\text{singlet} \rightarrow q\bar{q}$.(B) Inclusive cross section in the case of one emission, for the process $\text{singlet} \rightarrow q\bar{q}$.(C) Inclusive cross section in the case of two emissions, for the process $\text{singlet} \rightarrow q\bar{q}$.(D) Inclusive cross section in the case of three emissions, for the process $\text{singlet} \rightarrow q\bar{q}$.

FIGURE 5.10: The inclusive cross section for the process $V \rightarrow q\bar{q}$ as a function of the veto scale, ρ , colour order, d and the number of QCD colours, N_c . Gluon multiplicities are presented upto three emissions ($n = 0, 1, 2, 3$). The coefficients of the colour operators (see the text for more detail) in both the Sudakov and emission operators have been fixed to numerical values at the same order of magnitude. The plot marks denote the result generated using **CVoLver** whilst the unbroken curves correspond to the analytic result.

evolution cutoff scale, ρ , and Sudakov operators calculated in the $N^d\text{LC}'_V$ approximation, as a function of the number of QCD colours, N_c . These results depict the cross section values for the hard process, $V \rightarrow q\bar{q}$, for gluon multiplicities upto three emissions ($n = 0, 1, 2, 3$). They are illustrated as points

along with their corresponding errors.

Virtual ($k = 0, 1$)				Virtual ($k = 2$)				Emission			
i	j	k	$C_{ij}^{\Gamma,k}$	i	j	k	$C_{ij}^{\Gamma,k}$	i	j	k	$C_{ij}^{\Omega,k}$
a	b	0	0.13	a	b	2	0.1	a	b	1	0.04
b	a	0	0.11	a	1	2	0.18	b	a	1	0.03
a	b	1	0.12	a	2	2	0.13	a	b	2	0.02
a	1	1	0.15	b	a	2	0.2	a	1	2	0.07
b	a	1	0.16	b	1	2	0.15	b	a	2	0.06
b	1	1	0.14	b	2	2	0.17	b	1	2	0.08
1	a	1	0.18	1	a	2	0.18	1	a	2	0.09
1	b	1	0.17	1	b	2	0.12	1	b	2	0.01
				1	2	2	0.16				
				2	a	2	0.2				
				2	a	2	0.12				
				2	1	2	0.15				

TABLE 5.2: The fixed values of the kinematic and physical-constant coefficients (see the text for details). The variables i and j denote particle numbers, whilst k specifies the multiplicity at which the coefficients are used. Labels a and b denote the primary partons in the processes $V \rightarrow q\bar{q}$ and $H \rightarrow gg$.

The aforementioned simplifications to the anomalous dimension matrix and competition algorithm coefficients enable one to carry out analytic calculations upto two emissions. We begin by writing the NLC $'_V$ Sudakov matrix element in Eq. 4.28 as

$$|\tau| \mathbf{V} |\sigma\rangle = \delta_{\tau\sigma} e^{-N_c \Gamma'_\sigma} - \zeta \frac{1}{N_c} \Sigma_{\tau\sigma} R(\{\tau, \sigma\}), \quad (5.42)$$

where we have parameterised the subleading-colour correction with the variable ζ . This acts as a switch between the treatment of Sudakov operators in the LC $'_V$ and NLC $'_V$ approximation. Using the coefficient values in Table 5.2, we can write the zero emission cross section for $q\bar{q}$ production using the LC $'_V$ and NLC $'_V$ approximation, as

$$\Sigma_{q\bar{q},0}(\rho, N_c) \Big|_{\zeta=0} = \Sigma_{q\bar{q},0}(\rho, N_c) \Big|_{\zeta=1} = N_c \rho^{\frac{3(N_c^2-1)}{50N_c}}, \quad (5.43)$$

where we have left the veto scale and the number of QCD colours explicit. The

one emission cross section is

$$\begin{aligned} \Sigma_{q\bar{q},1}(\rho, N_c)|_{\zeta=0} &= \frac{9}{8}N_c\rho^{\frac{N_c^2-1}{10N_c}} \left(\frac{8\rho^{\frac{9N_c}{100}}}{13N_c^2-4} + \frac{2N_c^2\rho^{\frac{9N_c}{50}}}{2-11N_c^2} \right. \\ &\quad \left. + \left(\frac{2N_c^2}{11N_c^2-2} + \frac{8}{4-13N_c^2} + \frac{1}{N_c^2-1} \right) \rho^{-\frac{N_c^2-1}{25N_c}} \right. \\ &\quad \left. + \frac{1}{1-N_c^2} \right) \\ \Sigma_{q\bar{q},1}(\rho, N_c)|_{\zeta=1} &= \frac{9N_c(N_c^2-1)\rho^{\frac{3N_c^2-5}{50N_c}} \left(\rho^{\frac{1}{25N_c}} - \rho^{\frac{11N_c}{50}} \right)}{4(11N_c^2-2)}. \end{aligned} \quad (5.44)$$

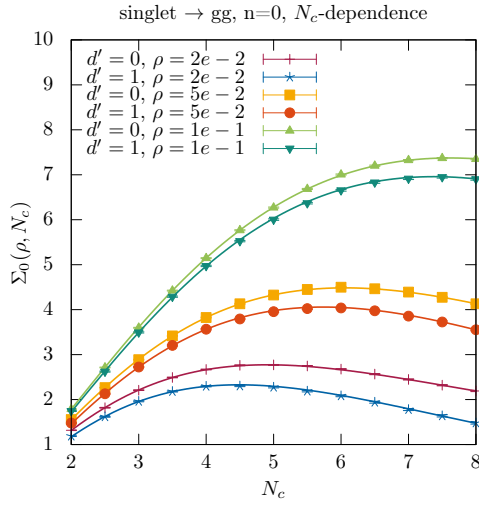
We do not present the two emission cross section here for the sake of readability. Eq. 5.43 and 5.44 and the analytic results for $\Sigma_2(\rho, N_c)$ at both $\zeta = 0, 1$ are presented in Figure 5.10 by unbroken curves, alongside the **CVolVer** results of the same colour.

Figures 5.10a, 5.10b and 5.10c exhibit good agreement between the analytic and **CVolVer** results. In particular, the **CVolVer** numerical results agree with the analytic curves to within 0.0001%, 0.15% and 0.2% for $n = 0, 1$ and 2 respectively. Their ratio is consistent with unity to within one standard deviation for all values of ρ and N_c . The $n = 3$ analytic results have not been calculated and as such are not presented. It is worth noting that the ratio between the $d' = 0$ and $d' = 1$ results for $n = 3$, at any given ρ are within 3%, indicating the size of the NLC'_V contributions.

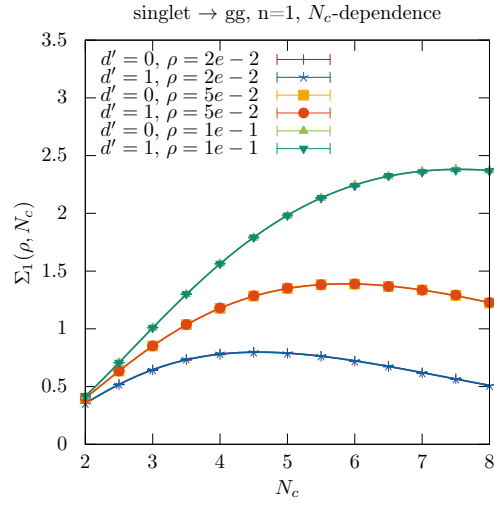
The close agreement between these results provides validation on a number of components within **CVolVer**. It supplements the results of Section 5.2.1, to confirm the correct sampling of emission matrix element basis tensors. Additionally, the correct ρ -dependence and accurate description of the emission operator eikonal factors verifies the competition algorithm implementation. As an initial test of the inclusion of Sudakov operators in Variant B, Figure 5.10 corroborates the findings of Section 5.1.5. That is, the method for sampling Sudakov matrix elements shared between Variant A and B, correctly chooses basis tensors in an unbiased way. Our results also provide additional confirmation on the correctness of the Sudakov matrix element approximation. Figure 5.10 also nicely showcases the ability of **CVolVer** to handle any number of QCD colours, N_c .

In order to further substantiate the findings of Figure 5.10, we present analogous results for the process $H \rightarrow gg$ in Figure 5.11, which makes use of the

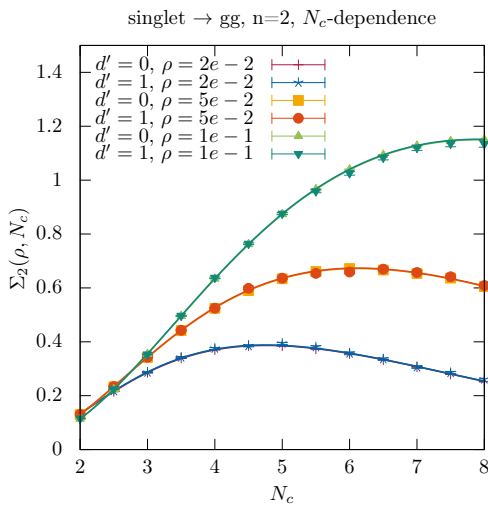
same coefficients depicted in Table 5.2.



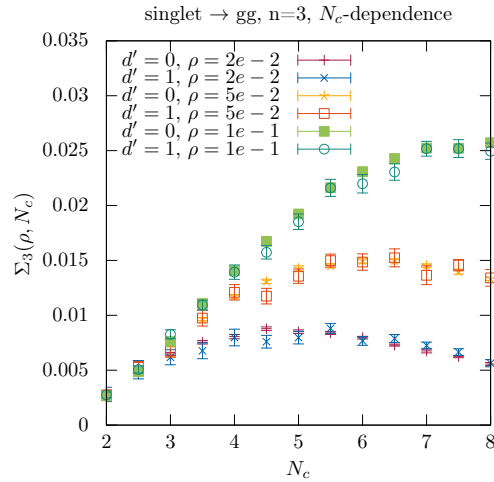
(A) Inclusive cross section in the case of zero emissions, for the process $\text{singlet} \rightarrow gg$.



(B) Inclusive cross section in the case of one emission, for the process $\text{singlet} \rightarrow gg$.



(C) Inclusive cross section in the case of two emissions, for the process $\text{singlet} \rightarrow gg$.



(D) Inclusive cross section in the case of three emissions, for the process $\text{singlet} \rightarrow gg$.

FIGURE 5.11: The inclusive cross section for the process $H \rightarrow gg$ as a function of the veto scale, ρ , colour order, d and the number of QCD colours, N_c . Gluon multiplicities are presented upto three emissions ($n = 0, 1, 2, 3$). The kinematic coefficients of the colour operators in both the Sudakov and emission operators have fixed numerical values at the same order of magnitude. The plot marks denote the result generated using `CVolver` whilst the unbroken curves correspond to the analytic result. Note that the overlap between the $d' = 0$ and $d' = 1$ results, for multiplicities $n \geq 1$, is a coincidence of the chosen kinematic coefficients.

The analytic cross sections for $\Sigma_{gg,0}(\rho, N_c)$ using the $H \rightarrow gg$ hard process in

the LC_V and NLC'_V approximation, are

$$\begin{aligned}\Sigma_{gg,0}|_{\zeta=0} &= N_c^2 \rho^{\frac{3N_c}{25}} - 2\rho^{\frac{3N_c}{50}} + 1 \\ \Sigma_{gg,0}|_{\zeta=1} &= (N_c^2 - 1) \rho^{\frac{3N_c}{25}},\end{aligned}\quad (5.45)$$

whilst those for $\Sigma_{gg,1}(\rho, N_c)$ and $\Sigma_{gg,2}(\rho, N_c)$ can be computed, as

$$\begin{aligned}\Sigma_{gg,1}|_{\zeta=0} &= -\frac{9}{26} (N_c^2 - 1) \rho^{\frac{3N_c}{25}} \left(\rho^{\frac{13N_c}{50}} - 1 \right) \\ \Sigma_{gg,1}|_{\zeta=1} &= -\frac{9N_c (N_c^2 - 1) \rho^{\frac{3N_c^2-5}{50N_c}} \left(\rho^{\frac{11N_c}{50}} - \rho^{\frac{1}{25N_c}} \right)}{4(11N_c^2 - 2)},\end{aligned}\quad (5.46)$$

and

$$\begin{aligned}\Sigma_{gg,2}|_{\zeta=0} &= -\frac{1}{146466320} \rho^{\frac{3N_c}{25}} \left(10974 \left(15169N_c^2 - 8711 \right) \rho^{\frac{13N_c}{50}} \right. \\ &\quad - 58848075 \left(N_c^2 + 1 \right) \rho^{\frac{7N_c}{25}} - 51026976 \left(N_c^2 + 1 \right) \rho^{\frac{31N_c}{100}} \\ &\quad - 31385640 \left(N_c^2 + 1 \right) \rho^{\frac{7N_c}{20}} + 55 \left(452899 - 458253N_c^2 \right) \\ &\quad \left. + 25534080 \rho^{\frac{59N_c}{200}} + 60869120 \rho^{\frac{63N_c}{200}} + 125542560 \rho^{\frac{33N_c}{100}} \right).\end{aligned}\quad (5.47)$$

The calculation of $\Sigma_{gg,2}$ at $\zeta = 1$ is not presented here for the sake of readability.

The numerical results from **CVolver** again show good agreement with the analytic results of Eq. 5.45, 5.46 and 5.47. Results in Figure 5.11a and Figure 5.11b agree to within 0.15%. In both cases, the ratio between the analytic and numerical results are consistent with unity to within one standard deviation. The $n = 2$ results agree to within 1% and their ratio is consistent with unity to within 1.5 standard deviations. In the case of $n = 3$, the $d' = 0$ and $d' = 1$ results are again within 3% for all values of ρ and N_c . The same validation conclusions can be drawn from Figure 5.11a. Indeed, the case of $H \rightarrow gg$ has an additional colour flow at each multiplicity (i.e. after two emissions there are 24 possible basis tensors as opposed to the 6 in the case of $V \rightarrow q\bar{q}$). The $H \rightarrow gg$ process therefore provides an even stronger validation of the Sudakov basis tensor sampling.

Results analogous to those in Figures 5.10 and 5.11, using different sets of $C_{ij}^{\Gamma,k}$ and $C_{ij}^{\Omega,k}$ coefficients, have been produced. In particular, coefficient sets in which $C_{ij}^{\Gamma,k}$ and $C_{ij}^{\Omega,k}$ differ by orders of magnitude have been tested and similarly good agreement is found between analytic and numerical results up

to two emissions.

5.2.4 Fixed Order Validation

Similarly to Section 5.1.5, we now present results of the jet veto cross section generated by Variant B upto two emissions, providing a comparison with an independent numerical implementation, **FixedOrderB**.

FixedOrderB implements the $V \rightarrow q\bar{q}$ calculation presented in Section 5.1.1. It differs from **FixedOrderA** by the collinear cutoff prescription used - **FixedOrderB** adopts the one stated in Eq. 4.90. For the eikonal factors resulting from the emission operators, **FixedOrderB** uses

$$\omega_{ij}(k) = \frac{n_i \cdot n_j}{(n_i \cdot n_k + n_j \cdot n_k)} \left(\frac{\Theta(n_i \cdot n_k - \lambda)}{n_i \cdot n_k} + \frac{\Theta(n_j \cdot n_k - \lambda)}{n_j \cdot n_k} \right). \quad (5.48)$$

The integration over solid angle of the kinematic terms in the Sudakov exponent produces the same result for both Variant A and Variant B cutoff prescriptions, if we disregard terms suppressed by powers of λ . Thus, the $\Sigma_0(\rho)$ cross section for the $V \rightarrow q\bar{q}$ process is exactly the same for both cutoff prescriptions, whilst the $\Sigma_1(\rho)$ cross sections are within 0.2% of each other across the ρ range 10^{-3} to 1 when $\lambda = 10^{-3}$. Beyond one-emission, the jet veto cross sections produced by **FixedOrderA** and **FixedOrderB** have much larger differences, reaching 15% for $\Sigma_2(\rho)$ in the range of ρ values between 10^{-3} and 1 with $\lambda = 10^{-2}$. For a smaller cutoff, $\lambda = 10^{-3}$, this difference reduces to a maximum of 10%.

FixedOrderB also calculates the jet veto cross section for the $H \rightarrow gg$ process upto two emissions. To not get too embroiled in calculational details, we shall not present the explicit matrix forms for all of the colour charge operators in the colour flow basis. We simply note that at a given multiplicity, n , these matrices are $(n+2)!$ dimensional compared to those in the corresponding $V \rightarrow q\bar{q}$ calculation, which are $(n+1)!$ dimensional (as the initial gg process has an extra colour flow relative to $q\bar{q}$). An example of this can be seen with the $\mathbf{T}_q^1 \cdot \mathbf{T}_{\bar{q}}^1$

and $\mathbf{T}_{g_1}^1 \cdot \mathbf{T}_{g_2}^1$ colour charge products:

$$\mathbf{T}_q^1 \cdot \mathbf{T}_{\bar{q}}^1 = \begin{pmatrix} -\frac{N_c^2-1}{2N_c} & -\frac{1}{2} \\ 0 & \frac{1}{2N_c} \end{pmatrix}, \quad \mathbf{T}_{g_1}^1 \cdot \mathbf{T}_{g_2}^1 = \begin{pmatrix} 0 & 0 & 1 & 0 & 0 & 0 \\ 0 & 0 & 0 & \frac{1}{2} & \frac{1}{2} & 0 \\ 0 & 0 & -N_c & -\frac{1}{2} & -\frac{1}{2} & 0 \\ 0 & 0 & 0 & -\frac{N_c}{2} & 0 & 0 \\ 0 & 0 & 0 & 0 & -\frac{N_c}{2} & 0 \\ 0 & 0 & 0 & \frac{1}{2} & \frac{1}{2} & 0 \end{pmatrix}. \quad (5.49)$$

The zero-emission cross section is

$$\Sigma_{gg,0}(\rho) = 2C_A C_F \exp\left(-\frac{2\alpha_s}{\pi} \ln\left(\frac{1}{\rho}\right) C_A \ln\left(\frac{2}{\lambda}\right)\right), \quad (5.50)$$

while the one-emission cross section is

$$\begin{aligned} \Sigma_{gg,1}(\rho) &= 4C_A^2 C_F \frac{\alpha_s}{\pi} \int_{\rho}^1 \frac{dE_1}{E_1} \int_{\text{out}} \frac{d\cos\theta_1}{2} \omega_{g_1 g_2}(n_1) \\ &\times \exp\left[-\frac{2\alpha_s}{\pi} C_A \ln\left(\frac{1}{E_1}\right) \ln\left(\frac{2}{\lambda}\right)\right] \\ &\times \exp\left[-\frac{\alpha_s}{\pi} C_A \ln\left(\frac{E_1}{\rho}\right) \left(\ln\left(\frac{2}{\lambda}\right) - \ln\left(\frac{\lambda^2}{1 - \cos^2\theta_1}\right)\right)\right], \quad (5.51) \end{aligned}$$

where g_1 and g_2 denote the two primary gluons. The cross sections presented here adopt the parton momenta written in Eq. 5.3, with the parton labels g_1 and g_2 taking the place of q and \bar{q} . The two-emission cross section can be written as

$$\begin{aligned} \Sigma_{gg,2}(\rho) &= \left(\frac{\alpha_s}{\pi}\right)^2 \int_{\rho}^1 \frac{dE_1}{E_1} \int_{\text{out}} \frac{d\Omega_1}{4\pi} \int_{\rho}^{E_1} \frac{dE_2}{E_2} \int_{\text{out}} \frac{d\Omega_2}{4\pi} \\ &\text{Tr}(\mathbf{V}_{\rho,E_2} \mathbf{D}_2^{\nu} \mathbf{D}_1^{\mu} \mathbf{D}_{1\mu}^{\dagger} \mathbf{D}_{2\nu}^{\dagger} \mathbf{V}_{\rho,E_2}^{\dagger} \mathbf{S}_2) \\ &\times \exp\left[-\frac{2\alpha_s}{\pi} C_A \ln\left(\frac{1}{E_1}\right) \ln\left(\frac{2}{\lambda}\right)\right] \\ &\times \exp\left[-\frac{\alpha_s}{\pi} C_A \ln\left(\frac{E_1}{E_2}\right) \left(\ln\left(\frac{2}{\lambda}\right) - \ln\left(\frac{\lambda^2}{1 - \cos^2\theta_1}\right)\right)\right], \quad (5.52) \end{aligned}$$

where we can exploit colour conservation to write

$$\begin{aligned}
\mathbf{T}_1^2 \cdot \mathbf{T}_2^2 &= \mathbf{T}_{g_1}^2 \cdot \mathbf{T}_{g_2}^2, \\
\mathbf{T}_{g_2}^2 \cdot \mathbf{T}_2^2 &= \mathbf{T}_{g_1}^2 \cdot \mathbf{T}_1^2, \\
\mathbf{T}_{g_1}^2 \cdot \mathbf{T}_2^2 &= \mathbf{T}_{g_2}^2 \cdot \mathbf{T}_1^2, \\
\mathbf{T}_{g_2}^2 \cdot \mathbf{T}_1^2 &= -C_A - \mathbf{T}_{g_1}^2 \cdot \mathbf{T}_{g_2}^2 - \mathbf{T}_{g_1}^2 \cdot \mathbf{T}_1^2,
\end{aligned} \tag{5.53}$$

which can be used to simplify the exponent of the Sudakov factor, as:

$$\begin{aligned}
\mathbf{V}_{\rho, E_2} = \exp \left[-\frac{\alpha_s}{\pi} \ln \left(\frac{E_2}{\rho} \right) \left\{ C_A \mathbf{1} \ln \left(\frac{(n_{g_1} \cdot n_2)(n_{g_2} \cdot n_3)}{\lambda^2} \right) \right. \right. \\
- \mathbf{T}_{g_1}^2 \cdot \mathbf{T}_{g_2}^2 \ln \left(\frac{2(n_1 \cdot n_2)}{(n_{g_1} \cdot n_2)(n_{g_2} \cdot n_1)} \right) \\
\left. \left. - \mathbf{T}_{g_1}^2 \cdot \mathbf{T}_1^2 \ln \left(\frac{(n_{g_1} \cdot n_1)(n_{g_2} \cdot n_2)}{(n_{g_1} \cdot n_2)(n_{g_2} \cdot n_1)} \right) \right\} \right].
\end{aligned} \tag{5.54}$$

The independent `FixedOrderB` code implements the $\Sigma_n(\rho)$ cross sections (where $n = 0, 1, 2$) for the processes $V \rightarrow q\bar{q}$ and $H \rightarrow gg$. Just as in Section 5.1.1, it utilises the `GSL` implementation of the `VEGAS` Monte Carlo algorithm to perform the angular and energy integrations in Eq. 5.50, 5.51 and 5.52. The evolution operators in the case of the $\Sigma_{gg,1}(\rho)$ calculation are in the same dimension as those in $\Sigma_{q\bar{q},2}(\rho)$. Despite this, the simplicity of an all-gluon final-state allows us to simplify the $\Sigma_{gg,1}(\rho)$ colour structure solely in terms of Casimir operators. However, this is not the case for the ultimate Sudakov operator in $\Sigma_{gg,2}(\rho)$ for which we again employ the numerical exponentiation methods in `Armadillo`.

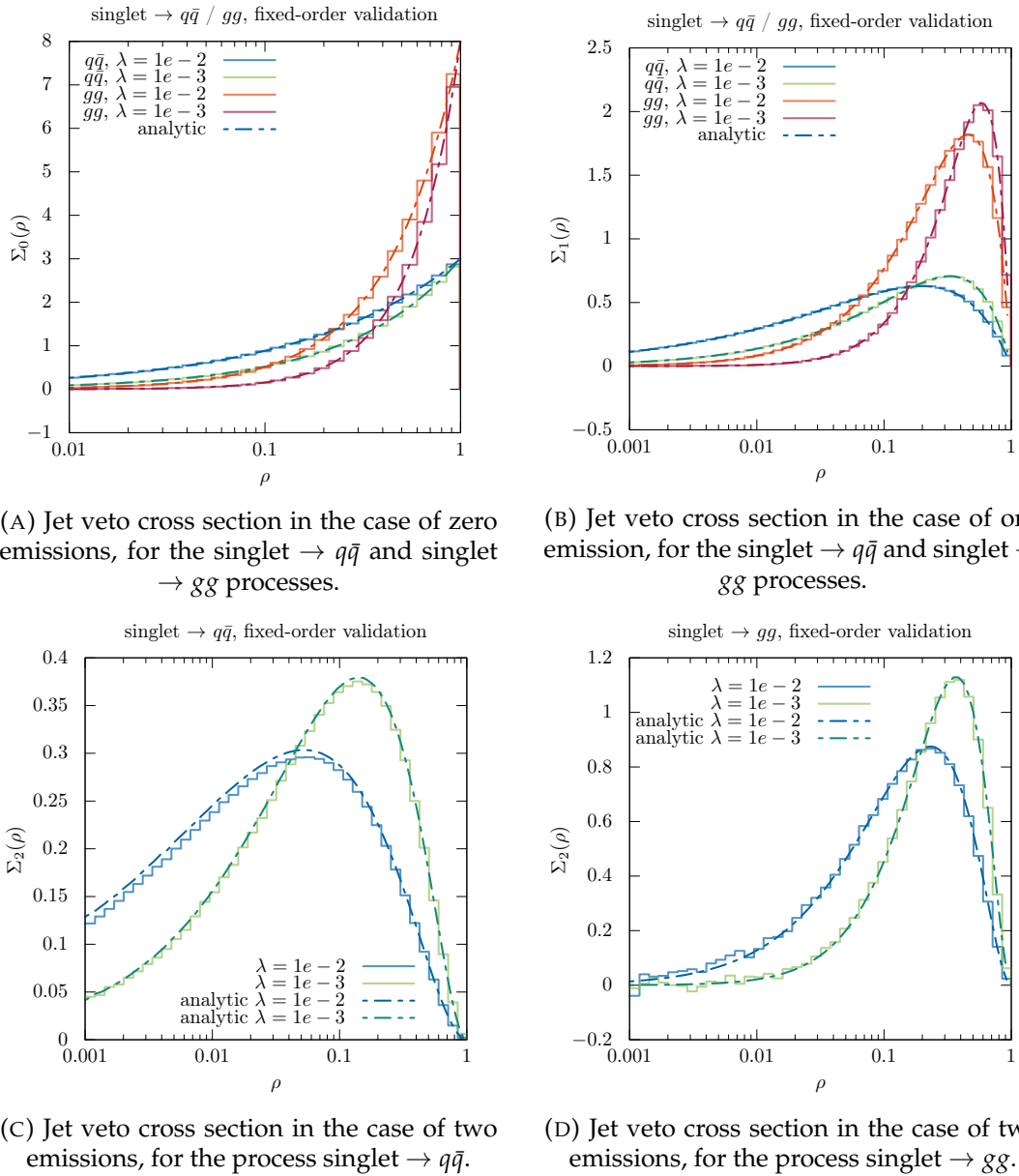


FIGURE 5.12: The jet veto cross section for the processes $V \rightarrow q\bar{q}$ and $H \rightarrow gg$. Gluon multiplicities are presented upto two emissions ($n = 0, 1, 2$). The stepped results pertain to those generated using **CVolver**, whilst the broken curves correspond to a numerical integration of the calculation in Section. 5.1.1

Figure 5.12 shows the veto cross section dependence on ρ for different gluon multiplicities up to $n = 2$. In all subfigures the stepped curves correspond to the **CVolver** results, whilst the dashed curves represent the results of **FixedOrderB** and are nomenclatured as ‘analytic’. The colour of each dashed curve is in-correspondence with the **CVolver** result of the same process and collinear cutoff. In order to capture the full-colour dependence in our **CVolver** results, we can see from the calculations in Section 5.1.1 and from Eq. 5.52 that

we must compute all Sudakov operator matrix elements to at least the NLC'_V approximation. Accordingly, all **CVoLver** results in this section are computed in the NNLC'_V approximation.

Figure 5.12a illustrates the zero-emission cross sections for the $V \rightarrow q\bar{q}$ and $H \rightarrow gg$ processes at cutoff values of $\lambda = 10^{-2}$ and 10^{-3} , presented alongside their corresponding ‘analytic’ results. The one-emission cross sections are depicted in Figure 5.12b with the same schema.

Figure 5.12a shows good agreement between the results of **CVoLver** and **FixedOrderB** for both collinear cutoff values. Indeed, the results are equal to within 0.5% for both $\lambda = 10^{-2}$ and $\lambda = 10^{-3}$ for a $q\bar{q}$ primary system and their ratios are consistent with unity to within one standard deviation. For the gg final process, we also find good agreement to within 0.5% for both cutoffs. Figure 5.12a also confirms some basic characteristics we expect of $\Sigma_0(\rho)$: namely that for a given process, both collinear cutoff values have the same value at $\rho = 1$ and that at a lower collinear cutoff the curve falls faster as ρ gets smaller. Additionally, the value of both curves tends towards 0 with smaller ρ . In particular, at $\rho = 1$ the inclusive cross sections take the values $\Sigma_{q\bar{q},0}(1) = N_c$ and $\Sigma_{gg,0}(1) = N_c^2 - 1$.

In the case of one-emission, Figure 5.12b illustrates close agreement between **CVoLver** and **FixedOrderB**. For both values of the cutoff, the $\Sigma_{q\bar{q},1}$ results agree to within 0.6% down to a ρ value of 5×10^{-3} , below which the agreement is to within 1.5%. This larger band of agreement is due to a greater sensitivity to fluctuations in the **CVoLver** results as the cross sections approach 0. Additionally, the ratio between the **CVoLver** and **FixedOrderB** results is consistent with unity to within two standard deviations across the entire range of ρ values. The $\Sigma_{gg,1}$ results agree to within 1% for $\lambda = 10^{-2}$ and 5% for $\lambda = 10^{-3}$, with their ratio being consistent with a value of 1 to within two standard deviations. The larger band of agreement for the lower cutoff value comes about due to a greater sensitivity to fluctuations in the **CVoLver** result as the cross section approaches 0. As already pointed out, this occurs at a larger value of ρ for a smaller cutoff.

Figures 5.12c and 5.12d show the two-emission cross section results of **CVoLver** and **FixedOrderB** for the processes $V \rightarrow q\bar{q}$ and $H \rightarrow gg$ respectively. They include the results for two cutoff values. We observe a discrepancy between the **CVoLver** and **FixedOrderB** results of at-most 10% for a $q\bar{q}$ final-state with a cutoff value of $\lambda = 10^{-2}$. This discrepancy reduces to 5%, above values of

$\rho = 10^{-2}$. For lower cutoff values, this difference reduces to 3%. Figure 5.12d confirms this disparity, where we find a difference between the **CVolver** and **FixedOrderB** results of at-most 4% above $\rho = 10^{-2}$ for both values of the cutoff.

This highlights an issue in the cross section results of **CVolver** Variant B, for two or more emissions. We have already provided validation (using a uniform direction sampling) in Section 5.2.1 and 5.2.3 of the emission and Sudakov operator basis tensor sampling and calculation of the corresponding matrix elements. Furthermore, the implementation of these components is shared between Variants A and B. The validation tests of Variant A performed in Sections 5.1.3, 5.1.4 and 5.1.5 further corroborate the findings of Section 5.2.1 and 5.2.3. This suggests that the discrepancy observed in Figures 5.12c and 5.12d is due to our direction sampling. Further weight can be added to this proposal with the observation of Section 5.2.2, that beyond one-emission the ratio between the angular correlation distributions of **AngularCorrelation** and **CVolver** deviates from unity. We saw in Figure 5.8b that this effect is less pronounced for the $H \rightarrow gg$ process, compared with the $V \rightarrow q\bar{q}$ process (for $n = 2$) - an observation which is mirrored in Figures 5.12c and 5.12d. Additionally, if one looks at the equivalent results to Figures 5.8a and 5.8b, but with $\lambda = 10^{-3}$, the ratio of angular correlation distributions for both the $V \rightarrow q\bar{q}$ and $H \rightarrow gg$ processes appears to fluctuate closer to unity (than for $\lambda = 10^{-2}$). Although, this is difficult to state concretely as smaller cutoff values cause greater overall fluctuations in the angular correlation distributions. Moreover, we can compare the results of **FixedOrderB** with all Sudakov operators set to the identity matrix, to the $\Sigma_{q\bar{q},2}^R(\rho)$ result generated by **CVolver**. If these results employ a uniform direction sampling across all phase-space (and we impose the collinear cutoff prescription by-hand), we find agreement between the two methods. One may ask, why then do we not adopt a simpler direction sampling in Variant B? The reason being, that Variant B was developed with the aim of minimising sampling weights. As it stands, Variant B utilises the density, $(\omega_{ij}(k)/\Omega_{ij}) d\Omega_k/4\pi$, to sample the latest emission direction, which is carried out in the ij zero-momentum frame, making the approximation that we are in the small- λ limit. If we were to sample according to a simpler density, such as that used for Variant A (where we sample uniformly in the out-gap region), we would have to introduce an additional source of weight, to include an explicit factor of $(\omega_{ij}(k)/\Omega_{ij}) d\Omega_k/4\pi$. In testing, such a factor can result in large weight fluctuations, particularly for events with a higher number of emissions. In summary, whilst we cannot firmly pin-point the issue causing

the discrepancy in Figure 5.12, there is a clear need for further investigation.

Conclusions can still be drawn from Figure 5.12 however. We find good agreement between the zero and one-emission cross sections calculated using **CVolver** and **FixedOrderB** for both of the processes $V \rightarrow q\bar{q}$ and $H \rightarrow gg$, at multiple values of the collinear cutoff. This provides a degree of validation for all components of the **CVolver** code. In addition, Figure 5.12c and Figure 5.3c present results determined using a similar number of events ($\sim 700\text{M}$). We observe fewer and less pronounced fluctuations in the curves of Figure 5.12c which indicates improved efficiency of the Variant B algorithm.

5.2.5 N_c -breakdown

Following on from the validation tests of Sections 5.2.1, 5.2.2, 5.2.3 and 5.2.4, we present the jet veto cross section for gluon multiplicities up to $n = 3$ for both processes $V \rightarrow q\bar{q}$ and $H \rightarrow gg$. We shall show results for these cross sections comparing the LC'_V , NNLC'_V approximations for $V \rightarrow q\bar{q}$ and LC_V , NNLC_V approximations for $H \rightarrow gg$, alongside their breakdown in terms of the powers of N_c that contribute. These results have been generated using **CVolver** at a cutoff of $\lambda = 10^{-2}$.

Figures 5.13a, 5.13b, 5.13c and 5.13d, show the $V \rightarrow q\bar{q}$ veto cross section for different gluon multiplicities up to $n = 3$. We include curves generated using the LC_V ($d = 0$), LC'_V ($d' = 0$) and NNLC'_V ($d' = 2$) approximations. Also shown are the individual contributions at each order of N_c^k for both the $d' = 0$ and $d' = 2$ approximations. The former are depicted as dashed-dotted curves and the latter as solid curves. The strictly leading-colour cross sections, LC_{V+R} , are also presented with a solid green curve.

We can see that for multiplicities $n \leq 1$, the $d' = 0$ result is the exact result and equal to the $d' = 2$ curve. The zero and one-emission cross section can be written schematically (see Eq. 5.8 and 5.9), as

$$\begin{aligned} \Sigma_{q\bar{q},0}(\rho) &\propto N_c \exp\left(-\left(N_c \Gamma_{q\bar{q}} - \frac{1}{N_c} \Gamma_{q\bar{q}}\right)\right), \\ \Sigma_{q\bar{q},1}(\rho) &\propto \left(N_c^2 - 1\right) \omega_{q\bar{q}}(n_1) \exp\left(-\left(N_c \Gamma_{q\bar{q}} - \frac{1}{N_c} \Gamma_{q\bar{q}}\right)\right) \\ &\quad \times \exp\left(-\left(N_c \Gamma_{q1} + N_c \Gamma_{\bar{q}1} - \frac{1}{N_c} \Gamma_{q\bar{q}}\right)\right), \end{aligned} \quad (5.55)$$

to highlight their colour structures. From this we can straightforwardly see

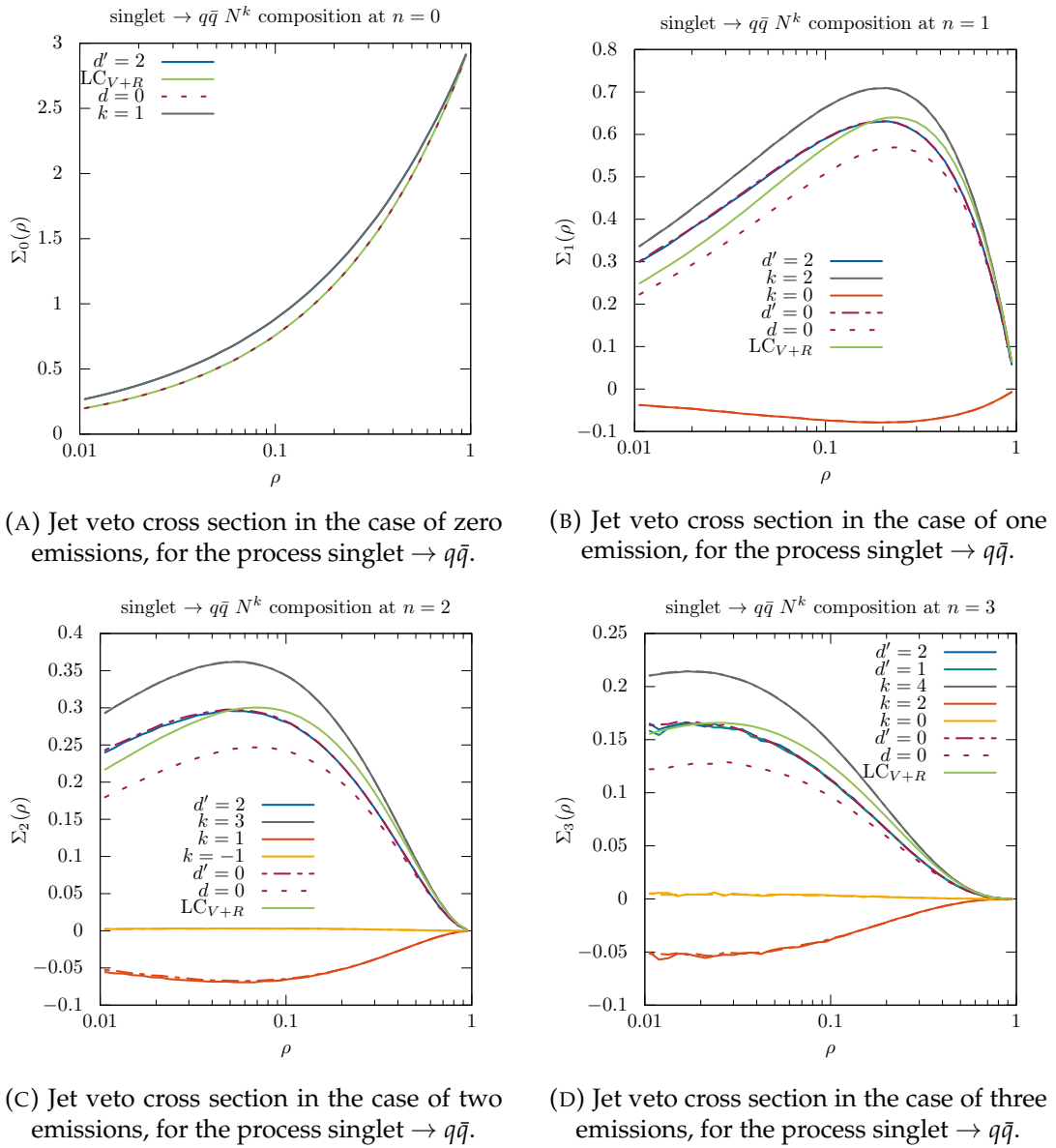


FIGURE 5.13: The jet veto cross section in $V \rightarrow q\bar{q}$ for different gluon multiplicities ($n = 0, 1, 2$ and 3). Also shown are the individual contributions at each order of N_c^k for $d = 0$ and $d' = 0, 2$. Solid curves (except that labelled LC_{R+V}) always correspond to $d' = 2$, dashed-dotted curves to $d' = 0$ and the dotted curve to $d = 0$. Figures modified from [155].

why the $d' = 0$ and $d' = 2$ results are equivalent: the cross section exponents only contain leading and sub-leading diagonal colour contributions. It is also clear that the $\Sigma_{q\bar{q},0}(\rho)$ strictly-leading colour cross section should be equal to the $d = 0$ result and that $\Sigma_{q\bar{q},0}^{(1)}(\rho)$ should be equal to $d' = 2$, as is evidenced in Figure 5.13a. In the case of $\Sigma_{q\bar{q},1}(\rho)$, we would expect that the $\Sigma_{q\bar{q},1}^{(0)}(\rho)$ cross section is negative, that the $d = 0$ and LC_{V+R} curves are not equal and that $\Sigma_{q\bar{q},1}^{(2)}(\rho)$ is the largest positive contribution. All of these features are evidenced

in Figure 5.13b. For higher multiplicities, $n = 2, 3$, it is interesting to note the success of the $d' = 0$ curves, whilst maintaining fewer fluctuations and being far less computationally expensive (than the $d' = 1$ and 2 results). Indeed, the differences between $d' = 0$, $d' = 1$ and $d' = 2$ are always less than 2%. The $d = 1$ curve has been included in Figure 5.13d to exhibit this. It is also a good validation of `CVolver`'s $1/N_c^k$ breakdown handling that the sum over all $\Sigma_n^{(k)}$ does indeed equate to the corresponding $d' = 2$ curve. This is true for all multiplicities $n = 0, 1, 2, 3$ in Figure 5.13.

Figures 5.14a, 5.14b, 5.14c and 5.14d show the jet veto cross section for the $H \rightarrow gg$ process at gluon multiplicities up to $n = 3$. For each multiplicity we present results using only the unprimed LC_V and NNLC_V approximations. In the case that the two primary jets and all subsequent emissions are gluons, the flow decomposition coefficients in the ρ -term of Eq. 4.22 cancel entirely (as they source from $U(1)$ singlet gluon contribution in the gluon propagator, which only interacts with quarks), and so the unprimed and primed forms of our approximation are equal. For the results presented here, the differences between the $d = 0$ and $d = 2$ results are within 3%.

The zero-emission cross section in Figure 5.14a, illustrates a peculiar feature of our LC_V approximation. There is a non-vanishing cross section at small ρ values, which occurs because of an unphysical N_c^0 contribution, present at $d = 0$ due to the subleading N_c terms in the scalar product and hard scattering matrices. The strictly leading-colour contribution corresponds to the well-behaved LC_{V+R} curve, which is equal to the $k = 2$ curve and is the same for $d = 0$ and $d = 2$. As further validation of our $1/N_c^k$ breakdown, we see that the sum over all $\Sigma_n^{(k)}$ corresponds to the $d = 2$ curve and is true for all multiplicities $n = 0, 1, 2, 3$ in Figure 5.14.

5.2.6 Emission Spectra

In the previous section we exhibited the jet veto cross section results as a function of ρ for gluon multiplicities up to $n = 3$ and discussed their N_c^k breakdown. For each multiplicity, we compared the cross section results using the LC_V , LC'_V and NLC'_V approximations for the Sudakov matrix elements, including the full- N_c dependence in the hard scattering, emission and scalar product matrix elements. Also shown, were the strictly leading-colour results, LC_{V+R} , to act as a benchmark against the colour capabilities of modern showers. Of course, state of the art parton showers can generate events with 10's of emis-

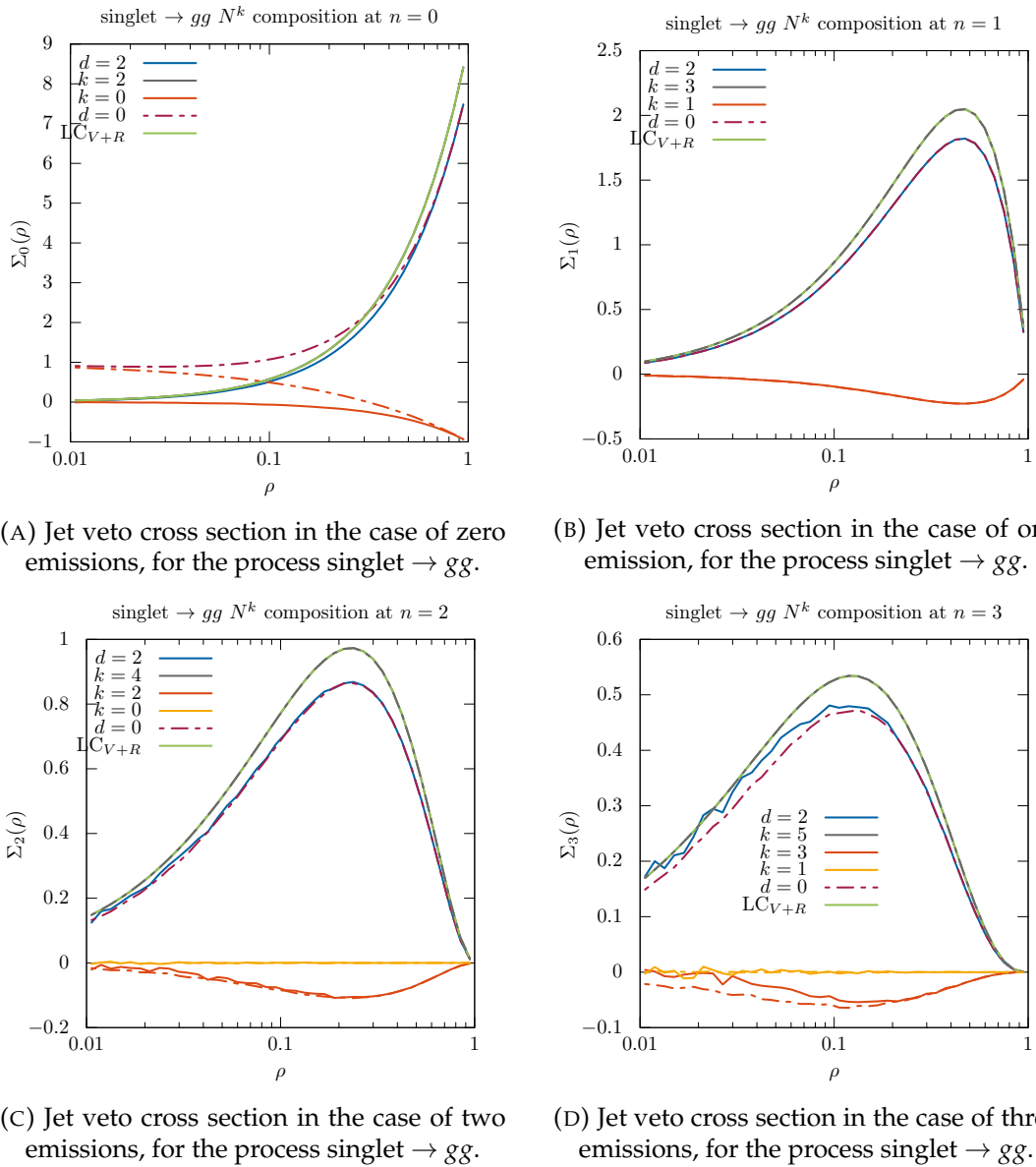


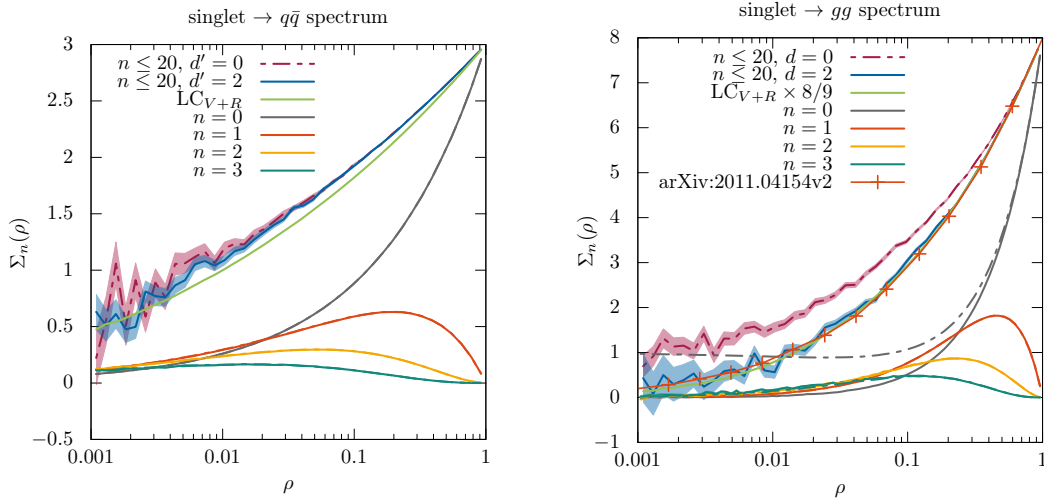
FIGURE 5.14: The jet veto cross section in $H \rightarrow gg$ for different gluon multiplicities ($n = 0, 1, 2$ and 3). Also shown are the individual contributions at each order of N_c^k for $d = 0$ and $d = 2$. Solid curves (except that labelled LC_{R+V}) always correspond to $d = 2$ and the broken curves always correspond to $d = 0$. Figures modified from [155].

sions. As such, we shall extend the deliberation of Section 5.2.5 to the sum over individual-multiplicity cross sections, $\Sigma_{q\bar{q}}(\rho)$ and $\Sigma_{gg}(\rho)$, upto 20 emissions.

In order to compute the summed cross section using **CVolver**, we set a toggle, **emit2max**, to 0. This adopts the scale sampling algorithm in Algorithm 8 with competition, which will carry on performing evolution steps until either the maximum multiplicity or the chosen veto scale is reached (whichever oc-

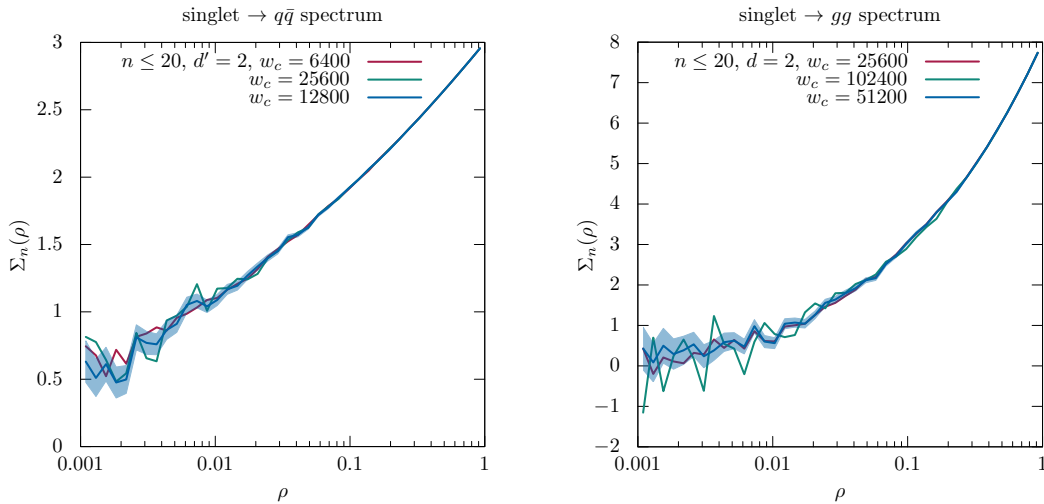
curs first). As previously described, Variant B of **CVolver** was developed in an attempt to ameliorate the problem of large, fluctuating weights illustrated in Section 5.1.6. We have seen in Section 5.2.5 that Variant B succeeds in this for fixed, low multiplicities. However, when we allow **CVolver** to freely emit up to higher multiplicities, such large-weight events reemerge, whose contributions dominate the cross section. It seems we are afflicted by something similar to the ‘no free lunch’ theorem, where the large event weights of Variant B are now concentrated into the (necessary) $1/\Delta_P(E|E')$ factor which results from the use of the competition algorithm at each evolution step. As a temporary remedy, we apply a ‘weight cut’ to each event weight, discarding those events with a value above our cut. This value is controlled with the command-line flag **weightCut** and introduces the necessity to find its optimal value, i.e. to find the lowest possible cutoff which has minimal effect on the cross section result.

Figures 5.15a and 5.15b show the total 20-emission cross section and the first few contributing lower-multiplicity cross sections for each of the processes $V \rightarrow q\bar{q}$ and $H \rightarrow gg$ respectively. The summation over all cross sections up to 20 emissions is denoted by $n \leq 20$. These figures have been produced using a collinear cutoff value of $\lambda = 10^{-2}$, with a corresponding ‘optimal’ **weightCut** value of 12800 in the case of $V \rightarrow q\bar{q}$ and 51200 for $H \rightarrow gg$. For comparison, Figures 5.15c and 5.15d present the total $n \leq 20$ cross section using these optimal **weightCut** values (denoted by w_c), alongside the total cross sections produced using $w_c/2$ and $2w_c$. Both the $w_c/2$ and $2w_c$ results are within two standard deviations of the w_c one in the case of $V \rightarrow q\bar{q}$ and three standard deviations for $H \rightarrow gg$. In Figures 5.15a and 5.15b, the difference between the $d' = 2$ (solid blue) and $d' = 0$ (dashed magenta) curves is 3.5% down to $\rho = 10^{-2}$. Below this veto scale the $d' = 0$ and $d' = 2$ curves fluctuate significantly more which makes a comparison of relative values difficult. The difference between the $d' = 2$ curves (solid blue) and strict leading colour ones (LC_{V+R}) is significant: they agree for large ρ values, but exhibit a difference of 8% at $\rho = 10^{-2}$ in the case of $q\bar{q}$ production. For gg production, the strictly-leading colour curve (multiplied by $8/9$) and $d = 2$ curve differ by 10% at $\rho = 10^{-2}$, which is dominated by the factor of $8/9$ arising from the hard scattering matrix element. Looking back to the Variant A $V \rightarrow q\bar{q}$ total cross section result presented in Figure 5.4, we find agreement between the $n \leq 10$ curve and the $n \leq 20$ curve in Figure 5.15a to within 3% down to ρ values of 10^{-2} . Below this ρ value, the curves differ by 7%, which is dominated by



(A) Breakdown of the jet veto cross section by multiplicity and colour order, for the process $\text{singlet} \rightarrow q\bar{q}$.

(B) Breakdown of the jet veto cross section by multiplicity and colour order, for the process $\text{singlet} \rightarrow gg$.



(C) The $n \leq 20$ jet veto cross section for the process $\text{singlet} \rightarrow q\bar{q}$. Each curve illustrates the total cross section for a different value of **weightCut**, denoted by w_c .

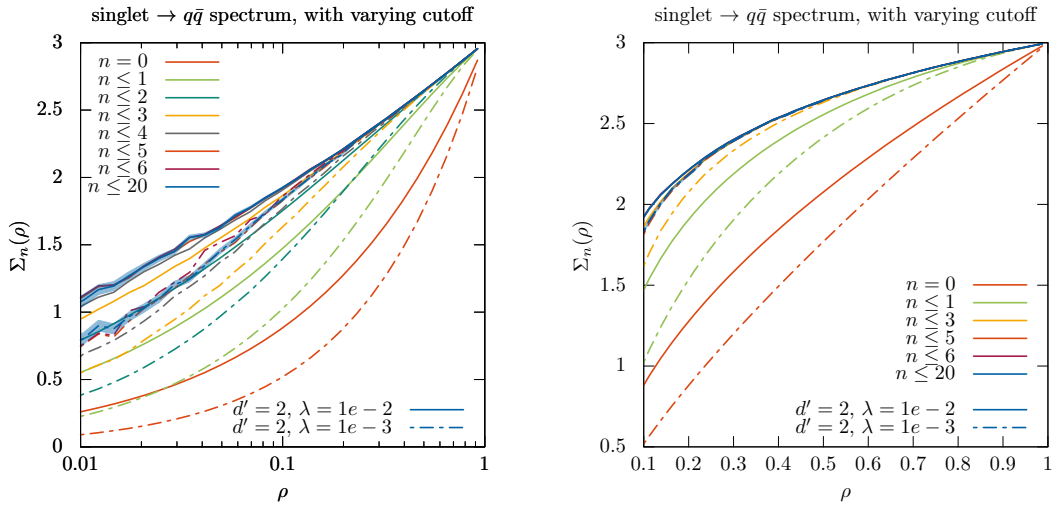
(D) The $n \leq 20$ jet veto cross section for the process $\text{singlet} \rightarrow gg$. Each curve illustrates the total cross section for a different value of **weightCut**, denoted by w_c .

FIGURE 5.15: The jet veto cross section in (a) for the $V \rightarrow q\bar{q}$ process and (b) for the $H \rightarrow gg$ process, for different gluon multiplicities ($n = 0, 1, 2, 3, \leq 20$). Results are shown for $d' = 0, 2$ and $d = 0, 2$ respectively using a **weightCut** value of $w_c = 12800$ and $w_c = 51200$. The contributions from $n = 0$ up to 3 emissions are also presented, however the total cross section result is a summation over all emissions. The total cross section here has been produced by **CVolver**, limited to $n \leq 20$ emissions. Figures modified from [155]. (c) and (d) compare the total cross section (with $n \leq 20$) for different values of the w_c .

fluctuations. The apparent success of our $d' = 0$ approximation in Figure 5.15a is also interesting to note, although we do not expect this to continue once we

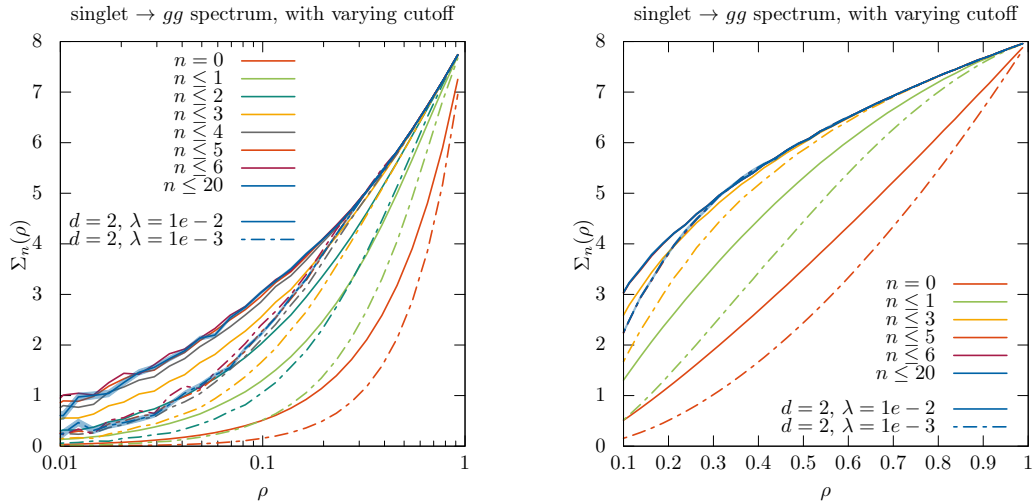
consider more sophisticated hard processes [167].

During the writing of this work, [167] presented results that can be directly compared with `CVolver` - these results have been included in Figure 5.15b and are depicted by red data points. The approach of Hatta and Ueda in [167] differs greatly from our own, providing a good finite- N_c benchmark: Hatta and Ueda have built on the work of [174] and developed a framework (in [175, 176]) which resums non-global logarithms for the jet veto and hemisphere jet mass observables. This is achieved by formulating the finite- N_c generalisation of the BMS equation (in [174]) in terms of Wilson lines, which can be written as a Fokker-Planck equation and solved using random walk trajectories in the SU(3) colour space. This random walk is simulated by discretising the particle coordinates $-1 \leq \cos \theta \leq 1$ and $0 \leq \phi \leq 2\pi$ onto a lattice. For the red points in Figure 5.15b, this is achieved with a lattice spacing of $1/80$ and $1/60$ for $\cos \theta$ and ϕ respectively. As we will see in a moment (in our upcoming discussion around Figure 5.16), the jet veto cross sections produced with a cutoff value of $\lambda = 10^{-2}$ should be reliable (with a minimal cutoff dependence) for $\rho \geq 10^{-2}$; these results also show good agreement with [167]. The lattice spacing used in [167] for $\cos \theta$ could have a similar effect on the cross section as our collinear cutoff, with a $1/80$ spacing corresponding to $\lambda \simeq 0.01$. However, [167] does not explore cutoff dependence.



(A) Jet veto cross section presented for logarithmically scaled values of the veto energy, for the singlet $\rightarrow q\bar{q}$ process.

(B) Jet veto cross section presented for linearly scaled values of the veto energy, for the singlet $\rightarrow q\bar{q}$ process.



(C) Jet veto cross section presented for logarithmically scaled values of the veto energy, for the singlet $\rightarrow gg$ process.

(D) Jet veto cross section presented for linearly scaled values of the veto energy, for the singlet $\rightarrow gg$ process.

FIGURE 5.16: The jet veto cross section in (a) and (b) for the $V \rightarrow q\bar{q}$ process and (c) and (d) for the $H \rightarrow q\bar{q}$ process, for summations over different gluon multiplicities ($n \leq 0, 1, 2, 3, 4, 5, 6$ and 20). Results are shown for $d' = 2$ for the $q\bar{q}$ final state and $d = 2$ for the gg final state. The blue shaded region corresponds to the $n \leq 20$ cross section (one standard deviation) error. Solid curves correspond to a collinear cutoff of 1×10^{-2} , whereas the broken curves correspond to a cutoff of 1×10^{-3} . In Figures (B) and (D), we are comparing the similarity between the total cross section results produced using two cutoff values at large ρ . For clarity: the $n \leq 5, 6$ cross section results in both figures, whilst plotted, reside under the $n \leq 20$ result for both cutoff values, and so are not visible. The $\lambda = 10^{-2}$ and $\lambda = 10^{-3}$ $n \leq 20$ curves are indistinguishable for large ρ values, down to $\rho = 0.1$ in (B) and $\rho = 0.2$ in (D), where their difference becomes apparent.

Figure 5.16 shows how the total 20-emission cross section is built up from different multiplicities, for two values of the collinear cutoff: $\lambda = 10^{-2}$ and $\lambda = 10^{-3}$. Curves produced using the former cutoff are represented with solid coloured lines, whereas those produced using the latter are dashed. All curves include the full- N_c dependence, with Sudakov matrix elements computed to the NNLC'_V approximation.

Figure 5.16a and Figure 5.16c exhibit the same principle features noted in Section 5.1.6. The $n = 0$ curves are described by an exponential function and fall faster as ρ gets smaller, for a lower cutoff. At $\rho = 1$, the zero-emission results have the same values (of N_c and $N_c^2 - 1$ for $V \rightarrow q\bar{q}$ and $H \rightarrow gg$), irrespective of the collinear cutoff used. Figure 5.15 illustrates how the $n > 0$ curves increasingly contribute less to the total cross section at high ρ -values and similar contributions at lower ρ . This feature is more pronounced for lower cutoff values, where the $n > 0$ curves become more peaked closer to $\rho = 1$. This characteristic manifests itself in Figure 5.16, where we see decreasing 'jumps' in the total cross section value for each successive emission at higher ρ and a steadier increase at low- ρ . For the limit of a zero-value cutoff and an infinite number of emissions to be well-approximated, we therefore expect to need a minimum number of emissions, to sufficiently populate the total cross section at low- ρ . Furthermore, we expect a higher number of real emissions to be necessary for a smaller cutoff. We notice in Figures 5.16a and 5.16c, that the total cross section is cutoff-independent down to $\rho = 0.1$ for the $V \rightarrow q\bar{q}$ process and $\rho = 0.2$ for $H \rightarrow gg$. This is highlighted more clearly in Figures 5.16b and 5.16d. Below these ρ values, the cross section result develops a cutoff dependence. The reason for this dependence requires further exploration. Also, examining Figures 5.16a and 5.16c, we see that for both cutoff values, the total cross section does not change (beyond fluctuations) past 6 emissions.

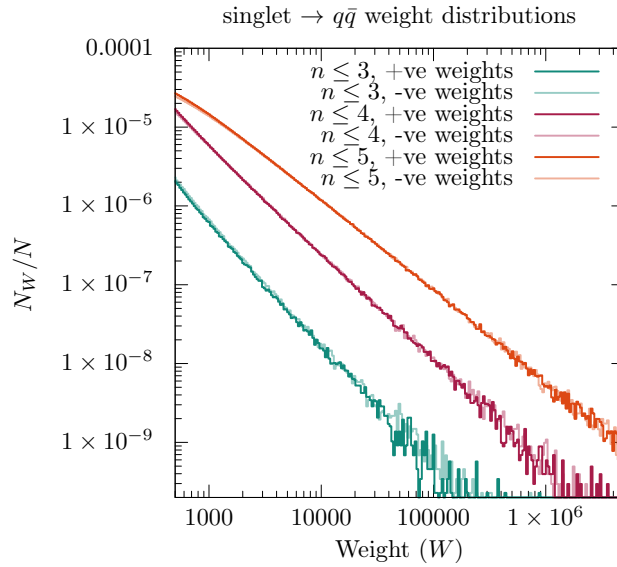


FIGURE 5.17: The event-weight distributions corresponding to the $n \leq 3, 4, 5$ total cross section for $\lambda = 10^{-3}$, produced using Variant B. Both the positive and negative event-weights have been plotted separately; for each n , the negative event-weights have been plotted in a lighter version of the same colour as the corresponding positive event-weights.

It is clear from Figure 5.16a, that fluctuations in the total cross section result begin to appear after four emissions. Figure 5.17 illustrates the distribution of positive and negative event-weights which contribute to the $n \leq 4$ total cross section in Figure 5.16a, with the $n \leq 3$ and $n \leq 5$ weight distributions for comparison. The event-weight distributions of Variant B are reminiscent of Variant A (see Figure 5.5b) as we see that with an increasing number of emissions, the weight distributions broaden and populate larger weights. Similarly to Figure 5.5b, there are outlier event-weights, however they occur less frequently for Variant B, represented by fewer fluctuations in the event-weight distributions of Figure 5.17. This in-turn, corroborates the improved stability of the Variant B jet veto cross section at lower multiplicities. Conversely, the event-weight distributions in Figure 5.17 differ from those in Figure 5.5b as the negative distributions are much closer to their positive counterparts for each n . Additionally, the event-weight distributions for Variant B broaden much more rapidly with increasing emissions than those of Variant A. We can see from Figure 5.17, that the positive and negative weights follow a distribution, $\frac{dN}{dw} \propto 1/w^2$; implying that the integral is formally not convergent. One can show that, for a distribution in which positive or negative weights are equally common, imposing a weight cutoff of $|w| < w_c$ is effective in dealing with

this issue. However, a weight cutoff also introduces a bias in the integrand evaluation that goes as $1/w_c$, whilst the variance is proportional to w_c . We are therefore forced to compromise between a larger w_c , giving a less biased result, and a smaller w_c giving better convergence.

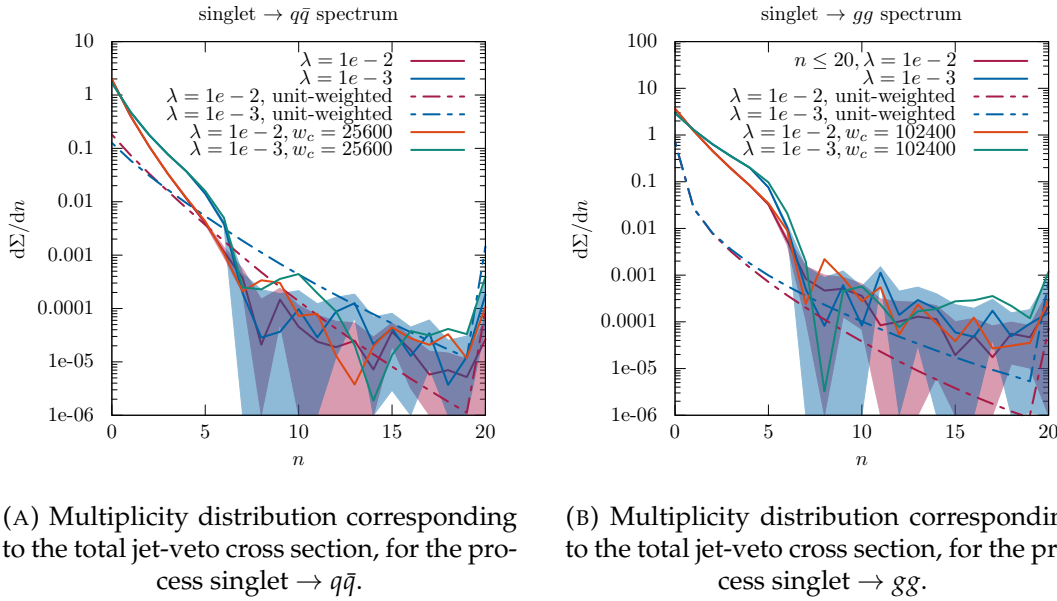


FIGURE 5.18: The multiplicity distributions corresponding to the total 20-emission cross section results in Figure 5.15. (a) presents the distributions for the $V \rightarrow q\bar{q}$ process at NNLC'_V and (b) for the $H \rightarrow gg$ process at NNLC_V for a **weightCut** of $w_c = 12800$ and $w_c = 51200$. Both (a) and (b) show the multiplicity distributions using total cross section-weighted events (solid curves) and unit-weighted events (dashed-dotted curves), for two values of the collinear cutoff: $\lambda = 10^{-2}$ and $\lambda = 10^{-3}$. The same distributions using a larger **weightCut** value, $2w_c$, are included.

Figure 5.18 presents the multiplicity plots corresponding to the 20-emission total cross section in Figure 5.16. The solid curves show the multiplicity distribution, weighted by the total cross section at a given multiplicity, n , for both cutoff values. These results use the optimal **weightCut** values, w_c . Also included, are the total cross section multiplicity plots for a larger **weightCut** value. The dashed curves represent the unweighted multiplicity distributions, i.e. the n th multiplicity bin simply counts events for an event with n emissions (the normalisation is a result of the histogramming process, in which each bin weight is divided by the number of ‘attempted’ points). Importantly, one can see from the unweighted distributions that 0.001% of events contain 20 emissions, and that this fraction is even less for a larger cutoff. This is expected, as the cutoff on each particle removes a portion of phase-space in which a subsequent emission

can reside. However, looking at the weighted multiplicity distributions, we see that past 6 emissions, the distributions drop off far too quickly for both cutoff values, developing large fluctuations. This corroborates the same observation in Figure 5.16. A similar trend is seen for the results produced using a higher `weightCut` value, $2w_c$. Whilst it appears that the $2w_c$ curves have larger values at higher multiplicities, there is also a strong increase in fluctuations, making any conclusion on this matter difficult. The exact cause of the rapid drop off past 6 emissions and large fluctuations is not known. It is worth mentioning, that we have deliberately chosen a challenging observable as a robust test of **CVolver**, where the phase-space of the emitted gluons is tightly constrained. And so, there is an some expectation of erratic behaviour related to numerical stability. Notwithstanding this point, the large fluctuations could be caused by, although not limited to, one of the following: the employed cutoff prescription (and its corresponding direction sampling), insufficient sampling of the factorially increasing colour space at higher multiplicities, the more rapid broadening of the event-weight distributions in Variant B or a potential artifact of the imposed weight cutoff. Given that higher-multiplicity contributions are necessary to populate the low- ρ total cross section, it is possible that one of these factors is the cause for the observed cutoff-dependences at low ρ .

It is clear that our **Hemispheres** implementation of the jet veto cross section underestimates the weights of high-multiplicity events, which additionally contain large weight fluctuations. However, our examination of the total cross sections in Figures 5.15, 5.16 and 5.18 vindicates the performance of **Hemispheres** for $\rho \geq 10^{-2}$.

Conclusions and Outlook

With the analyses at modern particle colliders frequently limited by theoretical uncertainties, improving the accuracy of general-purpose event generators (GPEGs) is becoming increasingly important. Precise predictions for observables at colliders often cannot be achieved without the resummation of logarithmically-enhanced contributions to all orders in perturbation theory. And particularly for non-global observables, the all-orders resummation can be a complicated task, largely due to unavoidable non-trivial colour correlations. It is the domicile of GPEG parton showers to provide an all-purpose approximation to this procedure. To drastically simplify the problem, they adopt the leading colour approximation and account for the leading logarithms of soft and collinear origin. However, there is a growing list of effects that parton showers do not account for, including in particular a full colour treatment of non-global logarithms. One crucial area therefore in which GPEGs can be improved, is by the inclusion of sub-leading colour corrections.

In spite of much progress in recent years [148–150, 174, 175, 177–182], it remains to develop an automated approach to resummation beyond the leading colour approximation. This thesis has built on the work [18–21], which encapsulates many of the aforementioned effects, to make progress in this direction. It uses algorithmic, recursive definitions of QCD amplitudes for soft gluon emissions, including the leading virtual corrections to all orders.

In Chapter 2 we presented a general evolution algorithm, which can be used as a basis for automated resummations. It was written in a differential form, apt for the calculation of multiple soft-gluon contributions to any observable, and suited to a Monte-Carlo implementation. To showcase the validity of this algorithm, we reformulated it in such a way, so as to make the cancellation of infrared divergences explicit. Using this rephrased algorithm, we calculated the non-global contributions to the hemisphere jet mass observable, finding agreement with [96, 104, 105] up to $\mathcal{O}(\alpha_s^3)$. We then turned our attention to the colour structures encountered in the evolution algorithm, expressing the

Sudakov and emission colour operators in the colour flow basis. A systematic procedure to calculate colour traces, and expand in contributing powers of $1/N_c^k$ was expressed. Using the leading colour terms in this expansion, we were able to re-derive the Banfi-Marchesini-Smye equation. We subsequently explored the first subleading-colour corrections in our expansion. This work gave us the requisite knowledge to build the beginnings of a parton shower, including contributions beyond leading colour.

Following on, in Chapter 4 we presented a Monte Carlo code, **Cvolver**, that utilises the amplitude-level evolution algorithm in Chapter 2 to simulate high-energy particle collisions. It sums the most important soft-gluon logarithms, although the framework is general enough to accommodate beyond this approximation. We began by expressing the evolution algorithm explicitly in terms of matrix elements to illustrate how we handle a large colour space - by sampling over intermediate colour states. Subsequently, we laid out the **Cvolver** framework, which provides the general colour machinery, upon which an observable **Implementation** can be interfaced. We addressed the calculation of the approximated Sudakov and full-colour emission matrix elements in the colour flow basis, and their implementation in **Core**. Approximating Sudakov matrix elements, $[\tau | \mathbf{V} | \sigma \rangle$, raised the challenge of sampling the basis tensor, $|\tau \rangle$, d swaps from $|\sigma \rangle$, which was tackled in Section 4.4. With these fundamental implementations settled, we proceeded to outline two variants of the **Hemispheres** implementation, which calculates the jet veto observable. This process is sensitive to wide-angle, soft-gluon emission and thus provides an ideal test of the framework. Variant A was our initial implementation, maintaining an inherently amplitude-level description. Whilst this is necessary for the inclusion of collinear emissions, spin dependence and Coulomb gluon effects [103], Variant A produces total cross section results contaminated by large weight fluctuations. Variant B on the other hand makes cross section-level Lorentz contractions, allowing for more efficient sampling strategies in an attempt to ameliorate these large weights. In Chapter 5 we presented the cross section results of these two variants. Comparing with independent results, we used both variants to validate the underlying colour machinery of **Cvolver**. In addition, we created independent test codes to verify the individual multiplicity cross sections up to two emissions. For Variant B we showed the cross section breakdown, in terms of the different powers of N_c that contribute, using the LC_{V+R} , LC_V , LC'_V and $NNLC'_V$ approximations. We observed significant deviations from the leading-colour approximation

in the jet veto observable, for both $V \rightarrow q\bar{q}$ and $H \rightarrow gg$ production, and small differences between the LC'_V and NNLC'_V approximations. Examining the total jet veto cross section (summing emissions up to $n \leq 20$) and the corresponding multiplicity distributions for multiple collinear cutoff values, we found that for $n \leq 6$ emissions and for $\rho \geq 10^{-2}$, the jet veto cross section calculated by `cVolver` appears accurate and largely cutoff-independent. For $H \rightarrow gg$ production, we also find our results are in good agreement with [167]. All of this represents a milestone in the progress towards a full-colour parton shower.

There are several directions which can be indicated for future works. Firstly, we identified a potential issue in the direction sampling of Variant B, which we believe to be caused by the deformation of the cutoff cones about each emission as they are boosted back to the lab-frame. To make a firmer conclusion on the exhibited cutoff dependence of Variant B, a more thorough study of the cutoff prescription and associated direction sampling should be carried out. Furthermore, Variant B was our attempt at alleviating the large weight fluctuations observed in Variant A. Whilst it achieved this for low multiplicities, an imposed weight cutoff was still required to attain stable total cross section results. Traditional showers, in the leading colour approximation, can achieve sampling algorithms which produce positive-definite weights. However, including sub-leading colour effects (and relatedly performing an amplitude-level evolution), necessitates the inclusion of negative weights, which in general can lead to largely varying weight distributions. We have observed such distributions accumulate emission-by-emission in `cVolver`. To improve this situation, the resampling strategy presented in [183] could be integrated into `cVolver`, to achieve a narrower weight distribution at each evolution step.

Additionally, we saw in Section 5.2.6 that for events with $n \geq 6$ emissions, the total cross section had grossly underestimated weights. As a partial remedy to this, one could tailor the basis tensor sampling in `cVolver` to return to the colour matrix diagonal before the shower cascade reaches 6 emissions, and henceforth evolve in the leading-colour approximation. Whilst the author has not explored this approach, it may prove to include a sufficient 'bulk' of the sub-leading colour corrections. `cVolver` should also be extended beyond the soft approximation, and to include incoming hadrons. This can be done using the results presented in [103], which improved on the algorithm presented in Chapter 2 to include collinear emissions, spin dependence and kinematic recoil.

Appendix A

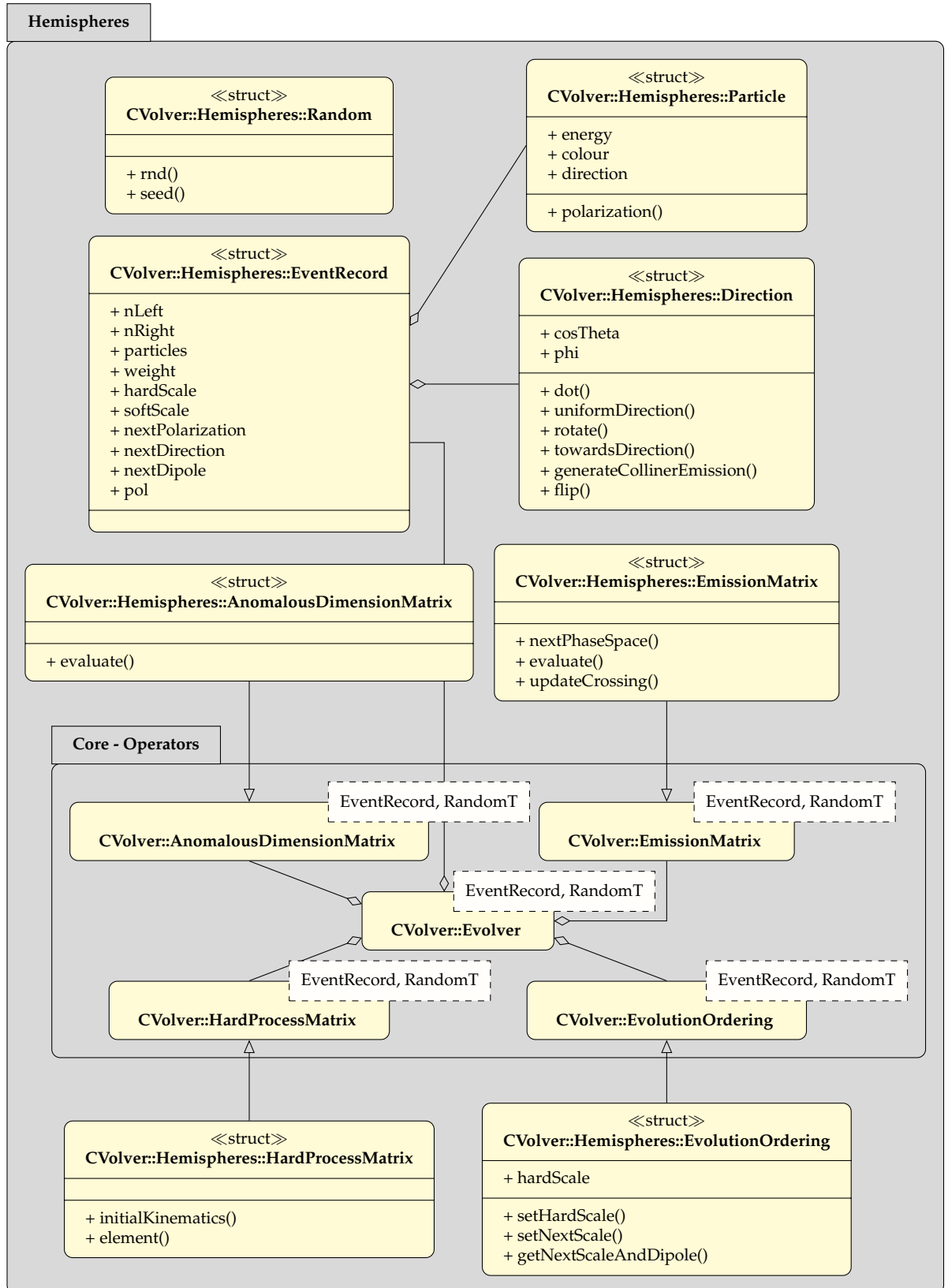
CVolver UML

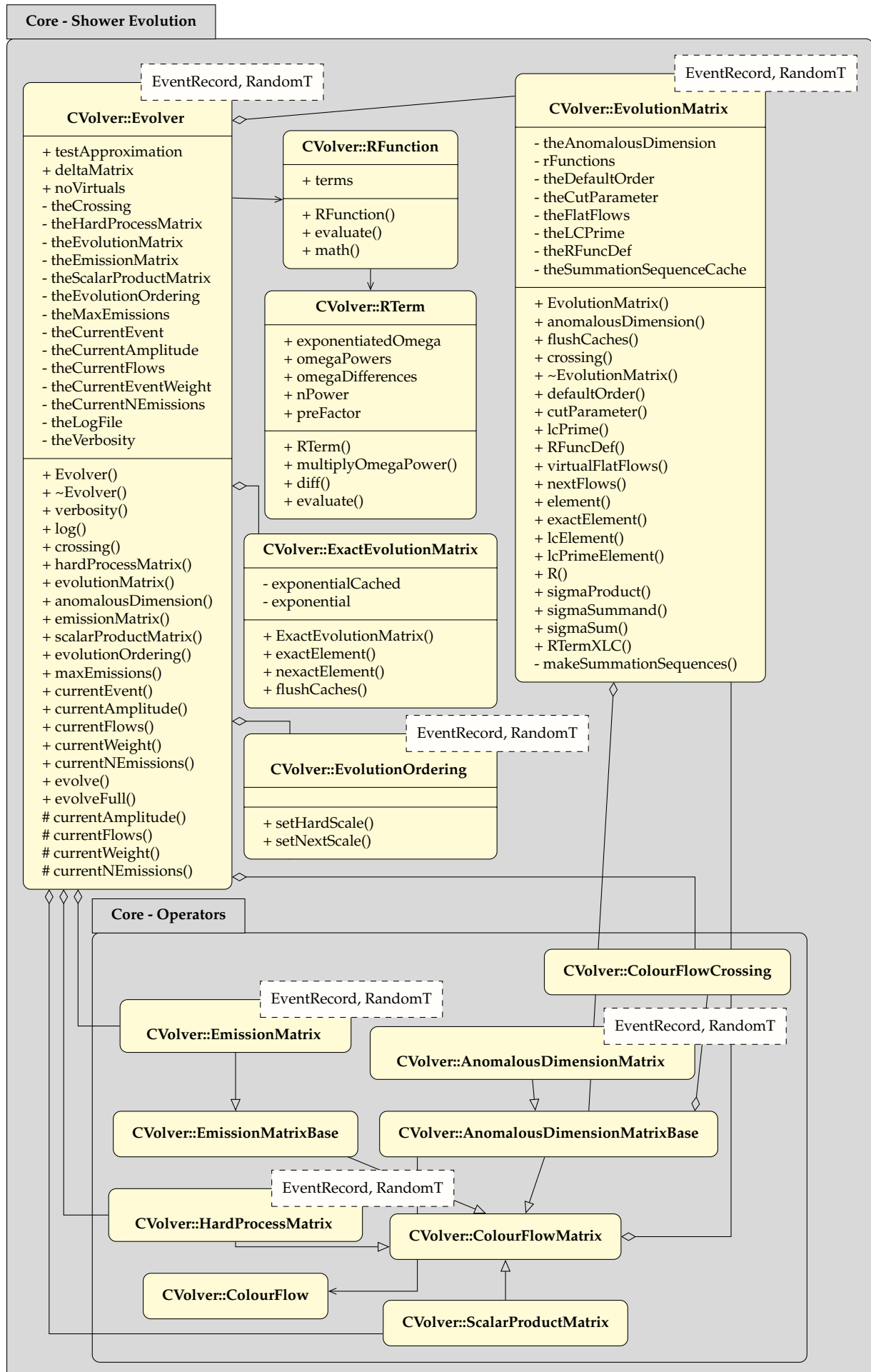
In this appendix, we present the Unified Modeling Language (UML) class diagrams of the **CVolver** framework upon which we build the **Hemispheres** implementation. This simulates high-energy particle collisions and is tailored to the production of two-jet systems, in which there is a restriction on the amount of radiation lying in some angular region of phase-space, outside of the jets: the jet veto observable. The exact implementation of **Hemispheres** is discussed in Chapter 4 for two variants, Variant A and Variant B, whilst the corresponding cross section results are presented in Chapter 5. This appendix aims to provide the reader with a more detailed review of the **CVolver** code to assist in future improvements.

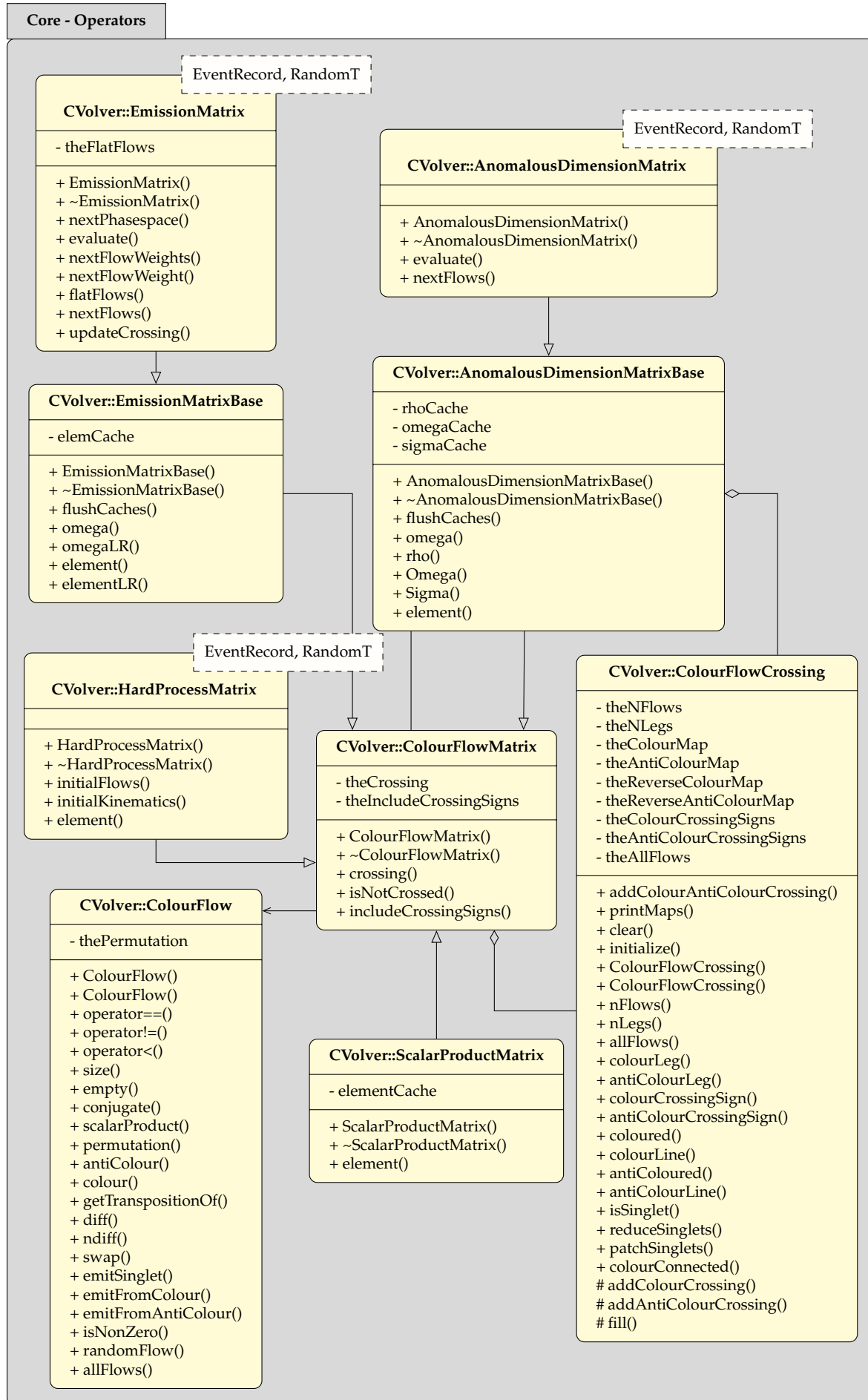
To aid the reader, we provide a quick overview of class diagram notation. Class diagrams are a type of structure diagram, presenting the systems' classes: their attributes, methods (i.e. what they do) and their relationship to other classes. These are represented in each system by a yellow box, which are split into three sections: the class name (with its scope signified by the operator `::`, e.g. `CVolver::`), the class attributes, and the class methods. The **Hemispheres** implementation is split into three 'systems'. First, we have the implementation of the operator classes and the event recording for the jet veto observable (in the grey box entitled 'Hemispheres'). Secondly, **Hemispheres** inherits from **Core**. This provides an archetype of an operator class, defines the necessary operator class methods, and handles all of the required colour manipulation machinery (the grey box entitled 'Core - Operators'). Thirdly, **Core** also carries out the important Sudakov operator colour approximation (in **EvolutionMatrix**) and orchestrates the shower evolution (in **EvoLver**). This is described in the 'Core - Shower Evolution' box.

The visibility of each class attribute or method (collectively termed 'members')

is specified by: + for a public member, – for a private member and # for a protected member; ~ denotes a class destructor. Relationships between classes are represented by lines and differ by the arrow-head. A normal arrow represents an association, which simply indicates the ‘use’ of another class. An open triangle denotes inheritance, whilst an open diamond indicates an aggregation association. This is more specific than a normal association and indicates that one class ‘has’ an instance of another; likely contained in the class as an attribute.







Bibliography

- [1] P. Bagnaia et al. “Evidence for $Z^0 \rightarrow e^+e^-$ at the CERN $\bar{p}p$ Collider”. *Phys. Lett. B* 129 (1983), pp. 130–140.
- [2] G. Arnison et al. “Experimental Observation of Isolated Large Transverse Energy Electrons with Associated Missing Energy at $\sqrt{s} = 540$ GeV”. *Phys. Lett. B* 122 (1983), pp. 103–116.
- [3] F. Abe et al. “Observation of top quark production in $\bar{p}p$ collisions”. *Phys. Rev. Lett.* 74 (1995), pp. 2626–2631. arXiv: [hep-ex/9503002](#).
- [4] S. Abachi et al. “Observation of the top quark”. *Phys. Rev. Lett.* 74 (1995), pp. 2632–2637. arXiv: [hep-ex/9503003](#).
- [5] K. Kodama et al. “Observation of tau neutrino interactions”. *Phys. Lett. B* 504 (2001), pp. 218–224. arXiv: [hep-ex/0012035](#).
- [6] S. Chatrchyan et al. “Observation of a New Boson at a Mass of 125 GeV with the CMS Experiment at the LHC”. *Phys. Lett. B* 716 (2012), pp. 30–61. arXiv: [1207.7235 \[hep-ex\]](#).
- [7] G. Aad et al. “Observation of a new particle in the search for the Standard Model Higgs boson with the ATLAS detector at the LHC”. *Phys. Lett. B* 716 (2012), pp. 1–29. arXiv: [1207.7214 \[hep-ex\]](#).
- [8] Y. Fukuda et al. “Evidence for oscillation of atmospheric neutrinos”. *Phys. Rev. Lett.* 81 (1998), pp. 1562–1567. arXiv: [hep-ex/9807003](#).
- [9] M. C. Gonzalez-Garcia and M. Maltoni. “Phenomenology with Massive Neutrinos”. *Phys. Rept.* 460 (2008), pp. 1–129. arXiv: [0704.1800 \[hep-ph\]](#).
- [10] M. Bähr et al. “Herwig++ Physics and Manual”. *Eur. Phys. J. C* 58 (2008), pp. 639–707. arXiv: [0803.0883 \[hep-ph\]](#).
- [11] J. Bellm et al. “Herwig 7.0/Herwig++ 3.0 release note”. *Eur. Phys. J. C* 76.4 (2016), p. 196. arXiv: [1512.01178 \[hep-ph\]](#).
- [12] J. Bellm et al. “Herwig 7.1 Release Note” (2017). arXiv: [1705.06919 \[hep-ph\]](#).
- [13] T. Sjöstrand, S. Mrenna, and P. Z. Skands. “PYTHIA 6.4 Physics and Manual”. *JHEP* 05 (2006), p. 026. arXiv: [hep-ph/0603175 \[hep-ph\]](#).

- [14] T. Sjöstrand, S. Mrenna, and P. Z. Skands. “A Brief Introduction to PYTHIA 8.1”. *Comput. Phys. Commun.* 178 (2008), pp. 852–867. arXiv: [0710.3820 \[hep-ph\]](#).
- [15] T. Sjöstrand et al. “An Introduction to PYTHIA 8.2”. *Comput. Phys. Commun.* 191 (2015), pp. 159–177. arXiv: [1410.3012 \[hep-ph\]](#).
- [16] T. Gleisberg et al. “Event generation with SHERPA 1.1”. *JHEP* 02 (2009), p. 007. arXiv: [0811.4622 \[hep-ph\]](#).
- [17] J. Bellm et al. “Herwig 7.2 release note”. *Eur. Phys. J. C* 80.5 (2020), p. 452. arXiv: [1912.06509 \[hep-ph\]](#).
- [18] J. R. Forshaw, A. Kyrieleis, and M. H. Seymour. “Super-leading logarithms in non-global observables in QCD”. *JHEP* 08 (2006), p. 059. arXiv: [hep-ph/0604094 \[hep-ph\]](#).
- [19] J. R. Forshaw, A. Kyrieleis, and M. H. Seymour. “Super-leading logarithms in non-global observables in QCD: Colour basis independent calculation”. *JHEP* 09 (2008), p. 128. arXiv: [0808.1269 \[hep-ph\]](#).
- [20] R. Ángeles-Martínez, J. R. Forshaw, and M. H. Seymour. “Coulomb gluons and the ordering variable”. *JHEP* 12 (2015), p. 091. arXiv: [1510.07998 \[hep-ph\]](#).
- [21] R. Á. Martínez, J. R. Forshaw, and M. H. Seymour. “Ordering multiple soft gluon emissions”. *Phys. Rev. Lett.* 116.21 (2016), p. 212003. arXiv: [1602.00623 \[hep-ph\]](#).
- [22] M. De Angelis, J. R. Forshaw, and S. Plätzer. “Resummation and Simulation of Soft Gluon Effects beyond Leading Color”. *Phys. Rev. Lett.* 126.11 (2021), p. 112001. arXiv: [2007.09648 \[hep-ph\]](#).
- [23] E. C. Fowler et al. “A Diffusion Cloud-Chamber Study of Pion Interactions in Hydrogen and Helium”. *Phys. Rev.* 91 (1 1953), pp. 135–149.
- [24] V. E. Barnes et al. “Observation of a Hyperon with Strangeness Minus Three”. *Phys. Rev. Lett.* 12 (8 1964), pp. 204–206.
- [25] M. Gell-Mann. “The Eightfold Way: A Theory of strong interaction symmetry” (1961).
- [26] Y. Ne’eman. “Derivation of strong interactions from a gauge invariance”. *Nucl. Phys.* 26 (1961). Ed. by R. Ruffini and Y. Verbin, pp. 222–229.
- [27] G. F. Chew and S. C. Frautschi. “Principle of Equivalence for All Strongly Interacting Particles Within the S Matrix Framework”. *Phys. Rev. Lett.* 7 (1961), pp. 394–397.
- [28] P. D. B. Collins. “Regge theory and particle physics”. *Phys. Rept.* 1 (1971), pp. 103–234.

- [29] M. Gell-Mann. "A Schematic Model of Baryons and Mesons". *Phys. Lett.* 8 (1964), pp. 214–215.
- [30] G. Zweig. "An SU(3) model for strong interaction symmetry and its breaking." *Developments in the quark theory of hadrons*. Ed. by D. B. Lichtenberg and S. P. Rosen. Vol. 1. Feb. 1964.
- [31] E. D. Bloom et al. "High-Energy Inelastic e p Scattering at 6-Degrees and 10-Degrees". *Phys. Rev. Lett.* 23 (1969), pp. 930–934.
- [32] M. Y. Han and Y. Nambu. "Three Triplet Model with Double SU(3) Symmetry". *Phys. Rev.* 139 (1965). Ed. by T. Eguchi, B1006–B1010.
- [33] O. W. Greenberg. "Spin and Unitary Spin Independence in a Paraquark Model of Baryons and Mesons". *Phys. Rev. Lett.* 13 (1964), pp. 598–602.
- [34] D. J. Gross and F. Wilczek. "Asymptotically Free Gauge Theories - I". *Phys. Rev. D* 8 (1973), pp. 3633–3652.
- [35] H. Fritzsch, M. Gell-Mann, and H. Leutwyler. "Advantages of the Color Octet Gluon Picture". *Phys. Lett. B* 47 (1973), pp. 365–368.
- [36] G. 't Hooft. "Renormalization of Massless Yang-Mills Fields". *Nucl. Phys. B* 33 (1971), pp. 173–199.
- [37] L. D. Faddeev and V. N. Popov. "Feynman Diagrams for the Yang-Mills Field". *Phys. Lett. B* 25 (1967). Ed. by Jong-Ping Hsu and D. Fine, pp. 29–30.
- [38] G. 't Hooft. "An algorithm for the poles at dimension four in the dimensional regularization procedure". *Nucl. Phys. B* 62 (1973), pp. 444–460.
- [39] G. 't Hooft. "Renormalizable Lagrangians for Massive Yang-Mills Fields". *Nucl. Phys. B* 35 (1971). Ed. by J. C. Taylor, pp. 167–188.
- [40] D. J. Gross and F. Wilczek. "Ultraviolet Behavior of Nonabelian Gauge Theories". *Phys. Rev. Lett.* 30 (1973). Ed. by J. C. Taylor, pp. 1343–1346.
- [41] D. J. Gross and F. Wilczek. "Asymptotically Free Gauge Theories - II". *Phys. Rev. D* 9 (1974), pp. 980–993.
- [42] H. D. Politzer. "Reliable Perturbative Results for Strong Interactions?" *Phys. Rev. Lett.* 30 (1973). Ed. by J. C. Taylor, pp. 1346–1349.
- [43] H. Georgi. *Lie Algebras In Particle Physics: from Isospin To Unified Theories*. New York: Westview Press, 1999. ISBN: 0-7382-0233-9.
- [44] G. Abbiendi et al. "A Simultaneous measurement of the QCD color factors and the strong coupling". *Eur. Phys. J. C* 20 (2001), pp. 601–615. arXiv: [hep-ex/0101044](https://arxiv.org/abs/hep-ex/0101044).
- [45] G. 't Hooft. "A Planar Diagram Theory for Strong Interactions". *Nucl. Phys. B* 72 (1974). Ed. by J.C. Taylor, p. 461.

- [46] M. Moretti, T. Ohl, and J. Reuter. “O’Mega: An Optimizing matrix element generator” (2001). Ed. by Ties Behnke et al., pp. 1981–2009. arXiv: [hep-ph/0102195](#).
- [47] W. Kilian, T. Ohl, and J. Reuter. “WHIZARD: Simulating Multi-Particle Processes at LHC and ILC”. *Eur. Phys. J. C* 71 (2011), p. 1742. arXiv: [0708.4233 \[hep-ph\]](#).
- [48] A. Cafarella, C. G. Papadopoulos, and M. Worek. “Helac-Phegas: A Generator for all parton level processes”. *Comput. Phys. Commun.* 180 (2009), pp. 1941–1955. arXiv: [0710.2427 \[hep-ph\]](#).
- [49] G. Marchesini and B. R. Webber. “Monte Carlo Simulation of General Hard Processes with Coherent QCD Radiation”. *Nucl. Phys. B* 310 (1988), pp. 461–526.
- [50] R. K. Ellis, G. Marchesini, and B. R. Webber. “Soft Radiation in Parton Parton Scattering”. *Nucl. Phys. B* 286 (1987). [Erratum: *Nucl.Phys.B* 294, 1180 (1987)], p. 643.
- [51] S. Catani and M.H. Seymour. “A General algorithm for calculating jet cross-sections in NLO QCD”. *Nucl. Phys. B* 485 (1997). [Erratum: *Nucl.Phys.B* 510, 503–504 (1998)], pp. 291–419. arXiv: [hep-ph/9605323](#).
- [52] S. Plätzer and S. Gieseke. “Coherent Parton Showers with Local Recoils”. *JHEP* 01 (2011), p. 024. arXiv: [0909.5593 \[hep-ph\]](#).
- [53] S. Plätzer and S. Gieseke. “Dipole Showers and Automated NLO Matching in Herwig++”. *Eur. Phys. J. C* 72 (2012), p. 2187. arXiv: [1109.6256 \[hep-ph\]](#).
- [54] B.R. Webber. “A QCD Model for Jet Fragmentation Including Soft Gluon Interference”. *Nucl. Phys. B* 238 (1984), pp. 492–528.
- [55] F. Mandl and G. Shaw. *Quantum Field Theory*. Wiley, Apr. 2010. ISBN: 978-0-471-49683-0.
- [56] S. Weinberg. “Nonabelian Gauge Theories of the Strong Interactions”. *Phys. Rev. Lett.* 31 (1973), pp. 494–497.
- [57] C. Yang and R. L. Mills. “Conservation of Isotopic Spin and Isotopic Gauge Invariance”. *Phys. Rev.* 96 (1954). Ed. by Jong-Ping Hsu and D. Fine, pp. 191–195.
- [58] M. E. Peskin and D. V. Schroeder. *An Introduction to quantum field theory*. Reading, USA: Addison-Wesley, 1995. ISBN: 978-0-201-50397-5.
- [59] M. Srednicki. *Quantum field theory*. Cambridge University Press, Jan. 2007. ISBN: 978-0-521-86449-7, 978-0-511-26720-8.
- [60] A. Zee. *Quantum field theory in a nutshell*. 2003. ISBN: 978-0-691-14034-6.

- [61] G. 't Hooft and M. Veltman. "Combinatorics of gauge fields". *Nuclear Physics B* 50.1 (1972), pp. 318–353.
- [62] M. D. Schwartz. *Quantum Field Theory and the Standard Model*. Cambridge University Press, Mar. 2014. ISBN: 978-1-107-03473-0, 978-1-107-03473-0.
- [63] R. K. Ellis, W. J. Stirling, and B. R. Webber. *QCD and collider physics*. Vol. 8. Cambridge University Press, Feb. 2011. ISBN: 978-0-511-82328-2, 978-0-521-54589-1.
- [64] G. F. Sterman. *An Introduction to quantum field theory*. Cambridge University Press, Aug. 1993. ISBN: 978-0-521-31132-8.
- [65] G. 't Hooft and M. J. G. Veltman. "Regularization and Renormalization of Gauge Fields". *Nucl. Phys. B* 44 (1972), pp. 189–213.
- [66] G. 't Hooft. "Dimensional regularization and the renormalization group". *Nucl. Phys. B* 61 (1973), pp. 455–468.
- [67] J. C. Collins. *Renormalization: An Introduction to Renormalization, The Renormalization Group, and the Operator Product Expansion*. Vol. 26. Cambridge Monographs on Mathematical Physics. Cambridge: Cambridge University Press, 1986. ISBN: 978-0-521-31177-9, 978-0-511-86739-2.
- [68] G. Dissertori, I. G Knowles, and M. Schmelling. *Quantum Chromodynamics, High energy experiments and theory*. 2003. ISBN: 978-0-199-56641-9 978-0-521-31132-8.
- [69] M. Levy and J. Sucher. "Eikonal approximation in quantum field theory". *Phys. Rev.* 186 (1969), pp. 1656–1670.
- [70] D. J. Pritchard and W. J. Stirling. "QCD Calculations in the Light Cone Gauge." *Nucl. Phys. B* 165 (1980), pp. 237–268.
- [71] A. Bassetto, M. Ciafaloni, and G. Marchesini. "Jet Structure and Infrared Sensitive Quantities in Perturbative QCD". *Phys. Rept.* 100 (1983), pp. 201–272.
- [72] S. Catani and M. Grazzini. "The soft gluon current at one loop order". *Nucl. Phys. B* 591 (2000), pp. 435–454. arXiv: [hep-ph/0007142](https://arxiv.org/abs/hep-ph/0007142).
- [73] R. D. Field. *Applications of Perturbative QCD*. Vol. 77. 1989.
- [74] Gianluca Oderda and George F. Sterman. "Energy and color flow in dijet rapidity gaps". *Phys. Rev. Lett.* 81 (1998), pp. 3591–3594. arXiv: [hep-ph/9806530](https://arxiv.org/abs/hep-ph/9806530).
- [75] Gianluca Oderda. "Dijet rapidity gaps in photoproduction from perturbative QCD". *Phys. Rev. D* 61 (2000), p. 014004. arXiv: [hep-ph/9903240](https://arxiv.org/abs/hep-ph/9903240).
- [76] C. F. Berger, T. Kucs, and G. F. Sterman. "Energy flow in interjet radiation". *Phys. Rev. D* 65 (2002), p. 094031. arXiv: [hep-ph/0110004](https://arxiv.org/abs/hep-ph/0110004).

- [77] S. Catani, D. de Florian, and G. Rodrigo. "Space-like (versus time-like) collinear limits in QCD: Is factorization violated?" *JHEP* 07 (2012), p. 026. arXiv: [1112.4405 \[hep-ph\]](#).
- [78] J. R. Forshaw, M. H. Seymour, and A. Siodmok. "On the Breaking of Collinear Factorization in QCD". *JHEP* 11 (2012), p. 066. arXiv: [1206.6363 \[hep-ph\]](#).
- [79] T. Muta. *Foundations of Quantum Chromodynamics: An Introduction to Perturbative Methods in Gauge Theories*. 3rd. Vol. 78. World scientific Lecture Notes in Physics. Hackensack, N.J.: World Scientific, 2010. ISBN: 978-981-279-353-9.
- [80] F. Bloch and A. Nordsieck. "Note on the Radiation Field of the electron". *Phys. Rev.* 52 (1937), pp. 54–59.
- [81] T. Kinoshita. "Mass singularities of Feynman amplitudes". *J. Math. Phys.* 3 (1962), pp. 650–677.
- [82] T. D. Lee and M. Nauenberg. "Degenerate Systems and Mass Singularities". *Phys. Rev.* 133 (1964). Ed. by G. Feinberg, B1549–B1562.
- [83] S. Catani et al. "Resummation of large logarithms in e+ e- event shape distributions". *Nucl. Phys. B* 407 (1993), pp. 3–42.
- [84] S. Catani and B. R. Webber. "Resummed C parameter distribution in e+ e- annihilation". *Phys. Lett. B* 427 (1998), pp. 377–384. arXiv: [hep-ph/9801350](#).
- [85] Y. L. Dokshitzer et al. "On the QCD analysis of jet broadening". *JHEP* 01 (1998), p. 011. arXiv: [hep-ph/9801324](#).
- [86] V. Antonelli, M. Dasgupta, and G. P. Salam. "Resummation of thrust distributions in DIS". *JHEP* 02 (2000), p. 001. arXiv: [hep-ph/9912488](#).
- [87] C. F. Berger, T. Kucs, and G. F. Sterman. "Event shape / energy flow correlations". *Phys. Rev. D* 68 (2003), p. 014012. arXiv: [hep-ph/0303051](#).
- [88] A. Banfi, G. P. Salam, and G. Zanderighi. "Resummed event shapes at hadron - hadron colliders". *JHEP* 08 (2004), p. 062. arXiv: [hep-ph/0407287](#).
- [89] M. Dasgupta and G. P. Salam. "Event shapes in e+ e- annihilation and deep inelastic scattering". *J. Phys. G* 30 (2004), R143. arXiv: [hep-ph/0312283](#).
- [90] M. Dasgupta et al. "Logarithmic accuracy of parton showers: a fixed-order study". *JHEP* 09 (2018). [Erratum: *JHEP* 03, 083 (2020)], p. 033. arXiv: [1805.09327 \[hep-ph\]](#).

- [91] A. Banfi, G. P. Salam, and G. Zanderighi. “Generalized resummation of QCD final state observables”. *Phys. Lett. B* 584 (2004), pp. 298–305. arXiv: [hep-ph/0304148](#).
- [92] A. Banfi, G. P. Salam, and G. Zanderighi. “Phenomenology of event shapes at hadron colliders”. *JHEP* 06 (2010), p. 038. arXiv: [1001.4082 \[hep-ph\]](#).
- [93] E. Farhi. “A QCD Test for Jets”. *Phys. Rev. Lett.* 39 (1977), pp. 1587–1588.
- [94] R. W. L. Jones et al. “Theoretical uncertainties on alpha(s) from event shape variables in e+ e- annihilations”. *JHEP* 12 (2003), p. 007. arXiv: [hep-ph/0312016](#).
- [95] M. T. Ford. “Studies of event shape observables with the OPAL detector at LEP”. PhD thesis. Cambridge U., 2004. arXiv: [hep-ex/0405054](#).
- [96] M. Dasgupta and G. P. Salam. “Resummation of nonglobal QCD observables”. *Phys. Lett. B* 512 (2001), pp. 323–330. arXiv: [hep-ph/0104277 \[hep-ph\]](#).
- [97] F. Maltoni et al. “Color flow decomposition of QCD amplitudes”. *Phys. Rev. D* 67 (2003), p. 014026. arXiv: [hep-ph/0209271 \[hep-ph\]](#).
- [98] W. Kilian et al. “QCD in the Color-Flow Representation”. *JHEP* 10 (2012), p. 022. arXiv: [1206.3700 \[hep-ph\]](#).
- [99] R. Á. Martínez et al. “Soft gluon evolution and non-global logarithms” (2018). arXiv: [1802.08531 \[hep-ph\]](#).
- [100] M. Dasgupta and G. P. Salam. “Accounting for coherence in interjet E(t) flow: A Case study”. *JHEP* 03 (2002), p. 017. arXiv: [hep-ph/0203009](#).
- [101] Y. L. Dokshitzer and G. Marchesini. “Soft gluons at large angles in hadron collisions”. *JHEP* 01 (2006), p. 007. arXiv: [hep-ph/0509078](#).
- [102] S. Catani and M.H. Seymour. “The Dipole formalism for the calculation of QCD jet cross-sections at next-to-leading order”. *Phys. Lett. B* 378 (1996), pp. 287–301. arXiv: [hep-ph/9602277](#).
- [103] J. R. Forshaw, J. Holguin, and S. Plätzer. “Parton branching at amplitude level”. *JHEP* 08 (2019), p. 145. arXiv: [1905.08686 \[hep-ph\]](#).
- [104] Y. Delenda and K. Khelifa-Kerfa. “Eikonal gluon bremsstrahlung at finite N_c beyond two loops”. *Phys. Rev. D* 93.5 (2016), p. 054027. arXiv: [1512.05401 \[hep-ph\]](#).
- [105] K. Khelifa-Kerfa and Y. Delenda. “Non-global logarithms at finite N_c beyond leading order”. *JHEP* 03 (2015), p. 094. arXiv: [1501.00475 \[hep-ph\]](#).
- [106] G. Gustafson and U. Pettersson. “Dipole Formulation of QCD Cascades”. *Nucl. Phys. B* 306 (1988), pp. 746–758.

- [107] L. Lönnblad. “Ariadne version 4: A Program for simulation of QCD cascades implementing the color dipole model”. *Comput. Phys. Commun.* 71 (1992), pp. 15–31.
- [108] S. Plätzer and M. Sjö Dahl. “The Sudakov Veto Algorithm Reloaded”. *Eur. Phys. J. Plus* 127 (2012), p. 26. arXiv: [1108.6180 \[hep-ph\]](#).
- [109] T. Gleisberg and S. Hoeche. “Comix, a new matrix element generator”. *JHEP* 12 (2008), p. 039. arXiv: [0808.3674 \[hep-ph\]](#).
- [110] S. Gieseke et al. “Colour Reconnection from Soft Gluon Evolution”. *JHEP* 11 (2018), p. 149. arXiv: [1808.06770 \[hep-ph\]](#).
- [111] M. De Angelis. “Non-global Logarithms beyond Leading Colour”. QCD@LHC 2018. 2018.
- [112] A. Banfi, G. Marchesini, and G. Smye. “Away from jet energy flow”. *JHEP* 08 (2002), p. 006. arXiv: [hep-ph/0206076 \[hep-ph\]](#).
- [113] S. Ulam, R. D. Richtmyer, and J. von Neumann. “Statistical methods in neutron diffusion”. *Alamos Scientific Laboratory report LAMS-55 1* (1947).
- [114] G. Cullen et al. “GOSAM-2.0: a tool for automated one-loop calculations within the Standard Model and beyond”. *Eur. Phys. J. C* 74.8 (2014), p. 3001. arXiv: [1404.7096 \[hep-ph\]](#).
- [115] G. Cullen et al. “Automated One-Loop Calculations with GoSam”. *Eur. Phys. J. C* 72 (2012), p. 1889. arXiv: [1111.2034 \[hep-ph\]](#).
- [116] J. Alwall et al. “The automated computation of tree-level and next-to-leading order differential cross sections, and their matching to parton shower simulations”. *JHEP* 07 (2014), p. 079. arXiv: [1405.0301 \[hep-ph\]](#).
- [117] S. Badger, B. Biedermann, and P. Uwer. “NGLuon: A Package to Calculate One-loop Multi-gluon Amplitudes”. *Comput. Phys. Commun.* 182 (2011), pp. 1674–1692. arXiv: [1011.2900 \[hep-ph\]](#).
- [118] S. Badger et al. “Numerical evaluation of virtual corrections to multi-jet production in massless QCD”. *Comput. Phys. Commun.* 184 (2013), pp. 1981–1998. arXiv: [1209.0100 \[hep-ph\]](#).
- [119] F. Buccioni et al. “OpenLoops 2”. *Eur. Phys. J. C* 79.10 (2019), p. 866. arXiv: [1907.13071 \[hep-ph\]](#).
- [120] K. Arnold et al. “VBFNLO: A Parton level Monte Carlo for processes with electroweak bosons”. *Comput. Phys. Commun.* 180 (2009), pp. 1661–1670. arXiv: [0811.4559 \[hep-ph\]](#).
- [121] F. Campanario et al. “Electroweak Higgs Boson Plus Three Jet Production at Next-to-Leading-Order QCD”. *Phys. Rev. Lett.* 111.21 (2013), p. 211802. arXiv: [1308.2932 \[hep-ph\]](#).

- [122] S. Gieseke, P. Stephens, and B. Webber. “New formalism for QCD parton showers”. *JHEP* 12 (2003), p. 045. arXiv: [hep-ph/0310083](https://arxiv.org/abs/hep-ph/0310083).
- [123] B. Andersson et al. “Parton Fragmentation and String Dynamics”. *Phys. Rept.* 97 (1983), pp. 31–145.
- [124] T. D. Gottschalk and D. A. Morris. “A New Model for Hadronization and e^+e^- Annihilation”. *Nucl. Phys. B* 288 (1987), pp. 729–781.
- [125] T. Sjöstrand. “Status of Fragmentation Models”. *Int. J. Mod. Phys. A* 3 (1988), p. 751.
- [126] *HEPForge*. 2018. URL: <https://www.hepforge.org/> (visited on 03/18/2021).
- [127] A. Buckley et al. “General-purpose event generators for LHC physics”. *Phys. Rept.* 504 (2011), pp. 145–233. arXiv: [1101.2599](https://arxiv.org/abs/1101.2599) [hep-ph].
- [128] P. Skands. “Introduction to QCD”. *Theoretical Advanced Study Institute in Elementary Particle Physics: Searching for New Physics at Small and Large Scales*. July 2012. arXiv: [1207.2389](https://arxiv.org/abs/1207.2389) [hep-ph].
- [129] F. James. “Monte Carlo Theory and Practice”. *Rept. Prog. Phys.* 43 (1980), p. 1145.
- [130] G. Wahnström. *Monte Carlo Lecture Notes*. http://fy.chalmers.se/~tfsgw/CompPhys/lectures/MC_LectureNotes_171114.pdf. 2017.
- [131] J. Beringer et al. “Review of Particle Physics (RPP)”. *Phys. Rev. D* 86 (2012), p. 010001.
- [132] L. C. Noll, R. G. Mende, and S. Sisodiya. “Method for seeding a pseudo-random number generator with a cryptographic hash of a digitization of a chaotic system”. Pat. US5732138A. 1998.
- [133] S. Weinzierl. “Introduction to Monte Carlo methods” (2000). arXiv: [hep-ph/0006269](https://arxiv.org/abs/hep-ph/0006269).
- [134] G. Marsaglia. *The Marsaglia Random Number CDROM including the Diehard Battery of Tests of Randomness*. 1995. URL: <https://web.archive.org/web/20160125103112/http://stat.fsu.edu/pub/diehard/>.
- [135] D. E. Knuth. *The Art of Computer Programming, Volume 2 (3rd Ed.): Seminumerical Algorithms*. USA: Addison-Wesley Longman Publishing Co., Inc., 1997. ISBN: 0201896842.
- [136] Compaq. *Compaq Fortran Language Reference Manual*. formerly DIGITAL Fortran and DEC Fortran 90. Sept. 1999.
- [137] M. Matsumoto and T. Nishimura. “Mersenne Twister: A 623-Dimensionally Equidistributed Uniform Pseudo-Random Number Generator”. 8.1 (1998), 3–30.

- [138] Chudakov A. “On an Ionization Effect Related to the Observation of Electron Positron Pairs at very high Energies”. *Bull. Acad. Sci. USSR* (1955), pp. 589–595.
- [139] G. Marchesini and B. R. Webber. “Simulation of QCD Jets Including Soft Gluon Interference”. *Nucl. Phys. B* 238 (1984), pp. 1–29.
- [140] G. Altarelli and G. Parisi. “Asymptotic Freedom in Parton Language”. *Nucl. Phys. B* 126 (1977), pp. 298–318.
- [141] T. Sjöstrand. “Monte Carlo Tools”. *65th Scottish Universities Summer School in Physics: LHC Physics*. Nov. 2009. arXiv: [0911.5286 \[hep-ph\]](#).
- [142] T. Sjöstrand. “Monte Carlo Generators”. *2006 European School of High-Energy Physics*. Nov. 2006. arXiv: [hep-ph/0611247](#).
- [143] V. V. Sudakov. “Vertex parts at very high-energies in quantum electrodynamics”. *Sov. Phys. JETP* 3 (1956), pp. 65–71.
- [144] L. Lönnblad. “Fooling Around with the Sudakov Veto Algorithm”. *Eur. Phys. J. C* 73.3 (2013), p. 2350. arXiv: [1211.7204 \[hep-ph\]](#).
- [145] R. Kleiss and R. Verheyen. “Competing Sudakov Veto Algorithms”. *Eur.Phys.J.C* 76.7 (2016), p. 359. arXiv: [1605.09246 \[hep-ph\]](#).
- [146] S. Plätzer and M. Sjö Dahl. “Subleading N_c improved Parton Showers”. *JHEP* 07 (2012), p. 042. arXiv: [1201.0260 \[hep-ph\]](#).
- [147] Z. Nagy and D. E. Soper. “Parton shower evolution with subleading color”. *JHEP* 06 (2012), p. 044. arXiv: [1202.4496 \[hep-ph\]](#).
- [148] Z. Nagy and D E. Soper. “A parton shower based on factorization of the quantum density matrix”. *JHEP* 06 (2014), p. 097. arXiv: [1401.6364 \[hep-ph\]](#).
- [149] Z. Nagy and D. E. Soper. “Effects of subleading color in a parton shower”. *JHEP* 07 (2015), p. 119. arXiv: [1501.00778 \[hep-ph\]](#).
- [150] Z. Nagy and D. E. Soper. “What is a parton shower?” (2017). arXiv: [1705.08093 \[hep-ph\]](#).
- [151] Z. Nagy and D. E. Soper. “Effect of color on rapidity gap survival”. *Phys. Rev. D* 100.7 (2019), p. 074012. arXiv: [1905.07176 \[hep-ph\]](#).
- [152] Z. Nagy and D. E. Soper. “Parton showers with more exact color evolution”. *Phys. Rev. D* 99.5 (2019), p. 054009. arXiv: [1902.02105 \[hep-ph\]](#).
- [153] E. Bothmann et al. “Event Generation with Sherpa 2.2”. *SciPost Phys.* 7.3 (2019), p. 034. arXiv: [1905.09127 \[hep-ph\]](#).
- [154] S. Plätzer. “Summing Large- N Towers in Colour Flow Evolution”. *Eur. Phys. J. C* 74 (2014), p. 2907. arXiv: [1312.2448 \[hep-ph\]](#).

- [155] M. De Angelis, J. R. Forshaw, and S. Plätzer. *Resummation and simulation of soft gluon effects beyond leading colour*. 2020. arXiv: [2007.09648](https://arxiv.org/abs/2007.09648) [hep-ph].
- [156] S. Weinzierl. “Automated computation of spin- and colour-correlated Born matrix elements”. *Eur. Phys. J. C* 45 (2006), pp. 745–757. arXiv: [hep-ph/0510157](https://arxiv.org/abs/hep-ph/0510157).
- [157] J. Holguin. “QCD coherence and how it fails”. YTF (Young Theorists Forum) 12. 2019.
- [158] J. R. Forshaw and J. Holguin. “Coulomb gluons will generally destroy coherence”. Discussions with J. Forshaw and J. Holguin on forthcoming publication. 2020.
- [159] C. B. Moler and C. F. Van Loan. “Nineteen Dubious Ways to Compute the Exponential of a Matrix, Twenty-Five years Later”. *SIAM* 45 (1 2003), pp. 3–49.
- [160] A. H. Al-Mohy and N. J. Higham. “A New Scaling and Squaring Algorithm for the Matrix Exponential”. *SIAM Journal on Matrix Analysis and Applications* 31.3 (2010), pp. 970–989. eprint: <https://doi.org/10.1137/09074721X>.
- [161] M. De Angelis. “News on Colour Evolution with CVolver”. Parton Showers and Resummation 2019. 2019.
- [162] S. Roman. *The Umbral Calculus*. New York: Academic Press, 1984, pp. 59–63.
- [163] J. Riordan. *An Introduction to Combinatorial Analysis*. New York: Wiley, 1980.
- [164] B.R. Webber. “Monte Carlo Simulation of Hard Hadronic Processes”. *Ann. Rev. Nucl. Part. Sci.* 36 (1986), pp. 253–286.
- [165] M. L. Mangano and S. J. Parke. “Multiparton amplitudes in gauge theories”. *Phys. Rept.* 200 (1991), pp. 301–367. arXiv: [hep-th/0509223](https://arxiv.org/abs/hep-th/0509223).
- [166] L. J. Dixon. “A brief introduction to modern amplitude methods”. *Theoretical Advanced Study Institute in Elementary Particle Physics: Particle Physics: The Higgs Boson and Beyond*. 2014, pp. 31–67. arXiv: [1310.5353](https://arxiv.org/abs/1310.5353) [hep-ph].
- [167] Y. Hatta and T. Ueda. “Non-global logarithms in hadron collisions at $N_c = 3$ ”. *Nucl. Phys. B* 962 (2021), p. 115273. arXiv: [2011.04154](https://arxiv.org/abs/2011.04154) [hep-ph].
- [168] T. Williams, C. Kelley, et al. *Gnuplot 4.6: an interactive plotting program*. <http://gnuplot.sourceforge.net/>. Apr. 2013.
- [169] R. Mears. “Amplitude Level Evolution in QCD”. MA thesis. The University of Manchester, 2020.

- [170] B. Gough. *GNU Scientific Library Reference Manual - Third Edition*. 3rd. Network Theory Ltd., 2009. ISBN: 0954612078.
- [171] G. P. Lepage. “A new algorithm for adaptive multidimensional integration”. *Journal of Computational Physics* 27.2 (1978), pp. 192–203.
- [172] C. Sanderson and R. Curtin. “Armadillo: a template-based C++ library for linear algebra”. *Journal of Open Source Software* 1.2 (2016), p. 26.
- [173] Boost. *Boost C++ Libraries V 1.46.0*. <http://www.boost.org/>. 2011.
- [174] H. Weigert. “Nonglobal jet evolution at finite N_c ”. *Nucl. Phys.* B685 (2004), pp. 321–350. arXiv: [hep-ph/0312050](https://arxiv.org/abs/hep-ph/0312050) [hep-ph].
- [175] Y. Hatta and T. Ueda. “Resummation of non-global logarithms at finite N_c ”. *Nucl. Phys.* B874 (2013), pp. 808–820. arXiv: [1304.6930](https://arxiv.org/abs/1304.6930) [hep-ph].
- [176] Y. Hatta. “Relating $e^+ e^-$ annihilation to high energy scattering at weak and strong coupling”. *JHEP* 11 (2008), p. 057. arXiv: [0810.0889](https://arxiv.org/abs/0810.0889) [hep-ph].
- [177] M. D. Schwartz and H. X. Zhu. “Nonglobal logarithms at three loops, four loops, five loops, and beyond”. *Phys. Rev.* D90.6 (2014), p. 065004. arXiv: [1403.4949](https://arxiv.org/abs/1403.4949) [hep-ph].
- [178] S. Caron-Huot. “Resummation of non-global logarithms and the BFKL equation” (2015). arXiv: [1501.03754](https://arxiv.org/abs/1501.03754) [hep-ph].
- [179] A. J. Larkoski, I. Moult, and D. Neill. “Non-Global Logarithms, Factorization, and the Soft Substructure of Jets”. *JHEP* 09 (2015), p. 143. arXiv: [1501.04596](https://arxiv.org/abs/1501.04596) [hep-ph].
- [180] A. J. Larkoski, I. Moult, and D. Neill. “The Analytic Structure of Non-Global Logarithms: Convergence of the Dressed Gluon Expansion”. *JHEP* 11 (2016), p. 089. arXiv: [1609.04011](https://arxiv.org/abs/1609.04011) [hep-ph].
- [181] T. Becher et al. “Factorization and Resummation for Jet Processes”. *JHEP* 11 (2016). [Erratum: *JHEP*05,154(2017)], p. 019. arXiv: [1605.02737](https://arxiv.org/abs/1605.02737) [hep-ph].
- [182] Y. Hatta et al. “Resumming double non-global logarithms in the evolution of a jet” (2017). arXiv: [1710.06722](https://arxiv.org/abs/1710.06722) [hep-ph].
- [183] J. Olsson, S. Plätzer, and M. Sjö Dahl. “Resampling Algorithms for High Energy Physics Simulations”. *Eur. Phys. J. C* 80.10 (2020), p. 934. arXiv: [1912.02436](https://arxiv.org/abs/1912.02436) [hep-ph].